Edge-on Measurements on Planar Pixel Sensors for the CMS Phase 2 Upgrade

Dissertation zur Erlangung des Doktorgrades

an der Fakultät für Mathematik, Informatik und Naturwissenschaften

Fachbereich Physik

der Universität Hamburg

vorgelegt von

Caroline Elisabeth Niniane Niemeyer

Hamburg

2021

Eidesstattliche Versicherung

Hiermit versichere ich an Eides statt, die vorliegende Dissertationsschrift selbst verfasst und keine anderen als die angegebenen Hilfsmittel und Quellen benutzt zu haben. Die eingereichte schriftliche Fassung entspricht der auf dem elektronischen Speichermedium. Die Dissertation wurde in der vorgelegten oder einer ähnlichen Form nicht schon einmal in einem früheren Promotionsverfahren angenommen oder als ungenügend beurteilt.

Hamburg, den 18.06.2021   _____

Unterschrift

Abstract

In the development process of a new pixel detector for the Phase 2 upgrade of CMS, several variants of new n^+p, planar pixel sensors with pixel sizes of $50 \times 50\,\mu m^2$ and $25 \times 100\,\mu m^2$ and an active thickness of $150\,\mu m$ have been designed and bump bonded to ROC4SENS read out chips. Many weeks of beam tests with sensors irradiated up to fluences of 16×10^{15} neutrons/cm^2 have been completed at the DESY test beam facility. Previous studies into the dependence of charge collection on the depth in the silicon sensor have applied the grazing angle technique. This however suffers a lot from resolution effects with the thinner sensors, therefore the grazing angle technique was refined to the edge-on method, where the beam hits the sensor parallel to the sensor surface and travels at one depth through the entire length of the sensor.

The edge-on method is used to measure the charge collection of $25 \times 100\,\mu m^2$ pixel sensors as a function of depth for different operating conditions. Additionally, the influence of radiation damage from neutrons with an energy larger than $100\,keV$ and $23\,GeV$ protons on the charge collection profile is investigated. The depth performance of the sensors as a function of fluence and bias voltage is then compared to simulations with PIXELAV.

Due to the non-zero suppressed chip, it is possible to investigate the charge sharing between the neighboring pixels without any threshold effects. For the first time, with these so called edge-on tomography plots the negative charge induced in the neighboring pixels can be visualized. The position dependent charge collection can be obtained and provides insight into the radiation damage effects on the sensor.

Furthermore, the resolution of the pixel cell itself was measured for different angles of beam incidence without an external beam telescope as a reference plane. Instead the pixels before and after the hit pixel itself are used as reference and thus allow for in-silicon tracking as the beam hits the sensor edge-on. The resolution for a $25 \times 100\,\mu m^2$ pixel sensor was determined to be $2.2\,\mu m$ with errors on the nanometer level.

Kurzzusammenfassung

Im Entwicklungsprozess eines neuen Pixeldetektors für das Phase 2 Upgrade des CMS Experiments, sind mehrere Varianten von neuen n^+p, planaren Pixelsensoren mit Pixelgrößen von $50 \times 50\,\mu m^2$ und $25 \times 100\,\mu m^2$ und einer aktiven Dicke von $150\,\mu m^2$ entworfen und auf ROC4SENS-Auslesechips gebondet worden. Viele Wochen Strahltests mit Sensoren, bestrahlt bis zu Fluenzen von 16×10^{15} Neutronen/cm^2, sind am DESY-Teststrahl durchgeführt worden.

In früheren Studien über die Abhängigkeit der Ladungssammlung von der Tiefe im Siliziumsensor wurde die Streifwinkeltechnik angewandt. Diese leidet jedoch bei den dünneren Sensoren stark unter Auflösungseffekten, deshalb wurde die Streifwinkeltechnik zur Edge-on Methode verfeinert, bei der der Strahl parallel zur Sensoroberfläche auf den Sensor trifft und in einer gleichbleibenden Tiefe durch die gesamte Länge des Sensors verläuft.

Die Edge-on Methode wird verwendet, um die Ladungssammlung von $25 \times 100\,\mu m^2$ Pixelsensoren als Funktion der Tiefe für verschiedene Betriebsbedingungen zu messen. Zusätzlich wird der Einfluss von Strahlungsschäden durch Neutronen mit einer Energie größer als $100\,keV$ und $23\,GeV$ Protonen auf das Ladungssammlungsprofil untersucht. Die Ladungssammlung in der Tiefe der Sensoren als Funktion der Fluenz und der Biasspannung wird anschließend mit PIXELAV Simulationen verglichen. Aufgrund des ROC4SENS Chips, der keine Ladungsschwelle benötigt, ist es möglich, die Ladungsteilung zwischen benachbarten Pixeln zu untersuchen. Mit dieser sogenannten Edge-on Tomografie kann zum ersten Mal die in den benachbarten Pixeln induzierte negative Ladung sichtbar gemacht werden. Die positionsabhängige Ladungssammlung wird sichtbar und ermöglicht so tiefere Einsicht in die Strahlenschädigung des Sensors.

Desweiteren wurde die Auflösung der Pixelzelle selbst für verschiedene Strahleinfallswinkel ohne ein externes Strahlteleskop als Referenzebene gemessen. Stattdessen werden die Pixel vor und nach dem getroffenen Pixel selbst als Referenz verwendet und ermöglichen so eine Verfolgung der Spur im Silizium, da der Strahl den Sensor parallel zur Oberfläche trifft. Für einen Pixelsensor mit der Pixelgröße $25 \times 100\,\mu m^2$ wurde eine Auflösung von $2.2\,\mu m$ mit Fehlern im Nanometerbereich bestimmt.

Contents

1. Introduction

According to Oxford, science is 'the intellectual and practical activity encompassing the systematic study of the structure and behavior of the physical and natural world through observation and experiment' [1]. Everyday we observe the world and its phenomena around us, with solid matter playing a vital role in our daily life. To understand the very basics of the world around us, such as the fundamental constituents of matter, is the goal of modern particle physics.

Since the 1960s [2], the underlying theoretical framework for particle physics is the Standard Model (SM). The model represents the current expertise and summarizes all known particles and their interactions. Over the years it has explained many experimental results and by now it provides precise predictions for a range of phenomena. However, the model only describes about 4% of the known universe and open questions remain. In the search for answers particle collisions are used to probe further into the elementary constituents of matter. The underlying principle is Einstein's law $E = mc^2$ [3], which is used as particles are accelerated to high energies and are subsequently collided to produce new and unknown particles. These new particles were not necessarily part of the previously collided particles as the energy that is freed during the collision can form any new particle with a mass equal or smaller than the released energy, according to energy conservation.

To detect these potentially new particles and trace their origin, huge detectors are necessary with many components for detecting the precise tracks and energies of the newly produced particles. The Large Hadron Collider (LHC) at the European Organization for Nuclear Research (CERN) in Geneva is presently the world's leading accelerator complex. It has many different accelerators to achieve the highly energetic protons that are collided at the innermost points of four different detectors. One of these four is the Compact Muon Solenoid (CMS) detector, located in an underground cavern near Cessy in France. The detector is built in a cylindrical shape around the interaction point, with several subsystems arranged in multiple layers. The detector closest to the interaction point is the tracker, its purpose is the reconstruction of the trajectories of ionizing particles originating from the collisions. Hereby each measured particle is assigned to a vertex and thus the individual interactions are reconstructed.

To distinguish the different particles inside the tracker, detectors with a high position resolution are needed. Since the 1960s semiconductors have been used as particle detectors [4]. Silicon is the dominant semiconductor material used in the production of position

sensitive detectors for particle physics. The moderate band gap between the conduction and the valence band of 1.12 eV is large compared to the thermal energy at room temperature of 25.9 meV [5]. Thus cooling is only necessary in ultra-low noise applications or when needed to mitigate radiation damage effects. In addition, silicon is widely available, as it is a major part of the Earth's crust and thus it is found in practically all rocks and soils, combined either with oxygen as silica or with oxygen and other elements as silicates. Due to its availability and low price compared to other semiconductors, such as diamond, silicon is used in a number of applications, such as computers, solar cells, and telecommunication systems. Since the late 1980s silicon sensors have been widely used in collider experiments as silicon microstrip or silicon pixel detectors near the primary vertex [6]. SVX, the first Silicon VerteX detector at a hadron collider, was installed in the collider detector at Fermilab (CDF) for the start of Run 1A of the Tevatron in 1992 [7].

Since then silicon sensors have changed, the properties of silicon have been thoroughly investigated over the years and are well known. However, the link between microscopic defects in the silicon crystal and the resulting change in the silicon sensor performance especially after irradiation is still under investigation. For the high irradiation levels expected in the Phase II upgrade of the LHC, the influence of radiation damage on the sensor performance still needs to be investigated.

Several silicon sensors have been designed with different geometries and different isolation schemes. In this thesis the charge collection profiles of the pixel sensors for the Phase II upgrade of the CMS Inner Tracker are analyzed as a function of depth for different operating conditions. This will provide insight into the degradation of the sensor signal as a function of position in the sensor and can be used as input for simulation studies. Additionally, the intrinsic resolution of the single pixel cell is measured as a function of angle.

This thesis begins with an introduction into the working principles of silicon sensors in Chapter 2. The properties of semiconductors and their use as tracking detectors are discussed. In addition, an overview of the effects of radiation damage on the performance of the sensor is provided.

Chapter 3 provides a description of the LHC and a detailed overview of the different parts of the CMS Phase 1 detector. The changes for the Phase II upgrade are discussed with emphasis on the tracking detector.

In Chapter 4 the different pixel sensor designs, which were produced for the Phase 2 upgrade R&D phase, are introduced. For the sensor modules analyzed in this thesis, the irradiation processes and design differences are discussed in detail. As all sensors were bump bonded to ROC4SENS readout chips, an overview of the chip and its features is provided.

The experimental setup used for the analysis of the sensors is described in Chapter 5. All measurements were performed at the DESY II test beam facilities. The DATURA beam telescope used for the test beam studies is introduced as well as the obtained telescope track resolution. The measurement setup including the data acquisition structure is introduced.

The data taking process for the sensor modules under test is described in Chapter 6. The sensor alignment procedure and the gain calibration of the readout chip are introduced. In addition, the difference in response for different chips is analyzed.

The edge-on method used for measuring the sensors is introduced in Chapter 7. The analysis and the resulting charge collection profiles for irradiated and non-irradiated sensors are presented. A comparison to literature is included. The chapter closes with edge-on tomography plots, where for the first time the negative charge induced into the neighboring pixels is visualized.

Chapter 8 provides an overview of the Hamburg Penta Trap Model, used for simulating the electric field in the sensor. The simulation of the edge-on test beam is performed using PIXELAV, while the noise of the readout electronics and the telescope track resolution are simulated in ROOT.

In Chapter 9 the resolution of the pixelated sensor is measured for different incidence angles of the beam without the help of an external beam telescope as a reference plane. The results are compared to other measurement methods.

Finally, in Chapter 10 the results are summarized and discussed in view of future usability and performance of the investigated silicon sensors.

2. Silicon Sensors

In the search for new particles in modern particle physics experiments, tracking detectors provide key information on the particle's direction and origin. The identification of particles belonging to one single interaction is crucial for experiments at high luminosity colliders, where many interactions occur during one readout cycle of the detector. In high energy particle physics semiconductor sensors are used as tracking detectors. The sensors with their electronics and support structures are the systems closest to the interaction point, as shown in the description of the CMS detector in Chapter 3.2 and thus they are exposed to the highest irradiation levels.

In general, tracking detectors provide information on the trajectory and momentum of charged particles traversing them. Germanium, silicon and diamond are the three semiconductor materials widely used in particle tracking detectors. Silicon, however, is the standard material for vertex and tracking detectors in high energy physics, as it has a medium sized band gap and a low ionization energy, resulting in a high signal-to-noise ratio at room temperature. In addition, silicon profits from established fabrication processes for design and production of sensors available in industry, which results in relatively low production costs.

In all particle physics analyses the quality and performance of the track and vertex reconstruction are of utmost importance and therefore must be guaranteed over the entire running time of the detector. To ensure this, a detailed understanding of the effect of radiation induced damage to silicon detectors under long-term operation is vital.

In this chapter, silicon sensors and their basic properties as well as the underlying physics processes are described mostly based on [8]. As this work aims at a characterization of the sensors' properties after their exposure to irradiation, Section 2.4 provides an overview of the effects of irradiation on the sensors, introducing the physical damaging processes and the resulting consequences on their performance.

2.1. Silicon Semiconductors

Silicon is a widely used material for particle track detectors due to its electrical properties as a semiconductor. This section provides a brief description of the properties of semiconductors. A semiconductor is a material with a characteristic energy band structure, where electrons are confined to a number of bands and forbidden from other parts. The bands are formed by the degeneration of discrete energy levels for the electrons in the atomic shell of unbound atoms. The forbidden parts are the gaps between the energy bands.

Following the Fermi-Dirac distribution for electrons, the probability density function of electrons to be found at an energy level E is described by

$$f(E) = \frac{1}{e^{(E-E_F)/k_B T} + 1} \; ,$$ (1)

where k_B is the Boltzmann constant, T the temperature and E_F the Fermi level. The energy level at which the probability is $f(E_F) = 1/2$ is defined as the Fermi level. To derive a material's electric properties the energy bands closest to the Fermi level are the most relevant. The valence band is the highest energy band fully occupied with electrons at T$= 0$ K, while the band above is called conduction band. Electrons in the conduction band can move across the lattice and contribute to the electrical conductivity. The term band gap denotes the difference in energy between the bottom of the conduction band and the top of the valence band. For a semiconductor the band gap is non-zero but intermediately sized such that with increasing temperature thermal excitation of electrons into the conduction band is feasible while at T$= 0$ K the material is an insulator. The conductivity of semiconductors is therefore strongly dependent on the size of the band gap. The location of the Fermi level in semiconductors compared to insulators and conductors is shown in Figure 2.1. The size of the silicon band gap is $E_g = 1.12$ eV at room temper-
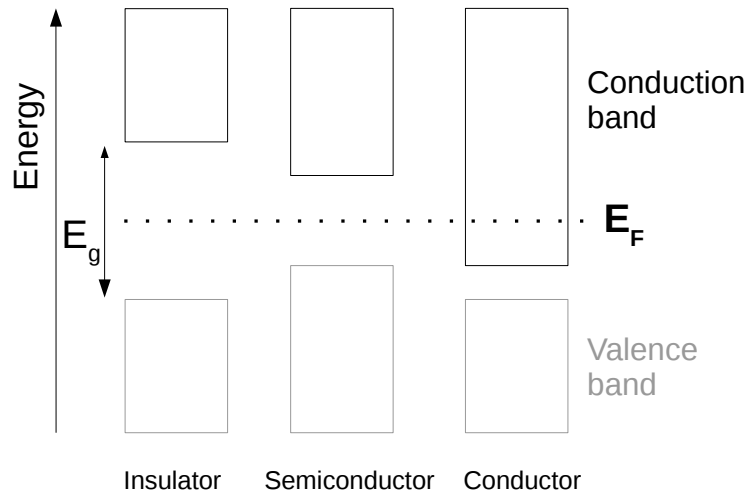
Figure 2.1 – Schematic of the location of the Fermi level in the energy band configuration for insulators, semiconductors and conductors. The band gap E_g is narrow for a semiconductor and for a conductor the Fermi level lies inside the conduction band. Redrawn from [9].

ature. Compared to germanium ($E_g = 0.66$ eV), silicon has a low probability of thermal excitation at room temperature and does not require cooling to mitigate the noise. Charged particles that travel through the semiconductor material deposit a part of their

energy in the sensor. Both energy and momentum must be conserved during this absorption process. Thus, for excitation of an electron into the conduction band, a simultaneous transfer of energy and momentum is required in Ge and Si. For silicon, an energy deposition of $E_e = 3.64\,\text{eV}$ is needed for an electron to be excited into the conduction band [10] and thus create an electron-hole pair. Therefore, the ionization energy is larger than the size of the bandgap, which means that the majority of the absorbed energy goes into phonon excitation. The excitation of one electron into the conduction band leaves a silicon atom with a missing electron, which is referred to as a hole, in the valence band. Both the electron and the hole are charge carriers and add to the electrical conductivity. A semiconductor is called intrinsic if the concentration of impurities is negligible compared to the thermally generated free electrons and holes [8]. However, most silicon sensors used in high energy particle physics are not intrinsic but doped with a small fraction of other materials to alter their conductivity. Silicon is either doped with an element from the third group of the periodic table (e.g. boron) or the fifth group (e.g. phosphorus, arsenic). The latter ones have a weakly bound electron that can easily be released into the conduction band and they are therefore called donors. This can be explained by introducing shallow energy levels, so called donor levels, in the band gap for each doping atom. These donor levels are very close to the conduction band, which means that at room temperature nearly all donor states are ionized and the concentration of electrons n_e equals the concentration of donor atoms N_D. Silicon doped with an element from the fifth group of the periodic table is called n-type silicon, where the electrons are the majority carriers and holes the minority carriers. Boron however has one electron less than silicon in the outer shell and therefore can trap an electron from the valence band to form a covalent bond to the neighboring silicon atom. As this leaves a free hole, boron is called an acceptor. Since acceptor levels are close to the valence band, all boron atoms are ionized at room temperature and the acceptor concentration N_A and the concentration of holes n_h are nearly equal. Silicon doped with an acceptor is called p-type silicon, where holes are the majority carriers and electrons the minority carriers.

2.1.1. The p-n Junction

The working principle of silicon sensors is based on a reversely biased p-n junction. An electric field is built up that collects the signal charge and suppresses the leakage current. In the transition region of n-type and p-type silicon, some of the majority charge carriers of one side diffuse into the other side due to a difference in concentration. Recombination occurs until an equilibrium is achieved which leads to a region close to the junction depleted from free charge carriers. This region is called the depletion zone. It is electrically

charged due to the acceptor and donor ions being left without their reversely charged free carrier and therefore it is also known as the space charge region (SCR).

With the concentrations of donors N_D and acceptors N_A of the types of silicon, the electrical potential within the p-n junction can be calculated by solving Poisson's equation,

$$
\Phi(x) = \begin{cases} -\dfrac{eN_A}{2\epsilon_{\mathrm{Si}}\epsilon_0}(x+d_p)^2, & \text{for } -d_p \le x \le 0 \\[2mm] \dfrac{eN_D}{2\epsilon_{\mathrm{Si}}\epsilon_0}(x-d_n)^2, & \text{for } 0 \le x \le d_n\,, \end{cases} \tag{2}
$$

where e is the elementary charge, ϵ_{Si} the dielectric constant for silicon and ϵ_0 the vacuum permittivity, while d_p and d_n are the widths of the SCR reaching into the p- and n-type parts.

The resulting electric field mitigates the diffusion and is characterized by the built-in voltage V_{bi}, the potential difference across the SCR. The built-in voltage can be determined with the total width of the depletion zone d and the intrinsic silicon charge carrier concentration n_i from

$$
V_{bi} = \frac{k_B T}{e} \cdot \ln\left(\frac{N_A N_D}{n_i^2}\right) = \frac{e\,|N_{tot}|}{2\epsilon_{\mathrm{Si}}\epsilon_0}\cdot d^2\,. \tag{3}
$$

N_{tot} is the total effective doping concentration, which is the difference between the doping concentrations N_D and N_A. The width of the SCR can be changed with an external voltage applied in the same direction as the built-in voltage, leading to a reversely biased junction. With the reverse bias voltage $V_{bias} > 0$, the width of the space charge region can be calculated by extending and inverting Equation 3 to

$$
d = \sqrt{\frac{2\epsilon_{\mathrm{Si}}\epsilon_0}{e\,|N_{tot}|}(V_{bias} + V_{bi})}\,. \tag{4}
$$

Typically, the built-in voltage of approximately $0.5\,\mathrm{V}$ is very small compared to the bias voltage, exceeding $50\,\mathrm{V}$ in most cases [8] and the SCR extends over the entire sensor for operation. The depletion voltage V_{dep} is the voltage needed to extend this mobile-free charge carrier zone to the full depth of the sensor. Neglecting the built-in voltage, the depletion voltage can be determined for a sensor thickness t from

$$
V_{dep} = \frac{e}{2\epsilon_{\mathrm{Si}}\epsilon_0}\cdot|N_{tot}|\cdot t^2\,. \tag{5}
$$

2.1.2. Energy Deposition in Silicon

As most particle physics experiments measure the trajectories of charged particles, this section describes the charge generated by them. Through multiple scattering with electrons of the absorbing material along the particle track, charged particles deposit part of their energy in the sensor. The number of electron-hole pairs generated by moderately relativistic charged heavy particles traversing the silicon sensor can be derived from their average energy loss given by the Bethe-Bloch formula [11]

$$-\left\langle \frac{dE}{dx} \right\rangle = K z^2 \frac{Z}{A} \frac{1}{\beta^2} \left[\frac{1}{2} \ln \frac{2m_e c^2 \beta^2 \gamma^2 W_{max}}{I^2} - \beta^2 - \frac{\delta(\beta\gamma)}{2} \right], \tag{6}$$

with

$\dfrac{dE}{dx}$	energy loss of the particle usually given in $eVg^{-1}cm^2$, since the path dx is defined as the surface density with $dx = \rho \cdot dl$, with the material density ρ and actual path length dl
K	$4\pi\, N_{Av}\, r_e^2\, m_e c^2$ with Avogadro's number N_{Av} and the electron radius r_e
z	primary particle's charge number
Z	atomic number of absorber
A	mass number of absorber
m_e	electron mass
I	mean excitation energy
$\delta(\beta\gamma)$	density effect correction to ionization energy loss
W_{max}	maximum energy transfer to an electron in a single collision.

This formula is valid for a large region of velocities or momenta ($0.1 < \beta\gamma < 1000$). For energies of $\beta\gamma < 1000$ ionization losses are dominating, while at higher momenta the losses from bremsstrahlung prevail. The Bethe-Bloch formula has a minimum at $\beta\gamma \approx 3$, around which the particle is called a minimum ionizing particle (MIP), compare Figure 2.2. By dividing the deposited energy by the average energy needed for ionization I_0, which for silicon is $3.64\,eV$, the number of electron-hole pairs $N_{e,h}$ can be calculated. In silicon the average energy loss is about $390\ eV/\mu m$ for a MIP [6]. This results in

$$N_{e,h} = \frac{390\, \frac{eV}{\mu m}}{3.64\,eV} = 108\, \frac{\text{e-h pairs}}{\mu m}. \tag{7}$$

For a standard volume of $1 \times 1 \times 0.150\,cm^3$ this leads to an average of $16\,200$ electron-hole
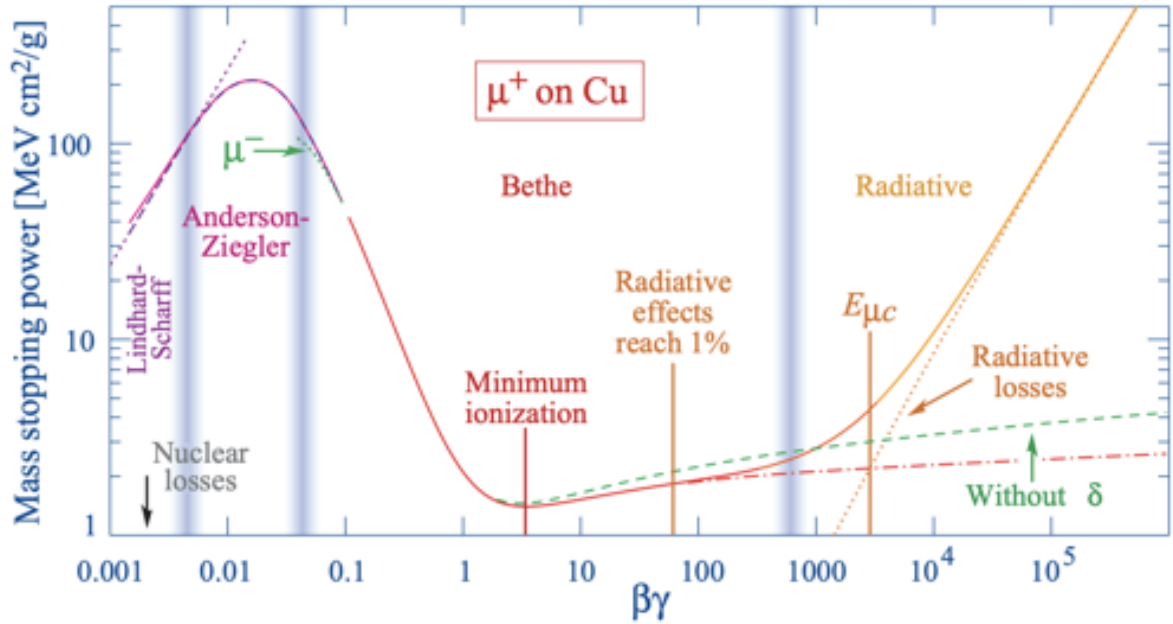
Figure 2.2 – Mean energy loss for a muon in copper. Vertical bands indicate boundaries between different approximations, the central part, which is discussed in this section, is described by the Bethe-Bloch formula. Figure adapted from [11].

pairs created by a MIP in 150 µm silicon.

Landau distribution

The fluctuations of energy loss by ionization of a charged particle in a thin layer of matter were theoretically described by L. Landau [12]. An example of a Landau distribution is shown in Figure 2.3. If a particle continues to travel outside of the sensor, the response fluctuates around the peak of the distribution with a considerable probability of high signals. For thinner sensors, the fluctuation around the maximum of the Landau distribution increases. The mean value of the Landau distribution, calculated from Equation 7, is higher than the most probable value (MPV) of the distribution, due to this tail towards higher energies. The main reason for this are δ-electrons or knock-on electrons which obtain enough energy by the primary ionizing collision to become ionizing particles themselves. Since the direction of the δ-electrons is generally perpendicular to the direction of the incoming particle, they result in irregular charge clusters and degradation of the spatial resolution. Generally the MPV of the energy transfer is about 30% lower than the mean value [6]. This explains the approximation of the MPV for a minimum ionizing particle with unit charge of about 22 000 electrons in 300 µm of silicon [8], as 70% of previously calculated 16 200 electron-hole pairs for a thickness of 150 µm are 11 340.

9
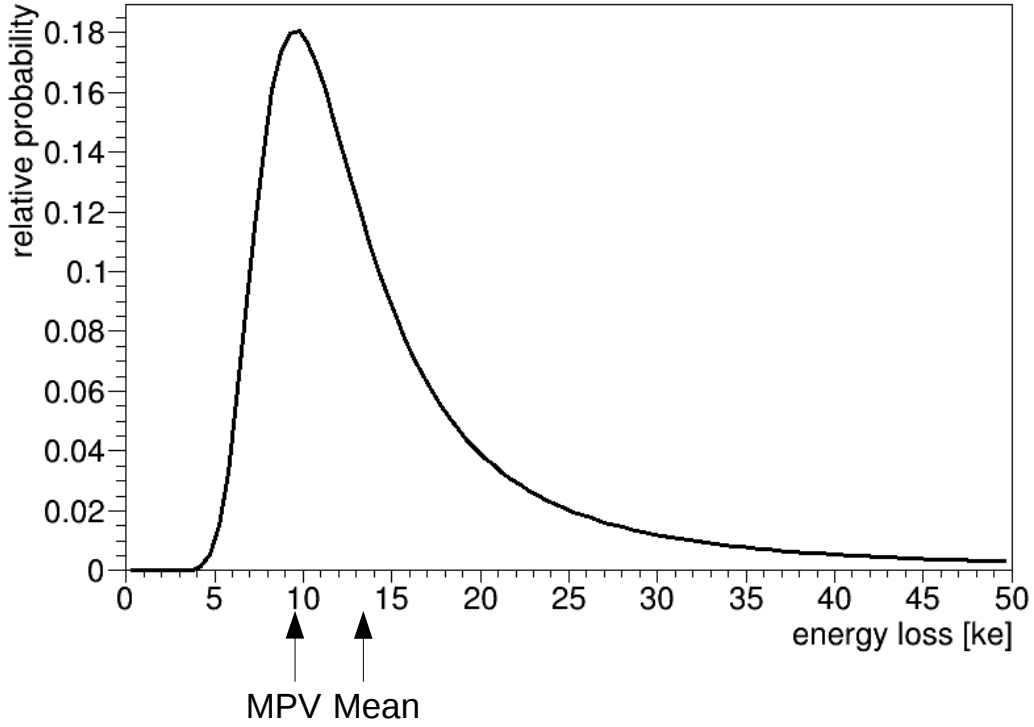
Figure 2.3 – An example of a Landau distribution. The mean value of the Landau distribution is higher than the most probable one due to the long tail of δ-electrons.

2.2. Signal Formation

During the drift time of the charge carriers in the electric field, a current I is induced at the electrodes. The Shockley-Ramo theorem describes the instantaneous signal in the readout electrode for electrons and holes, according to

$$I_{e,h} = \pm q \cdot \vec{E}_W \cdot \vec{\nu}_{e,h} = \pm q \cdot \mu_{e,h} \cdot \vec{E} \cdot \vec{E}_W \quad \text{with } I_h < 0 \text{ if } \vec{E} \cdot \vec{E}_W < 0 \ , \qquad (8)$$

where E_W is the weighting field and $\nu_{e,h}$ is the drift velocity for electrons and holes, respectively. The drift velocity can be expressed as the product of the electric field E and the charge carrier mobility μ, as shown in Equation 13. A negative signal of the holes occurs if the scalar product of the electric field and the weighting field is smaller than 0.

2.2.1. Weighting Field

The weighting field describes the coupling of the moving charge in the sensor to an electrode. In principle the weighting field is time-dependent, however it has recently been shown that for sensors irradiated to fluences $\phi_{\text{eq}} > 10^{14} \, \text{n}_{\text{eq}} \, \text{cm}^{-2}$ it can be considered time

independent [13]. It can therefore be calculated as the difference of the electric field in the biased sensor and 1V added to the readout electronics minus the electric field in the biased sensor [13].

To obtain the collected charge Q_c Equation 8 is integrated according to

$$Q_c = \int_0^t I \mathrm{dt} = q \int_{\vec{r}(0)}^{\vec{r}(t)} \vec{E}_W \ \mathrm{d}\vec{r} \,. \tag{9}$$

As the weighting field is a conservative field it can be expressed in terms of the weighting potential Φ_W

$$\vec{E}_W(\vec{r}) = -\overrightarrow{\nabla} \Phi_W(\vec{r}). \tag{10}$$

Using Equation 10, Equation 9 can be rewritten as

$$Q_c = q \cdot [\Phi_W(\vec{r_2}) - \Phi_W(\vec{r_1})] \,. \tag{11}$$

The weighting potential defines the coupling of a charge at any position to an electrode. The weighting potential applies to a specific electrode. It is obtained by setting the potential of this electrode to $1\,\mathrm{V}$ and all other electrodes to $0\,\mathrm{V}$ [14].

2.3. Charge Transport

Signal pulses are induced by the separation and movement of the charge carriers to their respective electrical contacts. The readout electronics then detect the signal. This section provides a brief overview of the charge transport in a semiconductor system.

2.3.1. Drift and Diffusion

In a semiconductor, free charge carriers move randomly which implies that in case of a gradient in the carrier concentration, a carrier from an area of high concentration is more likely to go to an area of low concentration than vice versa. This effect is called diffusion, as it spreads out the charge carriers. The diffusion constant D can be calculated from the Einstein relation

$$D_{e,h} = \frac{k_B T}{q} \mu_{e,h}(\vec{E}) \,. \tag{12}$$

If an electric field is applied, the charge carriers created by the ionization processes drift through the sensor volume. Their direction depends on the electric field and their charge

sign. The drift velocity ν can be calculated from

$$\vec{\nu}_{e,h} = \pm\ \mu(\vec{E})\vec{E}. \tag{13}$$

The mobility of electrons is in the order of $\sim 10^3 \frac{\text{cm}^2}{\text{Vs}}$ [15] so that velocities in the range of $|\nu_e| = 50\,\mu\text{m/ns}$ are reached with an electric field of $|E| = 5\,\text{kV/cm}$. Thus, the collection of electrons takes only a few nanoseconds for silicon sensors with a thickness of $150\,\mu\text{m}$. However, the electric field inside an irradiated silicon detector is not constant, as shown in Section 2.4.2.

An illustration of charge diffusion and charge sharing is given in Figure 2.4. The sensor is segmented into pixels of size p in x and has a thickness t. A fast ionizing particle enters the pixel at position (x_0, z_0) and deposits energy along the y direction, resulting in an elongated cloud of charge carriers. The width σ of the charge cloud increases as it drifts through the depth of the sensor towards the collecting electrode.
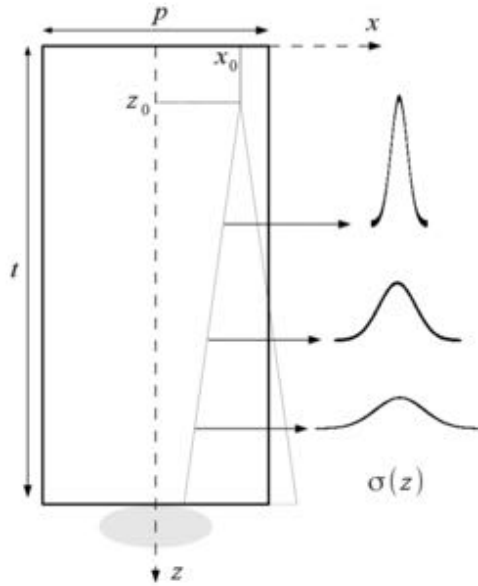
Figure 2.4 – Model of charge diffusion and charge sharing; the cloud is distributed according to a Gaussian profile in the x-direction, whose width $\sigma(z)$ increases as the carriers drift through the sensor depth t towards the collection electrode (at the bottom). Figure from [16].

2.4. Radiation Damage

As a crystalline material silicon is sensitive to radiation damage. This chapter provides an overview of the processes that lead to a radiation induced degradation of the sensor properties. Irradiation produces highly mobile point defects and increases the mobility of

already existing point defects [17]. Generally, there are two types of damage, bulk damage and surface damage. As surface damage has less impact on the sensor's performance, it is described only briefly. A sketch of surface damage in a pixel sensor is shown in Figure 2.5.
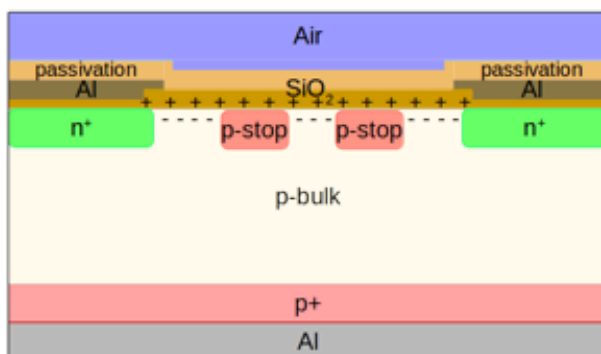
Figure 2.5 – Sketch of a pixel sensor geometry with surface damage. Holes create a positive charge region in the oxide layer and the electrons are thus attracted to the Si-SiO$_2$ interface, changing the electric field in the area between the pixel implants.

Electrons generated by the radiation diffuse out of the oxide layer, while the remaining holes create a positively charged region. In return, electrons are attracted to the Si-SiO$_2$ interface and change the electric field in the area between the pixel implants.

2.4.1. Bulk Damage

Bulk damage changes the sensor performance significantly as the crystal structure properties are altered. Atoms are displaced within the lattice, leading to interstitials and vacancies. Vacancies change the doping concentration within the silicon and reduce the charge carrier lifetime, as the induced vacancies capture the drifting charge carriers. With irradiation of the silicon sensors, charged defects, acting as donors and acceptors are introduced, leading to additional energy levels in the forbidden band gap, an overview is shown in Figure 2.6. This leads to an altered N_{tot} and a different depletion voltage. While shallow defects do not contribute to a change in charge collection at room temperature due to their fast detrapping time, deep defects are able to trap charge and thus lead to a lower charge collection efficiency. Levels that are introduced close to the midgap, which act as generation centers are most effective in changing the leakage current. In summary, properties such as the leakage current, the depletion voltage and the charge collection efficiency (CCE) are altered by radiation damage.
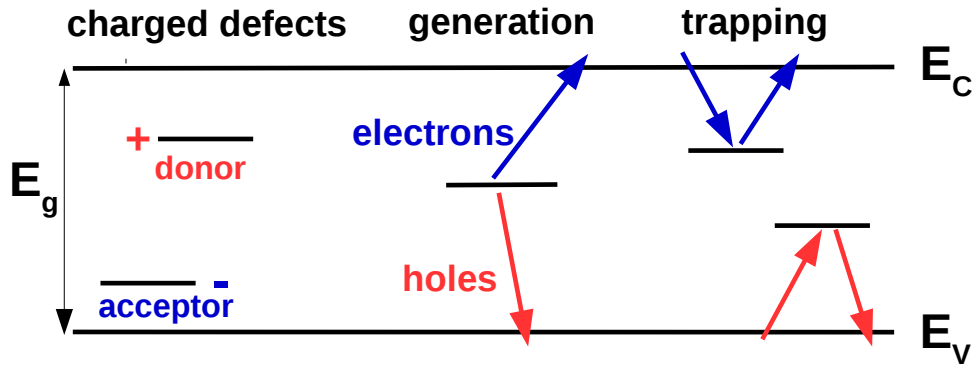
Figure 2.6 – An overview of the damage caused by irradiation of the silicon bulk. Charged defects, introduced in the forbidden band gap, which act as donors or acceptors, change the doping concentration. Deep defect levels lead to a reduced CCE due to trapping. Generation of charges close to midgap change the leakage current of the sensor.

2.4.2. The Double Junction Effect

Trapping of the mobile charge carriers from the generation-recombination current leads to a net positive space charge near the p^+ backplane of the sensor and a net negative space charge near the n^+ implant. As positive space charge density corresponds to n-type doping and negative space charge density to p-type doping, there are p-n junctions at both sides of the sensor [18]. Figure 2.7 shows this so-called double junction effect. On the left side the evolution of the space charge density as a function of depth y in the sensor is shown, while on the right side the evolution of the electric field is shown. The result is a double peaked electric field.

2.4.3. The NIEL Scaling Hypothesis

In radiation damage studies of silicon detectors microscopic and macroscopic effects are analyzed with respect to radiation fluence [19]. The type and energy of the primary particles in the irradiation process strongly affects the damage in the silicon sensor bulk, see Section 2.4.1. An irradiation with neutral particles results in a different behavior than for charged particles. However, the main properties changed by radiation damage such as leakage current, charge collection efficiency or depletion voltage can be compared by normalizing the fluences.

This normalization is done using the non-ionizing energy loss (NIEL) scaling hypothesis. All energy deposited in the crystal which has not been used for the fully reversible process
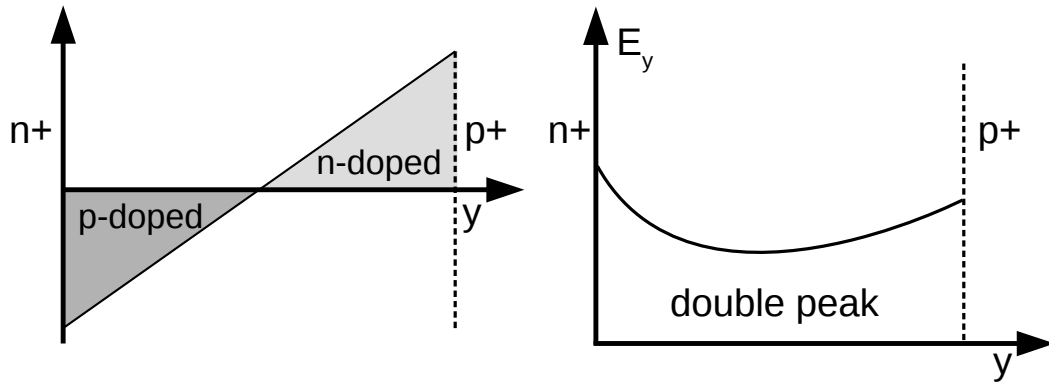
Figure 2.7 – Sketch of the space charge density as a function of depth y for an irradiated sensor. A positive space charge region (n-doped) near the p$^+$ implant is created and a negative space charge region (p-doped) at the n$^+$ implants, leading to a p-n junction on both sensor ends. On the right side the corresponding double peaked electric field is displayed.

of ionization is summarized and neutrons of 1 MeV are used as reference particles. Particle specific damage functions $D(E)$ describe the displacement cross section as a function of particle energy. In Figure 2.8 these functions are shown for different particle types normalized to 1 MeV neutrons. The energy-dependent hardness factor κ of an arbitrary
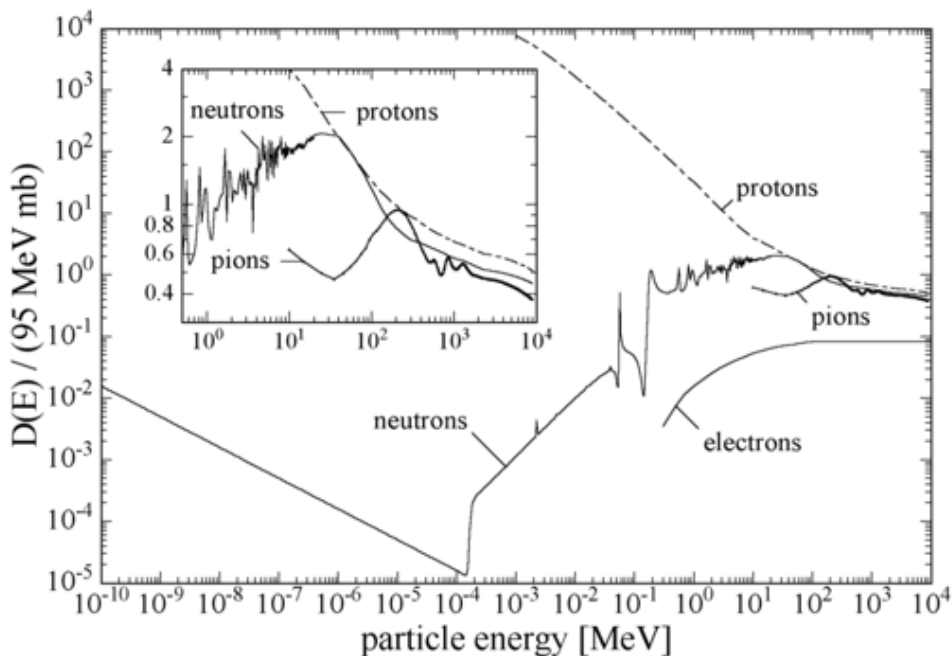
Figure 2.8 – Displacement damage functions $D(E)$ for various particles, the ordinate represents the damage equivalent to 1 MeV neutrons. The insert zooms into the region above 1 MeV. Figure taken from [20].

particle type i with a fluence spectrum $\phi_i(E)$ is defined as

$$\kappa_i = \frac{\int D_i(E)\phi_i(E)dE}{D_n(E = 1\,\mathrm{MeV})\int \phi_i(E)dE} \ , \tag{14}$$

where D_n represents the damage function for neutrons [21]. In case of an irradiation with a monoenergetic particle beam, Equation 14 can be written as

$$\kappa_{i,\mathrm{mono}} = \frac{D_i(E)}{D_n(E = 1\,\mathrm{MeV})} \ . \tag{15}$$

The conversion into the neutron equivalent fluence Φ_{eq}, using the total received particle fluence $\Phi_i = \int \phi_i(E)dE$, can be done via

$$\Phi_{eq} = \kappa_i \Phi_i \ . \tag{16}$$

However, the mechanism of radiation damage varies for different particle types and not all radiation effects can be directly compared. Previous studies into the microscopic defects introduced by radiation damage show that the behavior of sensors after irradiation differs significantly, depending on the particle type [22]. Deviations from the NIEL scaling hypothesis have also been found in simulations of radiation damage [23]. Nevertheless, the NIEL scaling provides a good approximation for the comparison of radiation damage effects introduced by different irradiation particles over a large energy range.

3. The CMS Experiment at the LHC

Particle accelerators are the most important machines for modern experimental particle physics, as they provide particle beam collisions at high energies. At these collision points the energy of the particle collisions gets transformed into mass, spraying particles in all directions. The increasing collision energies provide the opportunity to probe the fundamental constituents of matter and their interactions in ever more detail. Complex detector systems are surrounding the collision points to measure the characteristics of the resulting collision products.

With the discovery of the Higgs boson in 2012, the Large Hadron Collider accomplished an important milestone in modern particle physics and this achievement was acknowledged around the globe, bringing particle physics back into the public eye. This chapter describes some basic aspects of the LHC accelerator in Section 3.1. In Section 3.2 a more detailed description of the CMS experiment and its current subdetectors is provided.

3.1. The Large Hadron Collider

The largest and most powerful particle accelerator in the world is the Large Hadron Collider at the European Organization for Nuclear Research (CERN) in Geneva, Switzerland. It is hosted 175 meters below the surface in a 27 kilometer ring crossing the French border. Before the beams are injected into the LHC, they travel through a succession of particle accelerators, while each accelerator boosts the speed of the beam of particles before it is injected into the next one. An overview of the pre-accelerators to the LHC together with other accelerator-based experiments at CERN is shown in Figure 3.1.

Inside the LHC, two high-energy proton beams travel at a velocity close to the speed of light. The proton beams move in opposite directions in two tubes held at ultrahigh vacuum. A strong magnetic field, maintained by superconducting electromagnets, guides the beams around the accelerator ring. The beams are organized in 2700 bunches of 10^{11} protons per beam that propagate through the accelerator together with a $25\,\mathrm{ns}$ bunch spacing. The beams inside the LHC collide at four locations around the accelerator ring, with a particle detector at each interaction point (ATLAS, CMS, ALICE, LHCb). More details on the LHC accelerator complex can be found in [25].

To discover new particles at the LHC, an increase in luminosity and center-of-mass energy is needed . The luminosity is defined by the number of possible interactions per time and area. Generally, the luminosity increases with a larger number of particles per bunch, a larger number of bunches or a smaller transverse size of the bunches. The nominal luminosity of the LHC is $10^{34}\,\mathrm{cm^{-2}s^{-1}}$. The center-of-mass energy defines the achievable
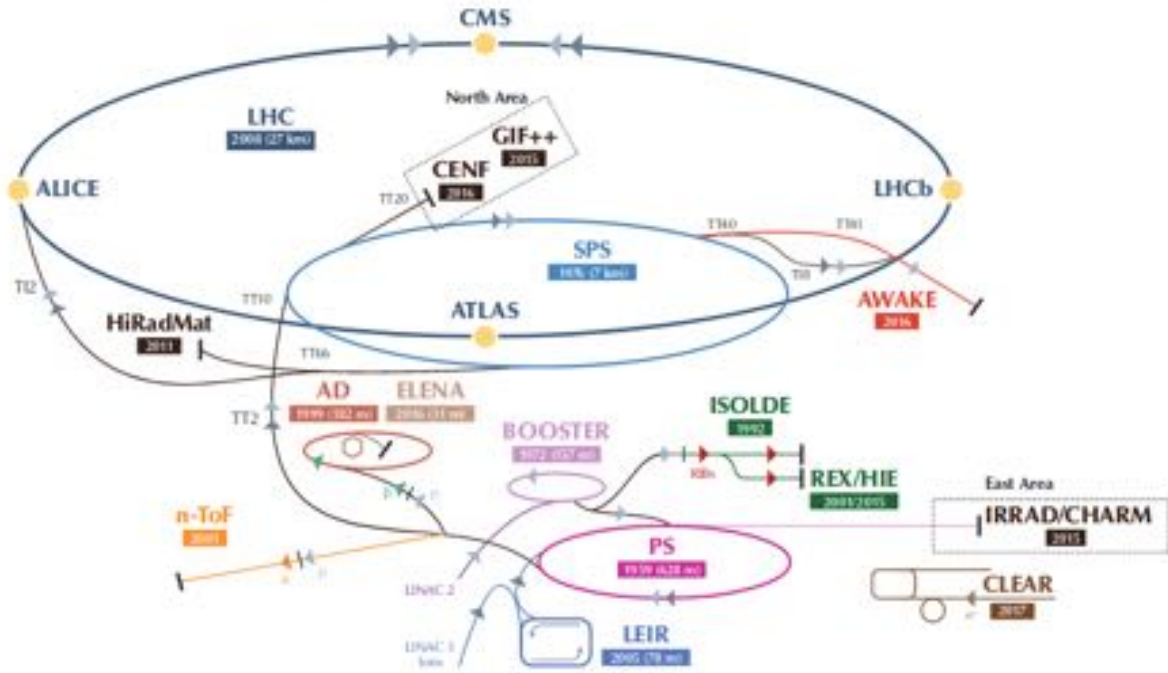
Figure 3.1 – An overview of the CERN accelerator complex, modified from [24]. The LHC and its four main experiments and the pre-accelerators are shown. The smaller accelerators provide particle beams for a variety of experiments, for example the proton irradiation facility IRRAD.

energy range of the produced particles, while the production of particles is a statistical process. The LHC was operated at an energy of 13 TeV from 2015 to 2018 and before that at energies of 7 and 8 TeV. For the upcoming run the LHC is expected to run at 14 TeV and the luminosity is steadily increased. For the years 2024-2026 a major upgrade of the accelerators and the detectors is foreseen, the so-called Phase 2 upgrade for the High-Luminosity LHC (HL-LHC). For the HL-LHC the peak luminosities are expected to be $5 - 7 \times 10^{34}\,\mathrm{cm}^{-2}\mathrm{s}^{-1}$ at a center-of-mass energy of 14 TeV [26]. Under these circumstances the event pileup (PU) will rise substantially with the average number of interactions in a single bunch crossing being approximately 140. In Section 3.3 the plans for the Phase 2 upgrade of the CMS detector for the HL-LHC are described with emphasis on the tracker barrel.

3.2. The Compact Muon Solenoid

The Compact Muon Solenoid (CMS) detector is one of two general purpose LHC experiments and is situated in an underground cavern near Cessy in France. It is named after its design, as with all its detector material contained within 15 m height and 21 m length,

it is quite compact and was designed to detect muons very accurately. Furthermore does it host the most powerful solenoid magnet ever made [27], which bends the paths of the particles.

The detector is built in a cylindrical onion-like shape around the interaction point (IP), with several subsystems arranged in multiple layers, as shown in Figure 3.2.
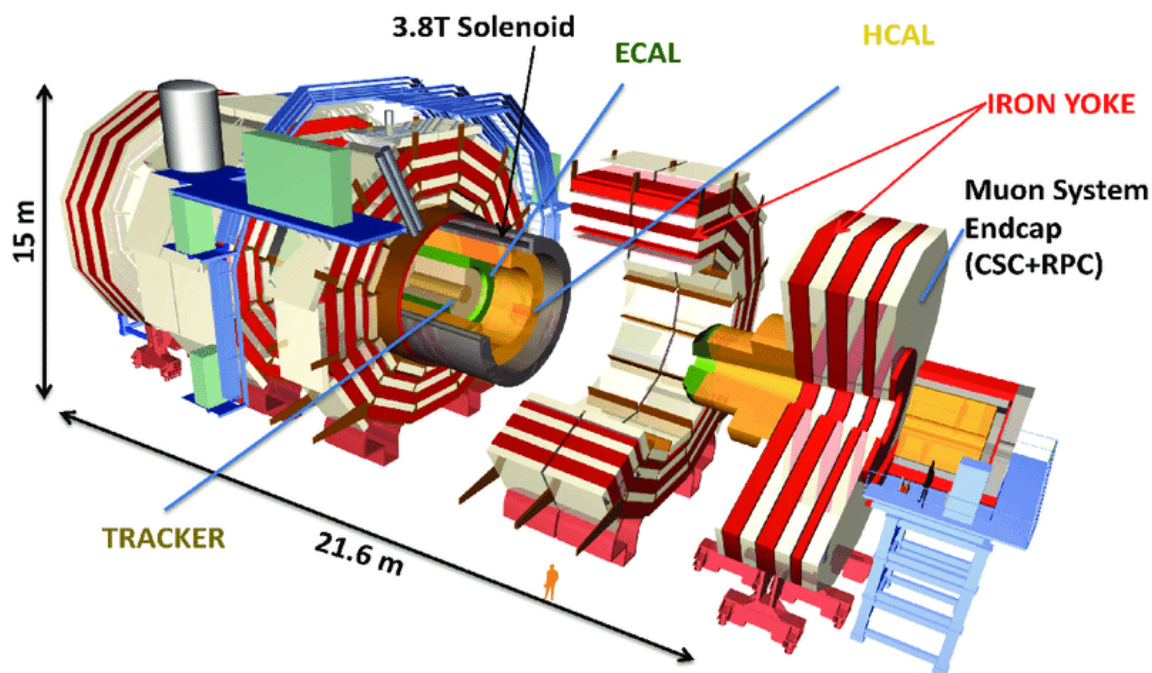
Figure 3.2 – A schematic view of the CMS detector and its subsystems, from [28].

One can understand the detector as a high-speed camera, that takes 3d images of particle collisions with up to 40 million frames per second. With the particles created by the collision typically decaying into other more stable particles, CMS has to identify all stable particles produced by a collision and measure the corresponding momenta and energies. By piecing together all information gathered the detector can recreate an image of a single collision for further analysis. Each detector component has two endcaps, placed at the ends of the purely cylindrical detector barrel.

Thus a large fraction of the full solid angle is covered to detect almost every particle stemming from the IP.

In the following, the coordinate system chosen within the experiment is described. The z-axis is defined along the beam pipe, which is also the symmetry axis of the cylindrical components. The x-axis points to the center of the accelerator and the y-axis upwards. Often polar or spherical coordinate systems (radius r, azimuthal angle ϕ and polar angle

θ) are used as well as the pseudorapidity η, defined in Equation 17.

$$\eta = -\ln\left(\tan\left(\frac{\theta}{2}\right)\right) \tag{17}$$

The individual subsystems of the CMS detector, as depicted in Figure 3.2, and their tasks in the reconstruction of particles are explained in the next sections.

3.2.1. Inner Tracking System

The detector closest to the IP is the tracker. Its purpose is the reconstruction of the trajectories of ionizing particles originating from the IP. Fine pitch silicon detectors are emploied to measure the position of the particle throughout the sensor. The resulting particle trajectory holds information necessary for the reconstruction of the exact interaction at the IP. Hereby each measured particle has to be assigned to a vertex, in order to reconstruct the individual interactions. To achieve this distinction a pointing resolution in the range of several microns is needed. This is especially important for the precise identification of secondary vertices from for example B hadrons. The tracker is located inside the solenoid, which provides a 3.8 T magnetic field oriented along the beam axis, resulting in bending of the trajectories of charged particles and an exact determination of the transverse momenta p_T.

The current pixel detector has four barrel layers (BPIX) at radii of 30, 68, 102 and 160 mm and three forward/backward discs (FPIX) to provide four-hit pixel coverage up to $\eta = \pm 2.5$ [29]. The current layout of the pixel detector is illustrated in Figure 3.3. In the
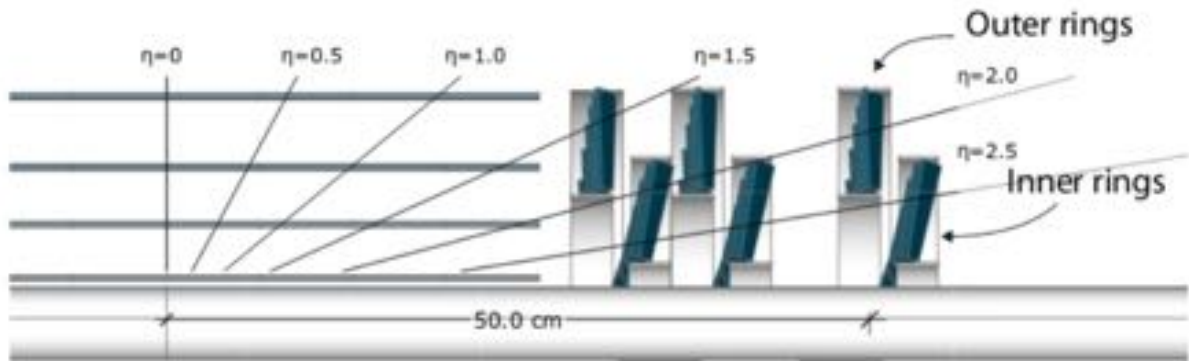
Figure 3.3 – Layout of the current pixel detector, modified from [29]. Four-hit pixel coverage is achieved up to $\eta = \pm 2.5$.

following the current BPIX detector is described in more detail, further information on the FPIX detector can be found in [29]. Each layer has a varying number of 22 mm wide

facets populated with a total of 1148 rectangular modules. The total number of pixels is 79 million. The modules are mounted on a low-mass support structure with embedded cooling tubes. While the barrel detector consists of two half-barrels, each with four layers, the division results in the same geometry for all facets and modules. The modules do not overlap along the z-direction, leading to an insensitive region in between of 2.2 mm, which corresponds to 3.3 % of the active area [29].

Modules

All layers are equipped with 2×8 readout areas with a total active area of $16.2 \times 64.8 \, \mathrm{mm}^2$. Every readout area contains 52×80 pixels. Each pixel has a size of $100 \times 150 \, \mu\mathrm{m}$ and a thickness of $285 \, \mu\mathrm{m}$. The last pixel row or column at three of the edges of a readout area has a double pitch to create a margin for the edges and the ROC placement. These pixels are called big pixels.

The sensors are n^+-in-n technology with a p-spray pixel isolation. The sensor backplane is processed with a uniform p-doping. With this sensor design electrons are collected.

After irradiation, the n-doped bulk material undergoes type inversion and thus the sensor will be depleted from the implants [30]. The individual pixel cells can be tested via an aluminum bias grid with a punch-through at the bias dots.

The sensors are bump bonded to 16 ROCs forming a module with 66 560 pixels. While the ROCs for the innermost layer are thinned to $75 \, \mu\mathrm{m}$ thickness, for the BPIX layers 2-4 the ROCs are thinned to $\sim 180 \, \mu\mathrm{m}$. A high density interconnect (HDI) is glued on top of the sensor with wirebond pads to connect to the corresponding pads on the ROCs. The signal and power distribution for the ROCs and the token bit manager chip (TBM) is provided by the HDI. The TBM chips are glued and wirebonded to the HDI. Two ROCs were designed, the PROC600V2 for the innermost barrel layer [31] and the PSI46digV2.1respin for all other modules [32]. The modules with their individual settings and parameters are tested and trimmed intensively according to the module testing reference guide [33] before they are installed in the CMS detector. Noisy pixels are flagged and the gain of each individual ROC pixel is measured and stored for later calibration. The signal calibration to electrons is then determined using the characteristic energy spectrum peaks of monochromatic X-rays from different targets such as Ag, Mo, Zn and Sn.

In the barrel, the pixel are mounted with the $100 \, \mu\mathrm{m}$ pixel pitch in the ϕ-direction and the $150 \, \mu\mathrm{m}$ pitch parallel to the beam axis. A Lorentz drift of the charge carriers along the $100 \, \mu\mathrm{m}$ pitch is induced by the magnetic field parallel to the beam axis. This can result in a lateral drift of one pixel pitch and thus optimal charge sharing between pixels which leads to an optimal resolution. The resolution as a function of incidence angle for non-

irradiated sensors has been thoroughly investigated in previous test beam measurements and is shown in [34]. Whereas for irradiated CMS Pixel detector modules, the Lorentz drift and the resolution as a function of inclined particle incidence are analyzed in [9].

Strip Tracker

The measurement of the particle's trajectory of the pixel detector is extended outward by the strip tracker. As the density of tracks is much lower at this distance further from the IP, strip detectors are used. The detector modules of the strip tracker vary in size, thickness, strip pitch and geometry. The strip pitches increase from 80 µm to 184 µm for larger radii. There are single-sided and double-sided strip modules, that consist of two strip sensors with different strip orientations enabling a two-dimensional hit position measurement. The strip tracker has radii from 20 cm to 116 cm and a total length of 5.8 m, as shown in Figure 3.4. The orientation of the strips is parallel to the z-axis for sensitivity in the r-ϕ-plane. The pixel detector with its BPIX and FPIX layers is shown in green while the single-sided (double-sided) strip modules are shown in red (blue). The strip tracker covers a region of up to $|\eta| < 2.4$.
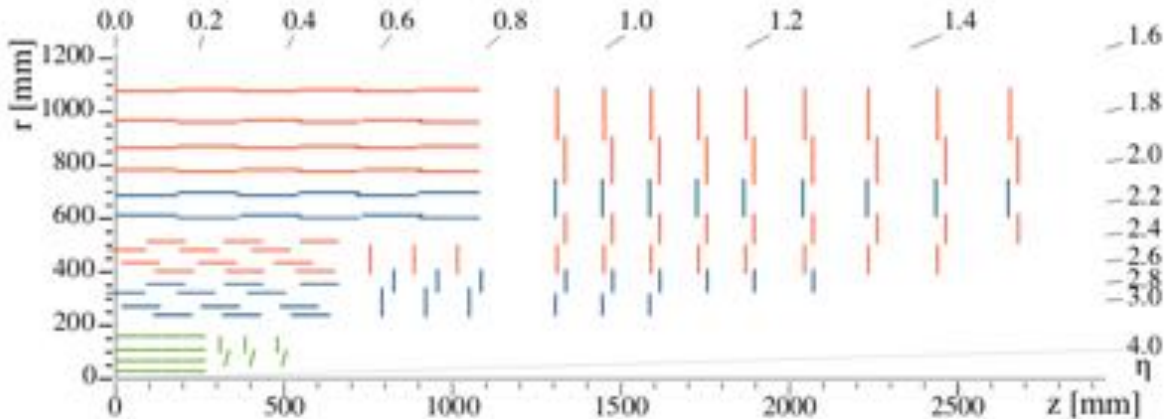
Figure 3.4 – Layout of one quarter of the current CMS Phase 1 tracking system in r-z view from [35]. The pixel detector is shown in green, while single-sided or double-sided strip modules are displayed as red or blue segments.

3.2.2. Calorimeters

Calorimeters are built to measure a particle's energy and direction for an electromagnetic or hadronic shower. In most experiments there is an electromagnetic calorimeter in front of the hadronic section, which has less sampling density in the back, so the hadronic cascade occurs in a succession of different structures [11].

Electromagnetic Calorimeter

The electromagnetic calorimeter (ECAL) of the CMS detector is a high-resolution, hermetic and homogeneous ECAL that consists of about $75\,000$ scintillating lead tungstate crystals ($PbWO_4$). The material is used for the initialization of particle showers and the creation of scintillating photons due to its high density $\rho = 8.3\,\mathrm{g\,cm^{-3}}$ and short radiation length ($X_0 = 0.89\,\mathrm{cm}$). The ECAL is composed of a barrel (EB) and two endcap (EE) parts, with a $3\,X_0$ lead silicon strip preshower (ES) detector in the endcap section, as shown in Figure 3.5. The ECAL covers a pseudorapidity region of $|\eta| < 3.0$. Between the EB and EE the crystals have a slightly different geometry. Their front and rear surfaces are quadratic with edge lengths of $22\,\mathrm{mm}$ to $30\,\mathrm{mm}$ and their lengths are $230\,\mathrm{mm}$ in the EB and $220\,\mathrm{mm}$ in the EE. With these lengths being equivalent to 25.8 and 24.7 radiation lengths most electromagnetic particle showers are fully contained within the ECAL.

The barrel consists of 61200 crystals divided into 36 supermodules and 2448 readout units, where each readout unit reads a matrix of 5×5 crystals [36]. In the barrel the crystals are connected to avalanche photodiodes (APDs), while in the EE vacuum phototriodes are used. The preshower contains two lead absorbers and two layers of silicon strip detectors to sample the shower profiles and provide an estimate in the endcap region. The excellent energy resolution of the ECAL, as well as its timing performance, are fundamental characteristics for the physics reach of the whole experiment, since electrons and photons are of particular interest for new physics and are also essential ingredients of some of the Higgs boson decay channels. With the position resolved measurement of the particle energy, the trajectories measured in the tracker can be assigned to energy depositions in the calorimeter.

Hadronic Calorimeter

A sampling hadron calorimeter (HCAL) with coverage up to $|\eta| = 3.0$ surrounds the ECAL Hadron calorimeters are particularly important for the measurement of hadron jets and neutrinos or other particles resulting in apparent missing transverse energy as an HCAL measures the timing and energy of hadronic showers and their angle and position. Since hadrons have a larger interaction length than electrons or photons, they require a larger amount of material for full absorption. Therefore brass absorbers which develop the particle shower alternate with plastic scintillator tiles which measure the number of secondary particles. The absorber thicknesses range from 50.5 mm to 79 mm, depending on their position in the calorimeter. Additionally, there are steel plates in front of and behind the sampling calorimeters. The thicknesses of the scintillator tiles are $3.7\,\mathrm{mm}$ to $10\,\mathrm{mm}$. The light is converted by wavelength shifting (WLS) fibres embedded in the
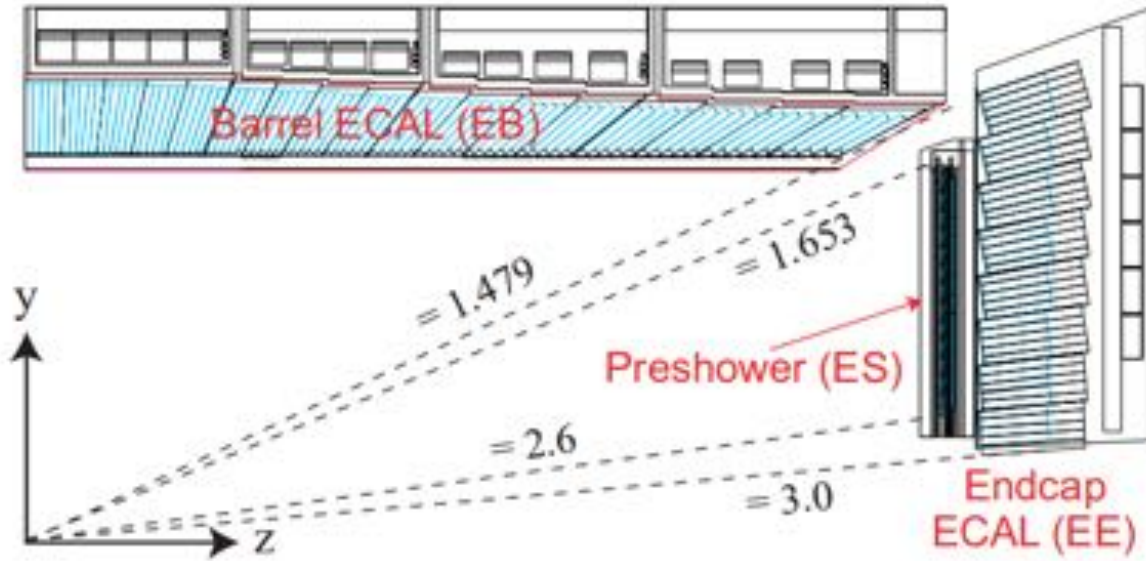
Figure 3.5 – The layout of one quarter of the CMS ECAL. It consists of a barrel part (EB) and endcap subsystem (EE) with a preshower (ES) in front, covering a pseudorapidity region of $|\eta| < 3.0$, from [37].

scintillator tiles and channeled via clear fibres for readout to hybrid photodiodes (HPDs) or silicon photomultipliers (SiPMs) that are operational in high axialmagnetic fields [38]. The CMS HCAL is divided into four parts. Only the barrel hadron calorimeter (HB) and the endcap hadronic calorimeter (HE) are inside the solenoid. The barrel calorimeter is complemented by an outer calorimeter (HO) or tail-catcher just outside the cryostat ensuring that highly energetic hadronic showers are sampled with nearly eleven interaction lengths and thus fully contained,see Figure 3.6. Coverage up to $|\eta| = 5.2$ is ensured by an iron/quartz-fiber forward calorimeter (HF). Photomultipliers detect the Cherenkov light emitted in the quartz fibers. The HF provides nearly full geometric coverage for the measurement of the transverse energy in the event. It is situated at a distance of 11.2 m from the IP and consists of steel absorbers for about ten interaction lengths, traversed by quartz fibers as scintillators.

3.2.3. Superconducting Solenoid

A solenoid is a magnet made of coils of wire that produce a uniform magnetic field when electricity is flowing through them. In this case NbTi coils are used and their superconductivity is ensured by cooling the cold mass of the magnet with liquid helium such that an operating temperature of 4.5 K is achieved. As aforementioned the solenoid is an indispensable part of the CMS experiment, as only with the homogeneous 3.8 T magnetic field along the beam axis in the bore, an exact measurement of the particle

Figure 3.6 – The layout of one quarter of the CMS HCAL. It consists of a hadron barrel part (HB) and endcap system (HE), outer (HO) and forward calorimeters (HF), covering a pseudorapidity region of $|\eta| = 5.2$, from [39].

trajectory in the Inner Tracker is possible. The bore contains the tracking detector, the ECAL and the HB and HE calorimeters. It has a diameter of 6.3 m and a length of 12.5 m. The muon detectors are intertwined with a 12-sided iron structure, that surrounds the magnet coils and contains and guides the field. This so-called return yoke consists of three layers and reaches out 14 m in diameter while it also acts as a filter such that only muons and weakly interacting particles can pass through. The return yoke guides the magnetic field outside the bore. This results in a magnetic field of 2 T in the barrel part of the HO and the barrel part of the muon system for an accurate measurement of the muon momenta. The weight of the magnet including the return yoke amounts to 10 000 t with a stored maximum energy of up to 2.6 GJ [39].

3.2.4. Muon Chambers

The detection of muons is of key importance for the CMS experiment, like the name suggests. An exact and reliable muon measurement was a main goal from the earliest design stages on. The muon system can reconstruct the momentum and charge of muons over the entire kinematic range of the LHC.

The muon system consist of a cylindrical barrel section and two planar endcap regions. For the muon identification three types of gaseous detectors are in use. The gas atoms

are ionized by the traversing particles and an electric field forces the electrons and ions to drift towards the electrodes, which results in an electric current [40].

In the barrel region the 4 T magnetic field is homogeneous and largely contained in the steel yoke, so that drift chambers with rectangular drift cells are utilized. The barrel drift tube (DT) chambers cover a pseudorapidity region of $|\eta| < 1.2$. The chambers have a pitch of 13 mm × 42 mm in r and ϕ, with a projected length in z of max. 2.4 m. The location of the particle transversal inside a chamber can be determined from the drift time of the electrons towards the anode readout wire with an accuracy of 250 µm. In the two endcap regions cathode strip chambers (CSC) are used, since here the muon rates and background levels are significant and the magnetic field is large and inhomogeneous [39].

The CSCs have a fast response time, fine segmentation and high radiation resistance and identify muons in a pseudorapidity region of $0.9 < |\eta| < 2.4$. The chambers are large gas volumes, that are separated by cathode panels, forming several gas gaps of 9.5 mm in height. Anode wires are centered in the gas gaps. They pass through the volume to shape the electric field, to detect the particles and to establish the location of the particle traversal in the radial coordinate. The cathode panels, which are segmented perpendicular to the wire orientation, are read out separately to obtain the particle's position in ϕ. This way the CSC system achieves a spatial resolution of 75 µm - 150 µm. In each endcap, there are four stations of CSCs. The chambers are positioned perpendicular to the beam axis and interspersed between the flux return plates.

An important characteristic of the DT and CSC subsystems is their ability to trigger on the p_T of muons with high efficiency and high background rejection, independent of the rest of the detector. The Level-1 trigger p_T resolution is approximately 15% in the barrel and 25% in the endcap. Nevertheless an additional trigger system, which consists of resistive plate chambers (RPC), complements both the barrel and endcap regions. The RPCs supply a fast, independent, and highly-segmented trigger with a sharp p_T threshold over the pseudorapidity range $|\eta| < 1.6$ of the muon system. The RPCs are parallel-plate chambers filled with gas, operated in avalanche mode to guarantee stable operation at high rates. They have a moderate spatial resolution but an outstanding time resolution ($\sigma \sim 3$ ns), comparable to scintillators. Trigger signals coming from the drift tubes, cathode strip chambers and the RPCs proceed in parallel until they reach the level of the global trigger logic. This provides redundancy for evaluating efficiencies and results in a higher efficiency and greater rate capability [41].

A schematic of the CMS detector including a detailed muon system is depicted in Figure 3.7. The muon reconstruction is performed utilizing the inner tracker at the center of
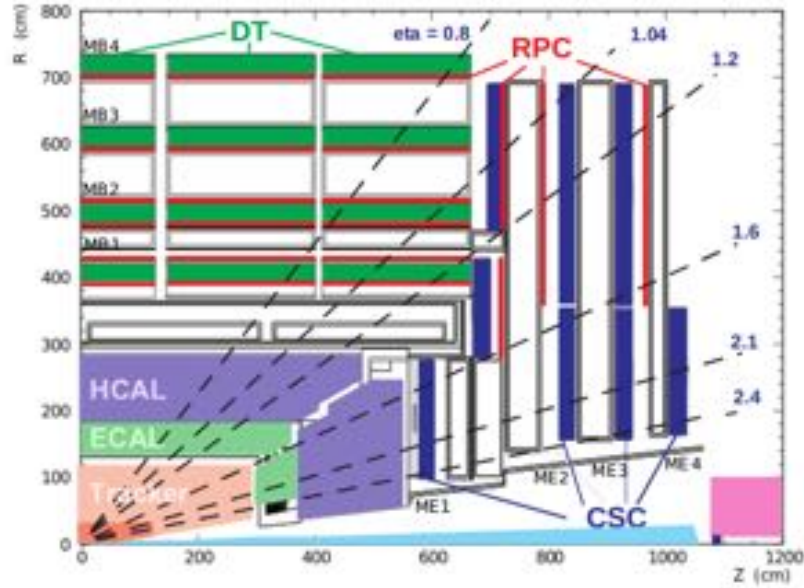
Figure 3.7 – The layout of one quarter of the CMS detector. The muon system with its four DT stations in the barrel are shown in green, the four CSC stations in the endcap in blue and the RPC stations in red, from [42]. The white areas in between the detectors represent the iron return yoke, that is interspersed between them.

the detector immersed in the 3.8 T solenoidal magnetic field and with a maximum of four stations of muon detectors that are installed in between the layers of the return yoke. In addition, muon energy deposits in the calorimeters are used for muon identification. The muon p_T can be determined with relative uncertainties of $1\% - 10\%$, depending on the pseudorapidity range and the particle momentum [42].

3.2.5. Trigger Systems

The task of the trigger system is to reduce the large amount of data that is produced by the high interaction rates of the LHC and select events of potential physics interest. The CMS experiment employs a two-level trigger system. The Level-1 (L1) trigger, consisting of custom hardware processors, selects events with interesting signatures and thus reduces the readout rate from the 20 MHz bunch-crossing frequency to a maximum of 100 kHz [39], the upper limit of the CMS readout electronics. The L1 trigger is a hardware system with a fixed latency. Using information from only the calorimeter and muon detectors, an event has to be accepted or rejected within 4 µs of a collision [43]. The L1 trigger selects events containing candidate objects, e.g. ionization deposits consistent with a muon or energy clusters consistent with an electron or jet.

The high-level trigger (HLT) is software-based and uses the full event information, in-

cluding the Inner Tracker, to further decrease the recorded event rate by a factor of 1000. The HLT processes all events accepted by the L1 trigger in a single processor farm [44]. It reconstructs only the detector information relevant for the physics object, before applying a set of selection criteria that reject background events and keeps the desired physics for further processing. Only data accepted by the HLT is stored for physics offline analyses. Still the data stored from LHC collisions amount to several petabytes per year.

3.3. Phase 2 Upgrade of the CMS experiment

To be able to exploit the increase in luminosity provided by the HL-LHC the CMS detector needs to be substantially upgraded. The increase in radiation levels demands an improved radiation hardness, while the larger pileup and the associated increase in particle density require a higher detector granularity to reduce occupancy, an increased bandwidth to accommodate higher data rates, and an improved trigger capability to keep the trigger rate at an acceptable level while not compromising physics potential [45].

This section gives a brief overview, based on the Technical Design Report [45], of the Phase 2 upgrade of the CMS experiment in general and the CMS tracker barrel detector in more detail.

The muon system will be enhanced in the forward region, both with improved RPCs and new chambers based on the gas electron multiplier (GEM) technique. The front-end electronics for the DT chambers and CSCs will be improved, while the muon chambers are expected to cope with the increased particle rates. The CMS trigger system consists of two stages, the first level hardware trigger and the HLT. Trigger rates will be limited to 750 kHz at L1 and 7.5 kHz at the HLT. The L1 trigger latency will be about 12.5 µs. The lead-tungstate crystals of the ECAL, which are read out with avalanche photodiodes, will be cooled to lower temperatures than currently used and the front-end electronics will be improved in order to cope with the trigger latency and bandwidth requirements. With new front-end boards the information from single crystals can be utilized in the L1 trigger, while the current system integrates the same information only in bundles of 5×5 crystals. The HCAL consists in the barrel region of brass absorber plates and plastic scintillator layers, read out by hybrid photodiodes, which will be replaced with SiPMs. The scintillator tiles close to the beam line will be replaced before the start of the HL-LHC. Both the electromagnetic and the hadronic endcap calorimeters will be replaced with a new combined electromagnetic and hadronic sampling calorimeter based primarily on silicon pad sensors. Plastic scintillator tiles, read out by SiPMs, will be used at large distances from the beam line in the hadronic section. In order to provide high transverse and longitudinal granularity, leading to improved pileup rejection and identification of

electrons, photons, tau leptons, and jets the silicon pad cells have sizes of $0.5 - 1\,\mathrm{cm}^2$ and 28 (12) sampling layers in the electromagnetic (hadronic) sections.

Due to the expected high PU conditions of the HL-LHC the entire tracking system has to be replaced with new detectors with higher radiation tolerance and enhanced functionality. The performance degradation has been studied in detail and is documented in the Technical Proposal for the CMS Phase 2 Upgrade [38]. Some of the main requirements for the upgrade of the Tracker from the Technical Proposal are summarized in the following:

- Radiation tolerance: The fluence that the individual sensors have to withstand after an integrated luminosity of $3000\,\mathrm{fb}^{-1}$ are simulated with FLUKA [46] for each particle type in Figure 3.8. This requirement must be fulfilled for the Outer Tracker over its entire lifetime while for the pixel detector a replacement is foreseen.
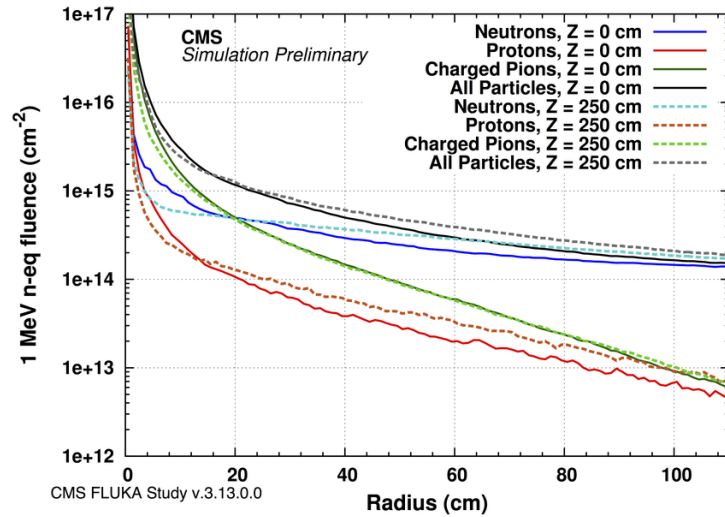
Figure 3.8 – FLUKA simulation of the fluence levels in the CMS Tracker after $3000\,\mathrm{fb}^{-1}$. The z-coordinate in the legend refers to the distance from the interaction point along the beam line, from [47].

- Increased granularity: The channel occupancy must be maintained below the 1% level in all tracker regions to ensure efficient tracking performance at an average of 140 collisions per bunch crossing.

- Extended tracking acceptance: The overall CMS physics capabilities will benefit from an extended coverage of the tracker and calorimeters in the forward region up to $\eta = \pm 4.0$. The layout of one quadrant of the Phase 2 Tracker is shown in Figure 3.9.
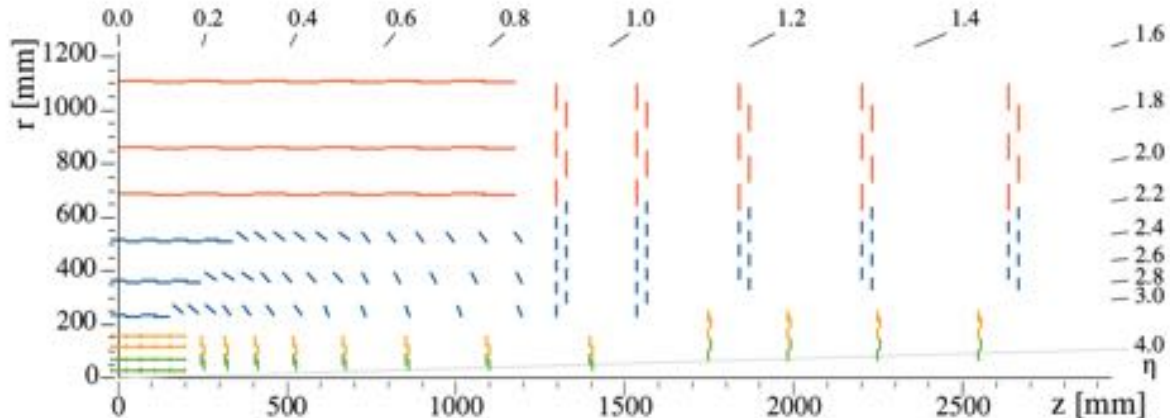
Figure 3.9 – Sketch of the layout of one quadrant of the Phase 2 tracker for CMS. The pixel detector with forward extension is shown in green (orange) for pixel modules with two (four) ROCs, while the blue lines correspond to PS modules and the red lines to 2S modules of the Outer Tracker, from [38]. The coverage is extended up to $\eta = \pm 4.0$.

The Outer Tracker (OT) consists of six barrel layers, complemented on each side by five endcap double-discs. There are three different types of subdetectors: the Tracker Barrel with PS modules (TBPS), the Tracker Barrel with 2S modules (TB2S) and the Tracker Endcap Double Discs (TEDD). All modules are p_T modules, implementing the L1 trigger functionality. In the p_T modules the strips of the top and bottom sensors of a module are parallelized. There are modules with two strip sensors (2-strip or 2S modules) and modules with a strip and a macro-pixel sensor (pixel-strip or PS modules). In the 2S modules the strips are about 5 cm long, while those in the PS modules are about 2.4 cm long. One of the two sensors in PS modules is subdivided into macro-pixels of about 1.5 mm length, providing the z (r) coordinate measurement in the barrel (endcaps). The accuracy on the z coordinates provided by the three PS barrel layers constrain the origin of the trigger tracks to a portion of the luminous region of about 1 mm, which enables partial discrimination of particles originating from different vertices.

The maximum expected fluences after 3000 fb^{-1} of pp collisions at 14 TeV that the individual parts of the tracker will have to withstand are shown in Table 1, as well as the positions in r and z at which this fluence is reached.

Tracker region	Max. fluence $\Phi_{eq}[\text{cm}^{-2}]$	r [mm]	z [mm]
IT barrel layer 1	2.3×10^{16}	28	0
IT barrel layer 2	5.0×10^{15}	69	0
IT barrel layer 4	1.5×10^{15}	156	89
IT forward ring 1	1.0×10^{16}	51	252
OT PS modules	9.6×10^{14}	218	129
OT 2S modules	9.6×10^{14}	676	2644

Table 1 – The maximum expected fluences from FLUKA simulation for the different regions of the tracker and the r- and z-positions at which the quoted maxima are reached. Table adapted from [45].

The Inner Tracker (IT) will consist of 4 barrel layers (TBPX) and eight small (TFPX) and four large endcap discs (TEPX) in forward direction. For the barrel layers 2-4 and the rings 2-4 in TFPX and all rings in TEPX planar silicon sensors will be used, while for layer 1 3D silicon sensors are considered. In the barrel the pixel modules are positioned in ladders. Neighboring ladders are mounted staggered in radius in each layer, so that $r - \phi$ overlap between ladders is reached. The modules on a ladder do not overlap in z. In TFPX and TEPX the modules are positioned in concentric rings. Each double-disc is built of two discs, which enables the installation of modules onto four planes. Each disc consists of two halves, which due to their D-shaped structures are referred to as *dees* . The pixel detector will contain an active surface of approximately $4.9\,\text{m}^2$. A sketch of the Inner Tracker layout and its components is shown in Figure 3.10.

There will be only two types of modules, differing exclusively in the sensor surface and number of readout chips. Modules with two ROCs and four ROCs, arranged as two by two, will be assembled. The entire pixel detector design is based on a ROC with active dimensions of $16.4 \times 22.0\,\text{mm}^2$. The charge collected from the pixel sensor is amplified, shaped, and digitized at $40\,\text{MHz}$, using the time-over-threshold (ToT) method, where the time during which the analogue pulse exceeds a certain threshold is digitized and taken as a measure of the deposited charge [45]. Together with the ATLAS collaboration there was a common R&D effort for the development of the readout chip in the $65\,\text{nm}$ CMOS technology [48]. The RD53A readout chip, a large scale demonstrator chip, has been developed within the RD53 collaboration. It has three different analogue front-ends (FE) which are still being investigated. Two of these front-ends are ToT front-ends using
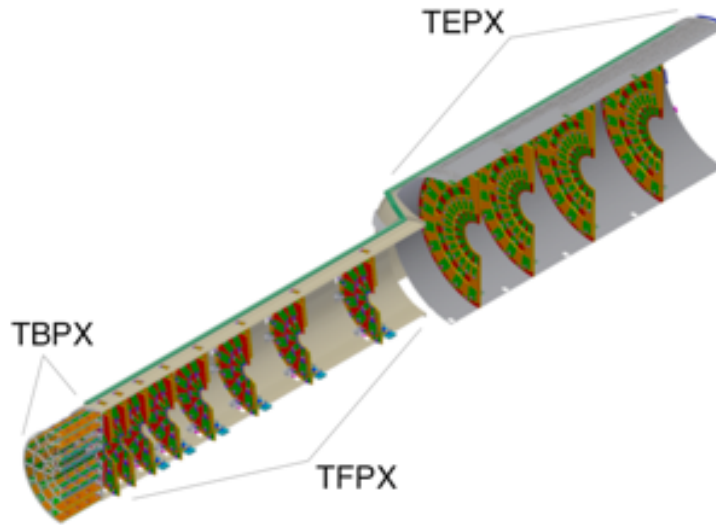
Figure 3.10 – Sketch of the layout of one quarter of the Inner Tracker, showing the TBPX ladders and TFPX and TEPX dees inside the supporting structures. The dees are depicted as red and orange surfaces while the pixel modules are shown in orange for the TBPX and in green for TFPX and TEPX, from [38].

local DACs for threshold adjustment, and are optimized for a 40 MHz (80 MHz using both clock edges) ToT charge conversion while the third front-end uses a novel auto-zero scheme, omitting the need of local threshold adjusting DACs, but requiring a periodic short time period for auto-zeroing [45].

The CMS collaboration decided to use the linear FE for the final readout chip for the Phase 2 Upgrade [49]. For the final modules ATLAS and CMS will again go separate ways and produce different readout chips. For details on the pixel sensor designs for Phase 2 the reader is referred to Chapter 4.

4. The CMS Pixel Modules for the Phase 2 Upgrade

Hybrid pixel detectors, where hybrid refers to the sensor and the readout electronics being separate parts, are widely used in particle physics. The connection of chip and sensor is done via solder bonds, as depicted in Figure 4.1. This offers the possibility to both test and optimize the devices individually. For the testing of the sensor designs for Phase 2 of
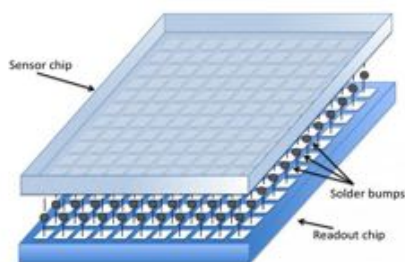
Figure 4.1 – An example of a hybrid pixel detector, where the readout chip and the sensor are separate components connected with solder bumps, from [50].

the CMS experiment all sensors were bonded to the ROC4SENS readout chip, described in Section 4.4, as at this time the RD53A readout chip was still being developed. The key criteria for the selection of a final pixel design are an efficiency of more than 99% for bias voltages lower than 800 V after the expected fluence for the pixel layer 2 of the CMS detector and a good spatial resolution.

List of own contributions The author's contributions to the results presented in this chapter include:

- investigation of the ROC4SENS pulse shape depending on various parameters at test beam,

- investigation of the sensor doping.

The investigated sensors were designed by Dr. J. Schwandt. The investigation of the sensor irradiation was performed with the help of F. Feindt.

4.1. Sensor Designs

Many different planar sensors were designed and produced for the CMS Phase 2 Pixel campaign by Hamamatsu [51]. All sensors are bump bonded to a readout chip, which

is wire bonded to a printed circuit board (PCB) that features a routing of signal lines to the adapter board. The sensors are all n^+p-pixel sensors, this means highly negative doped n^+-pixel implants in a positively doped p-bulk. Hence, electrons are collected at the pixel implants while holes drift to the backside. The sensor backplane is processed with a uniform p^+-doping. The full depletion voltage is $V_{dep} \approx 70\,V$. When a reverse bias voltage is applied to the sensor, the electric field starts to build up from the n^+-pixel implants. Thus after irradiation electrons can still be collected. Moreover, operating the sensor below the full depletion voltage due to the voltage limit of $800\,V$ is possible. The undepleted region is then located at the backplane and the collection of electrons at the implants is not hindered. The guard ring structure is implemented on the front side of the sensor as well as the n^+- implants. This side is connected to the ROC4SENS which is at ground potential. The readout chip is connected to the pixel implants via bump bonds. The implants are at a potential of approximately half the analog voltage of the preamplifier. Since the guard ring has a potential different to ground and is located at the sensor edge, sparking can arise between the sensor edge and the readout chip. To be able to test the sensors up to $800\,V$ at test beam the sensors were coated with Sylgard 184 [52], a flowable, transparent encapsulant. Sylgard cures into a flexible elastomer that protects the electronic components, as without it, sparks were already observed at voltages around $490\,V$ [53]. To avoid cluster merging and improve spatial resolution, there are two different pixel sizes, $50 \times 50\,\mu m^2$ and $25 \times 100\,\mu m^2$, which are both reduced by a factor of six in size compared to the current pixel size, which is described in Chapter 3.2.1. The sensors investigated in the edge-on analysis of this thesis are all $25 \times 100\,\mu m^2$. The $50 \times 50\,\mu m^2$ sensors have 155×160 rows and columns and the $25 \times 100\,\mu m^2$ sensors have 78×320 rows and columns. As isolation between the pixel implants, either p-spray or p-stop technology was used. For p-stop isolation a p^+- implant is introduced between the pixel implants. A typical dose of 10^{14} boron ions/cm^2 guarantees a good isolation even after the radiation-induced built-up of a positive surface charge [8]. For p-spray isolation the whole surface is covered by a medium dose boron implant. However, if the dose is too low, the isolation might not suffice. For this analysis only sensors with p-stop isolation are used but during the measurements also data with p-spray sensors has been taken and no disadvantage of p-spray has been found, however Hamamatsu recommends to produce p-stop wafers.

The sensors were ordered with a resistivity of $1\,k\Omega \cdot cm$ - $5\,k\Omega \cdot cm$. To deal with radiation induced trapping, a reduction of the drift distance and enlarged electric fields are realized by a reduced thickness of $150\,\mu m$ for these planar sensors. Additionally, different float zone wafer materials were used, direct bonded (FDB) ($150\,\mu m + 50\,\mu m$), thinned (FTH)

(150 µm) and deep diffused (FDD) sensors have been produced. For the FTH wafers, the backside of the wafer is thinned to the desired active thickness after most of the front side processing is done. Detailed information on the process of silicon wafer direct bonding can be found in [54]. In this analysis only FTH and FDB sensors were investigated, as the deep diffused technology was discarded right at the beginning of the measurement campaign. The geometry of a p-stop default design and the corresponding cross section of a $25 \times 100\,\mathrm{µm}^2$ pixel is shown in Figure 4.2. The cross section is along the red arrow in the left image. For a maximum implant design the implant size is $1080\,\mathrm{µm}^2$ compared to $743\,\mathrm{µm}^2$ for the default design. The geometry of a maximum implant design is shown in Appendix A.
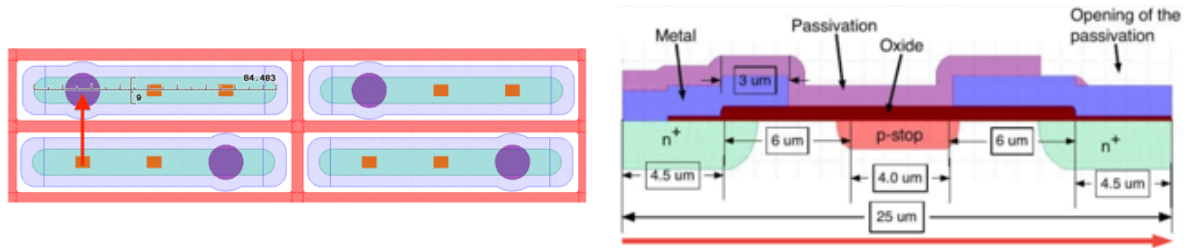
Figure 4.2 – An overview of a $25 \times 100\,\mathrm{µm}^2$ p-stop default design pixel geometry on the left and its cross section along the red arrow on the right.

During the initial production also sensors with a biasing grid, including a bias dot, were produced, to be able to test the sensor individually before bump bonding them to the chip. The bias dot however leads to losses in efficiency. A sensor design with a bias dot is shown in Appendix A.

4.2. Sensor Doping

For all six sensors used in the edge-on analysis the doping density N_{tot} can be determined from C-V measurements of pad diodes from the same wafer structure. As charges are built on both sides of the junction in the diode, the pn-junction capacitor can be considered as a charged parallel-plate capacitor, where the distance between the plates is the depletion zone and the capacitance C is given by

$$C = \epsilon_0 \cdot \epsilon_{\mathrm{Si}} \cdot \frac{A}{d},$$

(18)

35
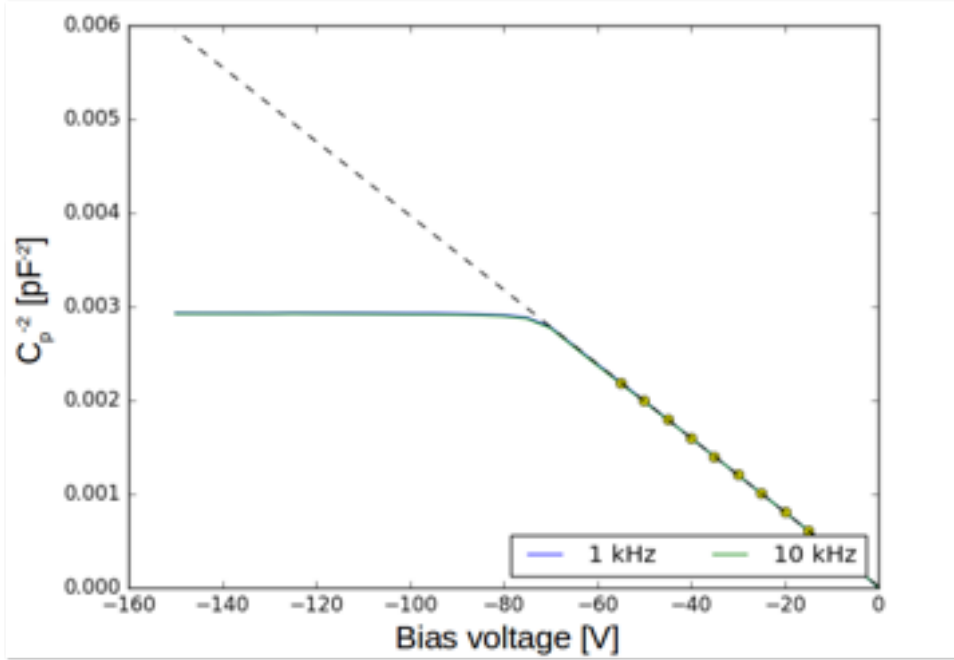
Figure 4.3 – $1/C^2$ as a function of bias voltage for a diode from a FTH wafer. The applied frequencies are $1\,$kHz and $10\,$kHz. The dotted line represents the fit to the data.

where d is the space between two plates or in case of the diode the depletion width, ϵ the dielectric constant of the sensor material and A the area [8]. From the C-V measurement, which is plotted as a function of $1/C^2$ one can derive the slope of the curve before full depletion, as for $V > V_{dep}$ the curve will be approximately constant.

The doping density can then be calculated as [55]

$$N_{tot} = \frac{2}{e \cdot \epsilon_0 \cdot \epsilon_{\text{Si}} \cdot A^2} \cdot \frac{1}{\mathrm{d}(\frac{1}{C^2})/\mathrm{d}V} \ . \tag{19}$$

The area of the diode is $0.25\,$cm^2, ϵ_0 is $8.85 \times 10^{-14}\,F/$cm and ϵ_{Si} is 11.75. The C-V measurements were performed inside a temperature-controlled probe station with bias voltages from 0 - 150 V in $1\,$V steps. The temperature was set to room temperature ($20°\,$C). The applied frequencies are $1\,$kHz and $10\,$kHz. The C-V curve is displayed in Figure 4.3, a first order polynomial was fitted to the central part of the curve (15 V - 55 V) to avoid outliers. A variation of the fit range ($\pm5\,$V) results in a systematic error on the calculated doping density of $\pm0.2\,$cm^{-3}.

For wafer 6, which is FTH material, the doping density was estimated to be $N_{tot} = 4.86 \times 10^{12}\,$cm^{-3}. The doping as a function of depth in the sensor was measured by J. Schwandt, UHH. The results are shown in Figure 4.4. The doping increases at the backside of the
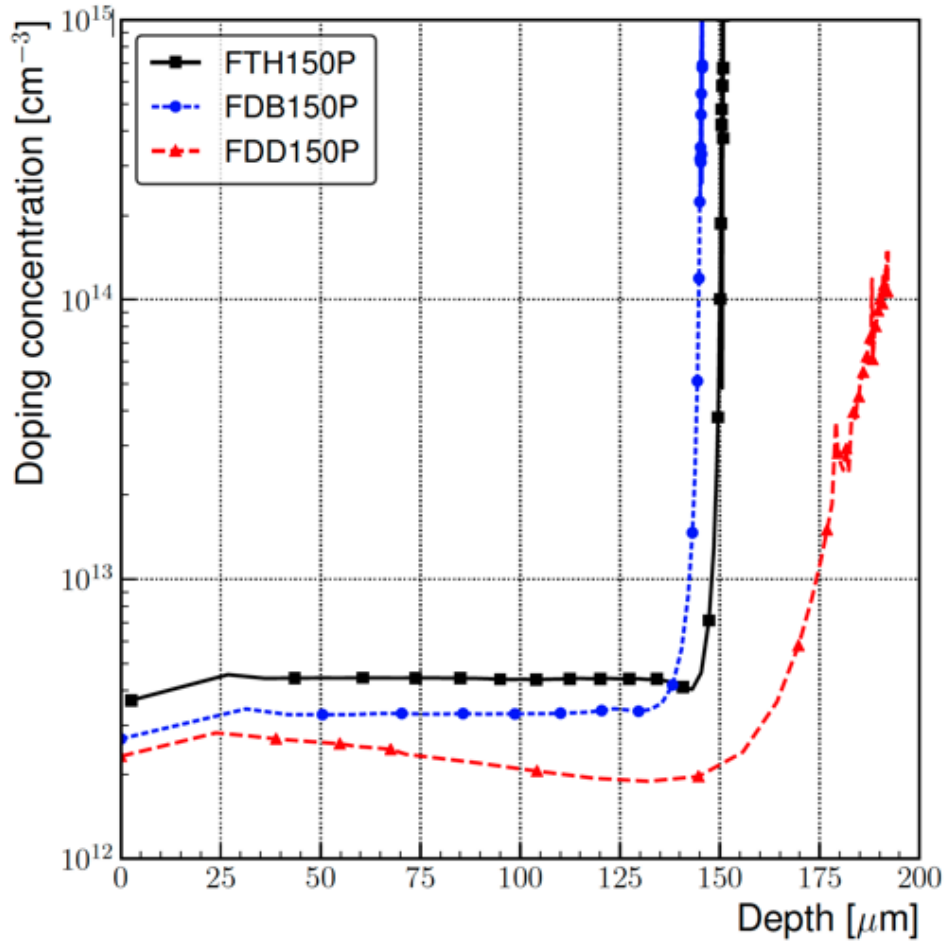
Figure 4.4 – The doping concentration for different wafer materials as a function of depth in the sensor. Figure from J. Schwandt.

sensor. It is also visible that the different wafer materials have a slightly different active thickness of the sensor. However, both wafers meet the ordered specifications of an active thickness of $150 \pm 10\,\mu\text{m}$. The differences in the active thicknesses are due to the different production processes.

4.3. Sensor Irradiation

As described in Chapter 3.3 the pixel sensors at the CMS experiment will have to be operated in a radiation field of photons, electrons, charged and neutral hadrons up to fluences of $\Phi_{eq} = 10^{16}\,\text{cm}^{-2}$ and ionizing doses of a few MGy. Therefore the sensors have been irradiated with different particle types to investigate the respective impact on the sensor properties.

4.3.1. Proton Irradiations

The sensors were irradiated with a 23 GeV/c proton beam at the CERN Proton Irradiation Facility (IRRAD). The proton spills are delivered with a maximum beam intensity of 2×10^{11} protons per spill to the irradiation area. With a defocusing-scanning system the beam can be spread out and produces a uniform irradiation spot over a surface that can vary from 2 to 25 cm [56]. The samples are placed in cardboards and are irradiated together with $1 \times 1 \, \mathrm{cm}^2$ aluminum foils for dosimetry. The quoted fluences are therefore an average of the size of the aluminum foils, which are big compared to the $8 \times 8 \, \mathrm{mm}^2$ sensor. The proton fluence is then determined by evaluating the ^{24}Na and ^{22}Na activity of aluminum foils produced via the nuclear reactions $^{27}\mathrm{Al}(p, 3pn)^{24}\mathrm{Na}$ and $^{27}\mathrm{Al}(p, 3p3n)^{22}\mathrm{Na}$, respectively. Additional information on the technique can be found in [57]. The error on fluences obtained with these activation techniques is 7% [56].

However, during data analysis it was found that the irradiation was not uniform over the size of the sensor. The existence of a beam spot center and its position are deducable from the data. The fluences were therefore recalculated from the beam profile monitor data of the irradiation facility. The samples were irradiated in zone 2 of the facility and the corresponding beam profile monitor data was analyzed. The insertion and extraction timestamps of the sensors are known, so that the exact beam information can be obtained in form of one dimensional (in x and y) profiles of the beam intensities, from which the beam profile can be calculated. An example of the available data from the irradiation to a proton fluence of $\Phi_p = 3.28 \times 10^{15} \, \mathrm{cm}^{-2}$ (fluence quoted from the dosimetry result of the aluminum foil) is shown in Table 2. For each irradiation the dosimetry results from the aluminum foils are known, in case of the higher proton irradiation additional information from the back side is available. For the higher irradiated sensors these results are $\Phi_p = 6.50 \times 10^{15} \, \mathrm{cm}^{-2}$ from the front side and $\Phi_p = 7.84 \times 10^{15} \, \mathrm{cm}^{-2}$ from the back. These numbers are averaged over the size of the aluminum foils and are therefore, if the sensor is shifted with respect to the foil and under consideration of the non-homogenous beam profile, in need of more accuracy.

From these data with nine data points in x, compare Figure 2, and seven data points in y the beam profile is obtained for each coordinate, where each data point is the sum of all beam profiles for all spills. As there is no information on errors available, they are assumed to be linear to the square root of the bin content. To extract the beam width σ_x in x, the profile is fitted with

$$f(x) = A \cdot \exp\left(-\frac{1}{2} \cdot \left(\frac{x - \bar{x}}{\sigma_x} \right)^2 \right), \tag{20}$$

TIMESTAMP	SPILL	x=-18	x=-13.5	x=-9	x=-4.5	x=0	x=4.5	x=9	x=13.5	x=18	y=-13.5	y=-9
2017-11-01 00:00:06	1	0.0312	0.19632	0.50607	1.00132	0.94345	0.61157	0.19845	0.04395	0.0212	0.0842	0.2527
2017-11-01 00:00:23	2	0.0357	0.19657	0.53095	1.03508	0.90732	0.52408	0.17532	0.04132	0.0202	0.09282	0.27332
2017-11-01 00:00:27	3	0.01195	0.09082	0.32482	0.75845	1.16795	1.02095	0.5937	0.15482	0.03745	0.11995	0.35307
2017-11-01 00:00:45	4	0.03045	0.1922	0.50345	1.01683	1.02595	0.8692	0.43807	0.09032	0.02732	0.0942	0.2782
2017-11-01 00:01:03	5	0.00607	0.02257	0.11832	0.33457	0.65082	1.23932	1.06633	0.46195	0.10595	0.0807	0.21795
2017-11-01 00:01:07	6	0.005	0.07025	0.29312	0.75276	1.20987	1.07338	0.52662	0.11325	0.02575	0.1215	0.36475
2017-11-01 00:01:25	1	0.01887	0.169	0.44675	0.933	0.99162	0.83375	0.36812	0.06412	0.017	0.08337	0.258
2017-11-01 00:01:43	2	0.00175	0.01975	0.12575	0.3305	0.66175	1.21863	1.06875	0.52212	0.11062	0.07637	0.21362
2017-11-01 00:01:47	3	0.00725	0.09062	0.31425	0.77525	1.252	1.09175	0.604	0.14137	0.029	0.12612	0.37787
2017-11-01 00:02:05	4	0.02562	0.19225	0.55675	1.12001	1.12888	0.82475	0.28212	0.05162	0.01737	0.09787	0.29687
2017-11-01 00:02:23	5	0.00187	0.01975	0.12187	0.33488	0.72737	1.276	1.06075	0.46337	0.0965	0.0855	0.23737
2017-11-01 00:02:26	6	0.007	0.08912	0.31538	0.78788	1.23312	1.01612	0.59787	0.15437	0.02962	0.12075	0.365

Table 2 – A part of the beam profile monitor data for the 2017 irradiation of the sensors. For each time stamp, the beam intensity is provided per spill in coordinates of x and y.

where $\bar{x}$ is the position of the beam spot in x. The calculations and the exact numbers were kindly provided by F. Feindt, UHH. The resulting beam profile in x and the fit results for the data introduced in Figure 2 are shown in Figure 4.5. It is estimated that the error on the width introduced by the fit range and the assumed bin errors is at most 3.5 %.
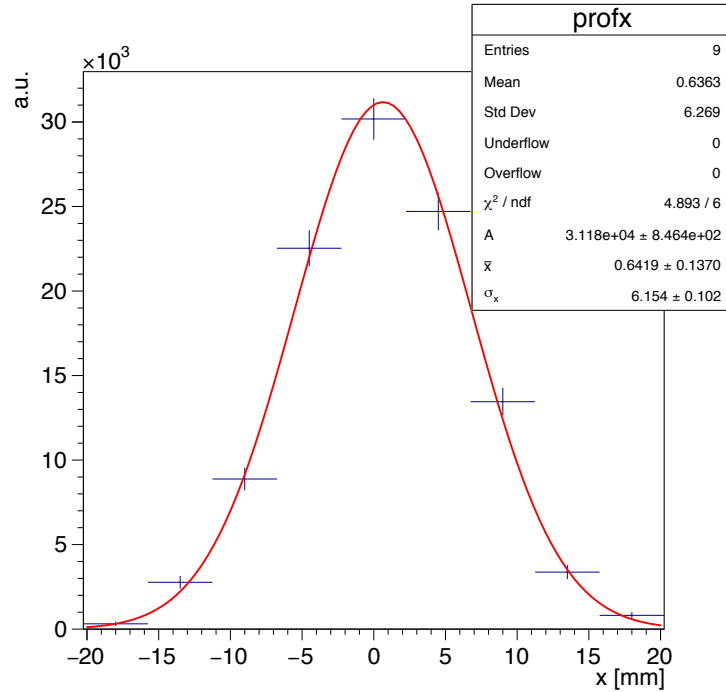
Figure 4.5 – The nine data points obtained in x from the beam profile monitor data and the results of the fit, plot provided by F. Feindt. The resulting beam width in x is 6.15 mm.

To obtain the final fluence map, the calculated beam widths for each direction are used, assuming the beam center in the middle of the dosimeter foil. The fitted beam widths are $\sigma_x = 6.15$ mm and $\sigma_y = 6.37$ mm for the lower proton irradiation and $\sigma_x = 6.44$ mm and $\sigma_y = 5.68$ mm for the higher proton irradiation. The shape of the fluence distribution is

given by

$$f(x, y) = \exp\left(-\frac{1}{2} \cdot \left(\left(\frac{x - \bar{x}}{\sigma_x}\right)^2 + \left(\frac{y - \bar{y}}{\sigma_y}\right)^2\right)\right).$$ (21)

The obtained function $f(x, y)$ has to be calibrated with the fluence, which the average fluence was calculated on. Thus, normalization to the dosimetry results with the fluence over the area f_N and the size of the aluminum foil (1 cm^2) yields the normalized fluence distribution $F(x)$ given by

$$F(x, y) = \frac{f(x, y) \cdot 3.28 \times 10^{15} \text{cm}^{-2}}{f_N},$$ (22)

with

$$f_N = \int_{-5}^{5} \int_{-5}^{5} f(x, y) \, \mathrm{dx} \, \mathrm{dy}.$$ (23)

In Figure 4.6 on the left the fluence map for the higher proton irradiation with an average fluence of $\Phi_p = 6.60 \times 10^{15}$ cm^{-2} is shown. Over the area of a sensor the fluence varies from 9×10^{15} cm^{-2} in the beam spot center to 6×10^{15} cm^{-2} at larger radii. The resulting fluence map for the 2017 irradiation is shown in Figure 4.6 on the right. Over the area of a sensor the fluence varies from $\Phi_p = 4 \times 10^{15}$ cm^{-2} in the beam spot center to $\Phi_p = 2 \times 10^{15}$ cm^{-2} at larger radii. In both fluence maps the sensor size is indicated by the black dashed square. The sensors' positioning in the beam with respect to the dosimetry foil however is unknown and needs to be determined, as the maps clearly show that the fluence is position dependent.

The position of the beam spot center is estimated from vertical incidence measurements on the same sensors. It is assumed that the minimum efficiency is at the area of the highest irradiation, the beam spot center. The obtained efficiency maps show a radial shape around the beam spot center, from which the point of minimal efficiency is determined by the difference of 1 and a 2-dim Gaussian fit and taken as the beam spot center, resulting in an almost circular spot in case of the sensors analyzed in this thesis, see Figure 4.7. The beam spot center coordinates for the sensor with the lower fluence are $(-0.12, 1.69)$ and for the higher irradiated sensor the beam spot center is at $(-2.56, 0.60)$. The resulting fluences are shown in Chapter 7, as the sensors are split into areas of different fluences. These maps show that for the analyzed sensors the beam spot center is indeed shifted significantly from the middle of the sensor, such that over the area of the sensor, there are areas of different fluences Φ_p, which need to be taken into account in the analysis. From the analysis of the edge-on data, the existence of the beam spot center was also confirmed as the sensor data showed different results for different areas of the sensor, see Chapter
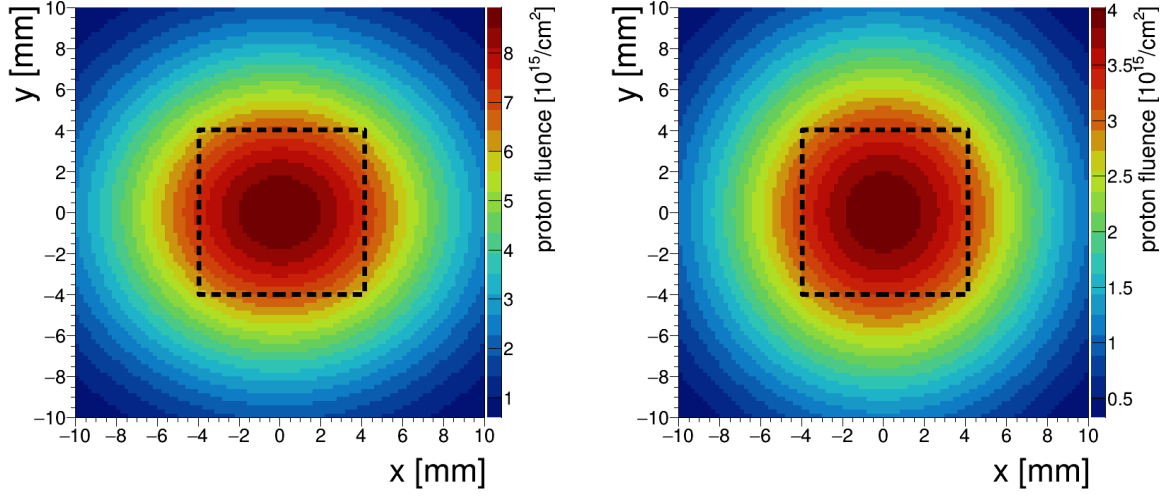
Figure 4.6 – The proton fluence map for the sensor with an average fluence of $\Phi_p = 6.60 \times 10^{15}\,\mathrm{cm}^{-2}$ on the left and for the sensor with an average fluence of $\Phi_p = 3.28 \times 10^{15}\,\mathrm{cm}^{-2}$ on the right. The fluence has its maximum in the beam spot center and decreases for larger radii. The sensor size is indicated by the black dashed square.
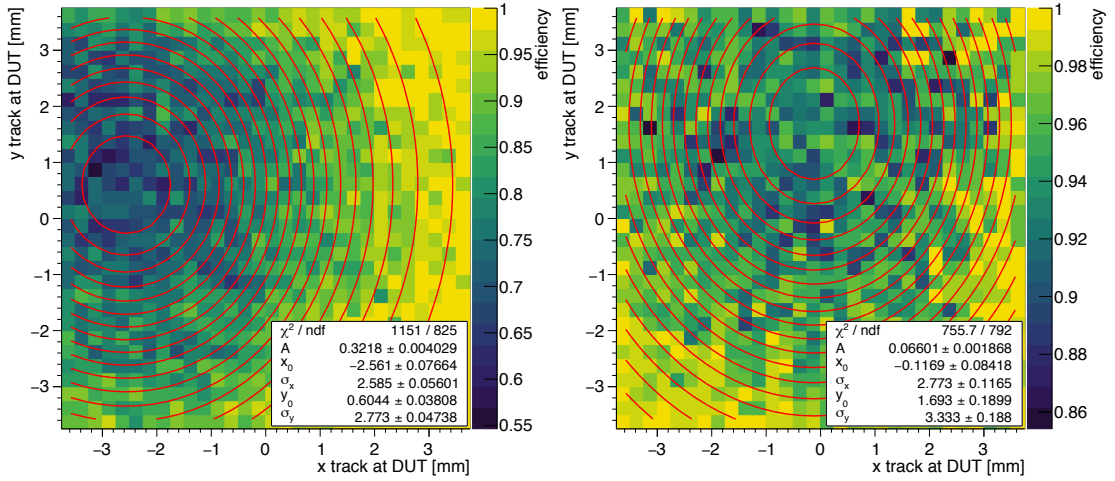
Figure 4.7 – On the left, the efficiency map of the sensor with the higher proton irradiation is shown, as well as the fitted beam spot and its position at (-2.56, 0.60) in telescope coordinates. On the right, the efficiency map from the sensor with the lower proton irradiation is shown, as well as the fitted beam spot center and its position at (-0.12, 1.69) in telescope coordinates. Both figures are from F. Feindt.

7.3.1.

The corresponding fluence maps for the sensors after determination of the position of the beam spot center are shown in Figure 4.8. For both sensors the fluence varies across the sensor by approximately a factor of 2.
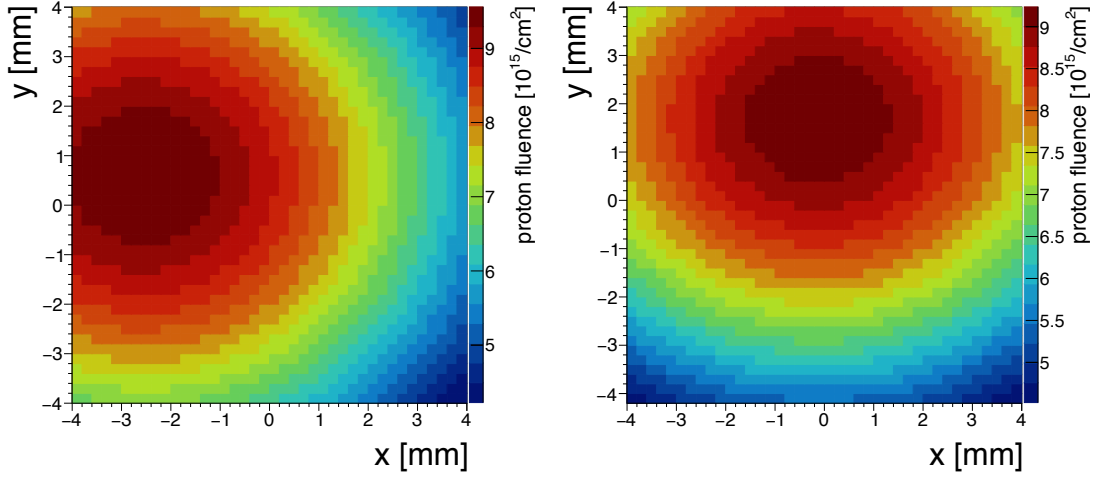
Figure 4.8 – On the left, the fluence map of the sensor with the higher proton irradiation is shown around the beam spot at the position (-2.56,0.60) in telescope coordinates. On the right, the fluence map from the sensor with the lower proton irradiation is shown around the beam spot at the position (-0.12,1.69) in telescope coordinates. For both cases the fluence varies over the area of the sensor.

The hardness factor of 0.62 ± 0.04 for $23\,\mathrm{GeV}$ protons, [58], has to be considered when expressing the calculated proton fluences as neutron equivalent fluences.

4.3.2. Neutron Irradiations

The sensors were irradiated with neutrons at the TRIGA Mark II reactor at the Jožef Stefan Institute in Ljubljana, Slovenia. It is a light water pool reactor type, that uses natural convection for cooling [59]. A continuous energy spectrum and a flux of fast neutrons with an energy larger than 100 keV enables an irradiation up to $2 \times 10^{13}\,\mathrm{n}_{eq}\,\mathrm{cm}^{-2}\mathrm{s}^{-1}$ at full reactor power of 250 kW in the very central channel out of 12 channels.

The sensors were irradiated to neutron fluences of $\Phi_n = 4 \times 10^{15}\,\mathrm{cm}^{-2}$, $\Phi_n = 8 \times 10^{15}\,\mathrm{cm}^{-2}$ and $\Phi_n = 16 \times 10^{15}\,\mathrm{cm}^{-2}$. As a result of an irradiation request of $\Phi_n = 6 \times 10^{15}\,\mathrm{cm}^{-2}$ which was not successful, as the mechanics which transport the sensor into the reactor seem to have malfunctioned, also a lower fluence was produced. Lab measurements on the leakage current suggest a fluence of $\Phi_n = 0.6 \times 10^{15}\,\mathrm{cm}^{-2}$, so 10 times lower than requested. For fast neutron irradiations the hardness factor is 0.90 ± 0.05 [60].

4.4. The ROC4SENS Readout Chip

The Read Out Chip (ROC) registers a pixel hit in the silicon. The basic operation of a ROC is to readout, store and out-put hit information for pixels with charge exceeding a certain threshold. Depending on the ROC, hits can consist of an address, a pulse height and time stamp information which are stored temporarily, until the read out is triggered. The ROC4SENS was developed as an analog general purpose ROC, dedicated to characterizing silicon pixel sensors. The design was done in the context of particle physics at the LHC, in particular the ROCs of the pixel detector of the CMS experiment, described in 3.2. Therefore the design could profit from already existing infrastructure, which eased its testing [61]. The chip was designed in a Complementary Metal-Oxide-Semiconductor (CMOS) 250 nm node technology and was made compatible with the testing hardware of the ROCs of the CMS pixel detector. Contrary to many other ROCs, the ROC4SENS has no zero suppression, so the analog pulse height of every pixel is read out. Furthermore, the ROC4SENS was designed to withstand a high level of irradiation to make it suitable for sensor irradiation tests. All sensors analyzed in this thesis were read out with the ROC4SENS version V1.1.

4.4.1. Geometry

The chip contains a pixel matrix of 155 (columns) $\times$ 160 (rows)= 24800 pixels with a pitch of $50 \times 50\,\mu\text{m}^2$. The total size of the chip is $7.848\,\text{mm} \times 9.778\,\text{mm}$. The bump pads are staggered such that the pads of every second column are offset by half a pitch ($25\,\mu\text{m}$), see Figure 4.9. This facilitates the bonding of several sensor geometries, including thin sensors with a $25 \times 100\,\mu\text{m}^2$ pitch, so half the width of the ROC pixel pitch, onto the ROC4SENS and it helps to mitigate crosstalk. To be able to share the same wafer test system and the same digital test board (DTB) as the CMS Pixel Phase 1 ROCs, the number of wire bond pads had to be equal. Thus in total there are 35 wire bond pads, which are placed with a pitch of $175\,\mu\text{m}$. Additionally, there are eight bump bond pads below the pixel array, which can be used to connect parts of the sensor, e.g. the guard rings, to ground. The chip is glued to a chip carrier PCB.

Since it is an asynchronous chip, there are no time stamps and the hold signal is synchronized with a clock in the DTB. The ROC4SENS is controlled via two shift registers (SR), one selects the pixel column (x-coordinate) and one the pixel row (y-coordinate). To select one pixel, one bit is clocked into the x- and one into the y-register. The content of each cell is shifted to the next by a clock cycle in the signal ϕ_1 and ϕ_2. At the moment that ϕ_1 changes from 0 to 1 the first cell gets the state of the input bit to the SR which is denoted RBI (Read Bit In) and the content of the last cell is sent to RBO (Read Bit
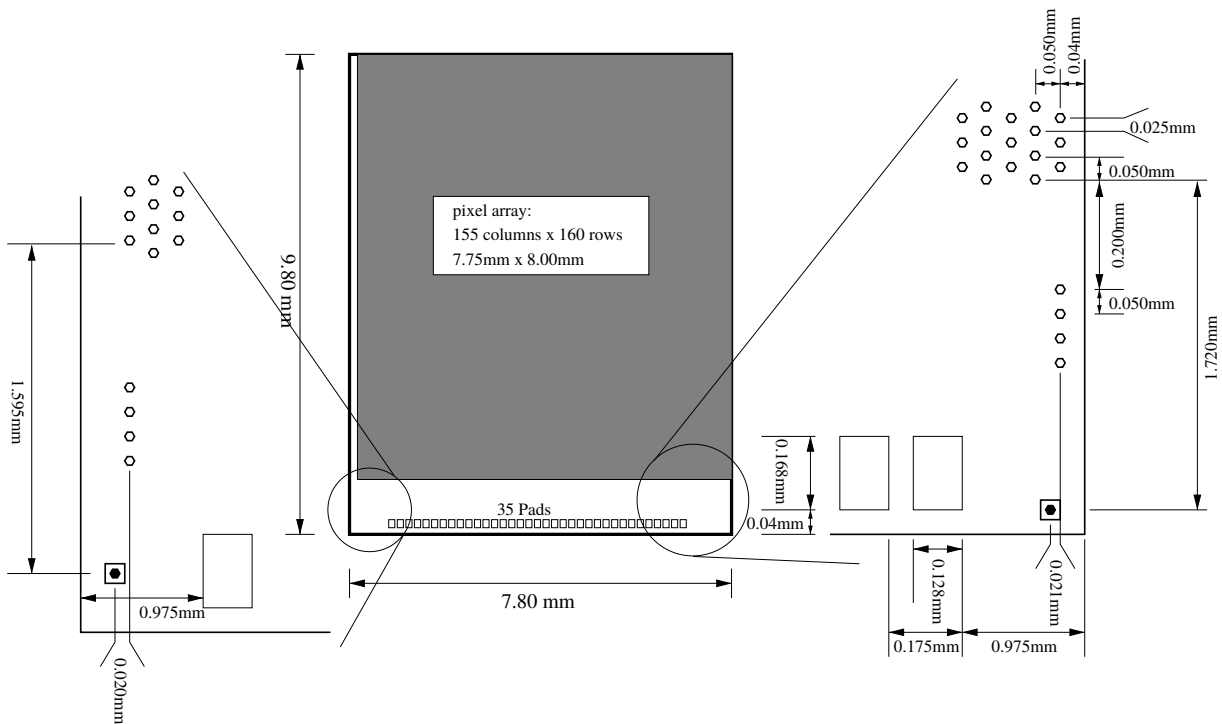
Figure 4.9 – Sketch of the ROC4SENS geometry from [62].

Out) as ϕ_2 changes from 0 to 1. The signal shown in Figure 4.10 at the bottom generates the state that is shown in the x-register on the left. This pattern has been tested up to a clock frequency of 100 MHz. More detailed information on the characteristics of the chip can be found in [61].

When a pixel is selected, a calibration pulse can be injected and the pixel's output is fed through the chip's output.
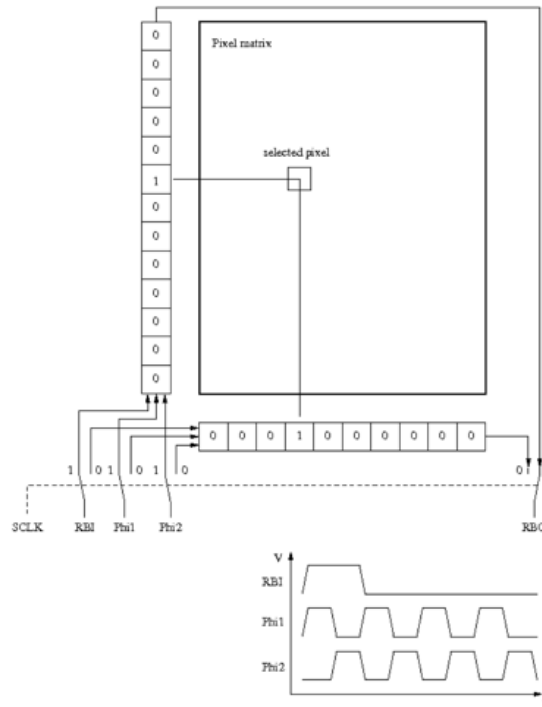
Figure 4.10 – ROC4SENS pixel selection by the two shift registers from [62].

4.4.2. Analog Readout Chain

The analog readout chain of the ROC4SENS is sketched in Figure 4.11. The bump pad of each pixel is connected to a charge-sensitive 2-stage amplifier with a preamplifier and a shaper. Both parts are DC-separated by a capacitor. With the amplifier feedback, V_{gpr} and V_{gsh}, the falling edge of the pulse can be controlled.

For analog operation ROC4SENS requires several voltage levels, which are provided from external sources. These voltage levels include:

- V_{ana}: analog supply voltage (1.9 - 2.1 V)

- V_{dd}: digital supply voltage (2.2 V)

- V_{ss}: analog ground

- GND: digital ground, V_{ss} and GND should be connected on the PCB

- V_{cal}: level of the calibration signal

- V_{gpr}: feedback of the preamplifier (0.4 -0.7 V)

- V_{gsh}: feedback of the shaper (0.4 -0.7 V)
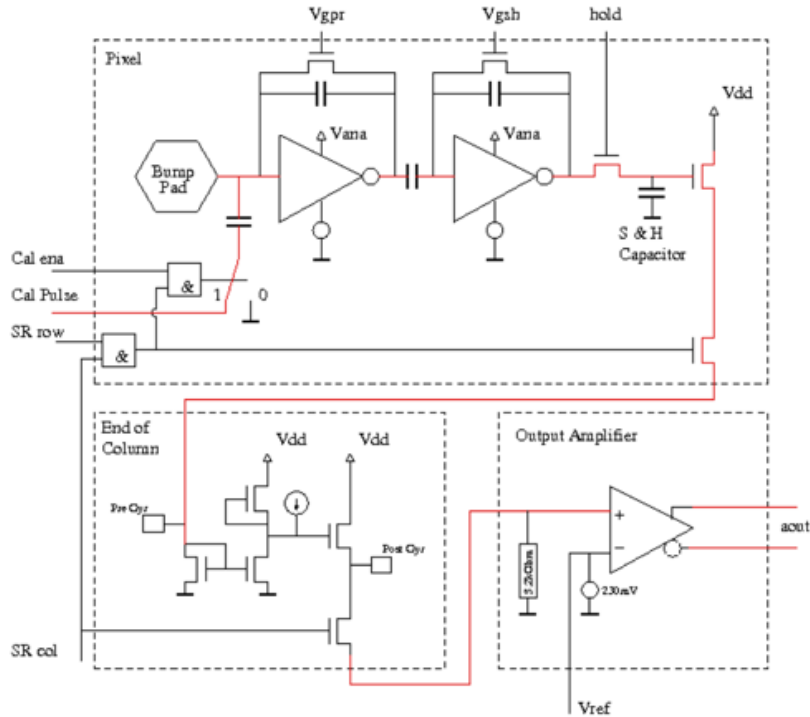
Figure 4.11 – Schematic of the analog read out chain, the red line depicts the path of an injected calibration pulse, from [62].

- V_{ref}: reference voltage for the output amplifier (230 mV)

An example of the sensitivity of the pulse shape on the amplifier feedback and shaping is shown in Figure 4.12. The rise time and amplitude of the signal changes with V_{gpr} and with increasing V_{gsh} the falling edge is slowed down.

The two feedback transistor are PFETs, which signifies that a small voltage means a strong feedback and a fast discharge of the feedback capacitor. Through the hold switch, the shaper output is connected to the sample and hold capacitor and the gate of the pixel's output transistor. As long as the hold switch is closed, the output of the transistor follows the shaper. Once it is opened, the charge on the capacitor is stored and the picture is frozen. In order to use the full dynamic range and have the best signal to noise ratio, the hold signal has to arrive at the maximum of the pulse.

To compensate for cable delays, delay of the NIM logic and internal delay of the trigger logic unit (TLU), the pulse has to be slowed down by reducing the analog voltage and/or increase the feedback resistance. The electric current from the output of the column bus is transmitted to the column amplifier at the end of the column, which in turn transmits the signal to the output amplifier that converts the current signal to a differential voltage to be transmitted out of the chip.
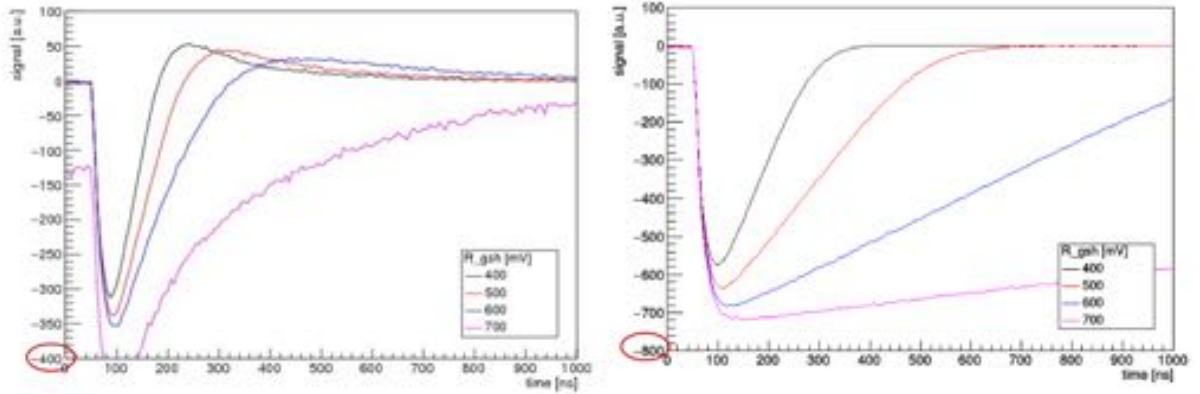
Figure 4.12 – Pulse shape for calibration pulse injection after preamplifier and shaper for different amplifier feedback and shaping, from [62]. The left plot shows the pulse shape for $V_{gpr} = 650\,\mathrm{mV}$ and the right plot for $V_{gpr} = 900\,\mathrm{mV}$. Note the different signal scales.

Full Readout at Test Beam

As there is no internal signal on the ROC4SENS which could indicate a hit, the moment of sampling has to be initiated externally and distributed to all pixels simultaneously. For use in test beam the hold signal is provided by a coincidence of two trigger scintillators. For each chip the pulse shape settings have to be chosen such that the hold signal arrives at the maximum of the pulse.

With V_{ana} the rise time of the amplifier can be adjusted. If the total analog current is set to $125\,\mathrm{mA}$, a peaking time of about 25 hold units is reached, where one hold unit corresponds to $6.25\,\mathrm{ns}$, see Section 4.5. It can be slowed down by reducing the analog current I_A. The difference between the pulse shapes of $I_A = 125\,\mathrm{mA}$ and $I_A = 50\,\mathrm{mA}$ is shown in Figure 4.13. For running with the telescope $I_A = 125\,\mathrm{mA}$ is too fast for the trigger, as the pulse needs to peak around 40 hold units. With $I_A = 50\,\mathrm{mA}$ the signal is more than slow enough for the trigger and there is also less sensor leakage current, as the self-heating of the chip is reduced. These pulse shapes were obtained with a $\Phi_p = 6.6 \times 10^{15}\,\mathrm{cm}^{-2}$ irradiated chip. As this measurement was taken with a calibration pulse, the shape of a signal in test beam might be different due to the irradiation. Therefore a delay scan with the same chip was also performed with the edge-on method, explained in detail in Chapter 7. These data were taken without the telescope to allow for trigger delays shorter than 40 hold units. The signal pulse height for the edge-on signal is the MPV of the cluster pulse height distribution which is obtained by a Landau fit to the data.

   The pulse shape of the calibration pulse and the delay scan of the edge-on measurement can be seen in Figure 4.14. The pulse shape for calibration pulses was scaled by a constant factor of 0.54 for a better comparison of both curves. They have a similar peaking time but the overall pulse shape is different. For the edge-on measurements, the maximum
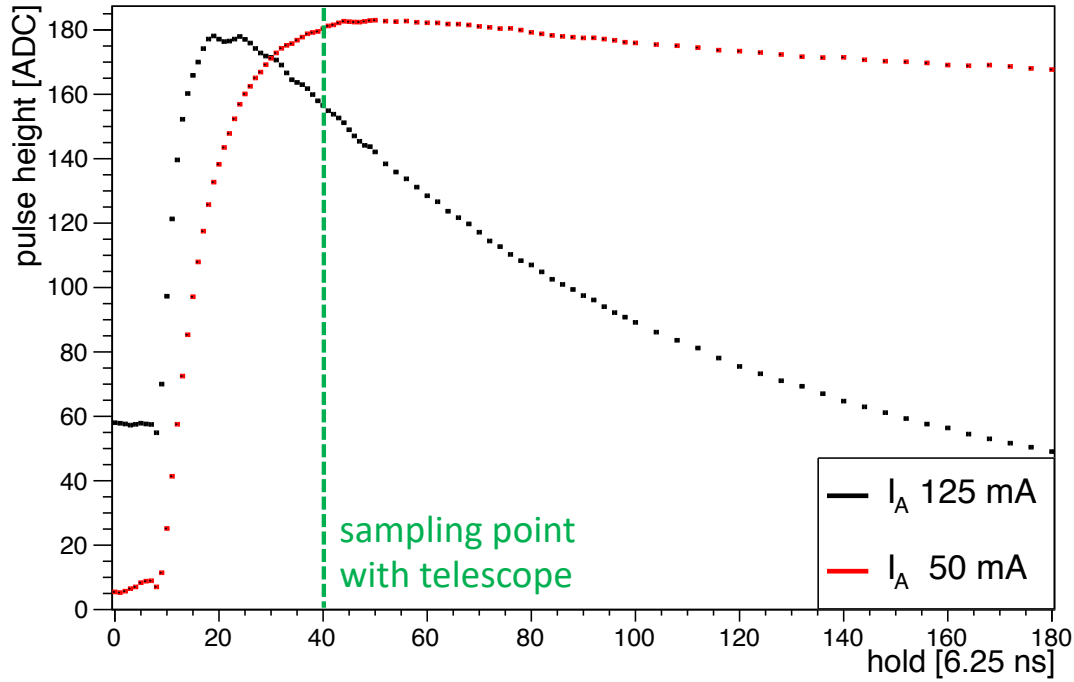
Figure 4.13 – Pulse shape for calibration pulse injection for different analog currents I_A as a function of hold units, measured after preamplifier and shaper. For measurements with the telescope (dashed green line) the peaking time needs to be around 40 hold units. For an analog current of $I_A = 125\,\mathrm{mA}$ the pulse shape peaks fast (around 25 hold units) and it has a steep decline afterwards. The pulse shape peaks later for a reduced $I_A = 50\,\mathrm{mA}$ and then it only gradually declines. The sensor is irradiated to $\Phi_p = 6.6 \times 10^{15}\,\mathrm{cm}^{-2}$ and the bias voltage is $800\,\mathrm{V}$ and the temperature is $-30°\mathrm{C}$.

pulse height is reached at 48 hold units, which corresponds to sampling with the telescope and a 50 ns delay.

Therefore for the data in this analysis, V_{ana} is chosen such that the total analog current is $40\,\mathrm{mA}$ ($\approx 2\,\mathrm{\mu A}$ per pixel).

For read out the whole pixel array both shift registers are first reset by setting both clocks high and the RBI low. Then one bit is injected into the column shift register. This way the first column can be scanned by moving a bit through the row shift register. After the first column is scanned the read bit in the column shift register is moved by one position, leading to a column-wise readout of the chip.

As the transfer of the signal to the periphery is done column-wise with all pixels of the same column connected to a column bus, which is connected to a column amplifier, the signal amplification might differ between different columns.
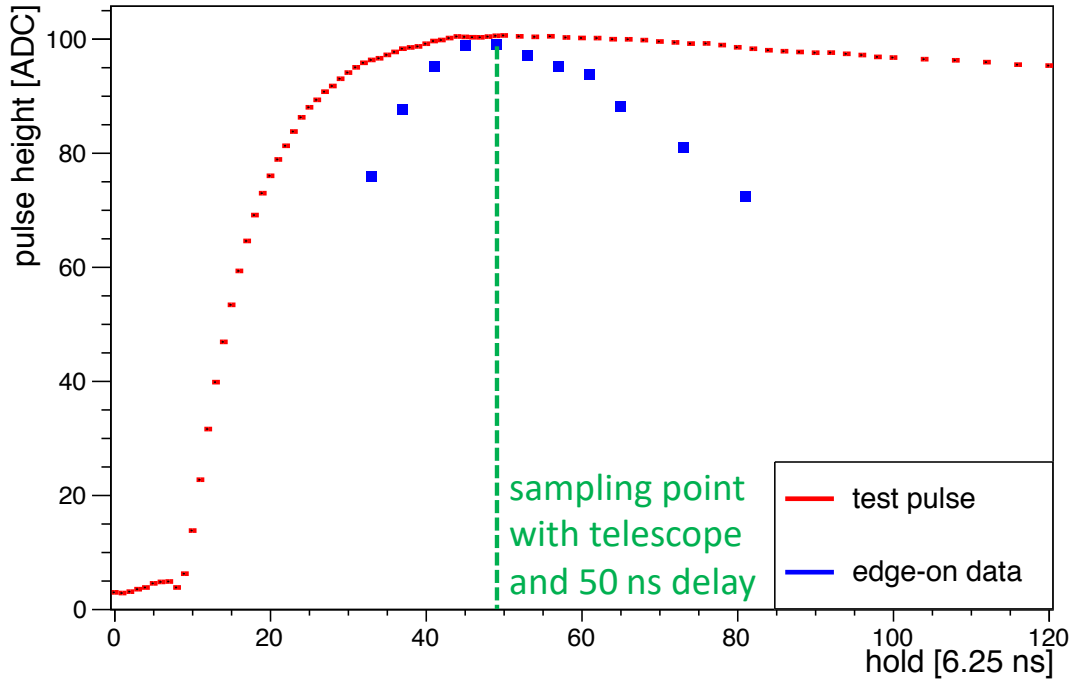
Figure 4.14 – Pulse shape for calibration pulse injection in comparison to the Landau MPV for the edge-on measurement of a sensor irradiated to $\Phi_p = 6.6 \times 10^{15}\,\mathrm{cm}^{-2}$ as a function of hold units. The analog current is set to $50\,\mathrm{mA}$. The edge-on pulse height reaches its maximum value at 48 hold units, which corresponds to measurements with the telescope and an additional delay of 50 ns (dashed green line). Both the calibration pulse and the edge-on measurements have a similar peaking time but the overall pulse shape is different.

4.4.3. Pulse Pileup

In general, the individual settings of the amplifier feedback and shaping and thus the exact shape of the pulses differs from chip to chip. However, during read out of a single chip, it was observed that it is possible for a new pulse to enter before the previous one is fully discharged. This pulse pileup, where the second pulse piles up on top of the first one and leads to a larger signal amplitude, is shown in Figure 4.15. However, as the mode of operation of the column amplifier is similiar to that of a damped electrical oscillator, it is also possible that the second pulse undershoots and when added on top, it results in a reduced signal amplitude. As the influence of the ADC sampling point is visible, it should be adjusted such that the sampling is done late in the clock cycle [63] and the influence of the previous pulse is minimized.

To correct for these piled up signal amplitudes, the pulse height of the next pixel $j+1$ as a function of the current read out pixel j is monitored and adjusted. The linear dependence of those two pulse heights should be zero and is corrected if a dependence of more than 3 % on the previous pulse height is visible. An example of the monitoring plot for the
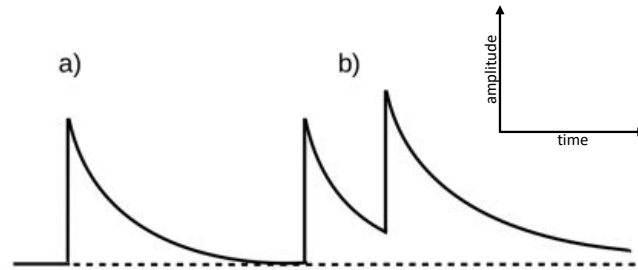
Figure 4.15 – a) Sketch of a tail pulse, b) Pulse pileup, a second pulse piles up on top of the first, resulting in a larger amplitude.

pulse pileup is Figure 4.16. As there is also real charge sharing between two pixels, the plot shows a maximum for low previous pulse heights, however due to the staggered bump bond pattern, this is the next pixel in the readout direction but physically the next to next pixel, compare Figure 6.3. The pulse pileup is not visible for the non-irradiated sensor, as for pulse height values around the Landau MPV (220 ADC) the next pixel pulse height does not show a linear dependence but instead a slope close to zero. The larger pulse height values are δ-electrons from the tail of the Landau distribution, compare Chapter 2.1.2.
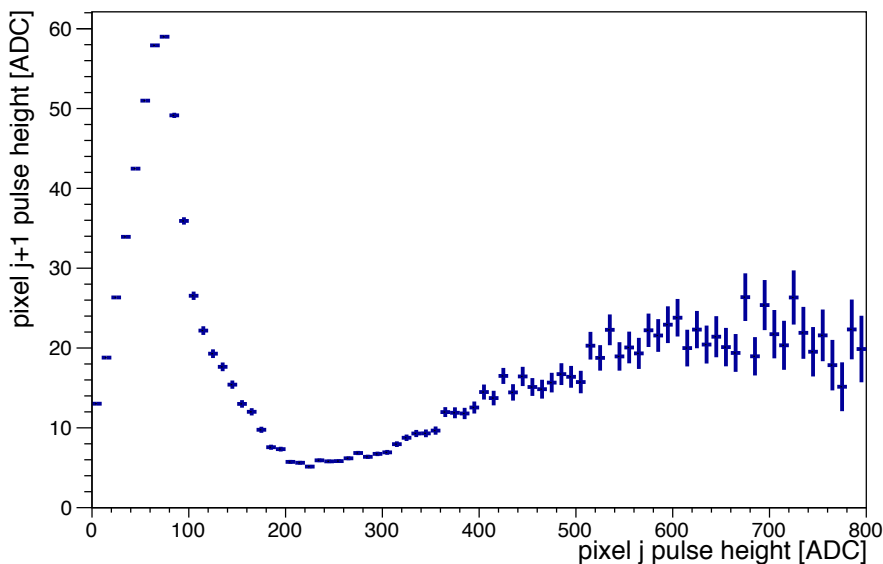
Figure 4.16 – An example of the next pixel pulse height monitored as a function of the current read out pixel for a non-irradiated sensor. The maximum at small pixel pulse heights corresponds to actual charge sharing between the two pixels. There is no pulse pileup visible for pixel pulse heights around the Landau MPV ($\sim$220 ADC).

Figure 4.17 shows an example of the same distribution before and after the correction for
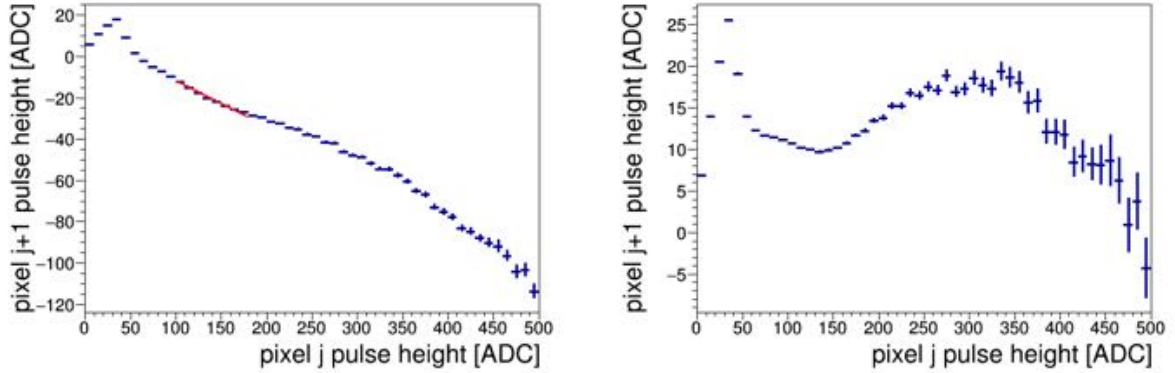
Figure 4.17 – The next pulse height as a function of the current one for the chip irradiated to $\Phi_p = 6.6 \times 10^{15} \, \mathrm{cm}^{-2}$ at $800\,\mathrm{V}$ without (with) the correction on the left (right). The red line represents the area that is fitted with a linear function to obtain the slope, which is used to correct the data. The slope is no longer visible after the correction is applied.

a sensor irradiated to $\Phi_p = 6.6 \times 10^{15} \, \mathrm{cm}^{-2}$ at $800\,\mathrm{V}$ bias voltage. The charge sharing peak at low pulse heights is again visible. Around the Landau MPV, which is close to $100\,\mathrm{ADC}$, a steep slope is visible instead of a minimum. The red line indicates the area over which the slope was fitted with a linear function. On the right side, the same plot is shown after the correction. This plot shows the previously mentioned possibility of the second pulse undershooting and thus resulting in a negative pulse height.

The origin of the pulse pileup is unknown, there are several positions where the signals can overlap. The pulse pileup can happen at the column gyrator, the differential output amplifier, at the receiver of the digital test board or the ADC on the DTB [64]. However, as it is dependent on the shape of the incoming pulse whether two pulses pile up, the pulse pileup varies for different read out chips. With increasing radiation of the chip the pulse shape also varies, leading to a more or less severe pulse pileup, again depending on the chip and its settings.

4.4.4. Leakage Current

During all measurements with the different chips the sensor current is measured to monitor the effect of leakage current and self-heating. All settings, as described in the previous part, were chosen such that the monitored current is below $1\,\mathrm{nA}$ per pixel. The increase in leakage current ΔI is generally expected to scale with the fluence according to

$$\Delta I = \alpha \cdot \phi_{eq} \cdot V \ , \tag{24}$$

where V is the applied bias voltage and the proportionality factor α is the current related damage rate [20]. The measured sensor currents for all edge-on measurements analyzed in this work are shown in Figure 4.18. The sensor current increases with fluence as expected. All currents stay well below the $1\,\mathrm{nA}$ per pixel limit, only the current for the $\Phi_n = 16 \times 10^{15}\,\mathrm{cm^{-2}}$ irradiated sample is lower as expected, since it does not differ much from the current for $\Phi_n = 8 \times 10^{15}\,\mathrm{cm^{-2}}$. The ambient temperature was lower for the measurement of the $\Phi_n = 16 \times 10^{15}\,\mathrm{cm^{-2}}$ irradiated sensor, as the cooling of the setup has been improved just before this measurement.
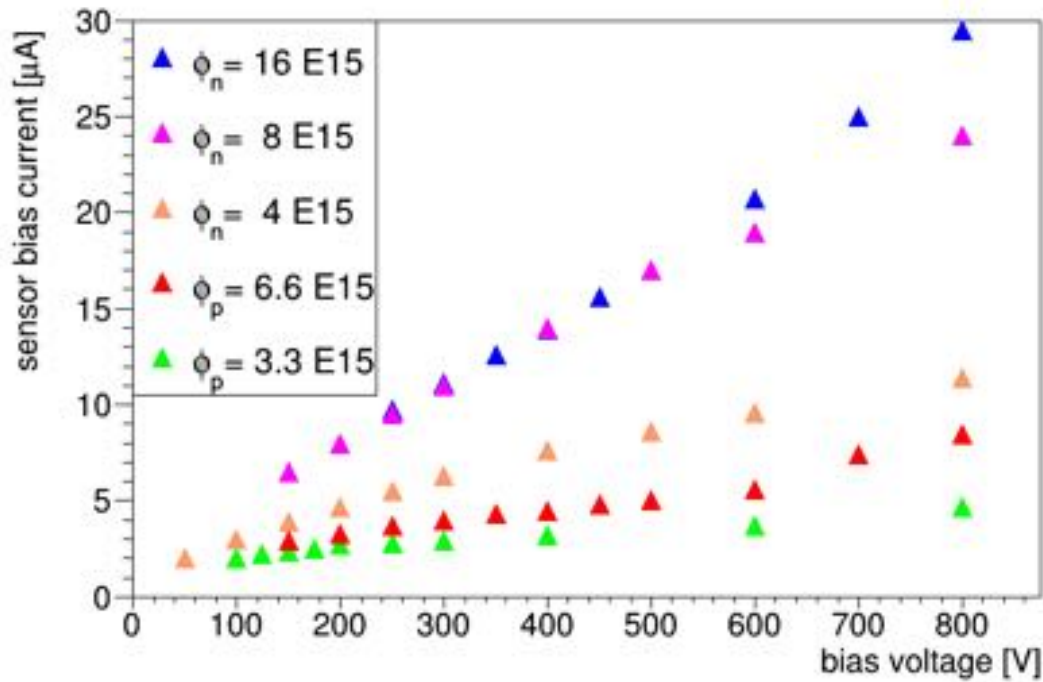
Figure 4.18 – Monitored sensor current for all edge-on measurements as a function of bias voltage. The current increases as a function of fluence. The current for the $\Phi_n = 16 \times 10^{15}\,\mathrm{cm^{-2}}$ irradiated sample is lower as expected, since it does not differ much from the current for $\Phi_n = 8 \times 10^{15}\,\mathrm{cm^{-2}}$. The ambient temperature was lower for the measurement of the $\Phi_n = 16 \times 10^{15}\,\mathrm{cm^{-2}}$ irradiated sensor, as the cooling of the setup has been improved just before this measurement.

In addition, lab measurements of the temperature dependence of the leakage current were performed. The leakage current of a sensor irradiated to an average fluence of $\Phi_p = 3.28 \times 10^{15}\,\mathrm{cm^{-2}}$ was measured as a function of applied bias voltage. The temperature was set with a Lauda chiller and a Peltier element. It is clearly visible in Figure 4.19 that the leakage current increases with temperature. To set a chip to a certain temperature at test beam, where no exact determination of the temperature on the chip is possible, these

curves are used for calibration. It was found that the most stable value is at a bias voltage of 400 V. Therefore to set a certain temperature at test beam, the value of the leakage current at 400 V for the desired temperature is matched. The comparison of Figure 4.19 and the measured current in Figure 4.18 for the chip irradiated to $\Phi_p = 3.28 \times 10^{15}\,\mathrm{cm}^{-2}$ shows that the achieved temperature during test beam operation is $-30°C$.
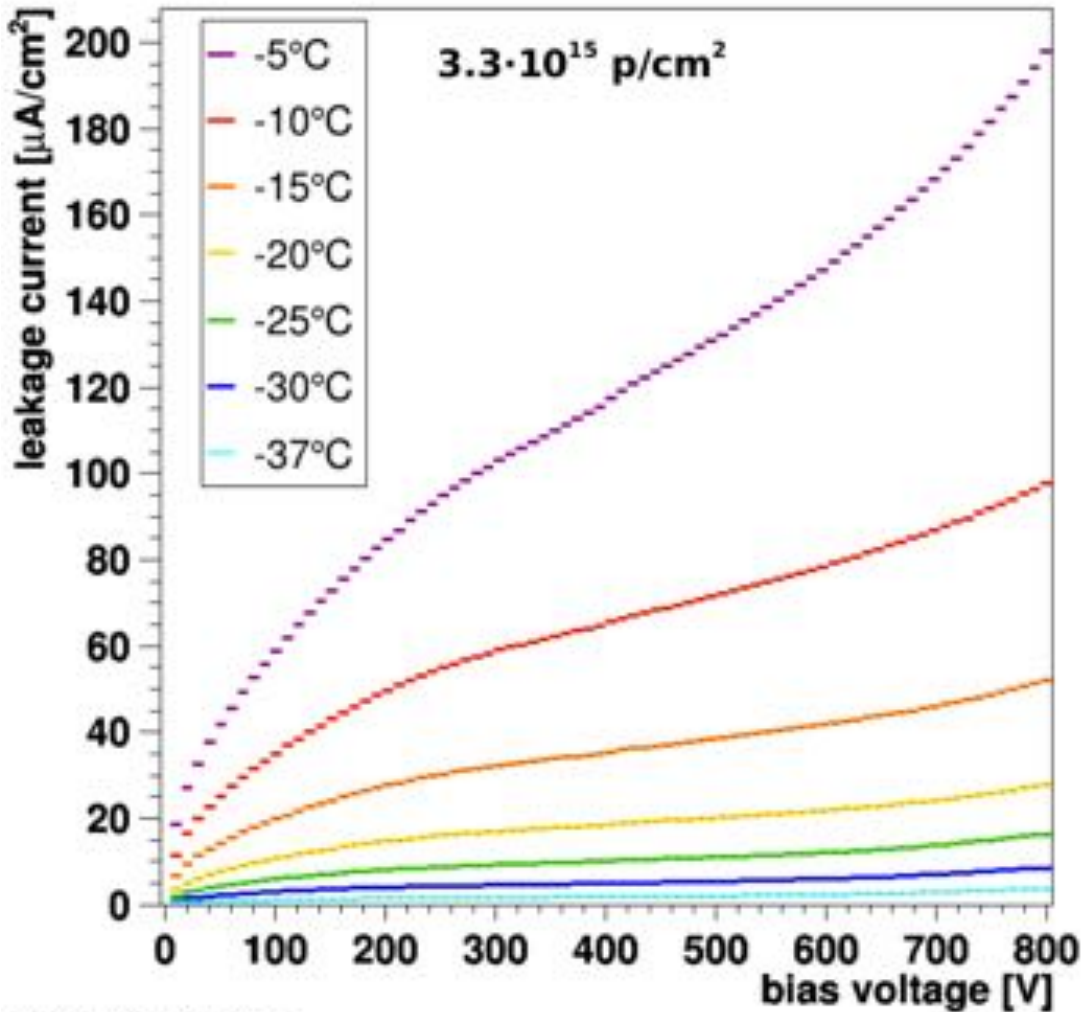
Figure 4.19 – Leakage current of a sensor irradiated to $\Phi_p = 3.3 \times 10^{15}\,\mathrm{cm}^{-2}$ measured as a function of bias voltage for different temperatures. Plot from D. Pitzl (DESY).

4.5. The Digital Test Board

The digital test board from the Phase 1 pixel campaign is reused for the readout of ROC4SENS modules, as it was designed to provide readout electronics for a variety of devices [65]. It contains the necessary components for detector operation, like IO modules and a high voltage relay for the bias voltage. Communication with the DTB is possible

via USB 2.0 or Ethernet. An Altera field-programmable gate array (FPGA) [66] hosts all required firmware modules for the data acquisition and communication with the ROC and provides an emulated central processing unit for the definition of test loops and data protocols. The DTB also has inputs for trigger signals and external clock signals. Via the LEMO port external triggers are accepted as TTL signals, whereas internal triggers can be generated for example as cyclic triggers. The devices are configured by the DTB, which also provides a clock and trigger information and reads out the data. A 72 pin flat ribbon cable connects the DTB to the module via an adapter card for communication and data transmission. The adapter card implements a routing of connected pins to the Kapton cable of the reference module (MOD) or the chip carrier PCB, see Figure 4.20.
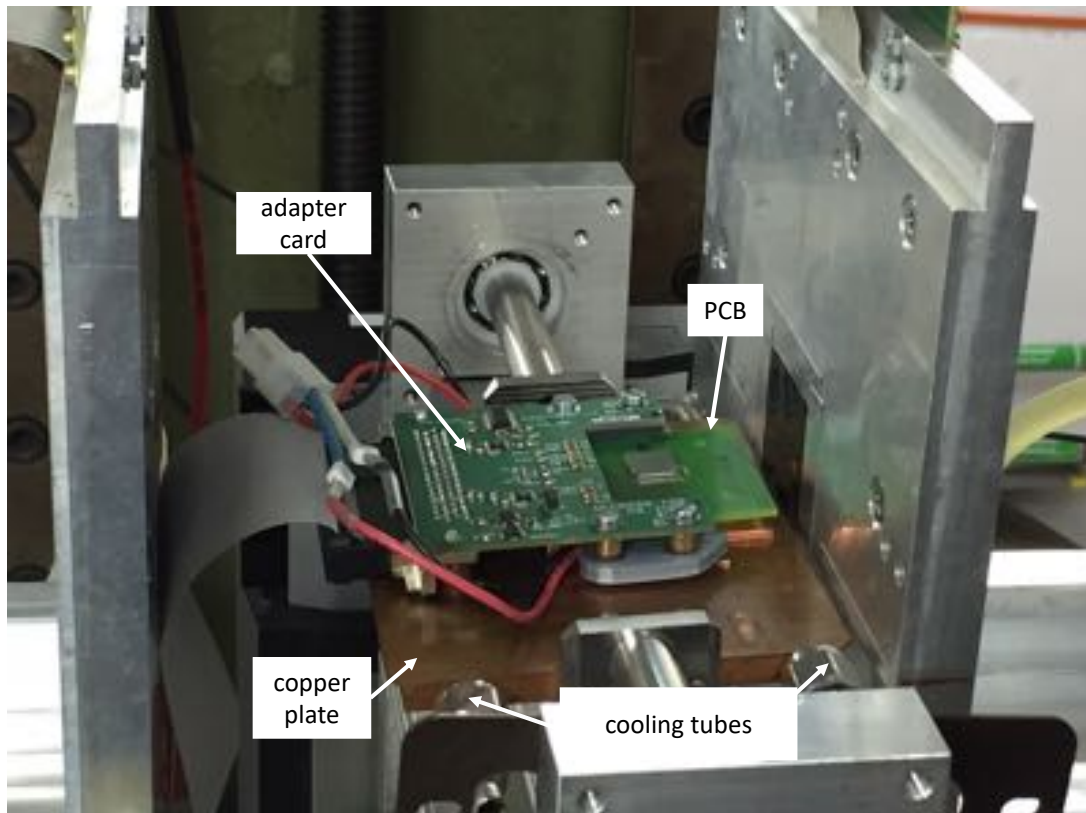
Figure 4.20 – View of the DUT on the chip carrier PCB in the adapter card, that is connected via the gray flat ribbon cable on the left with the DTB. The adapter card is mounted on a copper plate support structure for cooling purposes.

The communication between the PC and the DTB is implemented as a remote procedure call protocol and uses USB 2.0 as transport layers.

For communicating with the chip and to start the data acquisition with the previously determined chip settings a program was written to automate the process which is based on the R4S client software from Beat Meier, Paul Scherrer Institut.

The ROC4SENS transfers the analog pulses from each pixel to the DTB, where they are stored after digitization in memory blocks that have been allocated beforehand and are implemented as ring buffers. Ring buffers have one read and one write pointer to the allocated memory and implement a wrap-around at the end of the memory block. This enables continuous reading and writing of data. For the data analyzed in this thesis, the memory blocks where 200 events long. The DTB digitizes the pulses using a 12-bit analog-to-digital converter (ADC). The ADC has a range of 2 V and a resolution of less than 0.5 mV per count [61].

The part of the DTB forming the memory blocks is operated with a 40 MHz clock, corresponding to a clock cycle length of 25 ns. This clock frequency is fixed within the DTB and can only be changed by connecting an external clock to the DTB. The cycle generator takes the clock as input and produces a synchronous 160 MHz clock. So the smallest step in time with which the timing of the signals can be adjusted is 25 ns/4 = 6.25 ns [61]. This way it is possible to vary the delay of the HOLD signal. By repeating measurements varying this delay, the pulse shape can be scanned, see Chapter 6.2.

5. Beam Test Measurements at the DESY II Synchrotron

Particle beams offer the opportunity to test new particle detector prototypes in similar conditions as their final experiment. Test beam measurements can supplement laboratory tests and can provide additional information as input for simulations. The beam parameters, such as particle type, energy and the direction of the beam, can generally be chosen depending on the requirements of the measurement. The prototypes can be operated synchronized with the accelerator, including timing, as well as with externally provided triggers. In addition, they can also be operated in parallel with other devices which is an important part in the qualification of new detectors. For pixel detectors, detection efficiency, spatial resolution and charge collection efficiency of new sensor designs and the performance of new front-end electronics can be explored at beam tests.

List of own contributions The author's contributions to the results presented in this chapter include:

- track resolution measurements and the simulation using the GBL track resolution calculator,

- telescope alignment and data taking at DESY test beam.

The experimental setup was provided by the Detector Development Group lead by Prof. Dr. E. Garutti, including trigger and DAQ. I was introduced to test beam measurements and their analysis software by Dr. D. Pitzl.

5.1. The DESY II Beamlines

The DESY II synchrotron ring has an average radius of 46.6 m and its main purpose is the injection of particles to the PETRA III synchrotron light-source. The second user of DESY II, the DESY test beam facility provides electron/positron beams of a few GeV, with a maximum beam energy of 6.3 GeV. DESY II accelerates and decelerates in sinusoidal mode with a frequency of 12.5 Hz, so one DESY II magnet cycle takes 80 ms [67]. The revolution frequency is 1 MHz, the RF frequency 500 MHz and the bunch length around 30 ps.

The electron or positron beams are provided as sketched in Figure 5.1. A carbon fiber target is moved into the primary DESY II beam to produce bremsstrahlung. In a secondary target, either copper or aluminum, the photons are converted to electron/positron pairs.
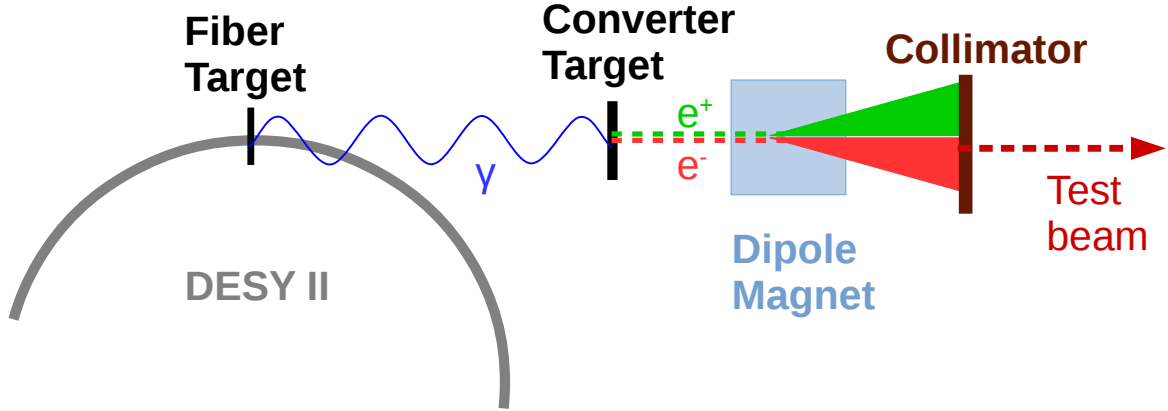
Figure 5.1 – Generation of the test beam at DESY II.

A dipole magnet spreads the beam and enables the selection of electrons or positrons in a certain energy range with a collimator. The beams then reach the hall with an obtainable rate of $10\,\mathrm{kHz/cm^2}$ up to $100\,\mathrm{kHz/cm^2}$. At the DESY test beam facility there are four areas available for beam tests, each with an individual beam extraction and momentum selection. The final test beams in the areas have a divergence of about $0.5\,\mathrm{mrad}$ and an energy spread of around 5% [68]. Further information on the beam generation and the features of the DESY test beam facility can be found in [67].

5.2. The DATURA Beam Telescope

The DATURA (DESY Advanced Telescope Using Readout Acceleration) is installed at the Beamline 21 of the DESY Test Beam facility. It is part of the family of EUDET-type telescopes which originate from the EUDET project [69]. The telescope's hardware components and software frameworks are still developing in the successive European-funded projects AIDA and now AIDA2020 [70]. The DATURA telescope consists of six silicon pixel detector planes, equipped with fine-pitch MIMOSA 26 sensors [71]. Four scintillators with photo multiplier tubes (PMTs) for trigger purposes, a TLU and time stamp information on the particle passage are available. A data acquisition system for readout is also provided. Each MIMOSA 26 sensor is composed of pixels sized $18.4\,\mathrm{\mu m}\times$ $18.4\,\mathrm{\mu m}$. In total there are 1152 columns and 576 rows. They are read out with a rolling shutter, leading to all columns being read out simultaneously. At a clock frequency of 80 MHz the MIMOSA 26 integration time amounts to $115.2\,\mathrm{\mu s}$. The detection threshold for particles is programmable, there are different configurations for the threshold levels

available, each in integer multiples of the RMS noise of the individual planes. For this analysis, a configuration with a sensor threshold setting of 6 was chosen, which corresponds to a collected charge in a single pixel of more than six times the noise. The telescope is divided into an upstream and a downstream arm, each holding three sensors, as indicated in Figure 5.2. A device under test (DUT) is typically inserted between the two telescope arms but can also be installed elsewhere. A stage system, the rotation stage, allows for the DUT to be moved in the beam. If installed on the xyφ-stages from Physik Instrumente (PI) [72], the DUT can be adjusted remotely along the horizontal (x) or vertical (y) beam axis with a 0.1 µm precision. The angle of the DUT towards the beam can be adjusted with a precision of 50 µrad [73]. A more detailed description of the telescope and its mechanical setup can be found in [74].
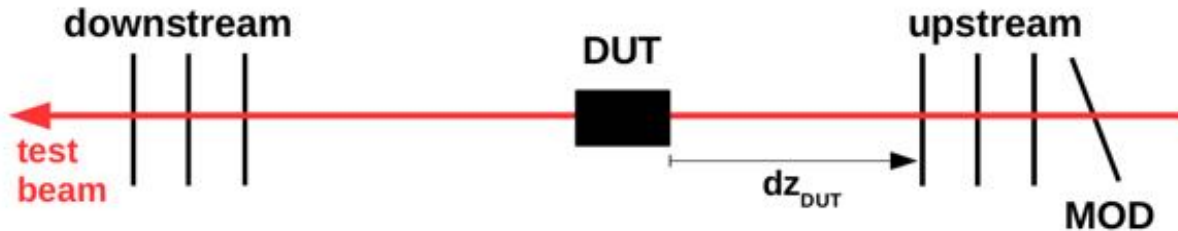
Figure 5.2 – Geometry of the edge-on set up in the beam telescope, featuring six tracking planes, three upstream and three downstream and the device under test (DUT) in between. A module (MOD) is placed in front of the telescope as a timing reference.

5.2.1. Timing Reference

As the track multiplicity fluctuates and is dependent on operational parameters such as the beam energy or the bunch filling of the DESY II synchrotron, a timing reference is required. Due to the long integration time of the MIMOSA 26 sensors, multiple tracks are recorded traversing the telescope after the trigger has been issued. The ROC4SENS only records the particle which caused the trigger to be issued. The MIMOSA 26 sensors do not provide time-of-arrival information for the individual pixels, hence a CMS Phase 1 pixel module is installed in front of the first MIMOSA 26 to select the correct track from the telescope, indicated as MOD in Figure 5.2. This module can be synchronized with the DUT by the same external trigger.

5.3. Trigger Logic

For the test beam measurements, the trigger logic is built on the EUDET trigger logic unit (TLU) and supplementary NIM electronics. The TLU is a programmable trigger logic

with a commercially available FPGA board as a basis and a custom-built coincidence unit
with four discriminator boards. More features of the TLU are explained in [75].

The TLU generates and distributes the common trigger signal to all connected detectors
and handles trigger veto conditions, e.g. busy signals. The attached detectors can use busy
signals to temporarily veto triggers during readout. A simple handshake is implemented
which requires the busy flag to be raised and pulled down again after every trigger sent.
This handshake is used by the DATURA telescope and the DUT to veto new triggers
arriving during the long read out time of the ROC4SENS. The trigger and busy signals
are exchanged via standard LEMO connectors with TTL or NIM signals. The TLU
itself is connected to a standard PC via USB and it is possible to remotely configure
the discriminator input, the coincidence masks, handshake modes and the DUT trigger
outputs. The trigger logic used for the test beam measurements of this work is shown in
Figure 5.3.
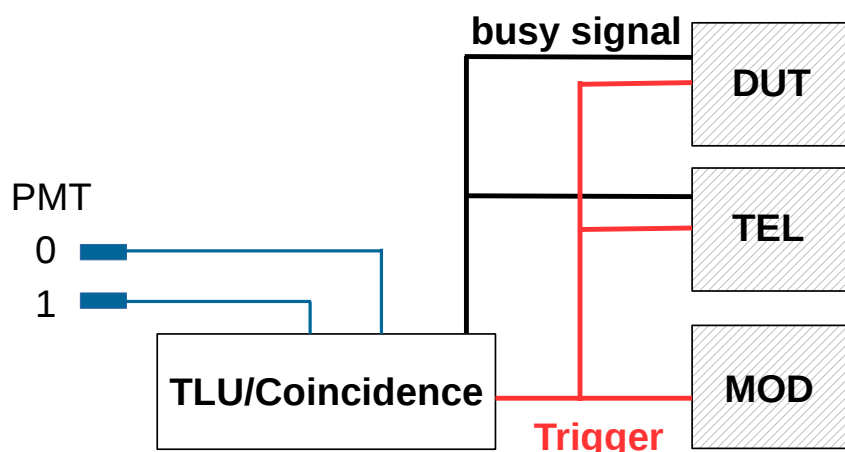
Figure 5.3 – Sketch of the test beam trigger logic used. A coincidence between two PMTs
is used as trigger for DUT, telescope and MOD. After each trigger the DUT can send a busy
signal to the TLU.

For the edge-on measurements a rectangular coincidence of $20 \times 1\,\mathrm{mm}^2$ between two PMTs
is taken as a trigger. A picture of the trigger setup at test beam is shown in Figure 5.4.

5.4. Data Acquisition

All data recorded by the different devices has to be stored for offline analysis. The
software used to store and analyze the telescope data is based on EUDAQ [76] only. The
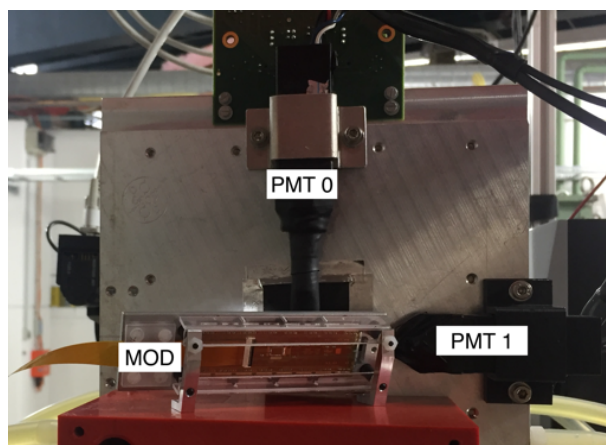
Figure 5.4 – Picture of the setup of the two PMTs at test beam. The module which provides a timing reference is in front of the telescope.

data from the DUT is acquired with the ROC4SENS client software and stored separately. In addition, the sensor leakage current is monitored and noted during data acquisition.

5.4.1. Online Monitoring

It is very important to be able to monitor the data quality during recording, as the test beam measurements involve detectors and front-end electronics still in their R&D phase. To monitor the quality of the test beam data and its coincidence with the MOD, the Online Monitor is available within the EUDAQ framework. It provides a set of continuously updated control plots and thus allows to verify the performance of the detectors. With correlation histograms the time synchronization and the spatial alignment of the different devices can be monitored. For the edge-on measurements, especially the correlation between the x or y position reconstructed in MOD and MIMOSA is important, as synchronization might get lost and a run needs to be aborted. A uniform distribution of entries indicates that the synchronization is lost, e.g. due to a missed trigger, and non-associative detector events are merged by the event reader. In case the devices are running synchronously, diagonals appear and indicate correlation in time, whilst the relative spatial orientation of the detectors are represented by the intercepts of these diagonals. An example of a correlation plot between two MIMOSA planes in the x-direction is shown in Figure 5.5.

In addition, online plots monitoring the quality of the data from the DUT have been developed, to monitor the noise, the pedestal or the number of hits. This online monitoring is done with the ROOT framework [77]. These plots are also necessary for the initial positioning of the edge-on DUT in the test beam.
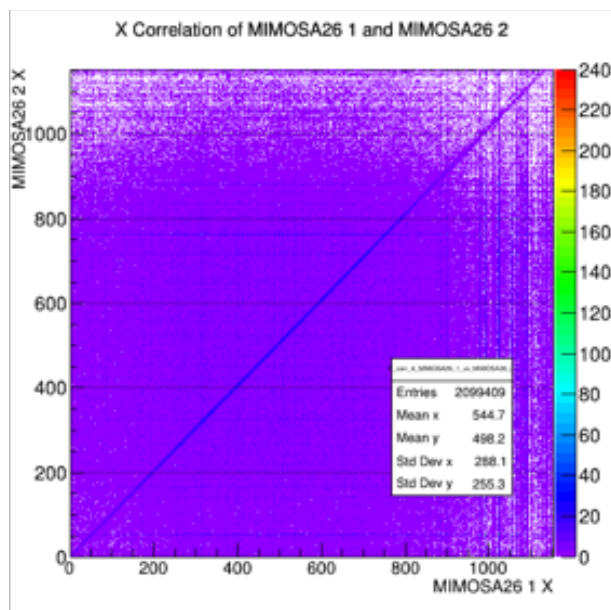
Figure 5.5 – Example of a correlation plot between two MIMOSA planes in the x-direction from the Online Monitor of the EUDAQ framework.

5.5. Telescope Alignment and Track Reconstruction

The particle trajectory is reconstructed from the hit positions in the global reference frame. A track model for optimal parametrization has to be chosen. For test beam measurements with a collinear beam and without a magnetic field, a simple straight line usually suffices. However, depending on the beam properties and the setup of the experiment, multiple scattering needs to be considered.

A relatively easy method to single out combinations of hits that originate most likely from the same traversing particle is the triplet method. With three measurements from the three MIMOSA 26 planes available, a straight line is defined through two of the hits. Due to the telescope mechanics and geometry the resulting track has only an x- and y- coordinate and the corresponding slope in the x- and y-direction. The track is then interpolated or extrapolated to the position of the third telescope plane. The difference between the extrapolated track position x_{track} and the measured hit position x_{meas} is called the residual dx and is given by

$$dx = x_{track} - x_{meas}. \tag{25}$$

The residual can be used as a discriminator for track candidates and the alignment, such that tracks with a residual below a certain threshold, i.e. $|dx| < thr$, are accepted, while others are rejected as random hit combinations. The track matching and alignment of the DUT are described in Chapter 6.

A programm called *tele*, which was developed in close relation to the EUTelescope framework but is completely independent of it, is used to analyze the test beam data [78]. At first the Mimosa raw data is unpacked by the EUDAQ framework. The encoded bitstream coming from any of the included DAQ systems is converted into an information on the hit pixels, including the pixel coordinates and their respective pulse heights.

Particles traversing a telescope plane may cause a signal in more than one pixel due to charge sharing. Pixel hits in adjacent pixels of one detector plane are grouped into clusters, within one *event*, which is one readout frame. To avoid hot pixels of the MIMOSA sensors, a calculation of the firing frequency of all pixels is done. If pixels exceed a configurable frequency threshold, they are marked as hot. A cluster with one or more hot pixels is removed from the list of possible track candidates as it is likely to be a noise hit. The cluster position is calculated as the center of gravity of all associated hit positions weighted with their signals. For the triplet formation the cluster positions are taken as hit positions.

As the accuracy of the mechanical positioning of the telescope planes is confined to a few millimeters, an additional alignment is necessary for high resolution tracks. In a pre-alignment process the correlations in x and y between hits in neighboring telescope planes are analyzed and the means are minimized by shifting the resulting residual distributions. A correction only for shifts in these two coordinates is performed in the pre-alignment. This step corrects global misalignments such that the selection of track candidates already benefits. The MOD and DUT detectors are not included in the telescope alignment process.

To find triplet candidates from the hits in the six MIMOSA planes, while allowing for multiple Coulomb scattering at the same time, the telescope is divided into its upstream and downstream arm as shown in Figure 5.2. Triplets are built individually in both the upstream and the downstream arm. To build a triplet any particle hit of the first plane (0) is combined with all registered hits in the third plane (2) and their hit positions are connected with a straight line. The coordinates of the connecting line at the second plane (1) are extrapolated and the residuals calculated, shown in Figure 5.6. For the triplet selection the residuals dx and dy in the x- and y-direction, respectively, are required to be below 0.05 mm and an additional cut on the angle is required.

As a next step the upstream and downstream triplets are combined and the straight lines describing them are extrapolated to the z-position of the DUT, where multiple scattering takes place. The resulting residuals are minimized for the alignment of the telescope and an isolation criterion is required. After this selection there still is an average of more than 2 tracks per event, shown in Appendix B. To reduce this number a link to the timing
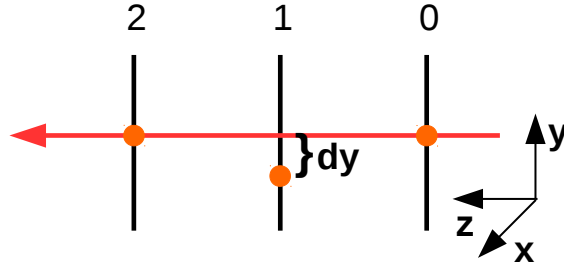
Figure 5.6 – Illustration of the triplet finding method. A hit in plane 0 is connected with a hit in plane 2 via a straight line. The coordinate of the connecting line at the position of plane 1 is extrapolated and the residual dy is calculated.

reference is required. The tracks are extrapolated to the position of the MOD and the residuals are calculated, like in the triplet finding method. A track is linked to a MOD hit, if the residual in x- and y-direction is below 0.15 mm. The number of tracks with a link to the MOD is on average one, as shown in Appendix B.

5.6. Track Resolution at the DUT

The precise knowledge of the resolution of the reconstructed tracks is important for all measurements with the beam telescope. The number of telescope planes used for the measurements and their intrinsic detector resolution dominate the track resolution σ_{track}. However, also the telescope geometry has an influence, due to extrapolation of the track. Minimizing the distance dz_{DUT}, indicated in Figure 5.2, between the DUT and the neighboring telescope planes as far as possible assists in reducing the track extrapolation uncertainty. In order to determine the track resolution of the telescope, the fourth telescope plane was taken as the DUT and the distance dz_{DUT} was varied in 10 mm steps with and without a cooling box in between. With a cooling box the minimal distance reachable is 90 mm, without one 40 mm is possible. For each measurement point the upstream triplet is extrapolated to the fourth telescope plane.

Determination of the Distribution Width

There are many possibilities to obtain the width of a distribution, therefore it is important to name the method used. A straight-forward choice is using the root mean square (RMS) of the full distribution or the full width at half maximum (FWHM) of a Gaussian fit to the distribution. However, not every residual pursues the shape of a Gaussian distribution, as for example δ-rays insert non-Gaussian tails into the distribution. Therefore the RMS of the distribution tends to overestimate the actual width. For more stability against

larger fluctuations and to be more flexible concerning the shape of the distribution an alternative fit function is used.

For these measurements the residual distribution is fitted with a Student's t-function given by

$$f(x) = a + \frac{b}{\sigma\sqrt{\pi\nu}} \frac{\Gamma((\nu+1)/2)}{\Gamma(\nu/2)} \exp\left(-\frac{\nu+1}{2}\ln\left(1+\frac{1}{\nu}\left[\frac{x-\langle x \rangle}{\sigma}\right]^2\right)\right), \qquad (26)$$

with the free fit parameters background a, area b, mean $\langle x \rangle$, σ and ν, while $\Gamma(x)$ designates the gamma function. The Student's t-function takes the non-Gaussian tails into consideration as it interpolates between a Gaussian distribution and a Breit-Wigner curve. The width of the function is the parameter σ, which is used for the spatial resolution $\sigma_{\mathrm{measured}}$. An example of a fit to the residual distribution at $\mathrm{dz_{DUT}} = 60\,\mathrm{mm}$ is shown in Figure 5.7.
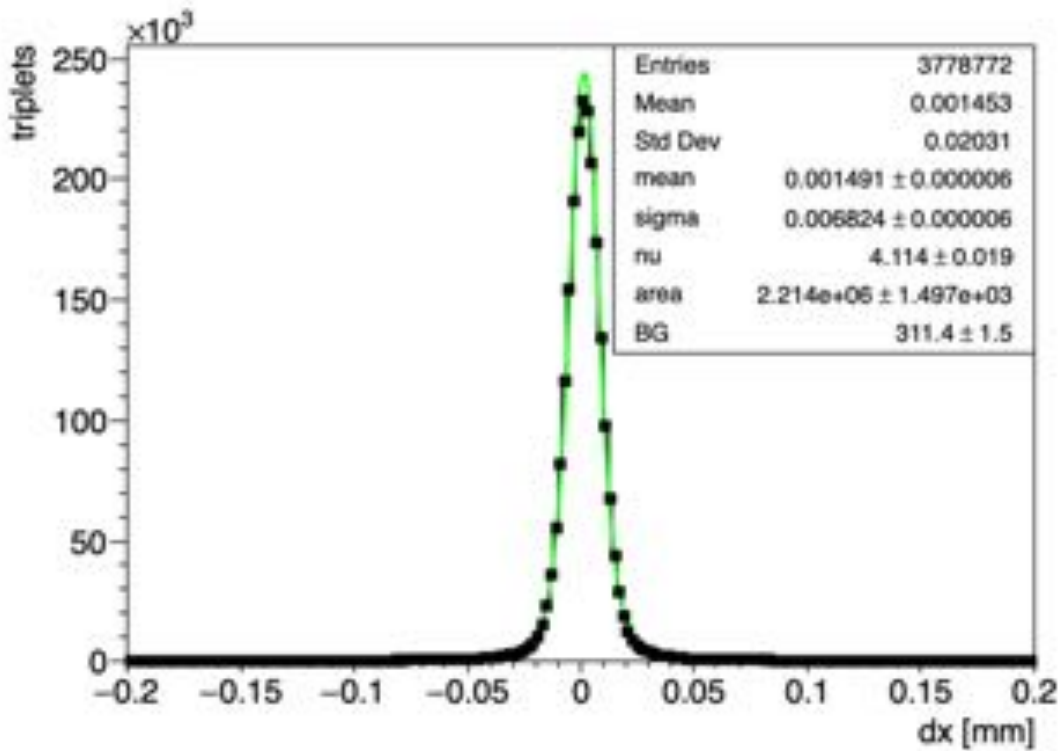
Figure 5.7 – The fit to the residual distribution at $\mathrm{dz_{DUT}} = 60\,\mathrm{mm}$. The resulting resolution is $\sigma_{\mathrm{measured}} = 6.82\,\mu\mathrm{m}$.

The resolution is acquired from the individual distributions of the various measurements positions.

To obtain the track resolution, the intrinsic plane resolution of the DUT has to be sub-

tracted from the fitted resolution, as shown in Equation 27.

$$\sigma_{\text{track}} = \sqrt{\sigma_{\text{measured}}^2 - \sigma_{\text{intrinsic}}^2} \tag{27}$$

The resulting track resolution as a function of dz_{DUT} and for two different beam momenta is indicated in Figure 5.8. For edge-on measurements a typical distance dz_{DUT} is around 63 mm, the track resolution for this distance is estimated to be 11 μm.
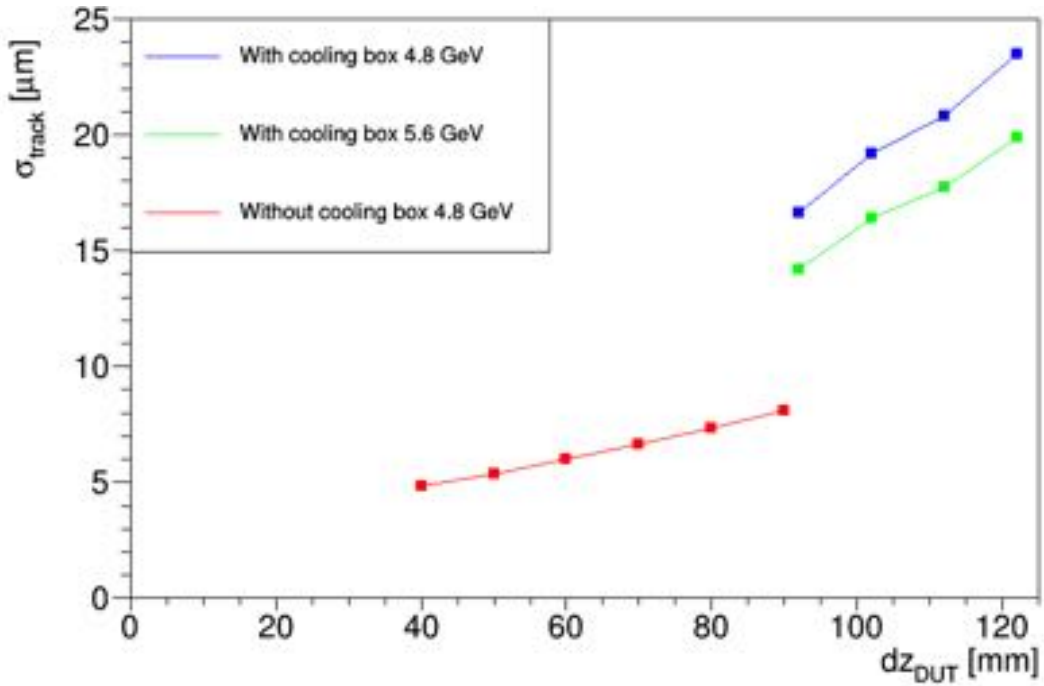
Figure 5.8 – The track resolution σ_{track} as a function of distance of the DUT to the telescope planes dz_{DUT}. In red for measurements without a cooling box between telescope plane and DUT for a beam momentum of 4.8 GeV and in blue and green with a cooling box for beam momenta of 5.6 GeV and 4.8 GeV, respectively.

To estimate the uncertainty of this resolution, the GBL track resolution calculator [79] was used for detailed studies of the systematics. Input to the resolution calculator are the telescope spacing of 150 mm, the three upstream planes only, the thickness of the MIMOSA 50 μm + 2 × 20 μm kapton foil, the telescope intrinsic resolution of 3.25 μm [65] and a beam energy p_{beam} of 4.8 GeV. The relevant parameters are varied to calculate the systematic uncertainty on the track resolution. As there is a beam energy spread of 5% the beam energy has been varied accordingly and the variation resulted in a shift of the resolution of 0.15 μm, see Figure 5.9.

The intrinsic resolution of the telescope is varied by its systematic uncertainty of 0.09 μm [34] for three plane tracking, the resulting shift of the track resolution at the DUT is
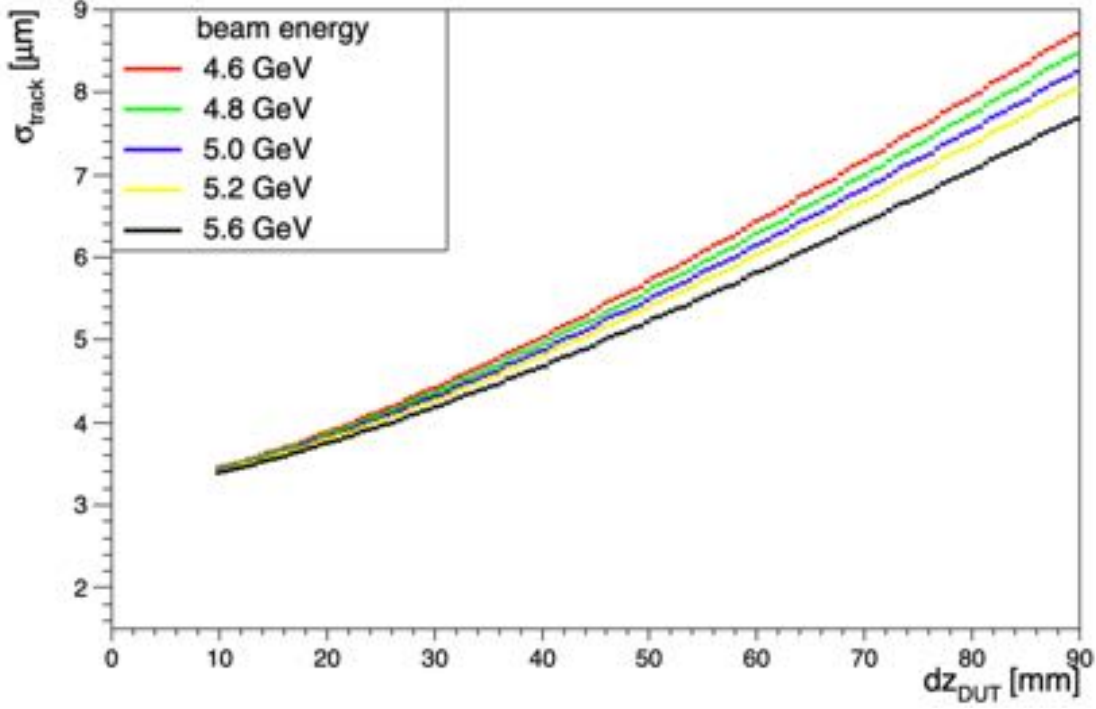
Figure 5.9 – The track resolution σ_{track} as a function of distance of the DUT to the telescope planes dz_{DUT} for varied beam energies. The shift of the resolution at $dz_{\mathrm{DUT}} = 63\,\mathrm{mm}$ is $0.15\,\mathrm{\mu m}$.

$0.09\,\mathrm{\mu m}$, compare Figure 5.10.

With the conservative estimate of the uncertainty of $\Delta dz_{\mathrm{DUT}} = 2\,\mathrm{mm}$ on the z-position of the DUT, the shift in track resolution for a shift in z is estimated to be $0.2\,\mathrm{\mu m}$. From all the variations of the input parameters of the GBL resolution calculator and their resulting shifts of the track resolution the total systematic uncertainty on the track resolution can be calculated according to Equation 28.

$$\Delta\sigma_{track} = \sqrt{\sigma^2_{dz_{\mathrm{DUT}}} + \sigma^2_{p_{\mathrm{beam}}} + \sigma^2_{\mathrm{intrinsic}}} \tag{28}$$

The systematic uncertainty on the track resolution at the DUT is $\Delta\sigma_{\mathrm{track}} = \pm 0.27$ µm. Variations in the detector alignment are of no concern as the alignment is checked for every run individually and the errors on the aligned x- and y-positions are negligible.

66
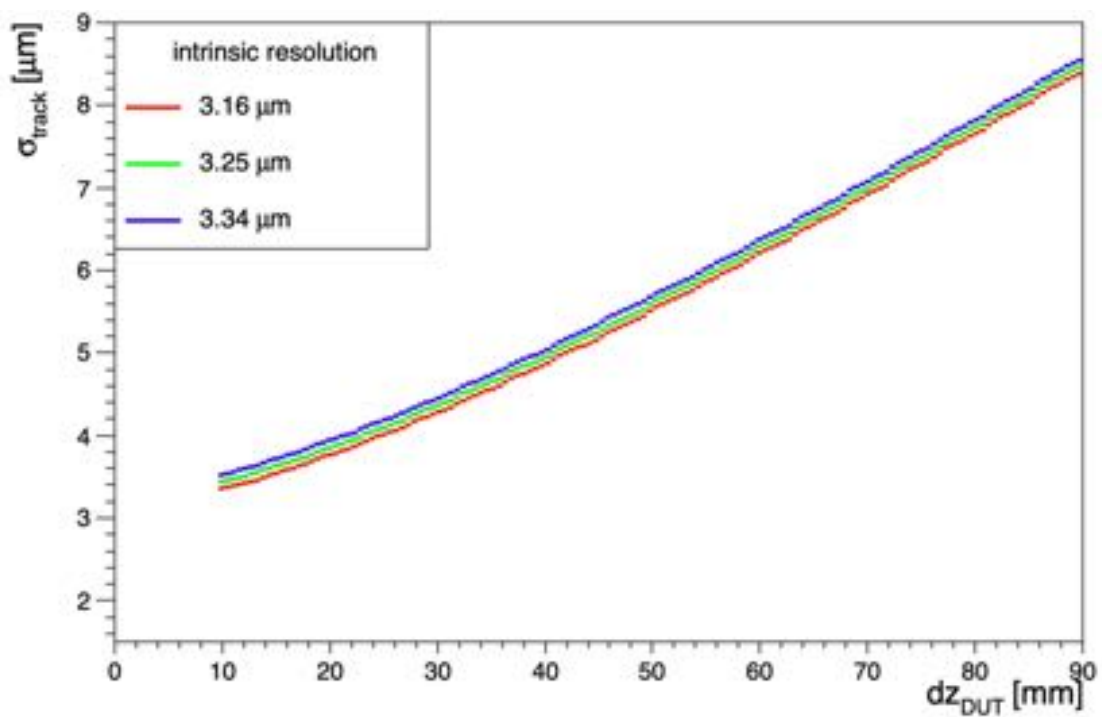
Figure 5.10 – The track resolution σ_{track} as a function of distance of the DUT to the telescope planes dz_{DUT} for varied intrinsic resolutions of the telescope. The shift of the resolution is $0.09\,\mu\mathrm{m}$.

6. DUT Data Acquisition

For installation of the DUT in the beam telescope the adapter card, explained in Chapter 4.5, is mounted on a copper plate support structure, see Figure 4.20. It is installed in the rotation stage, introduced in Chapter 5.2, so that different positions of the DUT in the beam can be acquired. For the comparability of all measurements the DUT was always enclosed in a custom made cooling box, encapsulated with 10 mm armaflex insulation. The box ensures a better cooling of the sensor, as an ethanol chiller is cooling the copper plate. Additionally, dry air is used to prevent condensation. To avoid multiple scattering before the beam can hit the sensor, the box has cutout windows for vertical and edge-on incidence. The whole setup at test beam is shown in Figure 6.1.
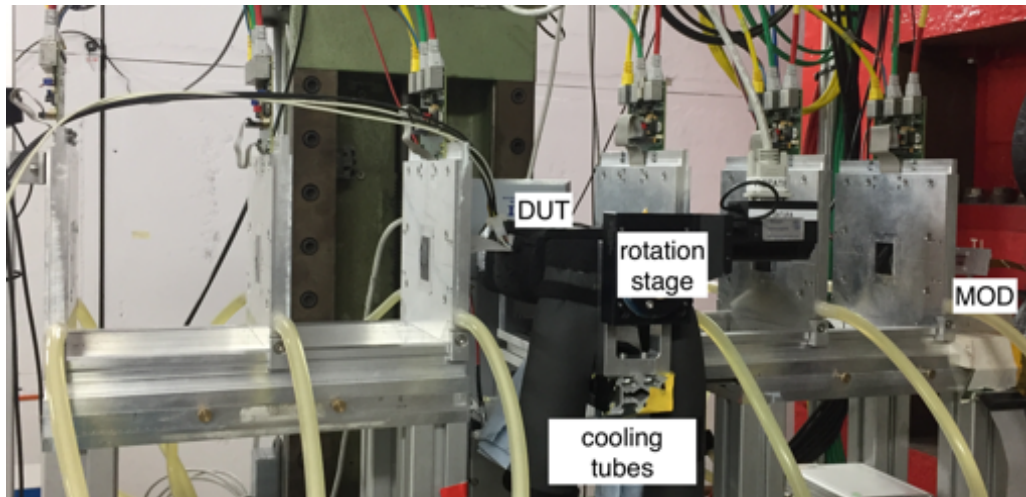
Figure 6.1 – The installation of the DUT in the cooling box at test beam. It is installed on the rotation stage and cooled by an ethanol chiller. The module used as timing reference is in front of the telescope. The beam enters from the right.

List of own contributions The author's contributions to the results presented in this chapter include:

- investigation of the chip gain,

- detector alignment for each data run.

The DUT DAQ was developed by F. Feindt. The investigation into the difference between ROC4SENS chips was done together with F. Feindt.

6.1. ROI Data Taking

As introduced in Chapter 4.4, the ROC4SENS has no zero suppression and data reduction is necessary, therefore zero suppression is performed by hit finding. To filter out the background, all data is first pedestal corrected online. The pedestal correction is initialized by a first block of 200 events without pixel hits. The initial pedestal PED_0 is calculated from the ADC values as

$$PED_0 = \sum\nolimits_{i=1}^{200} \frac{ADC_i}{200} \ . \tag{29}$$

The pedestal is updated continuously for every pixel during data taking, each event i without a pixel hit is used for this. With this update the initial pedestal from Equation 29 evolves into the continuous pedestal update in Equation 30.

$$PED_i = \frac{199}{200} PED_{i-1} + \frac{1}{200} ADC_i \tag{30}$$

Each pixel pulse height PH is therefore the difference between the initial ADC value and the pedestal

$$PH_i = ADC_i - PED_i \ . \tag{31}$$

To factor in common mode, which is a hardware effect of collective pixel signal variation due to synchronous variation of potentials on the readout chip or ADC at the readout process, there is a first correction for common mode fluctuation already done online. For the definition of a pixel hit, the difference ΔPH_j between the pixel pulse height PH_j and the previous one PH_{j-1} is used, according to Equation 32.

$$\Delta PH_j = PH_j - PH_{j-1} \tag{32}$$

A hit is then defined as a signal that is at least four times the noise RMS, for each pixel individually, so $\Delta PH_j / RMS_j < -4$. Like the pedestal, the RMS is only calculated for events without a pixel hit, an example of the average RMS is shown in Appendix B. With the aforementioned threshold set as a negative threshold th, pixel j is marked as a hit if $\Delta PH_j < th$ and pixel $j-1$ is marked as a hit if $\Delta PH_{j-1} > $ -th.

A Region Of Interest (ROI), an area of 7×7 (column × row) chip pixels is defined, centered around each pixel hit. The outer rows are used for offline common mode correction so that a 7×5 (column × row) area of common-mode corrected pixel pulse heights around each seed pixel remains for the analysis. The ROI data taking uses a sliding window technique around each seed pixel. This signifies that the position and pulse height of all pixels in the ROI, including the trigger number is stored, if not stored in a previous hit of the

same trigger number, as shown in Figure 6.2. The ROI is defined in chip row and column
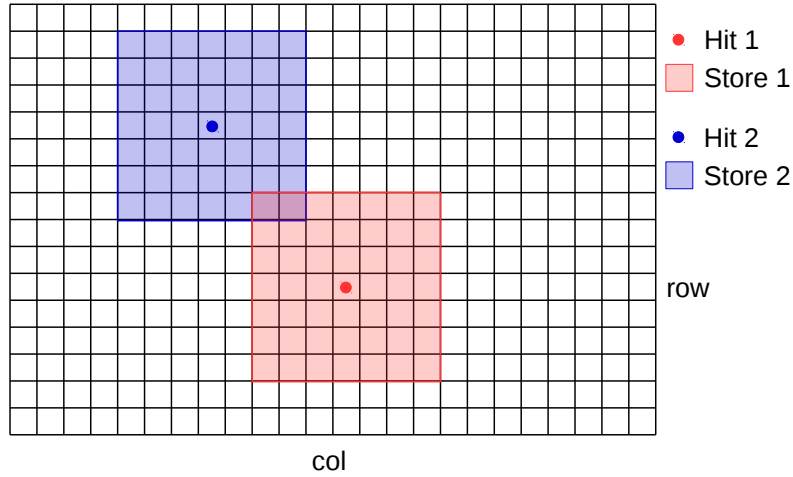
Figure 6.2 – Example of a ROI storage pattern, the position and pulse height of a pixel is stored if it was not stored in a previous hit of the same trigger number.

numbers which are the same for a $50 \times 50\,\mu m^2$ sensor but consequently the number of rows and columns is different for a $25 \times 100\,\mu m^2$ sensor. Here the ROI size translates to 3.5×14 (columns × rows) and subsequently leads to a size of 3.5×10 (columns × rows) after common-mode correction. The translation between ROC and sensor coordinates is illustrated in Figure 6.3. The half column is just named like this, as from the figure it is clear, that only every second sensor row in this column has a stored pulse height due to the staggered bump bond pattern.
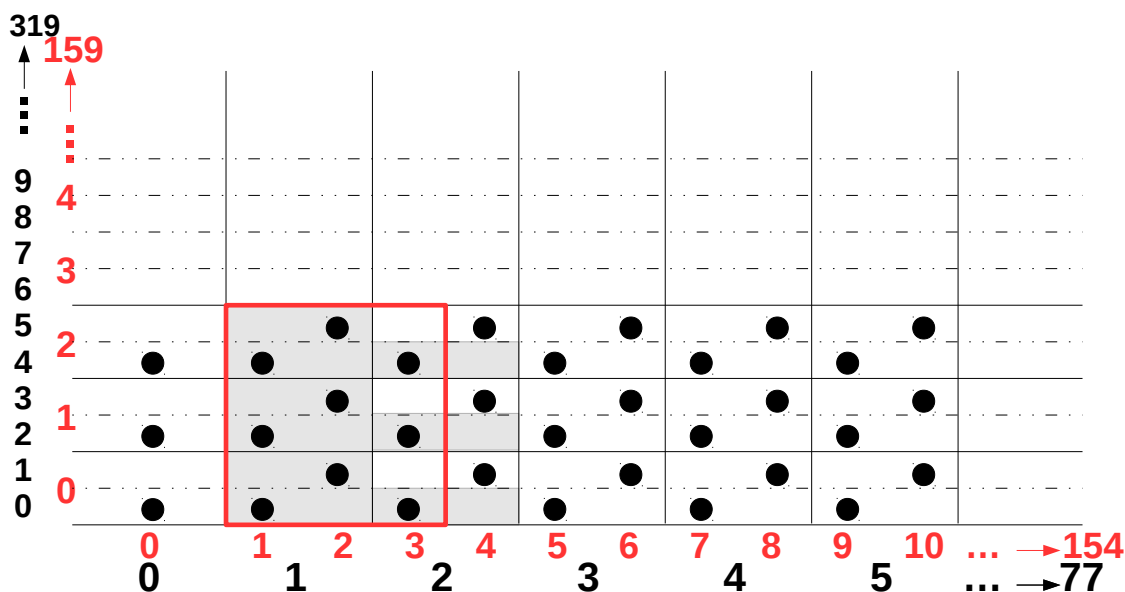
Figure 6.3 – Sketch of the translation of the geometry in ROC coordinates (red) to sensor coordinates (black). This is a sensor with 320×78 rows and columns in sensor coordinates. A 3×3 region (red box) in ROC coordinates translates to a $(1+ 0.5*1)\times 6$ region in sensor coordinates, as only every other row has a pixel with a stored pulse height, sketched in gray. The black dots are the bump bonds connecting the pixel sensors to the chip channels in a staggered way.

6.2. Gain Equalization

With the internal test pulse calibration of the ROC4SENS it is possible to gain insight on the response of the individual channels of the chip. There were two scans performed to investigate the distribution of the pedestal corrected pulse heights of all pixels. The pulse height was measured as a function of V_{cal} in mV or for a fixed V_{cal} as a function of the hold delay. Previous measurements have shown, that a varying of the calibration pulse amplitude V_{cal} results only in a slight shift of the peaking time of the pulse, see Figure 6.4 and thus the trigger delay does not need to be adapted to V_{cal} [61]. Therefore, the pulse height was first measured as a function of the hold delay to understand the pulse shape.

An example of hold delay scans for different chips is shown in Figure 6.5. The pulse peaks at around 40 hold units, the trigger delay that is necessary for readout with telescope. This plot displays the mean value of the pulse height for all pixels at a given hold delay, with the RMS used as an error bar to visualize the spread over the pixels. The differences between the individual 24 800 pixels of the different chips at hold 40 are shown in Figure 6.6. The standard deviation from the mean at 366 ADC, which is representative of the charge collected in a pixel from test beam, is around 10 ADC for the non-irradiated sensor, which corresponds to about 3%. The individual pixel gains therefore only differ slightly.
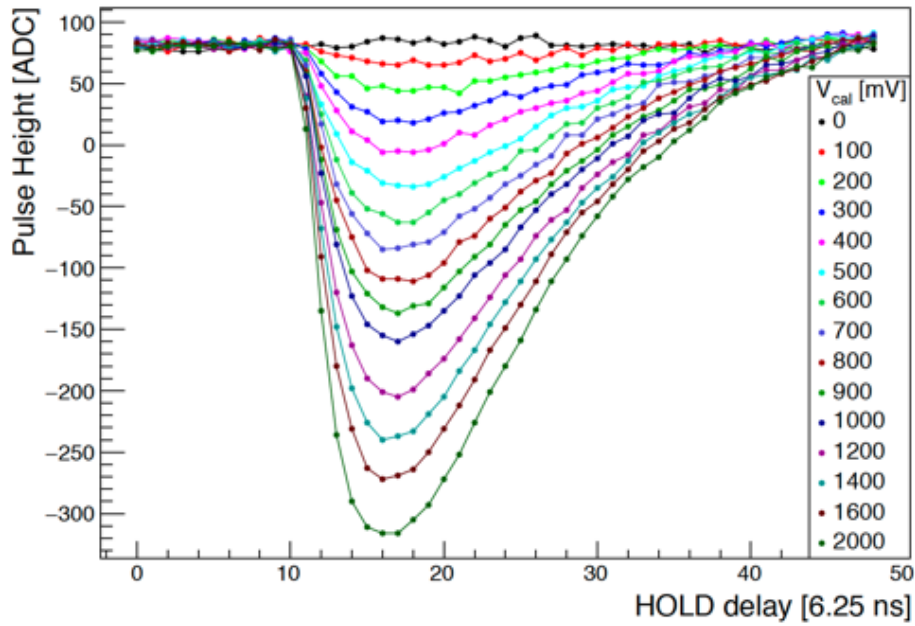
Figure 6.4 – The pulse height as a function of hold delay for different calibration pulse amplitudes V_{cal}. With increasing V_{cal} the peaking time shifts only slightly to shorter times. Figure from [61].
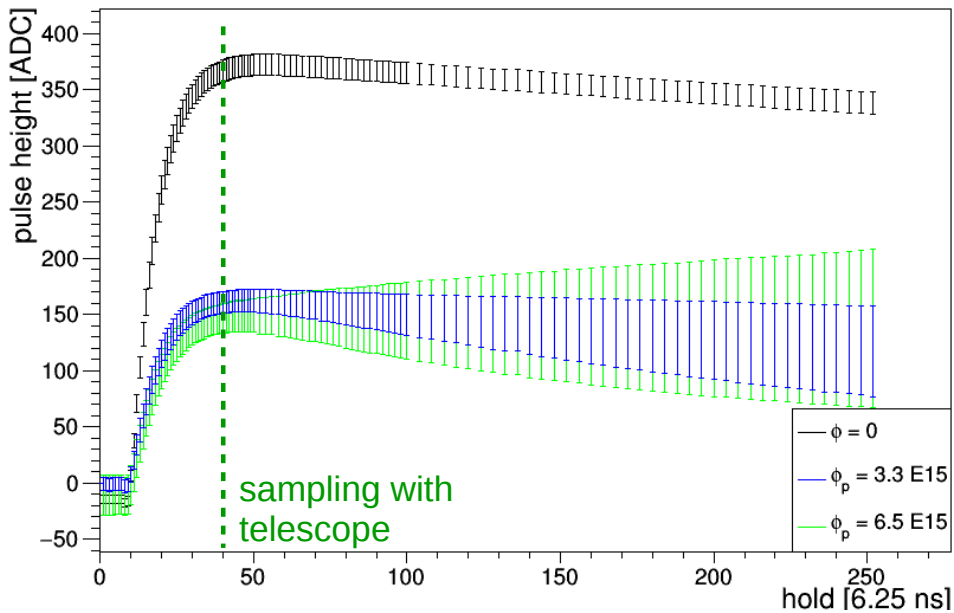
Figure 6.5 – The shape of the pedestal corrected pulse height as a function of hold units. The displayed values are the mean values of the distributions of all pixels at this timing. The RMS of all pixels is used as an error bar to visualize the spread over the pixels. Sampling with the telescope corresponds to 40 hold units, displayed as the dashed green line.
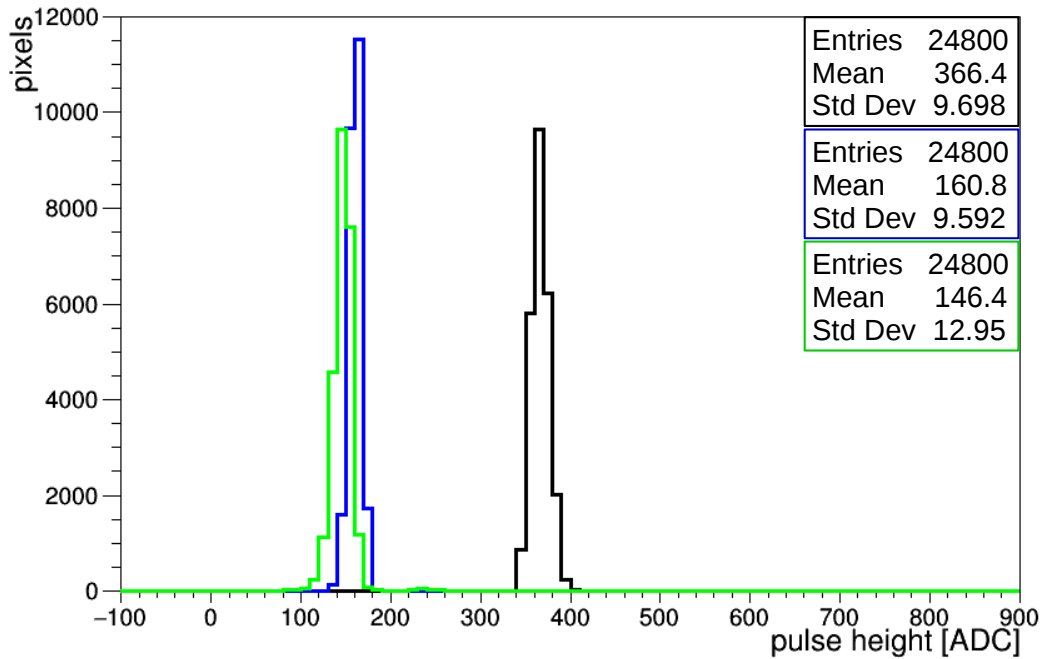
Figure 6.6 – Distribution of the pedestal corrected pulse height of all 24 800 pixels of the ROC4SENS at hold 40, color legend as in Figure 6.5. For the non-irradiated sensor the standard deviation from the mean is around 10 ADC, which corresponds to less than 3%. For the irradiated sensors, the standard deviation is 6% (8%) for $\Phi_p = 3.3$ (6.6) $\times 10^{15}\text{cm}^{-2}$.

In Figure 6.7 the pedestal corrected pulse height is shown as a function of position in the chip for a non-irradiated sensor on top and a sensor irradiated to $\Phi_p = 3.3 \times 10^{15}\,\text{cm}^{-2}$ at the bottom. One can see the pulse exhibits a dependence on the column, which is attributed to the different column gain, as described in Chapter 4.4.2. This however is taken into account in the common mode correction, see Chapter 6.1. The difference in pulse heights between the individual columns increases with irradiation, as in both figures the difference in pulse height is up to about 50 ADC between columns but the maximum pulse height differs by a factor of two.

For the gain equalization the calibration pulse is injected as a function of V_{cal} units at hold 40, compare Figure 6.8. The displayed values are the mean values of the distributions of all pixels for each V_{cal} unit. The pulse height saturates for $V_{cal} > 1000\,\text{mV}$. The standard deviation is used as error bars, so one can see the dependency of the standard deviation, from Figure 6.6, on the calibration pulse amplitude. The response of the individual pixels at $V_{cal} = 220\,\text{mV}$ is shown in Figure 6.9.

This value was chosen as the resulting pulse height corresponds to the size of the Landau MPV of the collected data. The standard deviation is 7.2 ADC, which is about 3% as
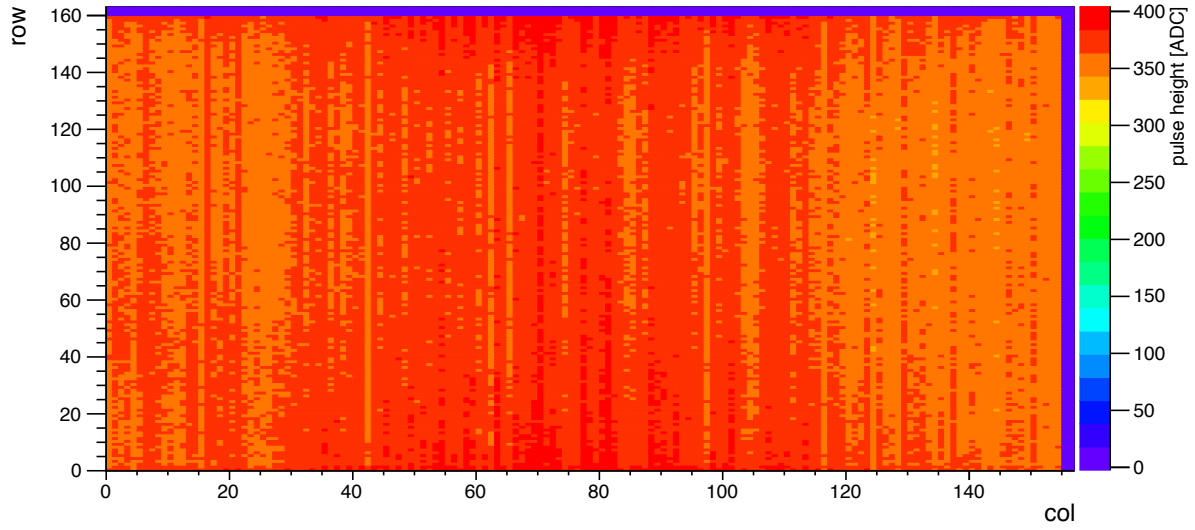
non-irradiated sensor
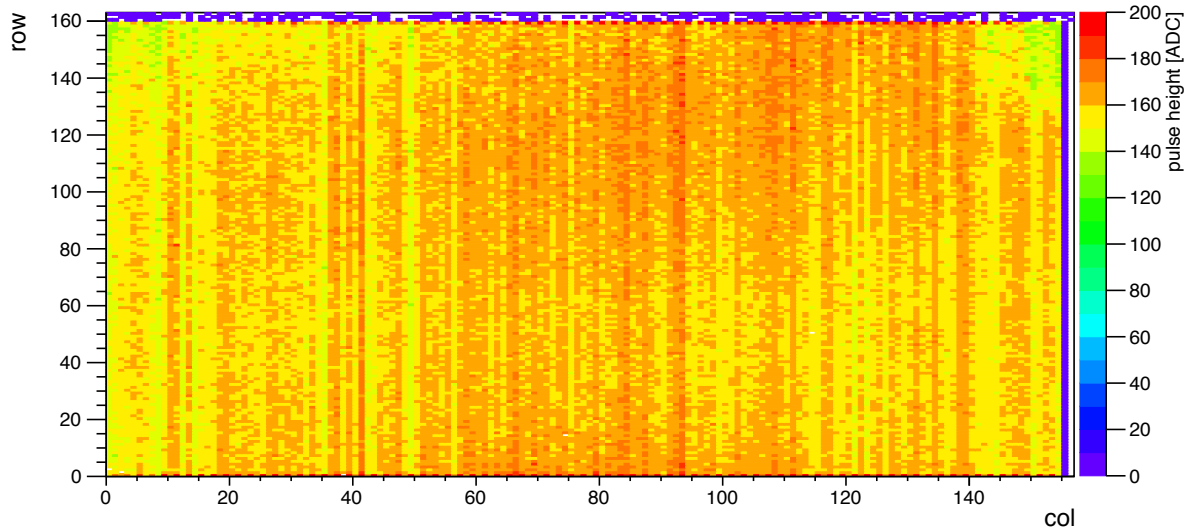
$$\Phi_p = 3.3 \times 10^{15} \, \text{cm}^{-2}$$

Figure 6.7 – The pedestal corrected pulse height is shown as a function of position in the chip at hold 40 for a non-irradiated sensor (top) and for a sensor irradiation to $\Phi_p = 3.3 \times 10^{15} \, \text{cm}^{-2}$ (bottom). A column dependence is visible, which is expected as each column has an individual column amplifier.

deduced previously from the hold delay scan.

However, this was just for one V_{cal} setting, to see if the same applies for all other settings, the RMS of each setting was divided by its mean pulse height PH to calculate the spread between the pixel responses as

$$\sigma_{PH} = \frac{\text{RMS}}{\text{PH}} \, . \tag{33}$$
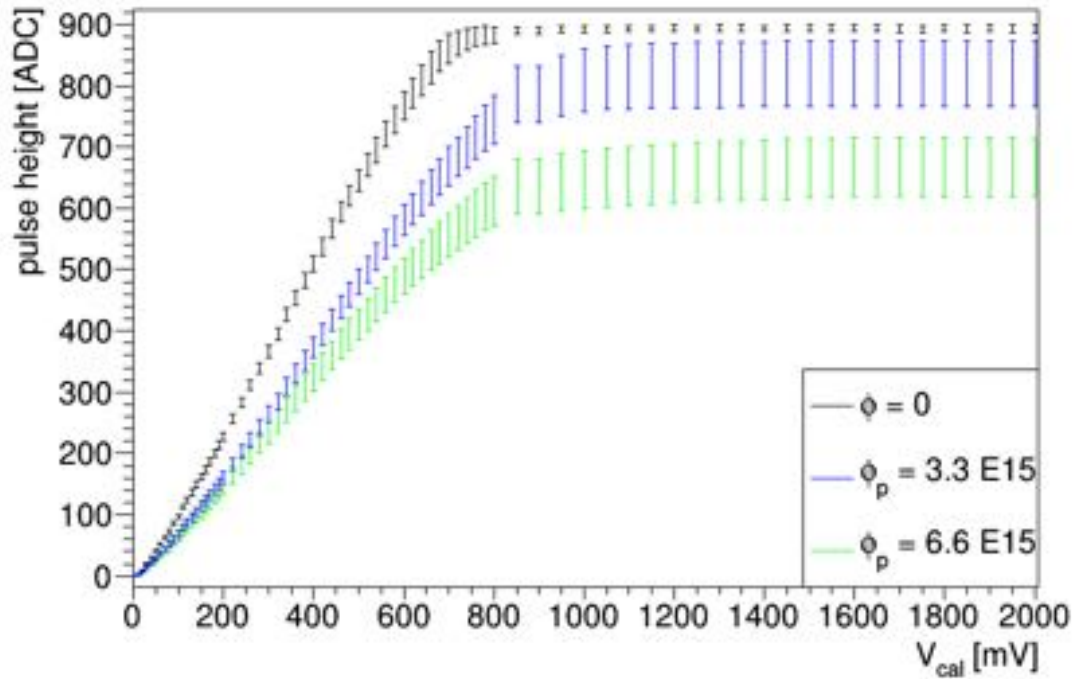
Figure 6.8 – Pulse height distribution of all pixels after pedestal correction as a function of V_{cal} units at hold 40, the displayed error is the standard deviation of the individual histograms, compare Figure 6.9.
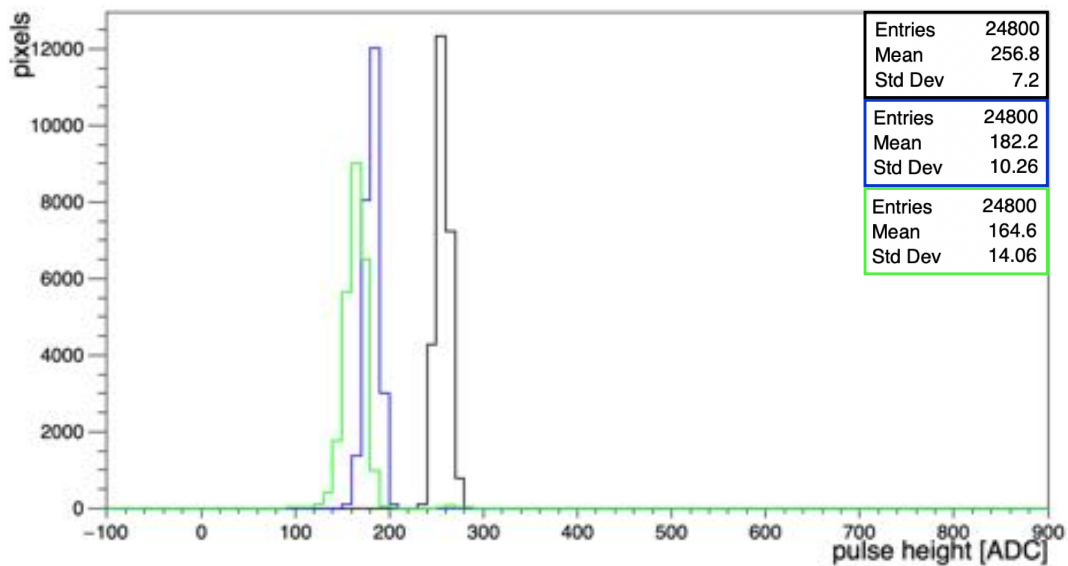
Figure 6.9 – Distribution of the pedestal corrected pulse height of all 24 800 pixels of the ROC4SENS at hold 40 and $V_{cal} = 220$ mV. This pulse height corresponds to the size of the Landau MPV of the collected data. The standard deviation is 7.2 ADC for the non-irradiated sensor, which amounts to about 3%.
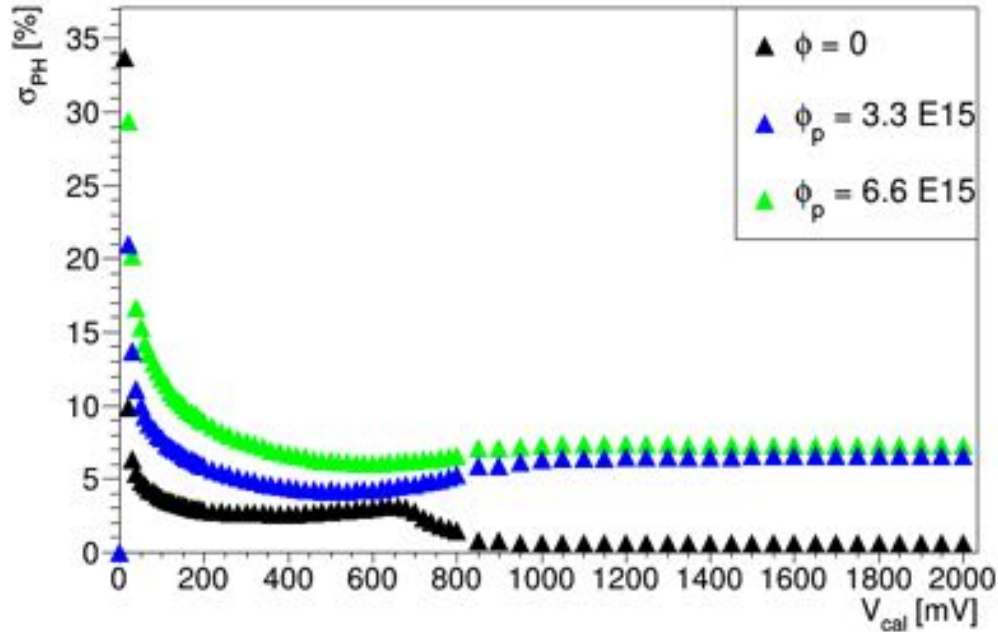
Figure 6.10 – The RMS divided by the mean pulse height as a function of V_{cal} at hold 40. The average spread is 3% for the non-irradiated sensor and 6% (8%) for $\Phi_p = 3.3\,(6.6) \times 10^{15}\,\mathrm{cm}^{-2}$.

The spread as a function of V_{cal} is shown in Figure 6.10 for the different sensor irradiations. For the non-irradiated sensor the bias voltage is 120 V. For the irradiated sensors, the bias voltage is 800 V, as at this voltage the difference in pulse height over the sensor area due the irradiation profile is small. All sensors show a large σ_{PH} for small calibration pulse amplitudes, which is decreasing until $V_{cal} \approx 250\,\mathrm{mV}$. For $V_{cal} > 1000\,\mathrm{mV}$, where the pulse height saturates, also the spread remains stable. It is visible that σ_{PH} increases with irradiation, the average spread increases from 3% for the non-irradiated sensor to 6% (8%) for $\Phi_p = 3.3\,(6.6) \times 10^{15}\,\mathrm{cm}^{-2}$. So for $\Phi_p = 3.3 \times 10^{15}\,\mathrm{cm}^{-2}$, the gain spread between the individual pixels doubles compared to a non-irradiated sensor, which was also visible when comparing Figures 6.7 top and bottom.

The spread in pixel response for a sensor proton irradiated to an average fluence of $\Phi_p = 6.6 \times 10^{15}\,\mathrm{cm}^{-2}$ is shown in Figure 6.11 for two different settings of the analog current I_A, explained in Chapter 4.4.2. The bias voltage is 800 V, and the measurements were taken at hold 40. The average spread at $I_A = 36\,\mathrm{mA}$ is 8% and thus 5% lower than for $I_A = 125\,\mathrm{mA}$. All measurements were taken at the same temperature of $-30°\mathrm{C}$. So with a higher analog current, the spread between the individual pixel responses increases.

To check the shape of the curve in Figure 6.8, the ratio between the mean pulse height and the inserted V_{cal} units was plotted as a function of the mean pulse height. It is visible in
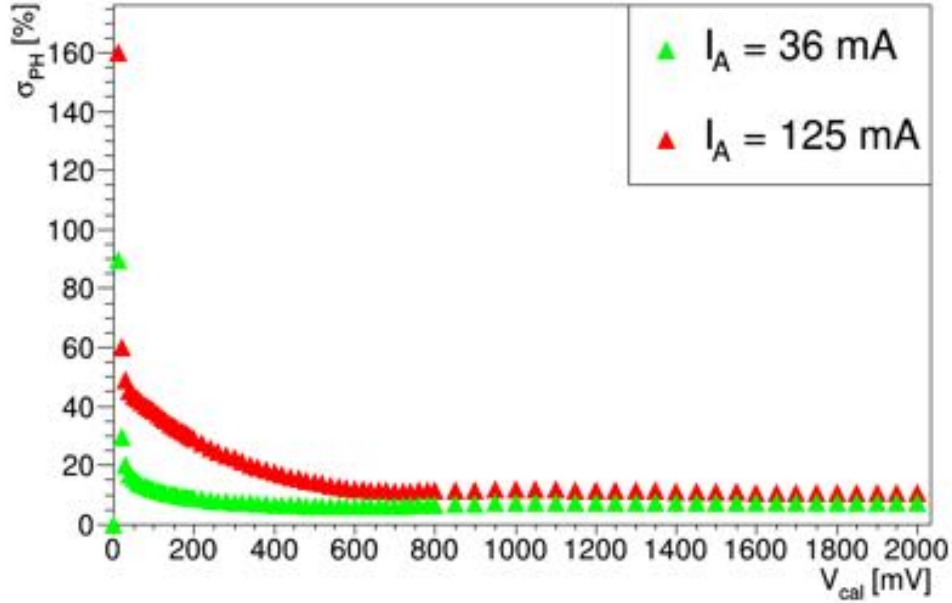
Figure 6.11 – The RMS divided by the mean pulse height as a function of V_{cal} at hold 40 for a sensor irradiated to $\Phi_p = 6.6 \times 10^{15}\,\mathrm{cm}^{-2}$. The spread at $I_A = 36\,\mathrm{mA}$ has a mean value of about 8% and a mean value of about 13%, at $I_A = 125\,\mathrm{mA}$, so an increase in analogue voltage leads to a larger spread.

Figure 6.12 that the relation between the applied V_{cal} units and the resulting mean pulse height is non-linear, as in that case a straight line would be visible. The pulse height saturates for high V_{cal} values, as visible in the steep decline at higher pulse heights. For pulse heights smaller than 100 ADC there is a steep increase. Only for intermediate pulse heights the relation can be considered linear.

For the gain calibration, the pedestal corrected pulse height as a function of V_{cal} in mV is used, as shown in Figure 6.8. The shape of the function is clearly non-linear, as shown in Figure 6.12, where the ratio of the mean pulse height and corresponding V_{cal} unit is shown as a function of mean pulse height. The pulse height saturates for high V_{cal} units, as visible in the steep decline. For small pulse heights up to $\approx 100\,\mathrm{ADC}$, the function shows a steep turn-on. Thus, Figure 6.8 is fitted by a logistics function for every pixel

$$\mathrm{PH_{Fit}} = p_3 + \frac{p_2}{1 + \exp(-u)}, \text{ with } u = \frac{V_{cal} - p_0}{p_1}. \tag{34}$$

The inverse function Q is used to calibrate the charge

$$Q(\mathrm{PH_{FIT}}) = V_{cal} \cdot k \tag{35}$$
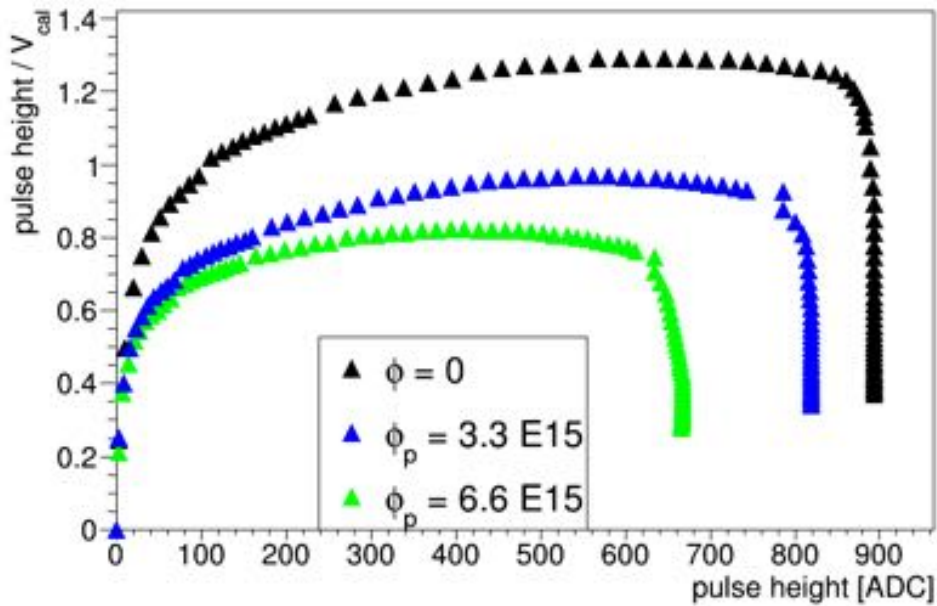
Figure 6.12 – The ratio of the mean pulse height and the corresponding V_{cal} units from the pulse height distributions of Figure 6.8 as a function of the mean pulse height.

with the calibration constant k. The individual fitting of each pixel corrects for the relative gain variations of about 3% between the pixels, so the resulting Landau distribution should be more narrow. The different pixel responses and their fits are shown for five pixels in Figure 6.13. The fit is applied over the range from $V_{cal} = 20\,\text{mV}$ to $V_{cal} = 800\,\text{mV}$.

As it is not possible with the ROC4SENS to determine the relation between the V_{cal} units and electrons using a source calibration, e.g. the characteristic energy spectrum of monochromatic X-rays, the expected charge in electrons is used for an absolute calibration of the collected charge. By using the in Chapter 2.1.2 mentioned charge of about 22 000 electrons in 300 µm of silicon for a MIP, which results in a MPV of the Landau distribution of 11 kilo electrons (ke) for 150 µm of silicon, the collected signal in ADC is calibrated with the calibration constant to this value. This corresponds to 7.3 ke for 100 µm of silicon, the distance of one pixel pitch used in the edge-on measurements. Figure 6.14 shows the charge distribution of the acquired signal before and after calibration for a non-irradiated sensor measured edge-on. The fitted Landau peak position after calibration fits the desired value of 7.3 ke. Also the gain equalization has made the Landau distribution more narrow, from 0.5 to 0.4 in FWHM divided by the MPV, as all pixel responses are equalized.

As the gain calibration of the ROC4SENS uses the internal calibration pulses V_{cal}, it is not suitable to use the gain equalization or calibration for the irradiated sensors, since
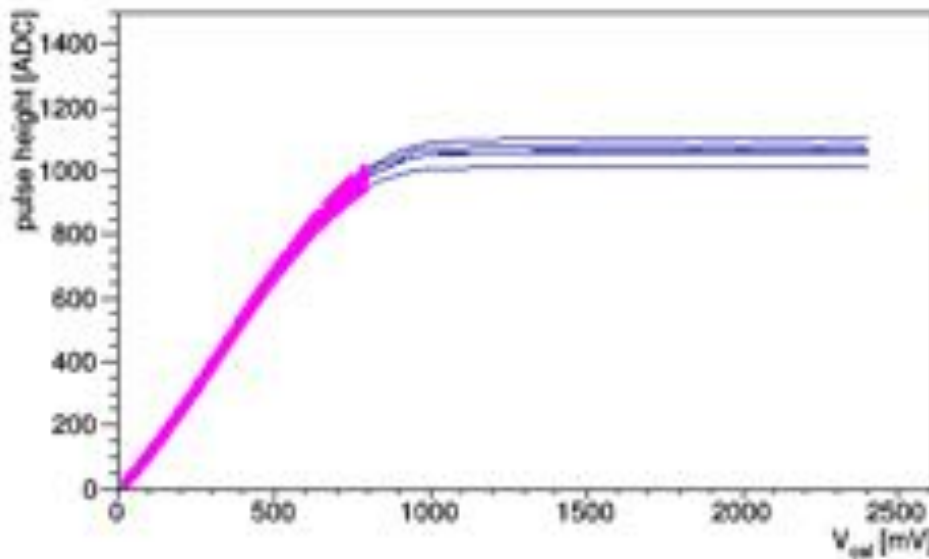
Figure 6.13 – Pixel responses and fit in magenta for five different pixels of the non-irradiated sensor. The individual gain variations are clearly visible.

the shape and timing of beam data and the test pulse are different, as shown in Figure 4.14. This also follows from Figure 6.15, where the gain calibration was also applied for an irradiated sample. It occurs that the relative spread of the Landau distribution increases from 60% to 90%, although the calibration should have the opposite effect. The gain equalization and calibration is therefore not used for the edge-on analysis in Chapter 7. To summarize, for all settings used in the edge-on analysis, the measurements from the test pulse indicate at most a 8% spread of the individual pixel responses for the high proton fluence and only about 3% for a non-irradiated sensor.
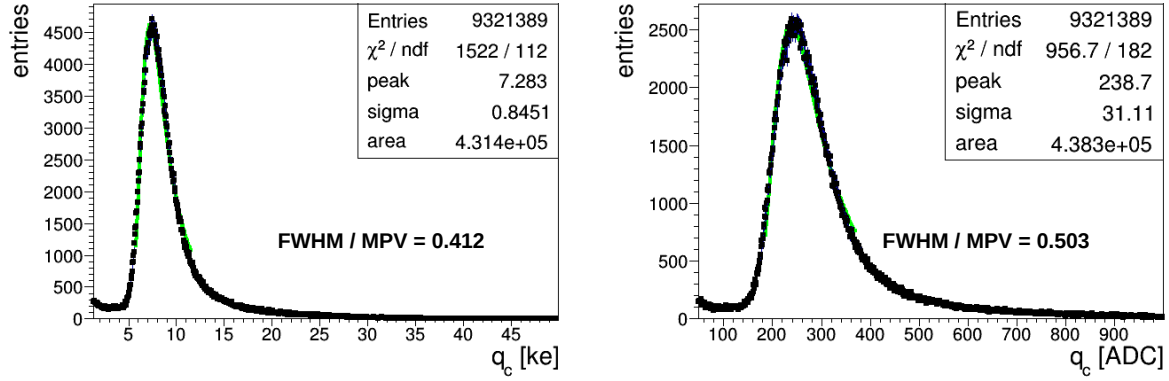
Figure 6.14 – Gain calibration for the non-irradiated chip. On the left: The Landau distribution of a non-irradiated sensor measured edge-on after gain calibration. On the right: The Landau distribution before calibration to kilo electrons. The gain equalization works as expected, since the Landau distribution is more narrow after calibration, as all pixel responses are equalized.
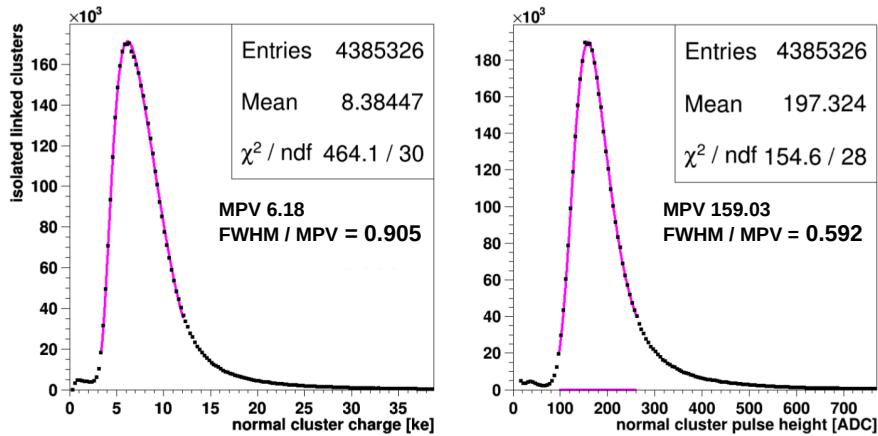
Figure 6.15 – Charge distribution of a chip irradiated to an average fluence of $\Phi_p = 6.6 \times 10^{15}\,\mathrm{cm}^{-2}$ at vertical incidence. Left: A fit to the gain calibrated distribution. Right: A fit to the raw distribution. The expected equalization of the different pixel gains was not successful, as the spread of 60% before the calibration is worse after calibration (90%). Plot adapted from D. Pitzl (DESY).

6.3. Difference between ROC4SENS chips

As shown in Chapter 4.4 the settings for the individual chips can be different and therefore can result in a different gain. To understand the gain variations between the individual chips, a reference measurement at vertical incidence with 27 non-irradiated ROC4SENS chips bonded to different pixel sensor designs was taken at $I_A = 125$ mA. From measurements with test pulses it was established that a larger analogue current leads to a faster rise time of the pulse, see Chapter 4.4.2. For each chip the pulse height distribution was fitted to understand how the Landau MPV changes. The resulting MPVs are shown in Figure 6.16 on the left in ADC, the individual chip responses differ by $\sigma_{PH} = 10\%$. In addition, the conversion to kilo electrons was done to check the performance of the gain equalization and the factor needed for calibration, see Figures 6.16 on the right and 6.17. After the gain equalization and calibration to kilo electrons the difference in response of the readout chips is negligible. The conversion factors for each readout chip are all within 3%, therefore the mean of $k = 0.0367$ was used for all further conversions.
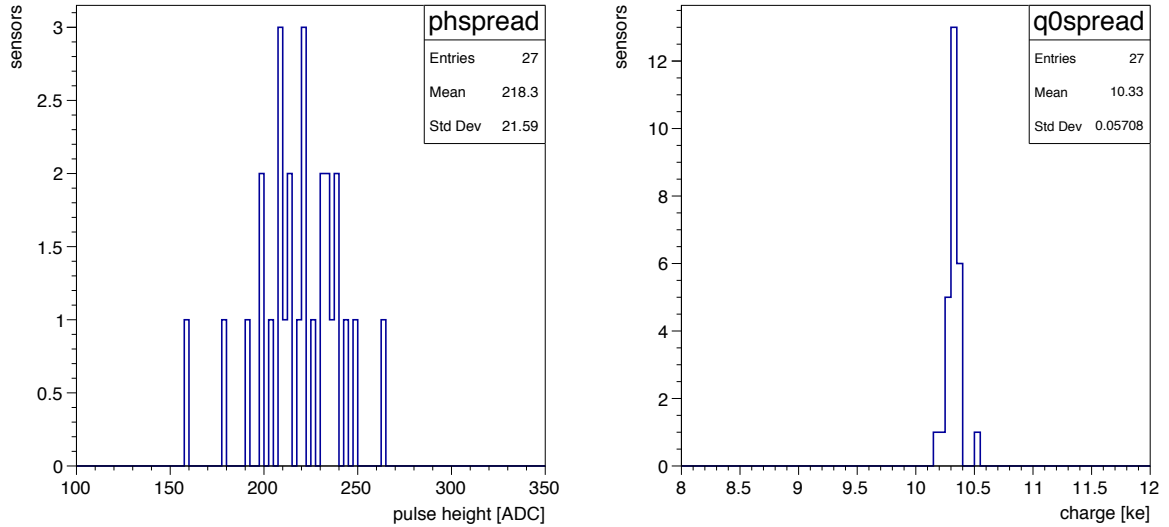
Figure 6.16 – Landau MPVs in ADC (ke) on the left (right), fitted with a Moyal distribution, of 27 non-irradiated ROC4SENS chips bonded to different sensor designs at $I_A = 125$ mA. Plots provided by F. Feindt.

To understand the pulse height spread between the individual chips at a lower analog current $I_A = 50$ mA, a reference measurement with 24 non-irradiated ROC4SENS chips bonded to different pixel sensor designs was taken. The chip settings were set to the same values for all chips and correspond to the settings used for the analysis. The settings used are $V_A = 2400$ V, $V_D = 2800$ mV, $V_{ana} = 1850$ mV, $V_{dd} = 2400$ mV, $V_{ref} = 250$ mV, V_{gpr}
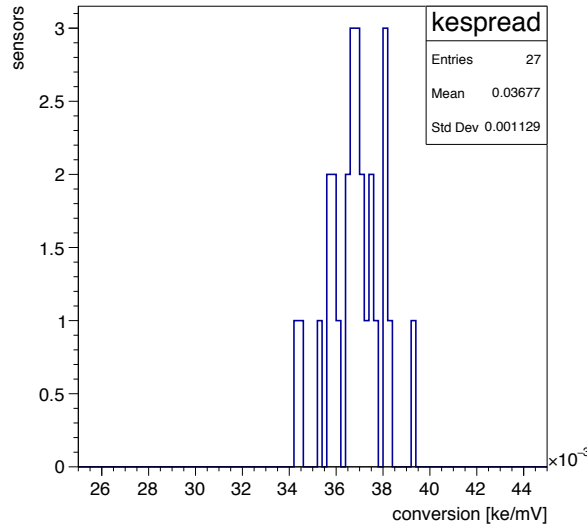
Figure 6.17 – Conversion factor k used to obtain the charge in ke for all 27 non-irradiated ROC4SENS chips. Plot provided by F. Feindt.

$= 900$ mV, $V_{gsh} = 670$ mV, ADCdel $= 10$, $I_{ana} = 55$ mA, and $I_D = 4.2$ mA. All sensors were at vertical incidence in the beam and for each chip 90 000 events were analyzed. The Landau MPV was fitted with a Moyal distribution and the resulting MPVs are shown in Figure 6.18. The mean value of the 24 MPVs is 246.4 ADC with a RMS of 18.09 ADC, resulting in a spread between chips of $\sigma_{PH} = 7\%$. This shows that the chosen working point of $I_A = 50$ mA leads to a smaller spread between the different chips, probably as the individual pixels have a smaller difference in gain. From the test pulse measurements in Section 6.2 it was established, that an increase in the analog current leads to a bigger spread between the individual pixels.

A comparison of measurements performed with different chips has to take into account this gain spread of 7%, especially as it might be more pronounced with irradiation.
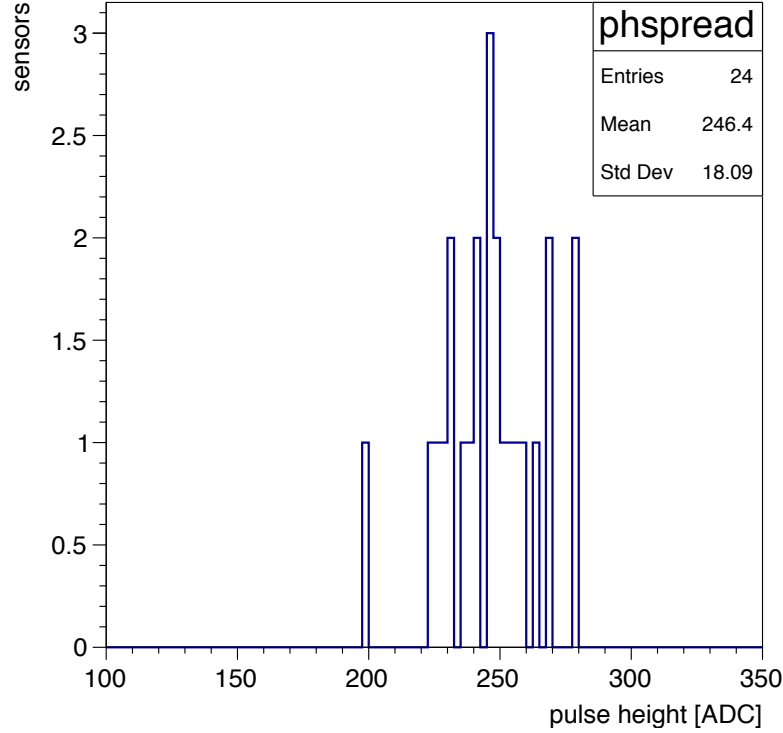
Figure 6.18 – Landau MPVs in ADC, obtained with a Moyal fit, of 24 non-irradiated ROC4SENS chips bonded to different sensor geometries at $I_A = 50\,\text{mA}$. In comparison to Figure 6.16 the spread σ_{PH} between the chips is smaller. Plot provided by F. Feindt.

6.4. Detector Alignment for DUT

The alignment of the DUT is performed in the telescope coordinate system and the DUT pixel coordinates are transformed using the passive rotation

$$\begin{pmatrix} x' \\ y' \\ z' \end{pmatrix} - \begin{pmatrix} a_x \\ a_y \\ 0 \end{pmatrix} = R_y(\omega)R_x(\alpha)R_z(\phi) \begin{pmatrix} x_{pix} \\ y_{pix} \\ z_{pix} \end{pmatrix} \text{ where } y_{pix} = 0. \tag{36}$$

The extrapolated position of the telescope upstream triplets to the DUT is used for the prealignment. The residual between DUT hits and the track impact is calculated.

The maximum of the residual distributions is shifted to 0 by shifts a_x and a_y for the x- and y- plane, respectively. In a second step the DUT is aligned in all three spatial directions a_x, a_y and a_z and afterwards as well for the three rotation angles ω, α and ϕ. The rotation angle ϕ is constrained by the DUT mechanics but for precision it is also aligned. The alignment is performed as an iterative procedure until the necessary re-alignments are in the order of their errors. Afterwards, the y-direction of each run is
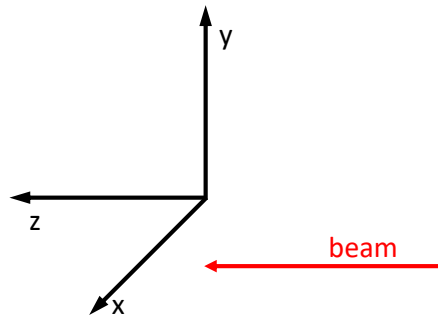
Figure 6.19 – Sketch of the coordinate system, the z-direction is along the beam direction.

aligned manually, such that the left edge of the charge collection profile is at -0.075 mm. The fitting procedure is explained in detail in Chapter 7.1.3. This step is done for a better comparison between runs. The DUT is realigned for every new run at full bias voltage to maximize the alignment precision.

7. Edge-on Analysis

This analysis investigates how the charge collection varies along the sensor depth and whether the signal is dominated by electrons or holes. In addition the difference of radiation damage from neutrons with an energy larger than $100\,\text{keV}$ and 23 GeV protons on the charge collection profile is analyzed. Previous studies into the dependence of charge collection on the depth in the silicon sensor have applied the grazing angle technique [8]. The sensor is grazed by the beam at a shallow angle to investigate the charge collected in the different sensor depths, with position information provided by the sensor and the telescope track. So far, this technique was applied on thicker sensors ($285\,\mu\text{m}$), for more details see [80].

However using this technique for the Phase 2 sensors with their active thickness of $150\,\mu\text{m}$ suffers a lot from resolution effects, so that no clear charge profile can be acquired. The grazing angle technique was therefore refined to the edge-on method, where the beam hits the sensor parallel to the sensor surface and travels at one depth, within the track resolution, through the entire length of the sensor. All measurements analyzed in this section were taken at $5.2\,\text{GeV}$ electron beam energy.

List of own contributions The author's contributions to the results presented in this chapter include:

- data taking, setup and data monitoring at test beam,

- data analysis including event selection and signal definition,

- investigation of alignment systematics.

Test beam shifts were also performed by Dr. A. Ebrahimi, F. Feindt, Prof. Dr. E. Garutti, Dr. P. Gunnellini, Dr. D. Pitzl, Dr. J. Schwandt, Dr. G. Steinbrück and I. Zoi.

7.1. Event Selection and Signal Definition

The following paragraphs describe the event selection process and the choice of signal definition for the edge-on analysis. The sensor has already been aligned in the beam, as explained in Chapter 6.4.

7.1.1. Track Impact Reconstruction on the DUT

From all reconstructed triplet tracks for one event, the tracks that correlate to the MOD measurement are selected and are used for matching with the sensor signal, after the DUT has been properly aligned. To match a DUT hit to a track only loose cuts are applied, the x-coordinate of the DUT hit is required to be within four pixel pitches of the x-coordinate of the track, so a difference no larger than $100\,\mu m$ is demanded. In the alignment procedure described in Section 6.4, the y-coordinate's origin is aligned to be the middle of the sensor. And as to not exclude a part of the sensor, in the y-direction the cut window is even wider and only a match within $150\,\mu m$, i.e. one sensor depth, is required, as there is no direct depth information from the sensor itself. To exclude edge-effects of the outer rows and columns of the sensor, only tracks with hits within the fiducial region are used. The fiducial region is defined as $|x| < 3.8\,cm$ and $|z| < 3.8\,cm$. For the following analysis, all pixel hits registered by the DUT, that are matched to a track with a reference hit in the module are considered.

7.1.2. Signal Definition

With the lack of zero suppression of the ROC4SENS and the ROI data taking, introduced in Chapter 6.1, there is the unique situation of having the collected signals of eight pixels per sensor column after the track matching criteria are applied. The definition of a signal is therefore necessary as there are many possibilities to sum the individual pixels and define a signal.

In Figure 7.1 an example of the data taking situation is displayed. The beam travels through the sensor along row i and passes columns $j+1$, j and $j-1$. The collected charge q_c and therefore the signal is defined for each column as the sum of the three pixels closest to the beam track, as indicated by the gray area:

$$q_c(j) = q_c(i,j) + q_c(i-1,j) + q_c(i+1,j) \tag{37}$$

As there is no dependence of the collected charge on the column the index j is dropped for the further analysis. The considered possibilities and their advantages and disadvantages that lead to this signal definition are described in the following paragraphs.

A threshold on the signal of each pixel or on the total charge of a cluster is often used in test beam analyses. This however includes losing signal that was below the defined threshold but it excludes noise. To study the effect of an applied threshold on the collected charge, a pulse height cut of four times the noise RMS, leading to 16 ADC, was applied.
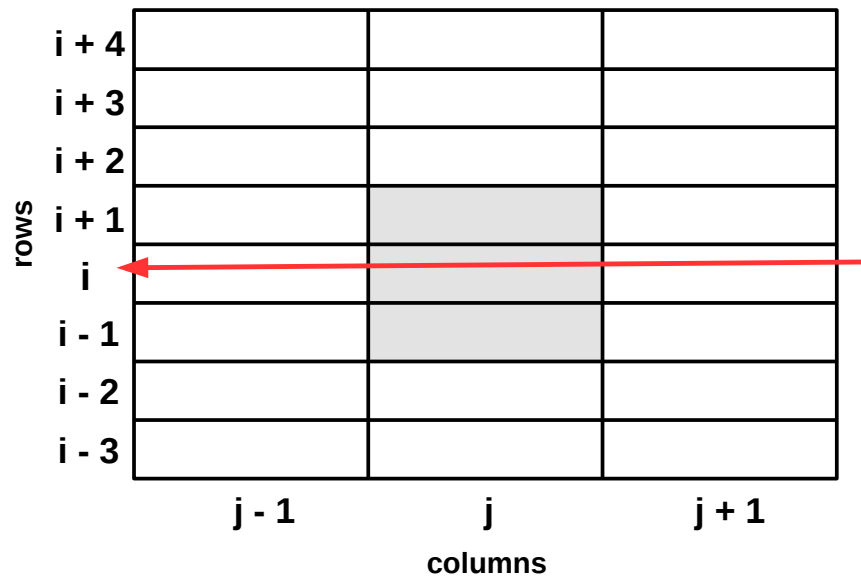
Figure 7.1 – An illustration of the ROI after data taking and the resulting signal definition. The beam (red) traverses the sensor along row i and passes columns $j + 1, j$ and $j - 1$. The gray area indicates the pixels that contribute, per definition, to the signal.

For diffusion studies in the sensor, a threshold cut is of advantage as one can see the number of pixels above threshold increasing with depth in the sensor. Signal induced further away from the readout electrodes is more likely to be collected by multiple pixels due electric field profile. The electric field builds up from the pixel implants and decreases towards the sensor backside. At a lower electric field there is more diffusion and more pixels collect a signal, as has been observed in data of a non-irradiated sensor, see Figure 7.2. With increasing depth in the sensor, the number of rows with pixels above threshold contributing to the signal increases. It is also visible that the effect is dependent on the applied bias voltage of the sensor. The underlying principle of charge diffusion and charge sharing is explained in Chapter 2.3.

Diffusion and its increase of pixels collecting charge is not directly visible in the number of rows if the signal is defined as a certain number of pixels, for example three. However for the purpose of looking at the total induced signal, a threshold cut always means losing charge below it.

To avoid losing small charges by introducing a cut on the pulse height, the summing up of one, three or five pixel rows i is considered for the collected charge. For such a consideration it is crucial to consider the consequences of defining a starting pixel,
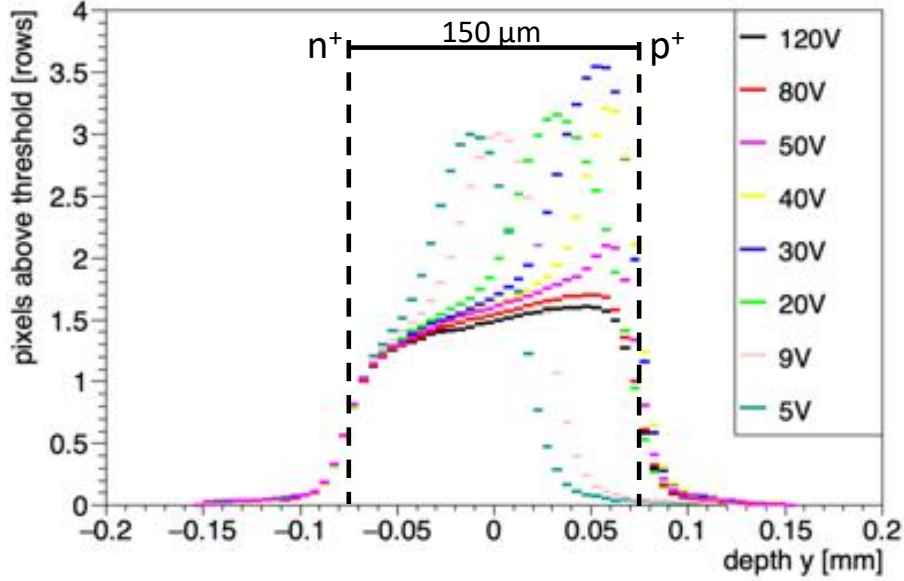
Figure 7.2 – Number of rows contributing to the signal as a function of depth y in the non-irradiated sensor. A threshold cut on the signal of 16 ADC, which equals four times the noise RMS, was applied. The different colors indicate the different bias voltages applied. With increasing depth in the sensor, the number of rows contributing to the signal increases.

that the signal of its neighbors is added to. There are several possibilities as the track resolution of 11 μm has to be considered, i.e. the pixel hit closest to the track is not necessarily the one with the largest pulse height. So possible starting points could be pixel with the largest signal or the one closest to the track, where closest to the track signifies the smallest Δx with

$$\Delta x = x_{track} - x_i \ , \tag{38}$$

where x_i is the x-coordinate of the row i, which is defined as the middle of the respective row. Both possibilities have been investigated and for the sum of three pixels and more per column the difference between those starting points was found to be negligible. As there is a non-uniformity of the chip in terms of charge, the starting point was defined as the pixel closest to the track.

However as previously shown in Figure 7.2 the number or pixel rows with charge (above threshold) depends on the depth of the track in the sensor, so the number of pixel rows added must be considered carefully as charge might be lost. Especially for the irradiated sensors the charge might be spread over many more pixel rows, however also the noise increases. Adding all available eight rows to the signal, effectively reduces the signal, as also negative charges are added. Therefore, as previously stated, the signal is defined as the charge of a constant number of rows for the scope of this thesis, according to Equation

37.

In Figure 7.3 the collected charge is shown for the signal definition in black and in blue the remaining background of the pixels in the ROI, compare Figure 7.1. The corresponding charge collection profiles are shown in Figure 7.4.
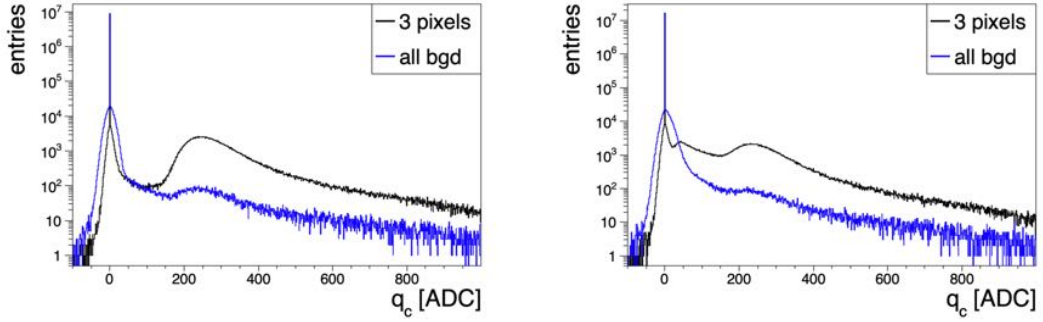
Figure 7.3 – The collected charge for the chosen signal definition and the remaining background for a non-irradiated sensor at 120 V bias voltage on the left and at 9 V on the right.
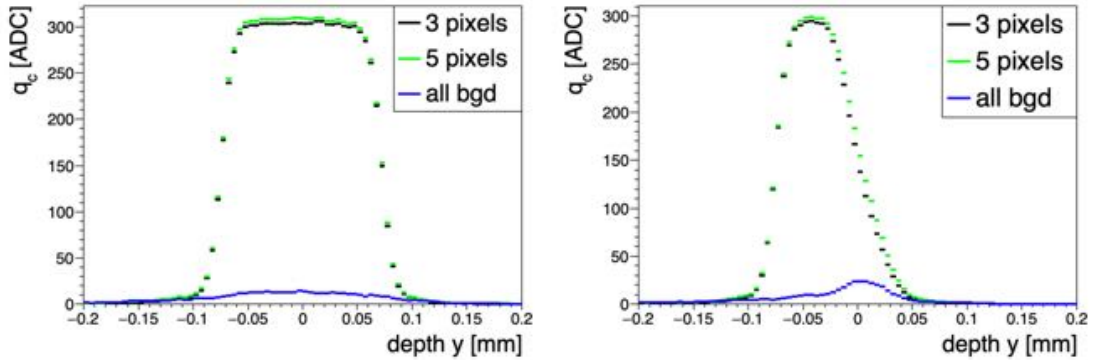
Figure 7.4 – The collected charge as a function of depth for different signal definitions of the non-irradiated sensor at 120 V bias voltage on the left and at 9 V on the right.

A higher number of rows has also been investigated but was found to distort the signal shape as especially on the edges of the sensor volume a lot of noise is added. Figure 7.5 shows a comparison of the different signal definitions for a sensor irradiated to $\Phi_p = 8.45 \times 10^{15} \, \text{cm}^{-2}$. The pixel with the smallest Δx is shown in red, the signal as defined for this thesis is shown in black and the signal as the sum of five pixel rows is shown in green. The latter shows that at the backside of the sensor a broader signal distribution increases the collected charge, however at the electrodes, the negative charge induced in the neighboring pixels decreases the collected charge, compare Chapter 7.5. For further considerations the single pixel is not further included, as it is clear, that by using just one pixel a significant amount of charge is lost. For 400 V the integral of the charge collection

profile over the entire sensor depth varies by 3 % when comparing three pixels and five pixels. While at 800 V the difference is 5 %, still this is within the overall uncertainty of the charge. The distributions at other bias voltages and the integrated charges can be found in Appendix C.

The negative charge that is added by additional pixels close to the implants is visible in Figure 7.6. The red curve shows the charge of the two pixels that are added to get from three to five pixels. At the pixel implants the collected charge decreases with the addition of more pixels, while it increases at the sensor backside. The blue curve shows for the remaining background for the chosen signal definition, including the charge of the red curve.
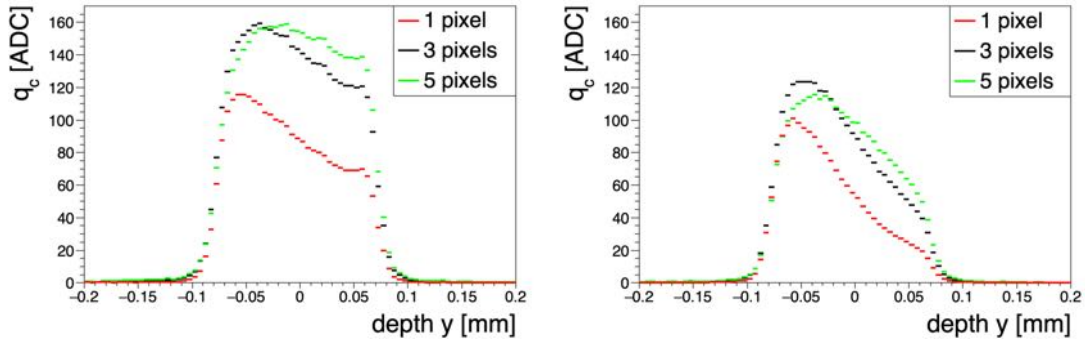
Figure 7.5 – The collected charge as a function of depth for different signal definitions of a sensor irradiated to $\Phi_p = 8.45 \times 10^{15}\,\mathrm{cm}^{-2}$ at 800 V bias voltage on the left and at 400 V on the right. The latter shows that at the backside of the sensor a broader signal definition benefits the charge collection, however at the pixel implants the negative charge induced in the neighboring pixels already decreases the collected charge.
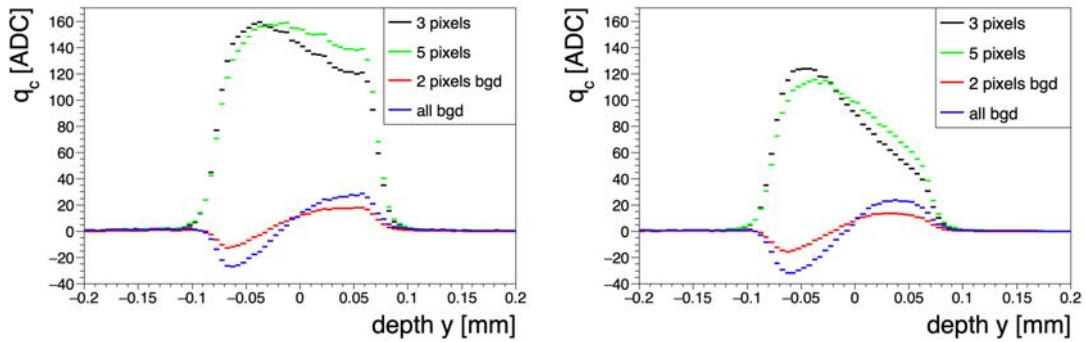
Figure 7.6 – The collected charge as a function of depth for different signal definitions and the remaining background of a sensor irradiated to $\Phi_p = 8.45 \times 10^{15}\,\mathrm{cm}^{-2}$ at 800 V bias voltage on the left and at 400 V on the right. The red curve shows the charge of the two pixels that are added to get from three to five pixels. In blue the charge of the remaining pixels not chosen for the signal definition is shown.
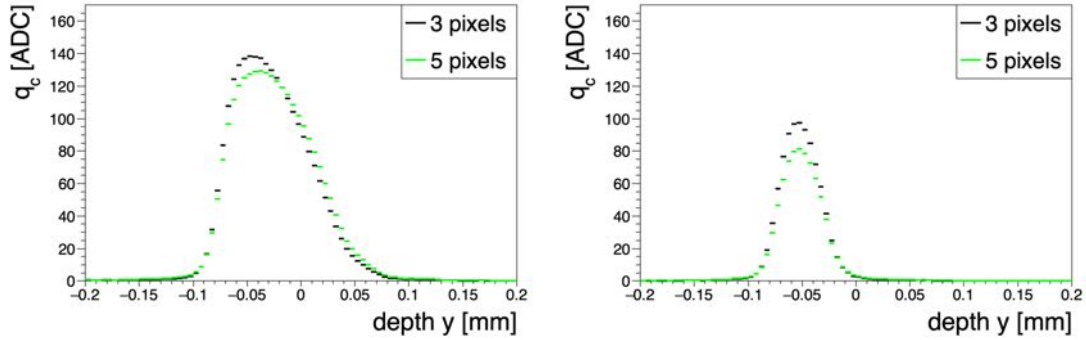
Figure 7.7 – The collected charge as a function of depth for different signal definitions of a sensor irradiated to $\Phi_n = 1.6 \times 10^{16}\,\mathrm{cm}^{-2}$ at 800 V bias voltage on the left and at 250 V on the right.

In Figure 7.7 on the left side, the difference between the different signal definitions is shown for a sensor irradiated to $\Phi_n = 1.6 \times 10^{16}\,\mathrm{cm}^{-2}$ at 800 V. The difference in the integrated charge is in the permille level and therefore negligible, at 250 V however the chosen signal definition collects visibly more charge than the sum of 5 pixels. So for this sensor a signal definition of five pixels decreases the charge.

To look in detail at the charge collection in the individual pixels distributed over the entire sensor depth, the edge-on tomography, the raw collected pulse heights of all the pixels are exploited.

7.1.3. Alignment Systematic

The active thickness of the sensor is chosen as an observable to see if the DUT alignment introduces a systematic error on the mean values. Considered are a x- and z-dependence for which the sensor is divided into four equal sectors in the respective plane and a time dependence for which a data run is divided into four sectors as well. No difference between the identical sectors of the sensor is expected for a good alignment. The segmentation in time provides an overview of the stability of the chip and its settings, as the chip temperature might have changed with time. The sensor geometry for splitting the sensor in the x-direction and the coordinate system is sketched in Figure 7.8. Each sector contains ~6200 pixels and the point of origin is in the middle of the sensor. The sectors are split in the x-coordinate direction as shown in Table 3.

The charge collection profiles for the different areas in x of the sensor and the corresponding charge distributions are shown in Figure 7.9. No significant difference between the charge collection of the different sectors of the sensor is visible.

The splitting of the sensor in the z-direction is performed as shown in Table 4. The corresponding charge collection profile for the different sectors in z are shown in Figure 7.10.
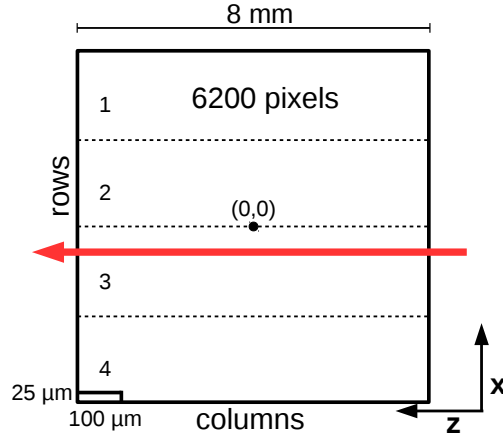
Figure 7.8 – The sensor coordinate system, the beam direction is along z and indicated in red. The dashed lines show the sensor split into four equal sectors in the x-direction, each containing 6200 pixels.

sector	boundaries in x
1	$2 \leq x < 3.8$
2	$0 \leq x < 2$
3	$-2 \leq x < 0$
4	$-3.8 < x < -2$

Table 3 – The x-coordinates for the different areas drawn in Figure 7.8.
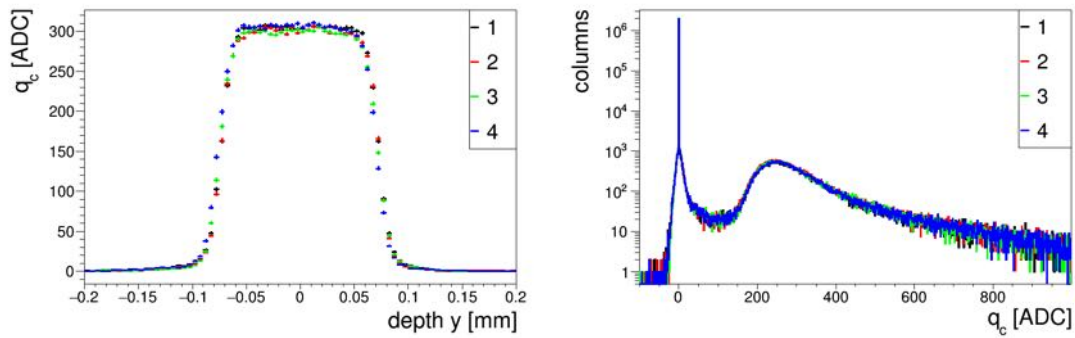
Figure 7.9 – On the left, the collected charge as a function of depth for the non-irradiated sensor divided into four equal sectors in the x-direction. No significant difference between the charge collection of the different parts of the sensor is visible. On the right, the corresponding charge histograms.

A small difference for the charge collection of the different sensors is visible. For a better comparison the total collected charge q_{tot} for each sector is calculated as the integral over

sector	boundaries in z
1	$2 \leq z < 3.8$
2	$0 \leq z < 2$
3	$-2 \leq z < 0$
4	$-3.8 < z < -2$

Table 4 – The z-coordinates for the different areas in z-direction.

the respective charge collection profile and divided by the mean total collected charge of the entire sensor. Figure 7.11 shows that the deviation is below 3% for the different sectors. As each column has an individual column amplifier, which can introduce a difference in charges along the z-axis, a slight difference along z compared to x is expected. It is therefore concluded, that the alignment procedure does not introduce a systematic error on the charge collection profile.
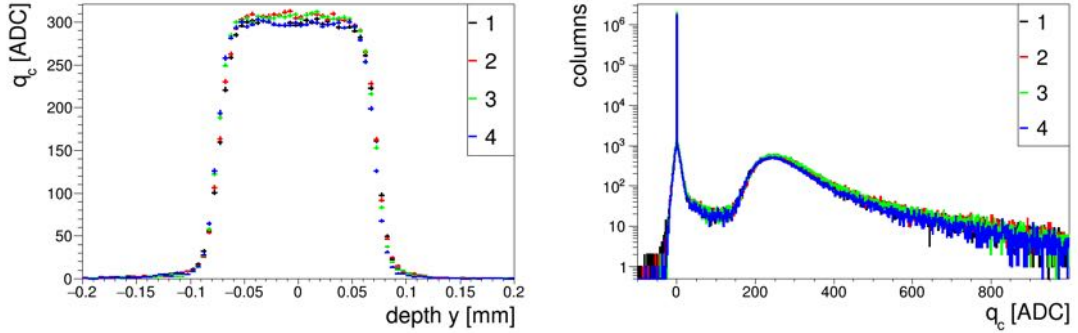
Figure 7.10 – On the left, the collected charge as a function of depth for the sensor divided into four equal sectors in the z-direction. On the right, the corresponding charge histograms.

The signal as a function of depth in the sensor is used to define the active thickness of the sensor. The edges of the distribution are fitted individually with the complementary error function to obtain the edges of the sensor and their resolution

$$erfc(x) = \frac{2}{\sqrt{\pi}} \int_{x}^{\infty} e^{-t^2} \mathrm{d}t \ . \tag{39}$$

The fit is applied twice on the data. The first time no cut on the fit range is applied and the second time the previously obtained edge and sigma of the fit are used as starting points, while the fit range is constrained to the two sigma region around the edge. The number of data points used for the fit is more stable this way and results in a better fit, compare χ^2/N_{dof} from Tables 5 and 6. In Figure 7.12 the fits on the non-irradiated
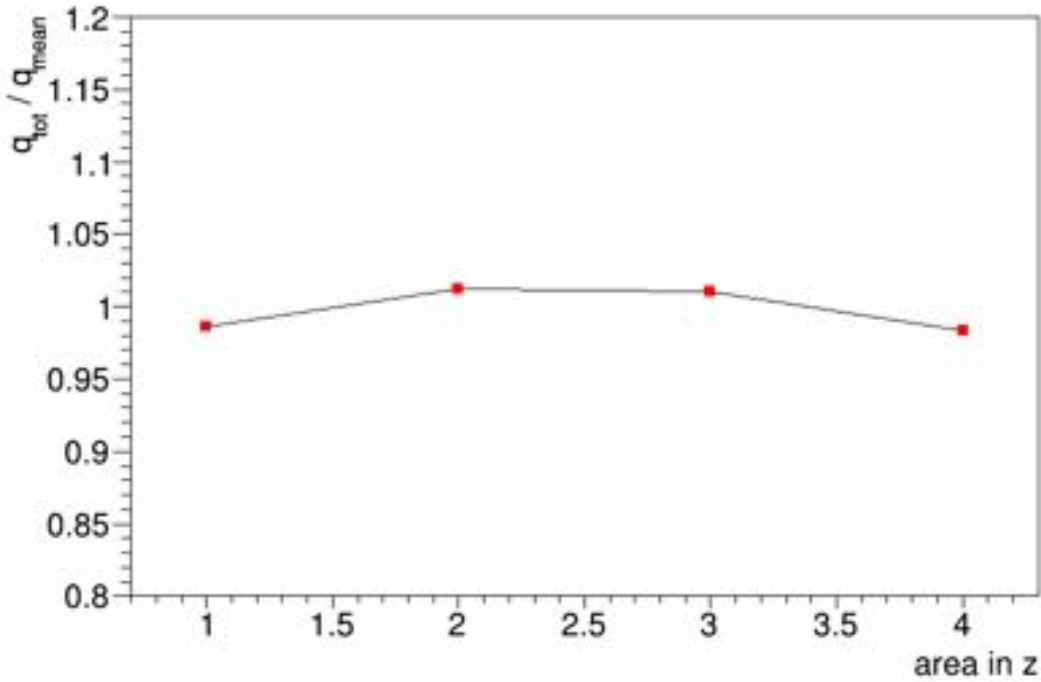
Figure 7.11 – Total collected charge q_{tot} of the distributions shown in Figure 7.10 divided by the mean charge of the whole sensor. The difference in charge between the different sectors is less than 3%.

distribution for a splitting of the sensor in z-direction are shown in magenta for the first iteration and in red for the second fit. The corresponding statistics are shown in Table 5 for the right edge of the distribution and in Table 6 for the left edge of the distribution. The obtained width represents the previously determined track resolution of around 11 µm, compare Chapter 5.6.

The thickness t is then defined as the distance from left edge e_{left} to right edge e_{right} and the corresponding error on the thickness is the sum of the squared errors of the edge positions.

$$t = |e_{left}| + |e_{right}| \tag{40}$$

$$\sigma_t^2 = \sigma_{left}^2 + \sigma_{right}^2 \tag{41}$$

In Figure 7.13 the thicknesses of the collected charge as a function of depth distributions for the different sectors in z of the non-irradiated sensor, see Figure 7.10, are shown. The last point corresponds to the thickness obtained from the fit results of Figure 7.12 via Equation 40. The individual thicknesses only deviate by 1 µm in this case.

The mean active thickness observed for different sensors differs from the 150 µm by max-

Fit Number	1	2
Edge [mm]	0.0704 ± 0.0001	0.0706 ± 0.0001
Width [mm]	0.0134 ± 0.0003	0.0119 ± 0.0002
Offset [mm]	0.3470 ± 0.0381	5.250 ± 0.8378
N_{data}	29	11
χ^2/N_{dof}	146.206 / 25	11.693 / 7

Table 5 – Fit parameter for the fit of the left edge of the distribution, the colors and values correspond to Figure 7.12.

Fit Number	1	2
Edge [mm]	-0.0761 ± 0.0001	0.0757 ± 0.0002
Width [mm]	0.0128 ± 0.0002	0.0116 ± 0.0003
Offset [mm]	0.5047 ± 0.0596	7.498 ± 0.7095
N_{data}	33	11
χ^2/N_{dof}	297.902 / 29	10.493 / 7

Table 6 – Fit parameter for the fit of the right edge of the distribution, the colors and values correspond to Figure 7.12 .
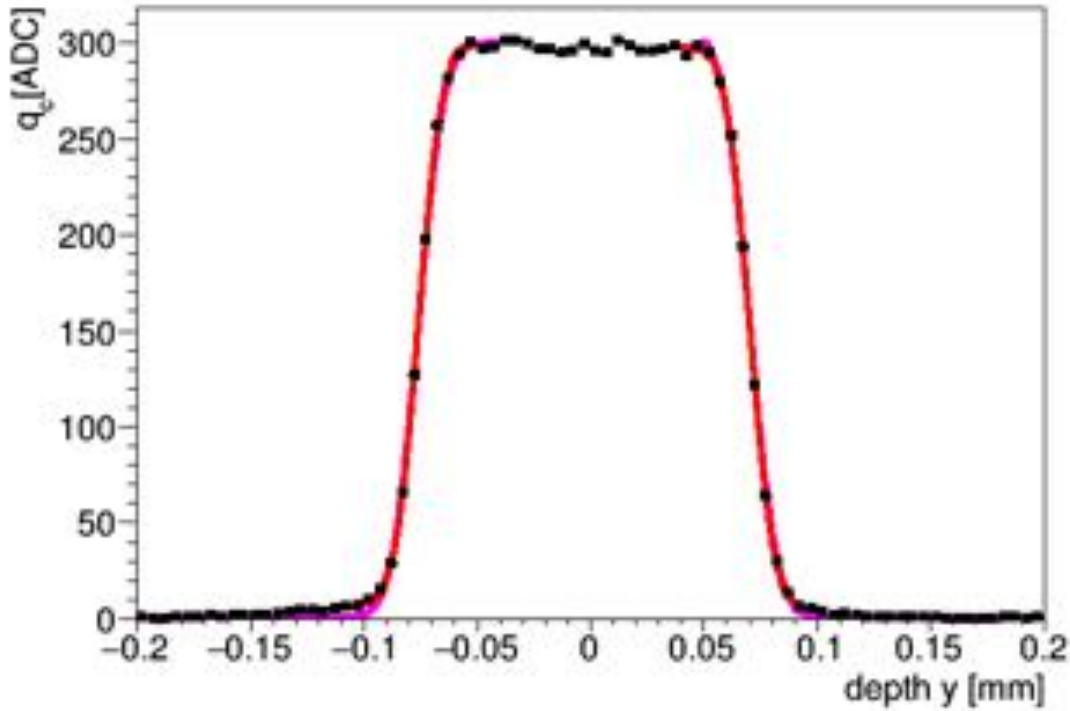
Figure 7.12 – Fit to the collected charge as a function of depth distribution of the non-irradiated sensor for the sector with $-3.8 < z < -2$ at 120 V. The edges of the distribution are fitted according to Equation 39. In magenta the first fit iteration and in red the second fit iteration is shown.

imal 4 µm. In this case for the non-irradiated sensor, which is FDB material an active thickness of 146.3±1 µm was calculated from Equation 40. Both proton-irradiated sensors are FTH material, for the lower irradiated sensor, an active thickness of 148.4 ± 1 µm was extracted and for the higher irradiated one 148.9 ± 1 µm.

These results are in agreement with C-V measurements of diodes, which resulted in an active thickness of 145 µm for FDB material and 148 µm for FTH material [81]. The different obtained thicknesses are summarized in Table 7. The difference between the wafer material was also observed in Figure 4.4.

An example of this deviation in time for the $6.6 \times 10^{15}\,\mathrm{cm}^{-2}$ proton irradiated maximum implant design is shown in Figure 7.14. As the difference of the charge collection profile is smallest at 800 V bias voltage for the different sectors of the sensor, the whole area of the sensor is taken for the division in time. The average thickness is approximately 149 µm, with an absolute deviation between the thickness of the first and the fourth quarter of events of 1.40 µm.
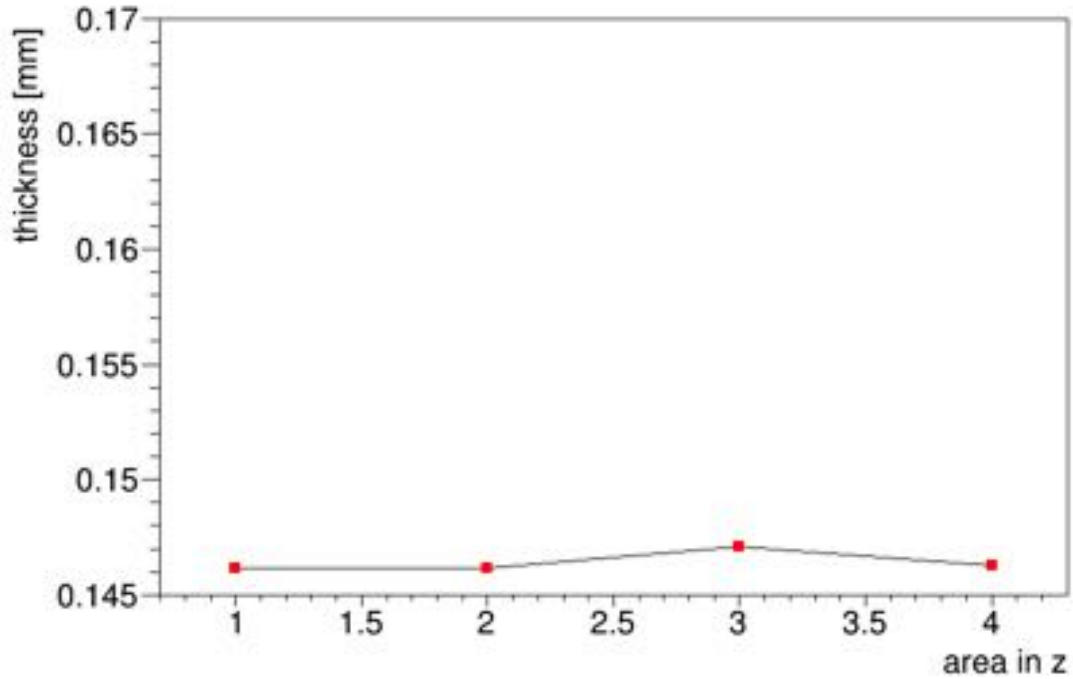
Figure 7.13 – Calculated thicknesses for the four different areas divided in z of the non-irradiated sensor at 120 V bias voltage. The individual thicknesses only deviate by 1 µm. The last point corresponds to the thickness obtained from the fit results of Figure 7.12 via Equation 40.

	sensor thickness from	
sensor type	C-V measurements	edge-on charge profile
FDB	145 µm	146 ± 1 µm for $\Phi = 0$
FTH	148 µm	148 ± 1 µm for $\Phi_p = 3.3 \times 10^{15}\,\mathrm{cm}^{-2}$
		149 ± 1 µm for $\Phi_p = 6.6 \times 10^{15}\,\mathrm{cm}^{-2}$

Table 7 – Overview of the sensor thicknesses obtained from the different measurements and sensor types.
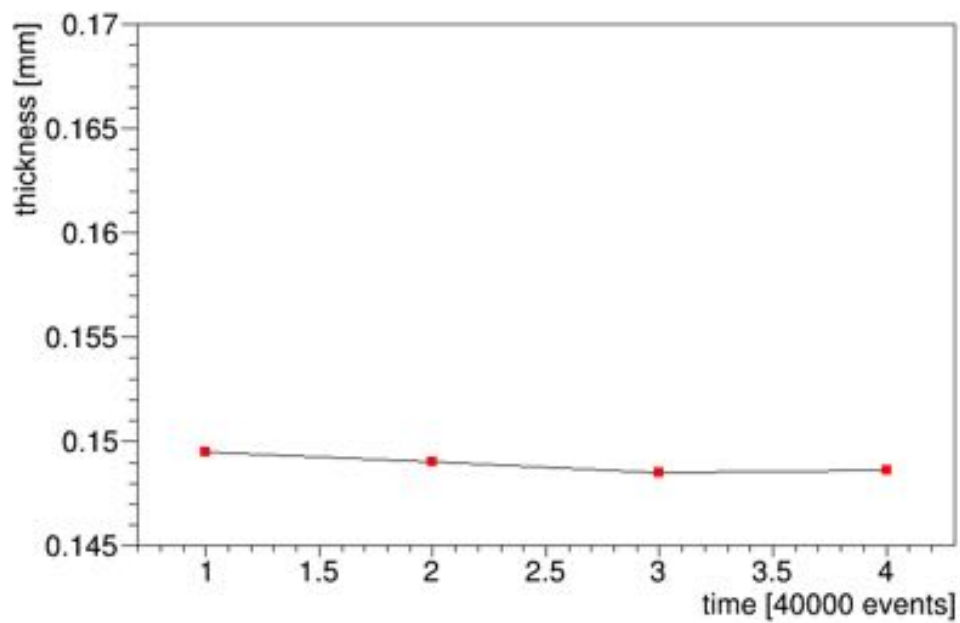
Figure 7.14 – Example of the active thickness calculated as a function of time for the sensor with the higher proton irradiation, a maximum implant design at 800 V. The average thickness is around 149 µm, with an absolute deviation between the thickness of the first and the fourth quarter of events of 1.40 µm.

Overall, there is no general systematic observed as all sensors tested show a deviation within 2 µm around the mean average thickness for a division in area or time.

7.2. Non-irradiated Sensors

After the event selection, described in Chapter 7.1, the expected columns hit per event for edge-on tracks are 78 and the length in z therefore 7.8 mm, the distribution of the track lengths of the selected events is shown in Figure 7.15. A maximum is observed for the entire length of the sensor. Entries with a length shorter than 7.8 mm are corresponding to non-parallel tracks, that travel a shorter distance through the sensor. The collected charge, defined in Equation 37, shows the expected Landau distribution, see Figure 7.16 on the right.
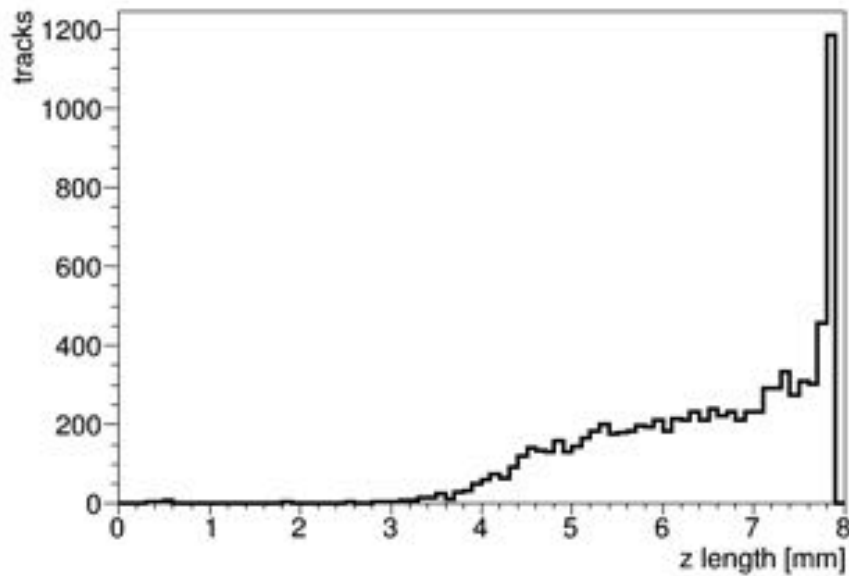
Figure 7.15 – The length of the tracks in the DUT in the z-direction. The maximum at 7.8 mm corresponds to the full sensor length.
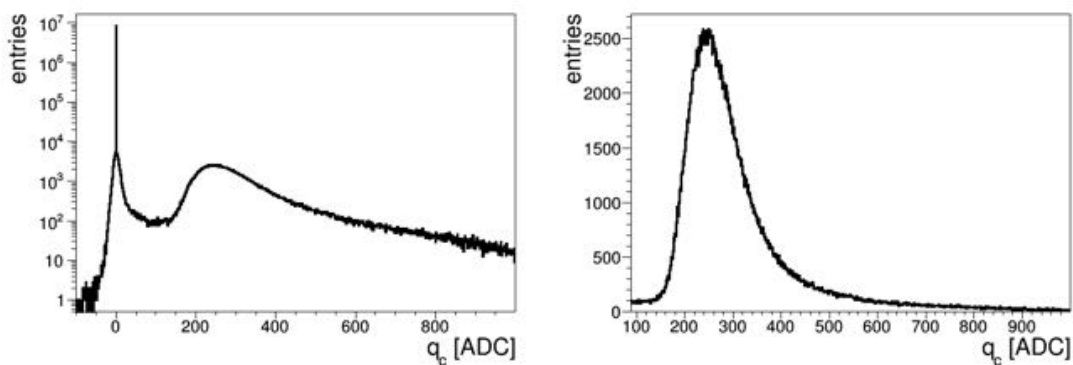
Figure 7.16 – The collected charge for the non-irradiated sensor at 120 V bias voltage, in logarithmic scale on the left and a zoom into the Landau peak on the right.

In Figure 7.17 the distribution of the track depth is shown for data taken at 20 V bias voltage. This reflects the beam profile, for which over the sensor area the number of tracks per depth only differs by 15 %. No cut into the beam profile from any alignment or selection step is visible.
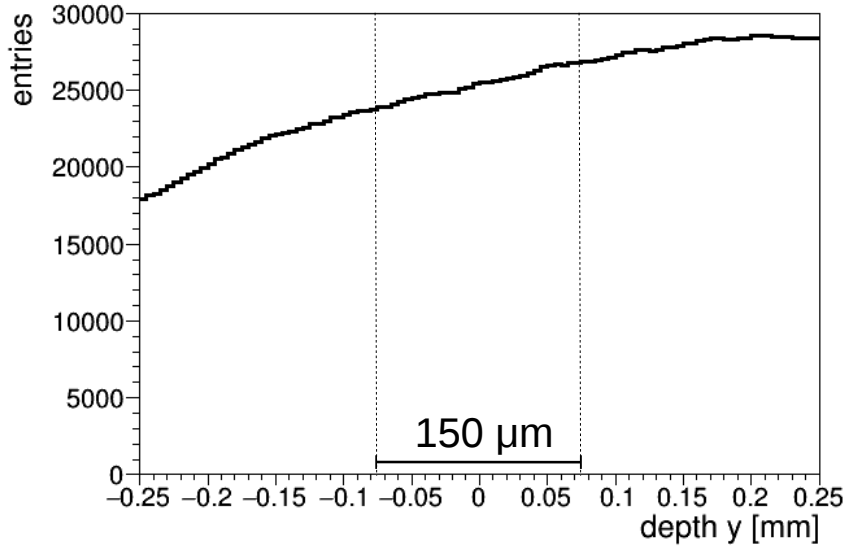
Figure 7.17 – The distribution of the number of events as a function of track depth for the entire measurements at 20 V. This essentially reflects the beam profile. The active area of the sensor is between the dotted lines.

The signal of the DUT is integrated over ca. 120 ns and is plotted versus the depth of the track in the sensor. Without resolution effects of the telescope and the binning width the signal should show a box shape, as there is no charge collected outside the sensor and inside the full charge is collected over the entire depth of the sensor if a bias voltage greater than the full depletion voltage is applied. For all measurements the pixel implants of the sensor are at $\sim -0.075\,\mathrm{mm}$ and the middle of the sensor is at $y = 0$.

An example of the collected charge distribution for different depths in the sensors are shown in Figure 7.18. Figure 7.18b and Figure 7.18d have approximately the same mean value, however the charge distributions look very different. Figure 7.18b corresponds to a depth where the active area of the sensor starts, so there are still many entries without collected charge, however if collected it is the full charge. Figure 7.18d at 20 V corresponds to a depth where the depleted area of the sensor ends, so many smaller charges are collected.

The mean value is 303.2 ADC, which is used for the entry in the profile in Figure 7.20, the plotted error e_{mean} is the standard error on the mean value, i.e. the standard deviation RMS divided by the square root of N, the number of entries,

(a) $-0.0100\,\mathrm{mm} \leq y < -0.095\,\mathrm{mm}$

(b) $-0.075\,\mathrm{mm} \leq y < -0.070\,\mathrm{mm}$

(c) $0.000\,\mathrm{mm} \leq y < 0.005\,\mathrm{mm}$

(d) $0.020\,\mathrm{mm} \leq y < 0.025\,\mathrm{mm}$
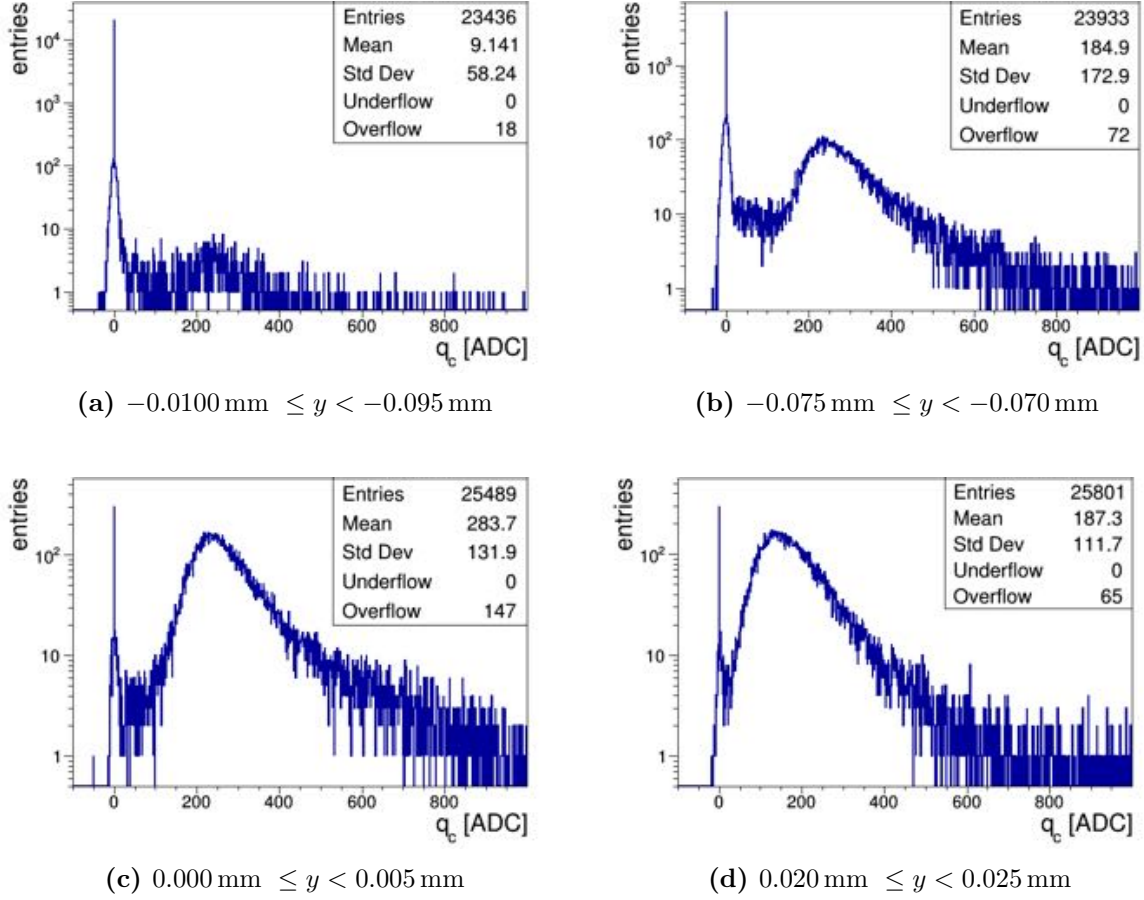
Figure 7.18 – The collected charge at different depths (**a-d**) for a non-irradiated sensor at 20 V bias voltage. The mean values at each depth are used for the charge collection profile in Figure 7.20.

$$e_{mean} = \frac{RMS}{\sqrt{N}} \ . \tag{42}$$

The errors are rather small due to the large number of entries and therefore barely visible. An example number for the error on the mean for the depth $0.000 \leq y < 0.005\,\mathrm{mm}$ is $e_{mean} = \frac{131.9}{\sqrt{25489}} = 0.83$. In Figure 7.17 it was shown that the number of entries for the different depths only slightly differs. To see how the number of events evolves over the sensor area, Figure 7.19 shows the number of all entries versus the number of events with a charge smaller than 1 ADC. One can see, that this inefficiency is small compared to the number of all events over the active area of the sensor. The number of small charges increases towards the sensor ends and outside the sensor, there is no more charge found. The width of this increasing region is caused by the telescope track resolution. The number of entries with charge smaller than 1 ADC corresponds approximately to the peak at 0 in Figures 7.18a-7.18d.
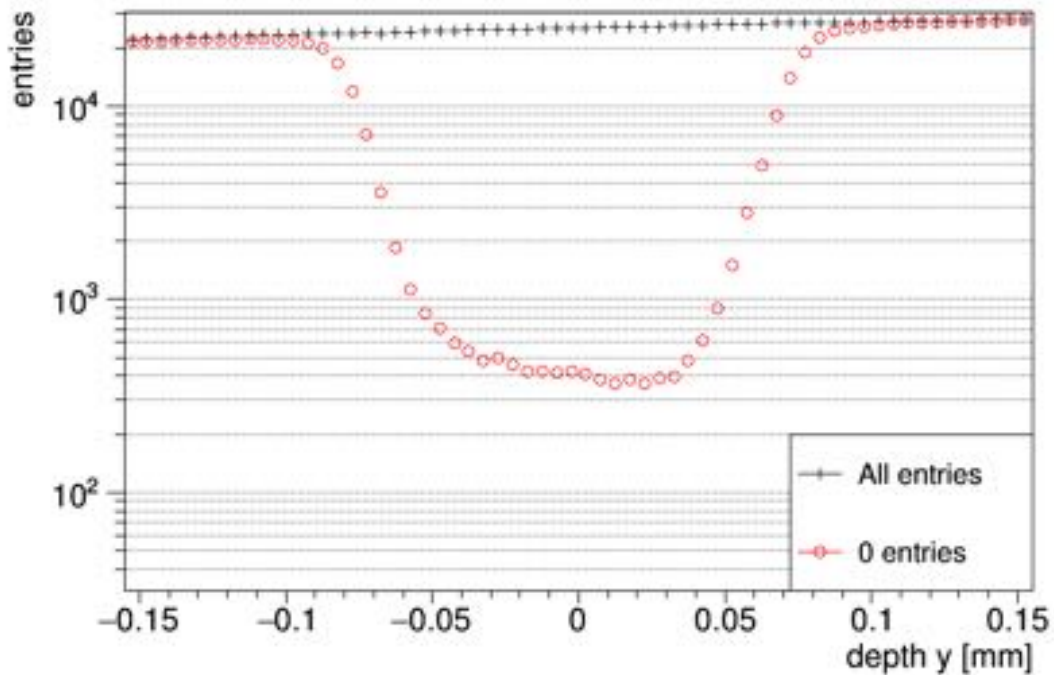
Figure 7.19 – The number of all entries for a non-irradiated sensor at 20 V in black versus the number of entries with charge smaller than 1 ADC, named 0 entries in red. Outside the active area of the sensor, both numbers are equal. In the active region of the sensor, the 0 entries are about 1% of all entries. Towards the sensor edges the number of entries with a small charge increases, the length of track depth over which this number is increasing is due to the track resolution.

In Figure 7.20 the collected signal is shown as a function of the depth for different applied bias voltages. The displayed charge is the respective mean value for each depth interval with the error calculated according to Equation 42. The observed signal does not show a straight box shape but rather a smeared one which is caused by resolution effects of the measurement setup. The expected track resolution of 11 μm was previously deduced in Chapter 5.6. Outside this smearing region the signal is zero as it is expected. For smaller bias voltages the active area of the sensor, which starts from the pixel implants, decreases. The charge collection depth is calculated from the active thickness of the sensor, explained in Chapter 7.1.3. For bias voltages above 50 V the signal is collected over the entire sensor depth, as shown in Figure 7.21, albeit from I-V and C-V measurements the full depletion voltage was established as 70 V. The difference is explained by the diffusion in the sensor leading to full signal collection over the entire sensor already below 70 V.

For comparison with charge collection from vertical incidence of the beam, the increase in total collected charge q_{tot} as a function of bias voltage is shown in Figure 7.22. The
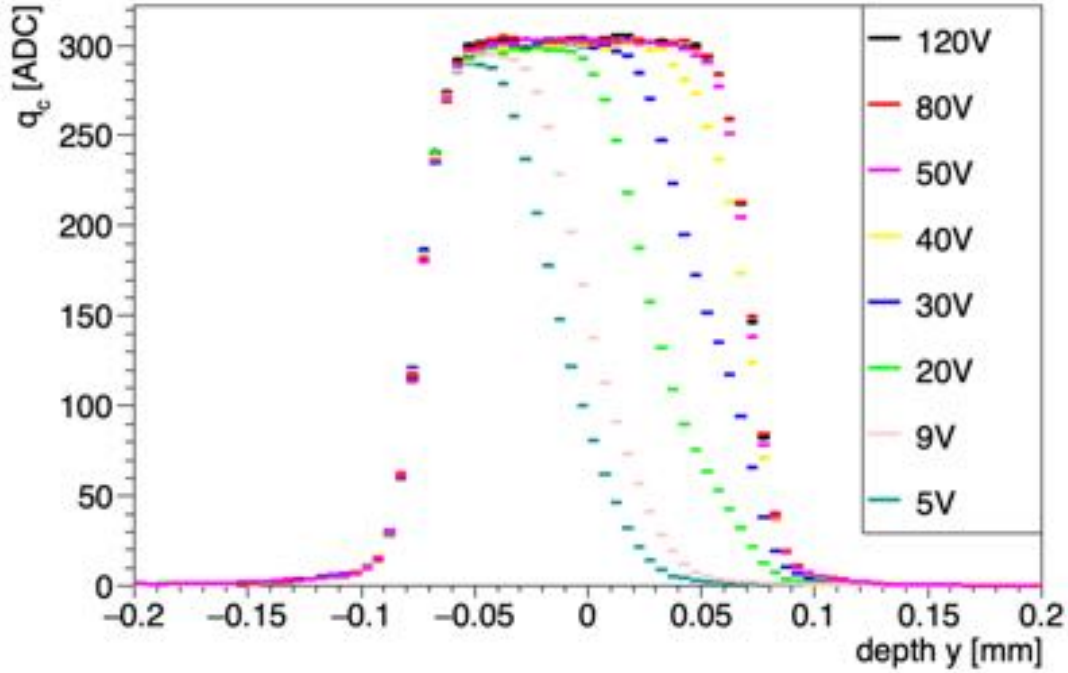
Figure 7.20 – Collected charge as a function of depth y in the sensor. The different colors indicate different bias voltages. For 50 V and higher the full charge is collected over the entire sensor.

collected signals per depth from Figure 7.20 are integrated over the active thickness $+\,2\sigma$ of the sensor to obtain the collected charge, which is approximated as the integral from -0.1 to 0.1 in y

$$q_{tot} = \int_{-0.1}^{0.1} q_c(y)\,\mathrm{d}y \ . \tag{43}$$

This approximation is chosen as especially for the proton irradiated sensors, the right edges of the profile are hard to fit precisely, as the profile shape changes, see Chapter 7.3.1. With this definition, the difference in total collected charge is calculated for the different signal definitions from Figure 7.4. In the entire background, outside of the signal definition, there is ($q_{tot} = 420\,\mathrm{ADC}$), which is less than 5% of the total collected charge at 120 V ($q_{tot} = 8935\,\mathrm{ADC}$). For completeness, the signal definition with five pixels was also calculated ($q_{tot} = 9092\,\mathrm{ADC}$) and adds below 2% to the total charge at 120 V.
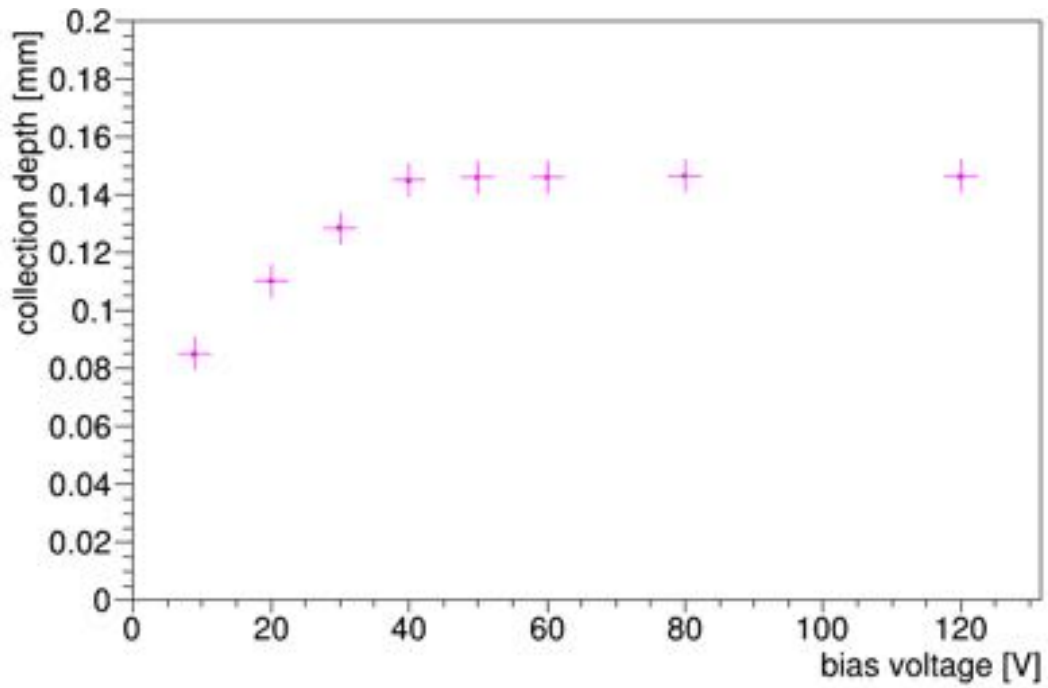
Figure 7.21 – Charge collection depth as a function of bias voltage. From 50 V bias voltage on the charge is collected over the entire sensor depth.
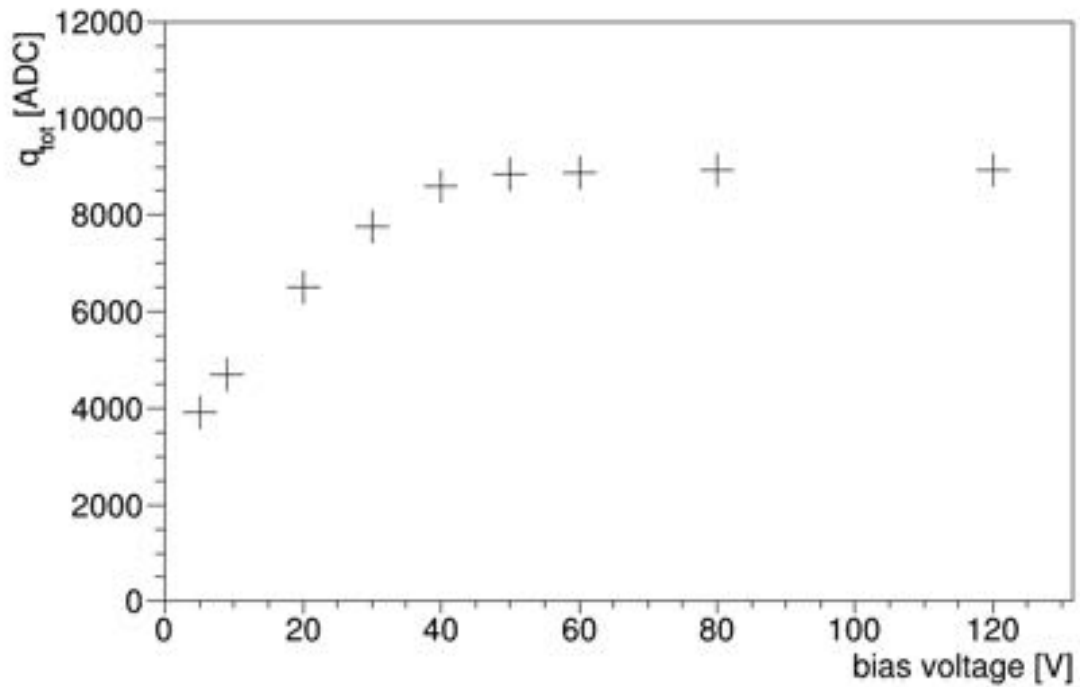
Figure 7.22 – Charge integrated over the sensor thickness as a function of applied bias voltage. From 50 V bias voltage on, the total collected charge saturates.

7.3. Irradiated Sensors

To investigate how irradiation changes the charge collection shape, six irradiated sensors with different fluences were measured edge-on. Additionally, the irradiations were done with different particle types, protons and neutrons. The influence of fluence and particle type on the charge collection profile will be investigated in this section. To ensure comparability, all measurements were taken at the same temperature of $-30°\mathrm{C}$, as the shape of the charge collection profile is expected to be dependent on temperature. While for the non-irradiated sensor only the position information of where the charge collection starts and ends in the sensor depth is obtainable, for the irradiated sensor additional information is available. As the total signal consists of the signal of electrons and holes, it is possible to gain information on their respective signal share and their absorption length. The absorption length or charge collection depth λ for a carrier i (electron or hole) is given by

$$\lambda_i = \mu_i \tau_i \, E \,, \tag{44}$$

with the charge carrier mobility μ, the trapping time τ and the applied electric field E. Electrons are about three times more mobile than holes, so $\mu_e > \mu_h$ [8], which makes the holes more prone to trapping. Thus, the collected charge is dominated by electrons, especially for a non-depleted sensor. In general, the collected charge is the sum of the hole signal q_h and the electron signal q_e, see Figure 7.23. The collected charge as a function of depth in the sensor, is always the sum of the two signals, with the electron signal dominating at the backside of the sensor and the holes dominating at the front side. Thus after irradiation, the signal pulse height generated by a beam close to the pixel implants allows for knowledge of the trapping of holes, as they have to travel through the entire sensor to be collected at the backside. Likewise the signal pulse height generated by a beam close to the backside provides information on the effective charge collection depth and trapping of the electrons.

7.3.1. Proton Irradiated Sensors

Two sensors have been irradiated with protons to average fluences of $\Phi_p = 3.28 \times 10^{15}\,\mathrm{cm}^{-2}$ and $\Phi_p = 6.60 \times 10^{15}\,\mathrm{cm}^{-2}$. The sensors are thinned float zone sensors with a p-stop default design in case of the lower fluence and a p-stop max implant for the higher fluence. Details on the different designs are described in Chapter 4.1. The irradiation process and the fluence determination procedure are described in Chapter 4.3.1. From the check of alignment systematics over the sensor area, as described in Section 7.1.3, it is visible that the irradiation is non homogeneous over the sensor. In Figure 7.24 the sensor is divided in
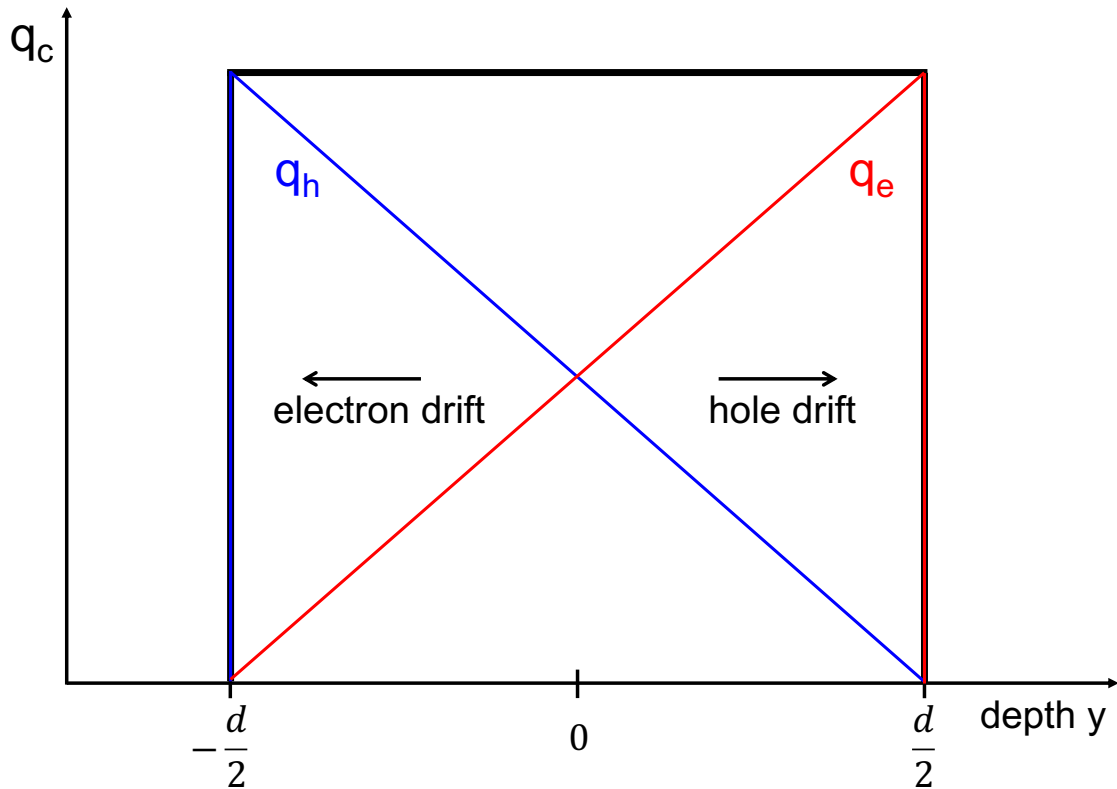
Figure 7.23 – Sketch of the charge collection from electrons q_e and holes q_h and their respective fraction adding to the entire collected charge q_c per depth in the sensor.

four equal parts in z and a difference in the charge collection profile is clearly visible. As a bias voltage 200 V was chosen, as the differences are less pronounced at higher voltages. The same trend is observed for a splitting of the sensor along the x-direction, see Figure 7.25.
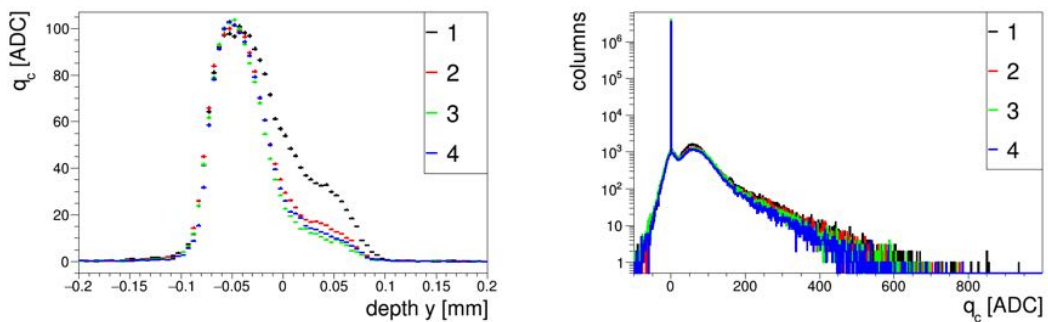
Figure 7.24 – On the left: The collected charge as a function of depth. The sensor with the high proton irradiation is divided in four equal parts in the z-direction. A difference in collected across the sensor is clearly visible. The bias voltage is 200 V. On the right: The corresponding charge histograms.
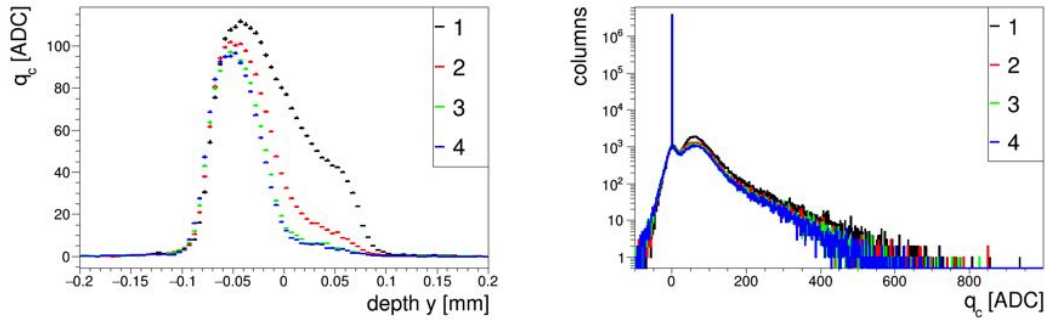
Figure 7.25 – On the left: The collected charge as a function of depth. The sensor with the high proton irradiation is divided in four equal parts in the x-direction. A difference in collected across the sensor is clearly visible. The bias voltage is 200 V. On the right: The corresponding charge histograms.

The coordinates of the beam spot from irradiation were calculated from the vertical beam incidence measurements. To identify how those coordinates translate into the edge-on position the sensor was additionally divided into four quarters, as shown in Figure 7.26.
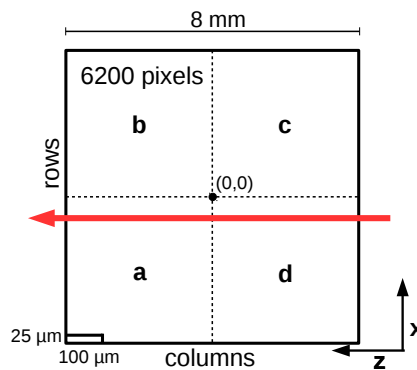
Figure 7.26 – Sketch of the sensor split into quarters (a-d). The red arrow indicates the beam direction.

The charge collected in quarter d is less than the charge collected in any other quarter due to a different fluence and therefore more radiation induced damage. Quarter d is thus assigned to the quadrant with the beam spot position, see Figure 7.27. This also coincides with the lowest fluences being in quarter b where the most charge is collected. This results in a beam spot position from irradiation of (-2.56, 0.60) for the higher irradiated sensor. The x-axis stays the same, the sensor is only tilted until it is edge-on and the former y-coordinate of the sensor is along the beam axis, now z. Depending in which direction the sensor is tilted a factor -1 has to be considered, as the splitting into four parts suggests in this case. For further investigation of the charge collection of the sensor,
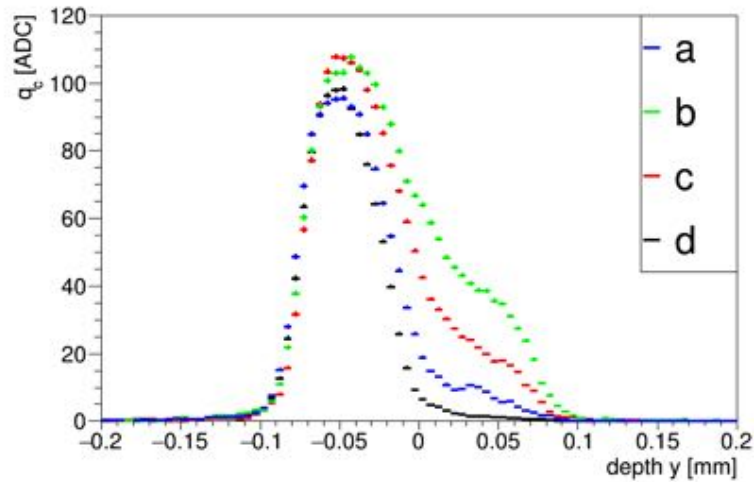
Figure 7.27 – The charge collection profile for the higher proton irradiated sensor split into quarters (a-d) at bias voltage 200 V.

it is therefore divided into multiple areas with different radii around the beam spot center, as indicated in Figure 7.28. Figure 7.29 shows the charge collection profile for different bias voltages for a radius of 2.8 mm around the beam spot center. To see how the charge collection profile varies over the entire sensor, the charge profile was plotted as a function of radius around the beam spot center, see Figure 7.30. The collected charge stems from the areas indicated in Figure 7.28, such that the different radii have no overlap. The radii were chosen such that the areas from which charge is collected all have the same size. However this assumes the beam spot center in the middle of the sensor, which is not the case.

For the lower irradiated sensor the beam spot position has also been determined by splitting the sensor into quarters. Figure 7.31 shows the charge collection profiles for the different sectors of the sensor at 200 V bias voltage, as for the higher irradiated sensor in Figure 7.26. Quarters a and b of the sensor are very similar in charge collection per depth as are quarters c and d. Additionally, the sensor was split into parts in the x- and z-direction to be able to determine the quarter that contains the beam spot center, see Figure 7.32. As a result, the beam spot position of the irradiation was determined as (-0.12, -1.69) for the lower proton irradiated sensor.
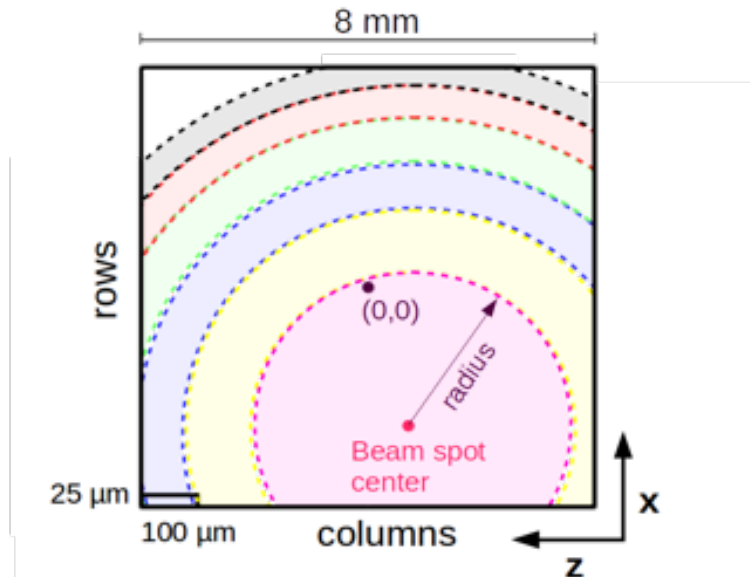
Figure 7.28 – Sketch of the radii across the beam spot center. The colors indicate the different radii, corresponding to Figure 7.30.
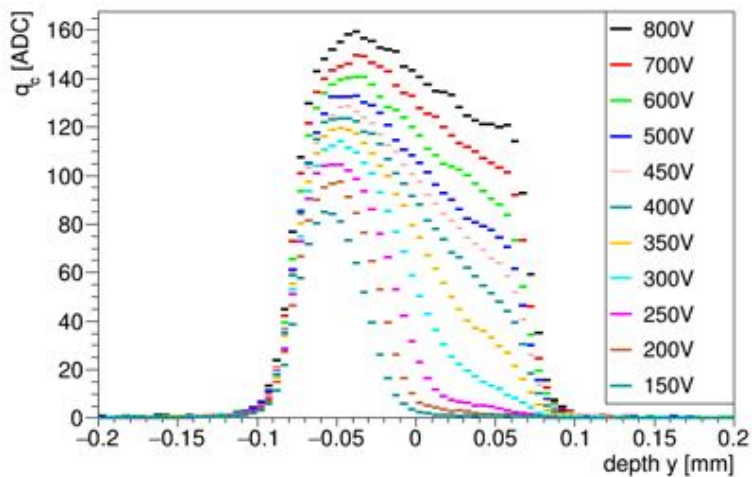
Figure 7.29 – Collected charge as a function of depth for the higher proton irradiated sensor over an area of $2.8\,\mathrm{mm}$ around the beam spot center.
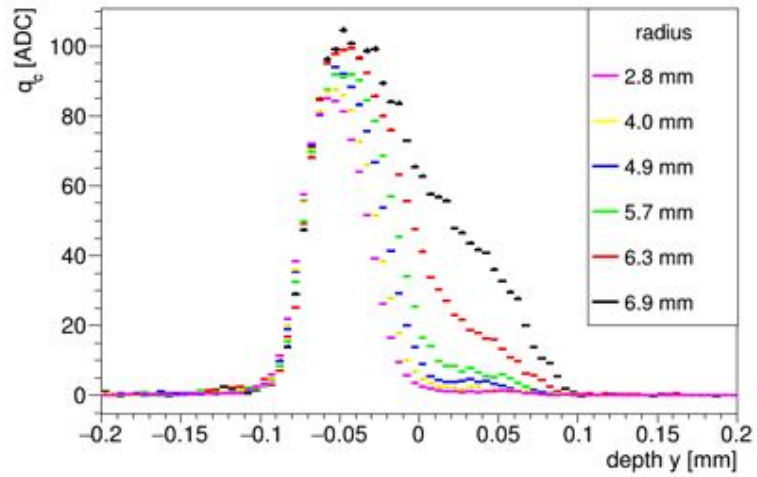
Figure 7.30 – The collected charge as a function of depth for different sectors of the sensor and their respective radii around the beam spot center at 150 V bias voltage.
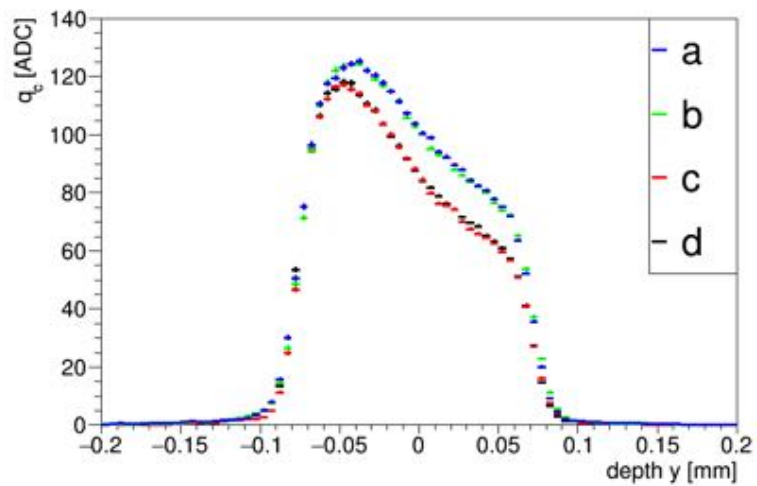
Figure 7.31 – The different sectors of the low proton irradiated sensor and their respective charge collection profile at 200 V bias voltage. Two quarters each have a similar collection.
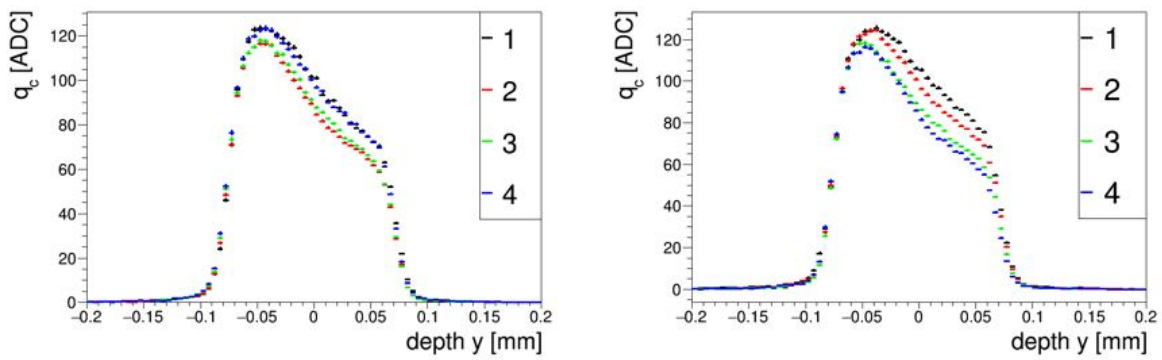
Figure 7.32 – On the left, the low proton irradiated sensor divided into four sectors along the x-axis and on the right divided along the z-axis, both at 200 V bias voltage.

In Figure 7.33 the collected signal is shown as a function of the applied bias voltage for a sensor with $\Phi_p = 3.92 \times 10^{15}\,\mathrm{cm}^{-2}$. The observed smeared box like shape of the signal is still visible for the higher bias voltages, however the signal decreases towards the backside of the sensor. For voltages under $300\,\mathrm{V}$ a wiggle is observed in the second half of the sensor. This can be attributed to the double junction effect, explained in Chapter 2.4.2, which is not very well visible due the small thickness of the sensor. Outside the region of the sensor the collected charge is zero again.

In Figure 7.34 the charge collection profiles are shown for the different fluences on this sensor due to the non-homogeneous irradiation of the sensor. At $800\,\mathrm{V}$ only slight differences in charge collection from the different areas of the sensor are visible. However, a difference in charge collection is clearly visible at bias voltages below $200\,\mathrm{V}$. The collected charge decreases with increasing fluence, especially on the back side of the sensor, the shape of the profile changes significantly. This indicates that the electron trapping increases considerably, while the fluence has only changed from $\Phi_p = 2.52 \times 10^{15}\,\mathrm{cm}^{-2}$ to $\Phi_p = 3.92 \times 10^{15}\,\mathrm{cm}^{-2}$.
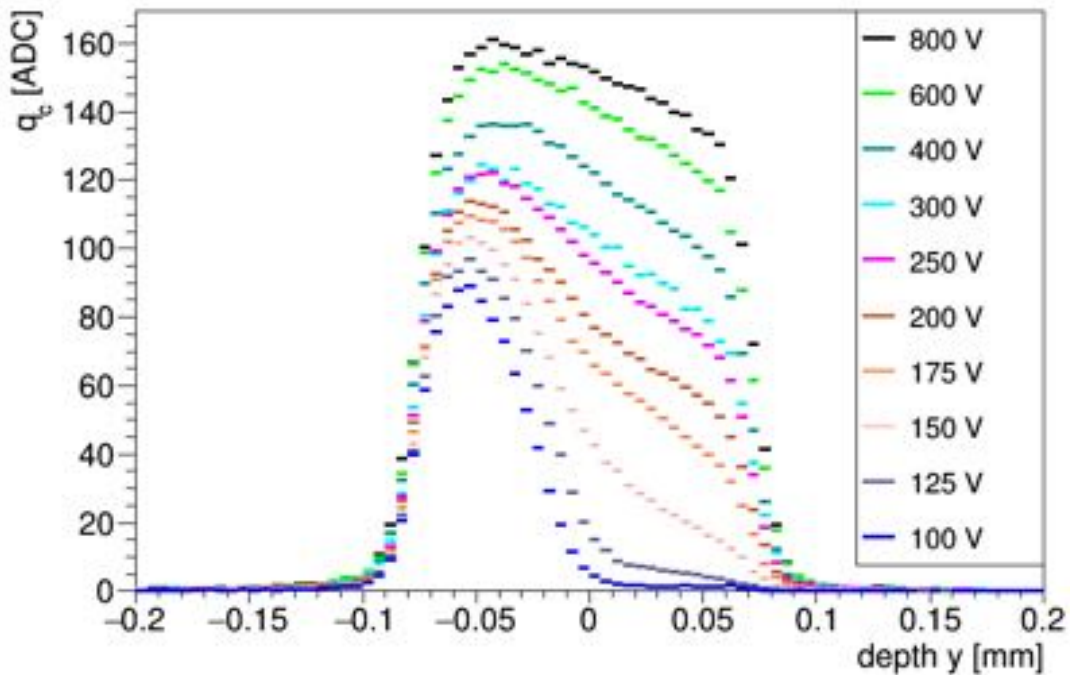
Figure 7.33 – Collected charge as a function of depth in the sensor for different bias voltages. This part of the sensor is irradiated with $\Phi_p = 3.92 \times 10^{15}\,\mathrm{cm}^{-2}$, which corresponds to a $2\,\mathrm{mm}$ radius around the beam spot center from irradiation.

800 V

400 V

250 V

200 V

150 V

100 V
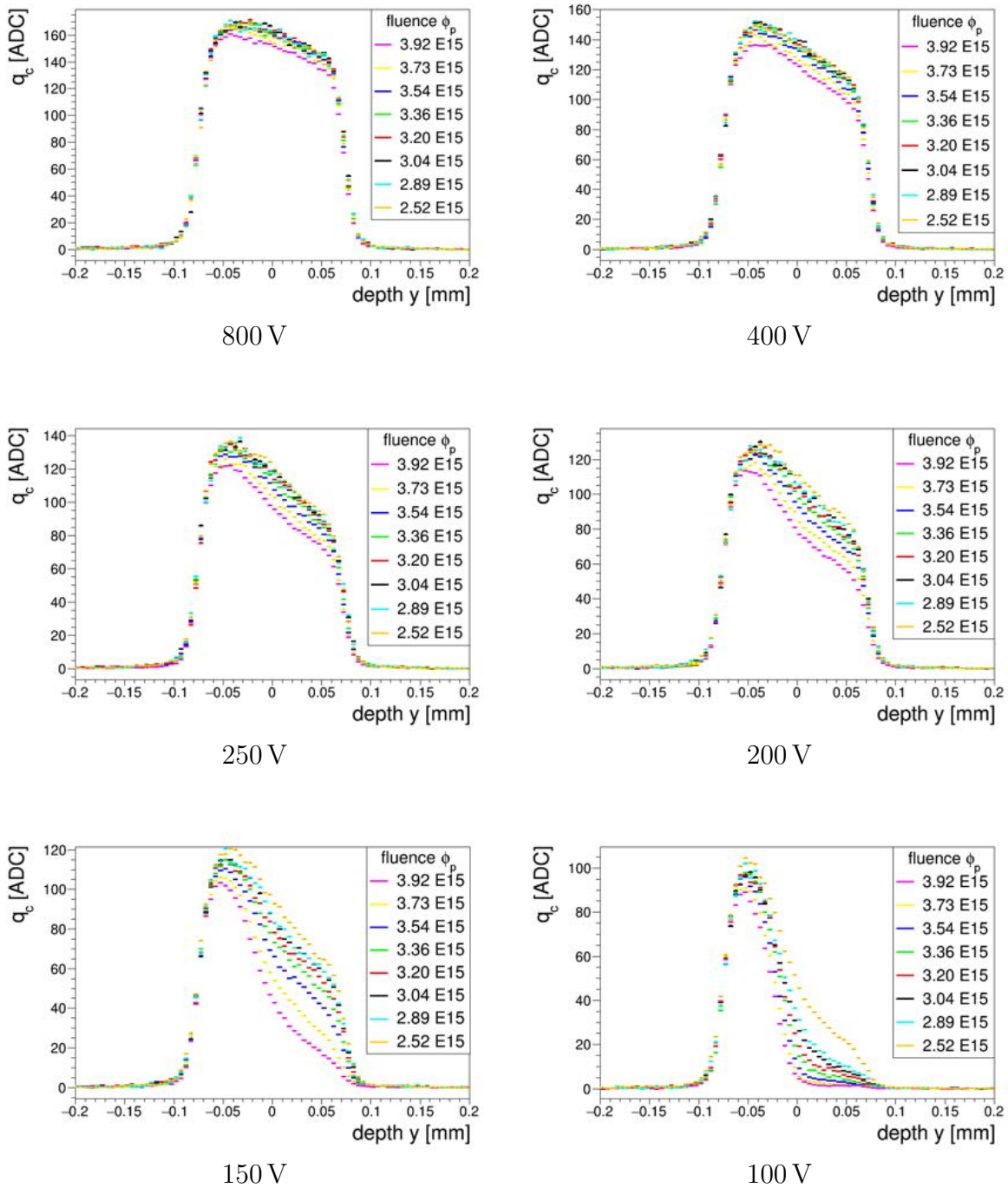
Figure 7.34 – Comparison of the charge collection profiles for the areas of different fluences. At 800 V only small differences in charge collection are visible, for 150 V and under however, the charge collection decreases with increasing fluence. The differences are most pronounced in the charge collection on the backside of the sensor.

The total collected charge as a function of bias voltage for a sensor area irradiated to $\Phi_p = 3.92 \times 10^{15}\,\mathrm{cm}^{-2}$ is shown in Figure 7.35. The increase in collected charge as a function of bias voltage starts to slow down from $600\,\mathrm{V}$ to $800\,\mathrm{V}$. However, for the sensor irradiated to $\Phi_p = 8.68 \times 10^{15}\,\mathrm{cm}^{-2}$ no onset of saturation is visible, the collected charge still increases almost linearly with increasing bias voltage, see Figure 7.36. To see how the total collected charge changes with fluence, the charge collection at $200\,\mathrm{V}$ for the different fluences is compared in Figures 7.37 and 7.38. This is done for each sensor individually as a comparison of the absolute charges between sensors might be misleading due to the different gains. The shapes of the charge collection profiles however are independent of the gain and can be directly compared.
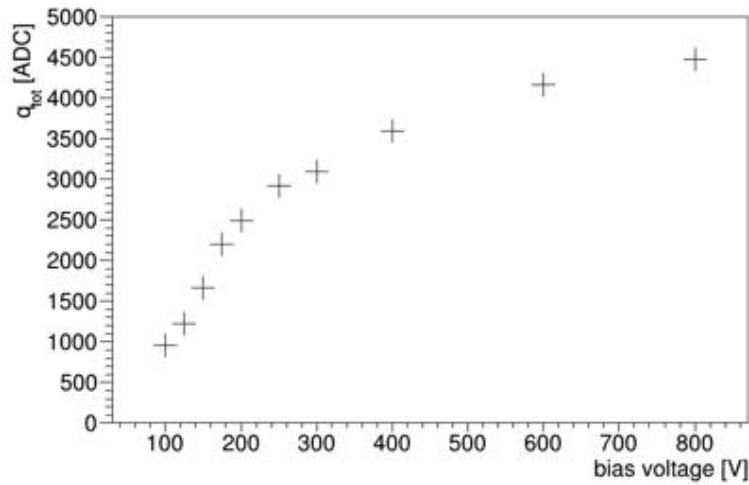
Figure 7.35 – Total collected charge as a function of bias voltage in the sensor irradiated with $\Phi_p = 3.92 \times 10^{15}\,\mathrm{cm}^{-2}$, which corresponds to a $2\,\mathrm{mm}$ radius around the beam spot center.

A comparison with the absolute values of the non-irradiated sensor is not possible due to the uncertain absolute gain of the ROC4SENS, as no calibration of the charge collected by an irradiated sensor to ke can be performed, compare Chapter 6.2.
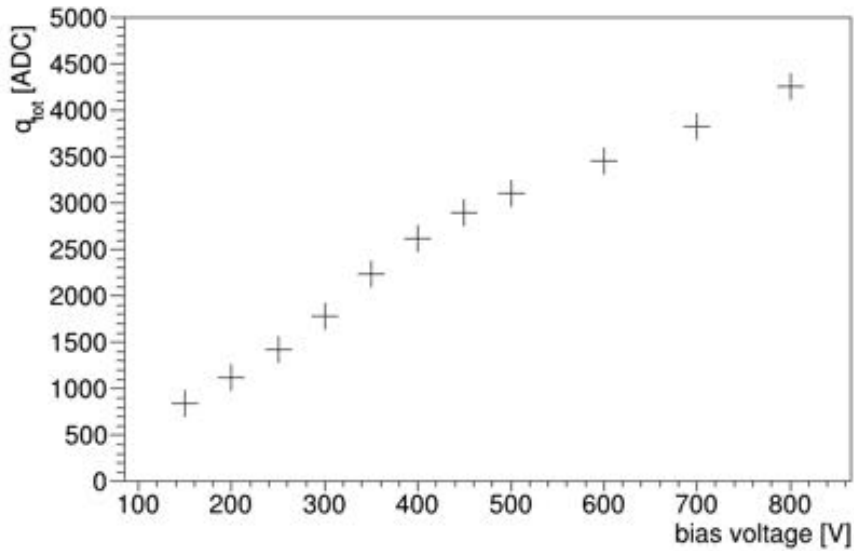
Figure 7.36 – Total collected charge as a function of bias voltage in the sensor irradiated with $\Phi_p = 8.68 \times 10^{15}\,\mathrm{cm}^{-2}$, which corresponds to a $2\,\mathrm{mm}$ radius around the beam spot center from irradiation.
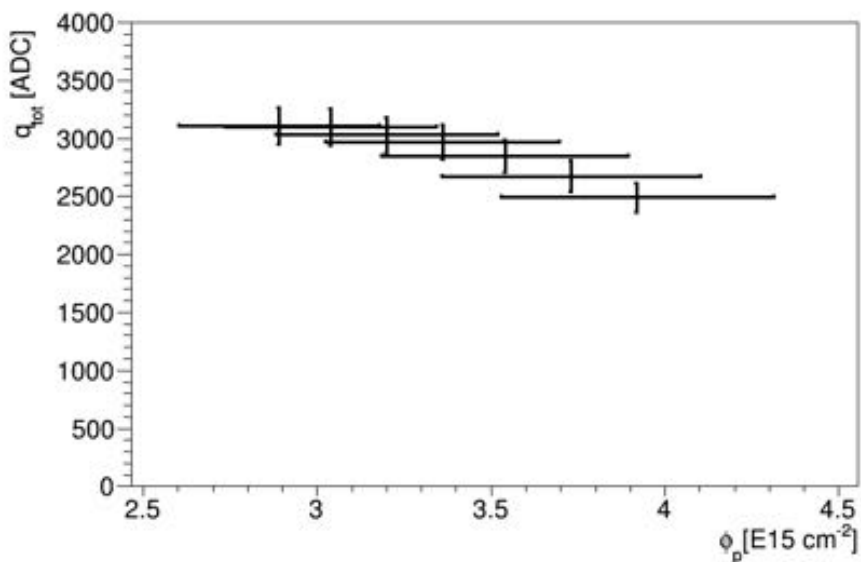
Figure 7.37 – At $200\,\mathrm{V}$ the total collected charge as a function of fluence. An error of 5 percent on the charge and 10 percent on the fluence is assumed.
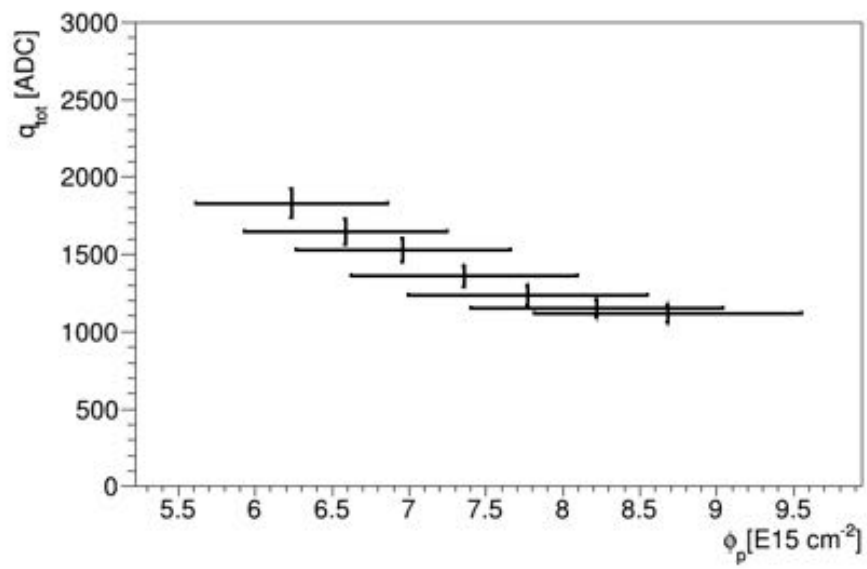
Figure 7.38 – At 200 V the total collected charge as a function of fluence. An error of 5% on the charge and 10% on the fluence is assumed.

7.3.2. Temperature Dependence

To verify the influence of temperature the lower proton irradiated sensor was remeasured at a temperature warmer than $-30°$C. This temperature was determined from lab measurements of the leakage current, as the leakage current increases with temperature, see Chapter 4.4.4. From the measured sensor current, compare Figure 7.39, the leakage current of 20 µA at 400 V bias voltage was used to estimate a temperature of $-18°$C. The value is in between the measurement curves at $-15°$C and $-20°$C of Figure 4.19, therefore an uncertainty of $1°$C on the temperature is assumed.
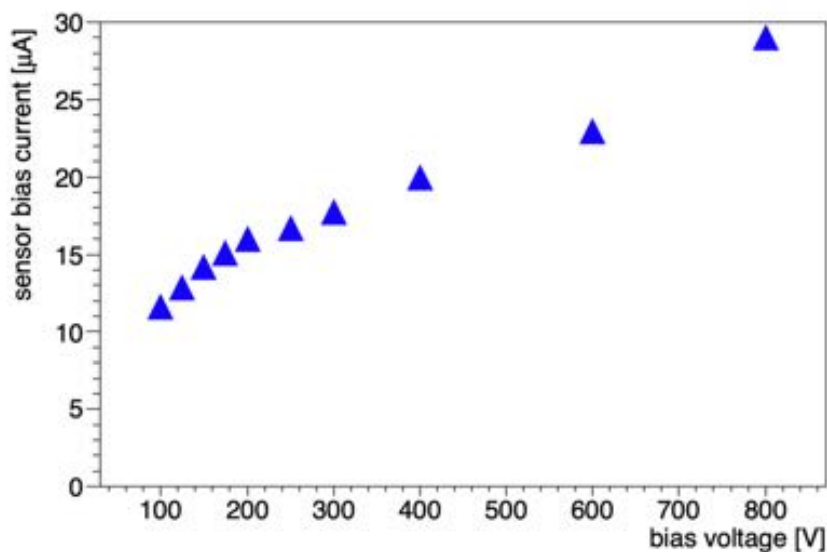
Figure 7.39 – Sensor leakage current for the chip at a warmer temperature. The leakage current of 20 µA at 400 V bias voltage was used to determine the temperature from Figure 4.19.

The response from a test pulse at both temperatures at test beam is shown in Figure 7.40. The RMS of the individual pulse height distributions increases with increasing temperature.

The difference between the temperatures in the charge collection profile for a radius of 2 mm around the beam spot, which corresponds to a fluence of $\Phi_p = 3.92 \times 10^{15}$ cm^{-2} is shown for different bias voltages in Figure 7.41 and Figure 7.42. For bias voltages over 400 V, the shapes are similar for the two temperatures, with the $-18°$C measurement collecting equally less charge at each depth. At 150 V bias voltage the profile shape is visibly different, especially the charge collection from the sensor backside. At 100 V bias voltage however the difference in shape at the backside has vanished.

Figure 7.43 shows the total collected charge at each bias voltage for both temperatures.
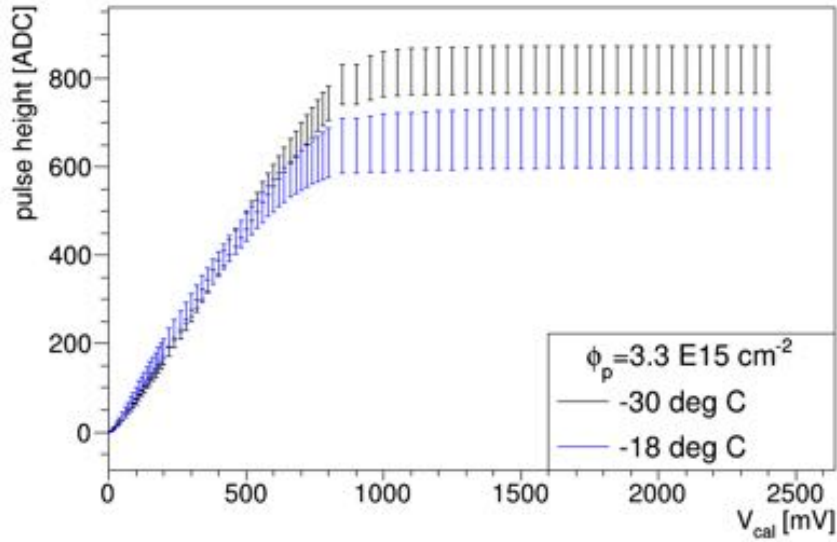
Figure 7.40 – Pulse height distribution of all pixels after pedestal correction as a function of V_{cal} units at hold 40, the displayed error is the RMS of the individual distributions. The RMS of the pixels at $-18°$C (blue) is bigger than for the cooler sample at $-30°$C (black).
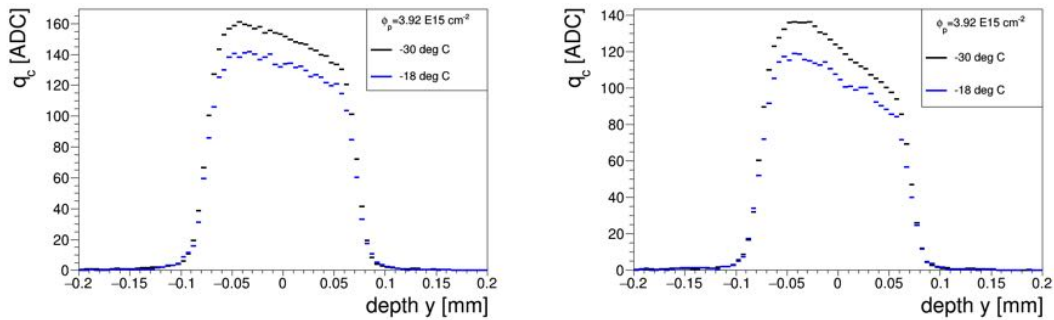
Figure 7.41 – The charge collection profile at $-18°$C (blue) and $-30°$C (black) for different bias voltages: 800 V left and 400 V right. The lower temperature leads to less collected charge but the shape is similar.

The ratio of the two curves is shown in Figure 7.44. The difference in total collected charge is about 15% for all bias voltages above 250 V. For bias voltages between 100 and 200 V the difference is up to 30%, this coincides with Figure 7.42, where it is visible that at this voltage the charge collection at the sensor backside has a completely different shape. However, the difference in gain of the chip which is dependent on leakage current has to be considered when comparing the total collected charge, such that the real loss in charge due to temperature might be less than 15%.

The temperature dependence of the CCE for 200 µm thick MCz n-type sensors for different fluences of 23 GeV protons was investigated by T. Pöhlsen [82]. The charge was generated
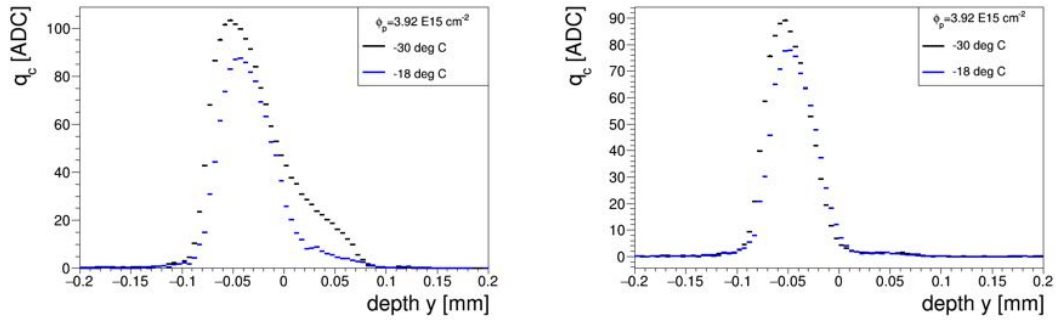
Figure 7.42 – The charge collection profile at −18°C (blue) and −30°C (black) for different bias voltages: 150 V left and 100 V right. For 150 V bias voltage the profile shape is visibly different, especially the charge collection from the sensor backside. For 100 V the shape is again very similar.
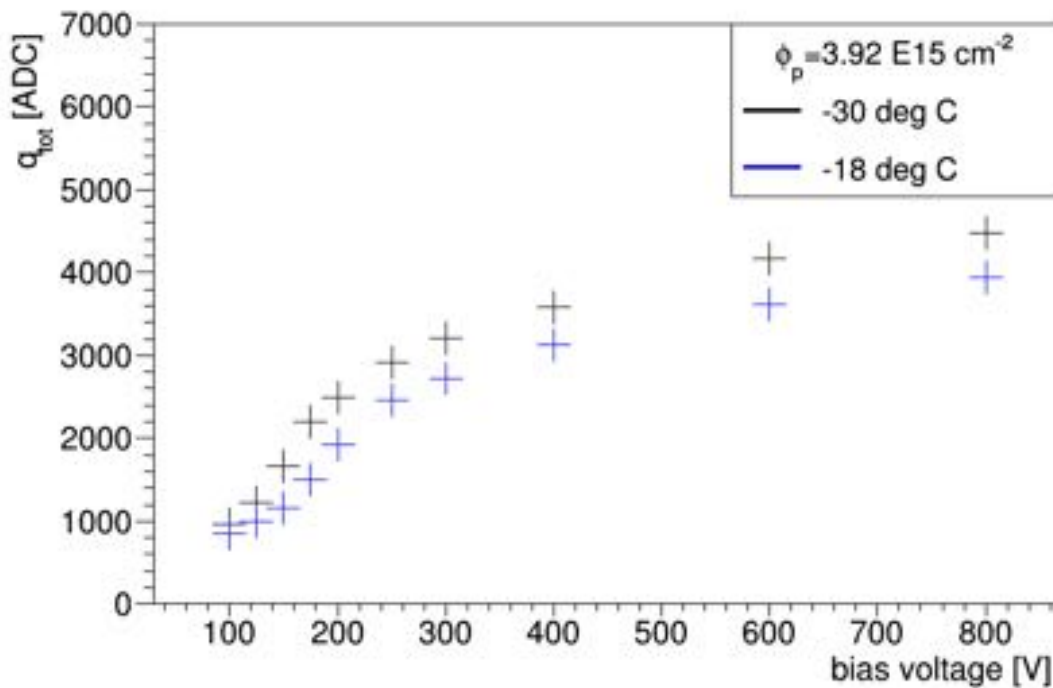
Figure 7.43 – The total collected charge at −18°C (blue) and −30°C (black) for different bias voltages.

using laser light with 1063 nm wavelength and measured at 0°C and −20°C. The results of this analysis are shown in Figure 7.45. The CCE is about 7% higher at −20°C compared to 0°C at intermediate bias voltages for $\Phi_{eq} = 30 \times 10^{15} \text{cm}^{-2}$. For the highest fluence, only a slight difference is visible, however the sign is the same as found in the analysis of this thesis: For lower temperatures the total charge collected increases, these differences
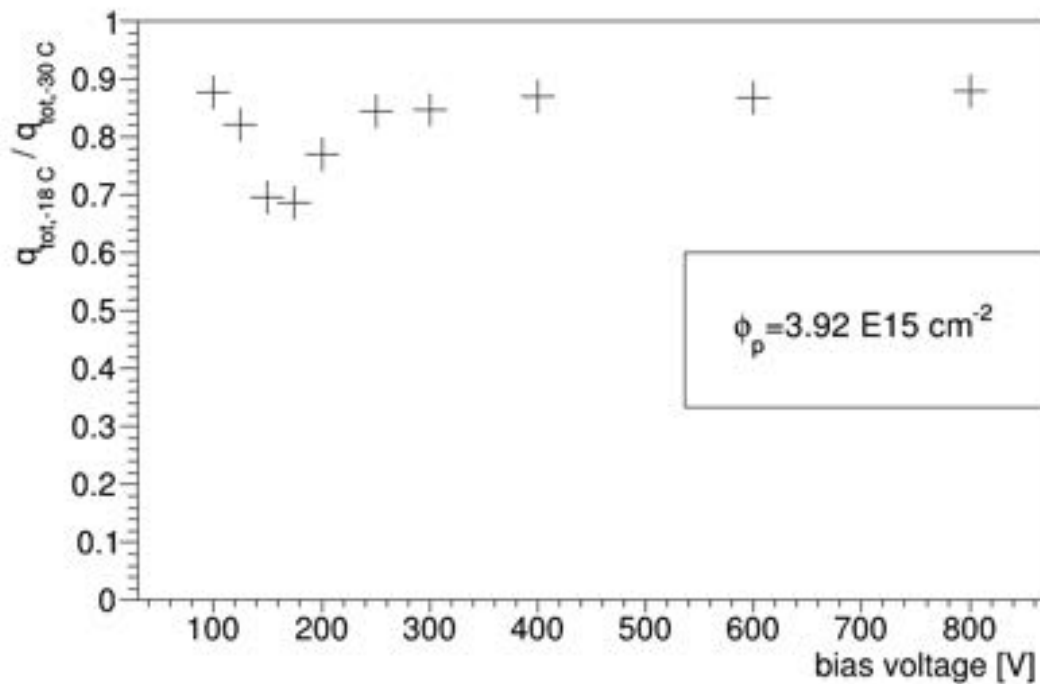
Figure 7.44 – Ratio of the total collected charge at $-18°$C and $-30°$C. On average the total collected charge is 15% less at $-18°$C. For bias voltages of 100 - 200 V the difference is larger.

are less pronounced at lower bias voltages. In general, changes in temperature lead to differences in the current generation, the drift velocity and the detrapping time. In addition, the CCE curves in Figure 7.45 also show, that for a sensor irradiated to $\Phi_{eq} = 13 \times 10^{15}\,\mathrm{cm}^{-2}$ the CCE does not saturate as a function of bias voltage for voltages below 1000 V. The same behavior was previously shown in Figure 7.36 for a sensor irradiated to $\Phi_p = 8.68 \times 10^{15}\,\mathrm{cm}^{-2}$.
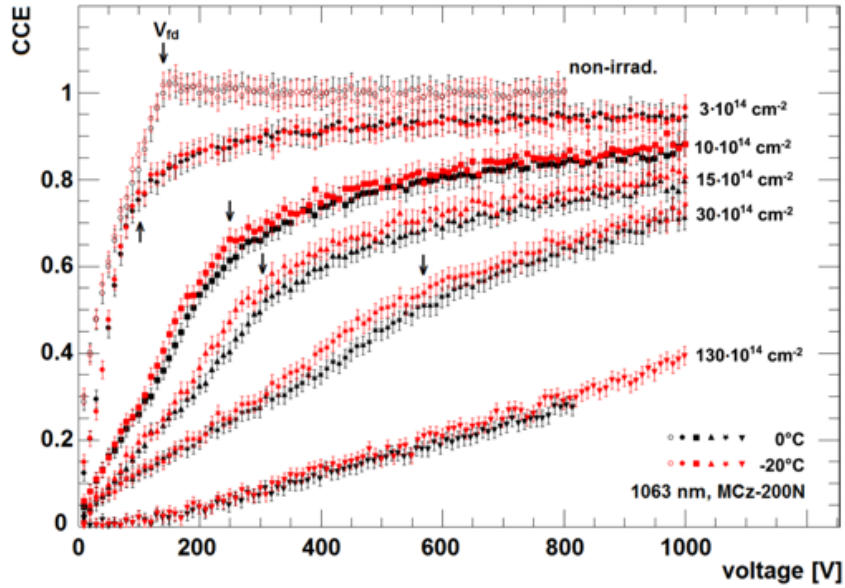
Figure 7.45 – CCE for 200 µm thick MCz n-type sensors for different fluences Φ_{eq} of 23 GeV protons. The measurements were taken at 0°C (black markers) and −20°C (red markers). Figure taken from [82].

7.3.3. Neutron Irradiated Sensors

Four sensors have been irradiated with neutrons, all are float-zone direct-bonded wafer material, the lower fluences are p-stop default and the highest fluence is a p-stop max implant design. The neutron fluences are $\Phi_n = 0.6, 4, 8 \text{ and } 16 \times 10^{15} \text{ cm}^{-2}$.

To check for possible alignment systematics over the sensor area, the sensor irradiated to $\Phi_n = 16 \times 10^{15} \text{ cm}^{-2}$ was divided in x and z, compare Chapter 7.1.3. The corresponding charge collection profiles at 250 V bias voltage are shown in Figure 7.46. No systematic difference in the x-direction and only a small difference in gain in the z-direction due to different column amplifiers was observed.

To check the influence of the chosen signal definition, compare Chapter 7.1.2, Figure 7.47 shows the Landau distribution of the signal in black and the remaining background in red for a sensor irradiated to $\Phi_n = 0.6 \times 10^{15} \text{ cm}^{-2}$ at 600 V bias voltage. It is visible that no significant amount of charge of a neutron irradiated sensor was lost due to the chosen signal definition.

The lowest neutron fluence is the lowest equivalent fluence tested in this analysis, the expected signal degradation is therefore expected to be the least. A bias voltage scan up to 600 V is shown in Figure 7.48a. For this fluence the box like shape of the non-irradiated sensor at full depletion is reached at 600 V, with only a small decline towards the back
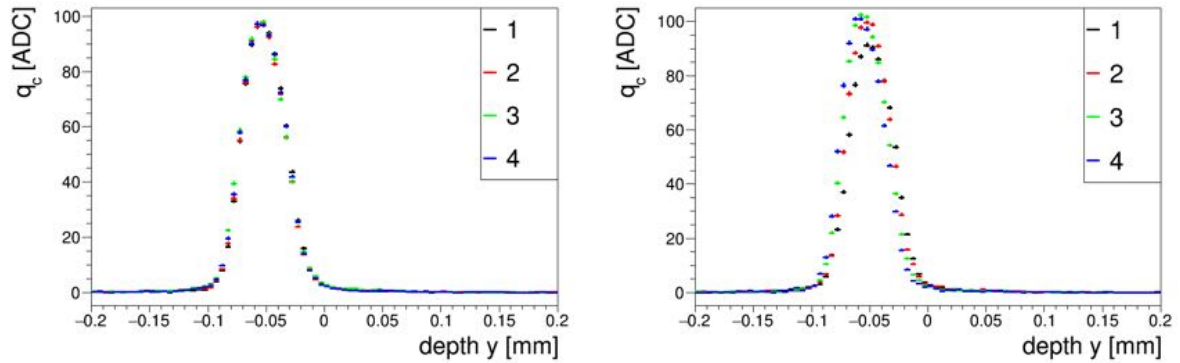
Figure 7.46 – On the left: The charge collection for the sensor $\Phi_n = 16 \times 10^{15}\,\text{cm}^{-2}$ at 250 V bias voltage, divided into four equal parts in the x-direction. No systematic difference is visible. On the right: The sensor divided into four equal parts in the z-direction. A small difference in gain is visible, as all columns have an individual column amplifier.
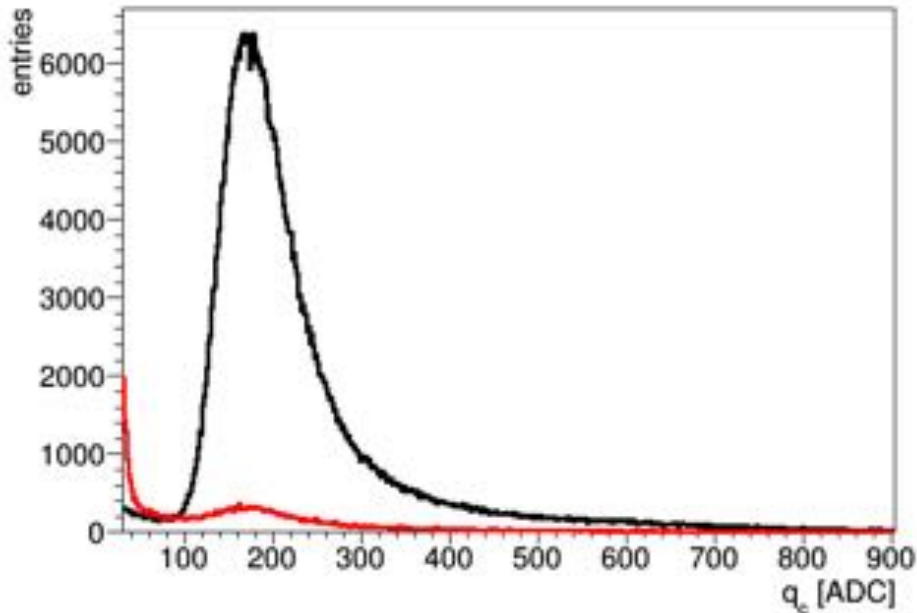
Figure 7.47 – The Landau distribution of the chosen signal, defined as the sum of three pixels, is shown in black and the charge of the remaining pixels in the ROI in red. The sensor is irradiated with $\Phi_n = 0.6 \times 10^{15}\,\text{cm}^{-2}$ and the bias voltage is 600 V.

side. For smaller bias voltages the typical steep decline towards the backside is dominant. Figure 7.48 shows the bias scans of all neutron fluences and allows for a shape comparison. The aforementioned box like shape is only visible at $\Phi_n = 0.5 \times 10^{15}\,\text{cm}^{-2}$, while for $\Phi_n = 4 \times 10^{15}\,\text{cm}^{-2}$ the drop in charge at the backside is still small, at $\Phi_n = 8 \times 10^{15}\,\text{cm}^{-2}$ the charge collected at the backside is only about 50% of the charge collected at the front. The bias scan of the highest neutron fluence is shown in Figure 7.48d. For 800 V the sensor does not collect charge over the entire sensor any more. There is also a very

steep decline in column signal towards the backside of the sensor for all bias voltages. Compared to the proton irradiated samples, there is no indication of a double junction. At lower bias voltage, all fluences exhibit the same shape of charge collection profiles, a steep decline towards the backside of the sensor.
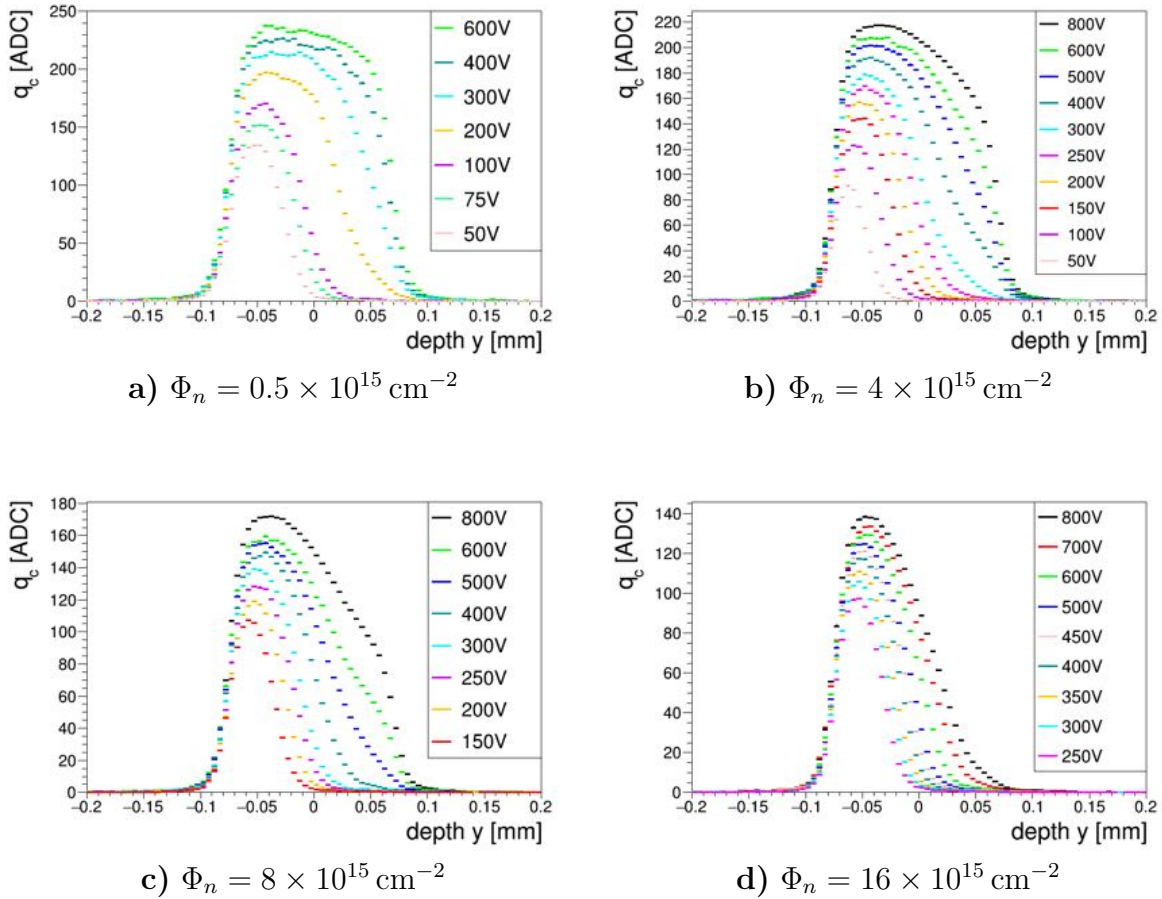
Figure 7.48 – Collected charge as a function of depth in the sensor for different bias voltages. The colors indicate the same bias voltage for all fluences if all were measured at that voltage. The shape of the collected charge profile differs for all fluences. For $\Phi_n = 0.5 \times 10^{15} \, \mathrm{cm}^{-2}$ (a) at 600 V, the signal shows a box like shape, with a small slope toward the backside. For $\Phi_n = 16 \times 10^{15} \, \mathrm{cm}^{-2}$ (d) the charge is no longer collected over the entire sensor depth at 800 V.

The total collected charge as a function of bias voltage is shown in Figure 7.49. The total collected charge is determined by integrating according to Equation 43. At 600 V the collected charge for the sensor irradiated to $\Phi_n = 0.6 \times 10^{15} \, \mathrm{cm}^{-2}$ starts to saturate, therefore the sensor was not measured at a higher bias voltage. An onset of saturation is also visible for the sensor irradiated to $\Phi_n = 4 \times 10^{15} \, \mathrm{cm}^{-2}$ at 800 V, while for the higher

fluences the total collected charge is still increasing. However, operating at a higher bias voltage was not possible in this measurement setup.
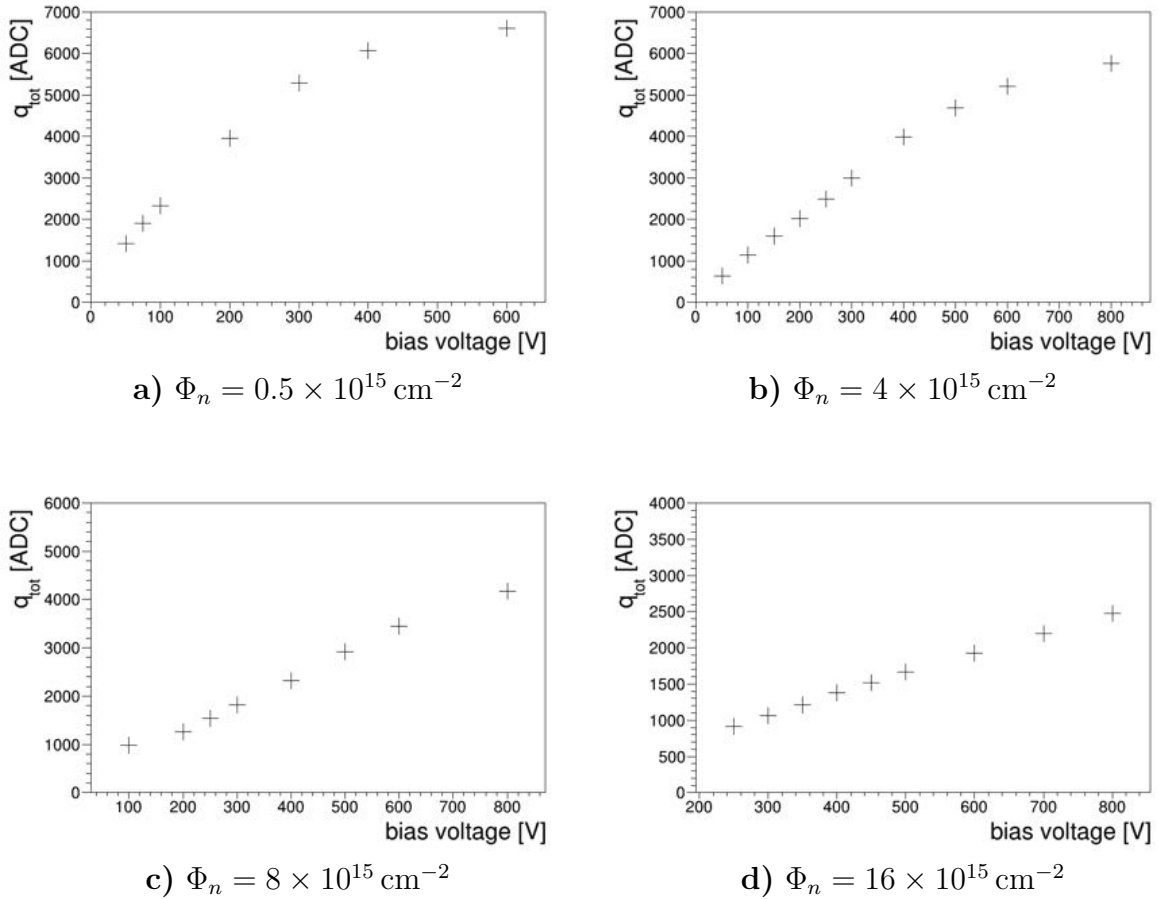
Figure 7.49 – Total collected charge as a function of bias voltage for all neutron irradiated sensors. For $\Phi_n = 0.5 \times 10^{15}\,\mathrm{cm}^{-2}$ (a) at $600\,\mathrm{V}$, the collected charge begins to saturate. For the higher fluences no saturation is visible, the total collected charge is increasing with increasing bias voltage.

For a more detailed comparison of the charge collection, the charge collection depth is shown as a function of fluence in Figure 7.50. The collection depth or active thickness of the sensors is obtained from the profiles from Figure 7.48 according to Equation 40. At a bias voltage of $800\,\mathrm{V}$ or $600\,\mathrm{V}$ in case of the lowest fluence, when comparing the effect of the different irradiations, only for the highest fluence a significant decrease in charge collection depth is visible. The error on the fluences is assumed as 10% or 50% for the lowest fluence, as the determination here was less precise, compare Chapter 4.3.2. At $300\,\mathrm{V}$ bias voltage the expected decrease of charge collection depth with increasing fluence is visible. This change in charge collection depth with increasing sensor fluence

needs to be taken into account for studies on the sensor resolution, as the optimal angle for charge sharing shifts towards larger angles for a smaller depth ($\tan \phi \sim \frac{1}{d}$).
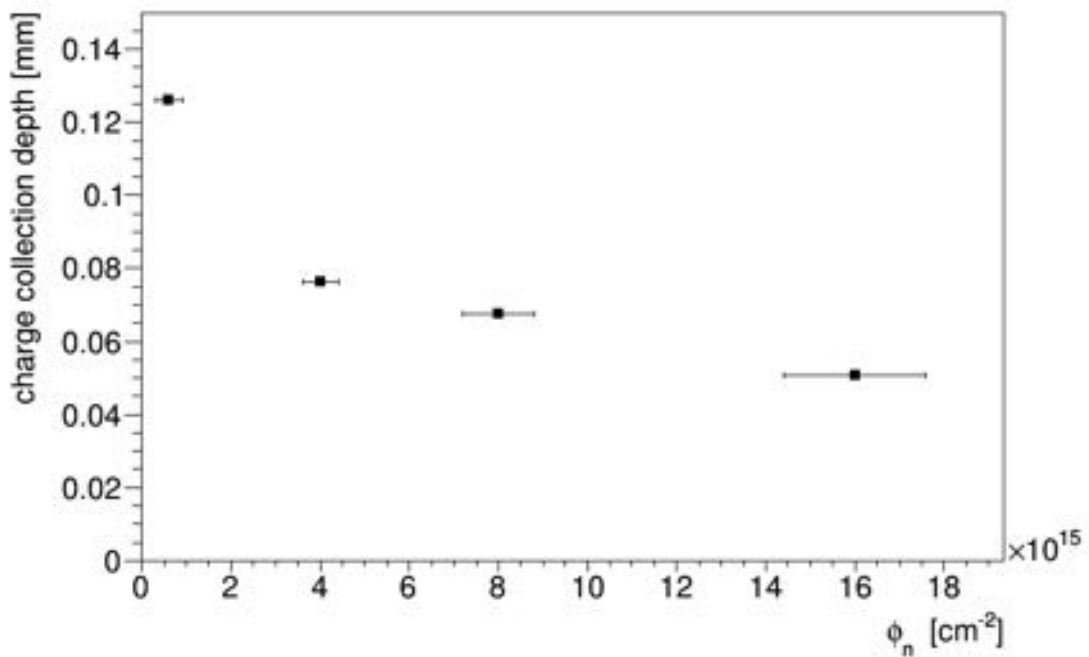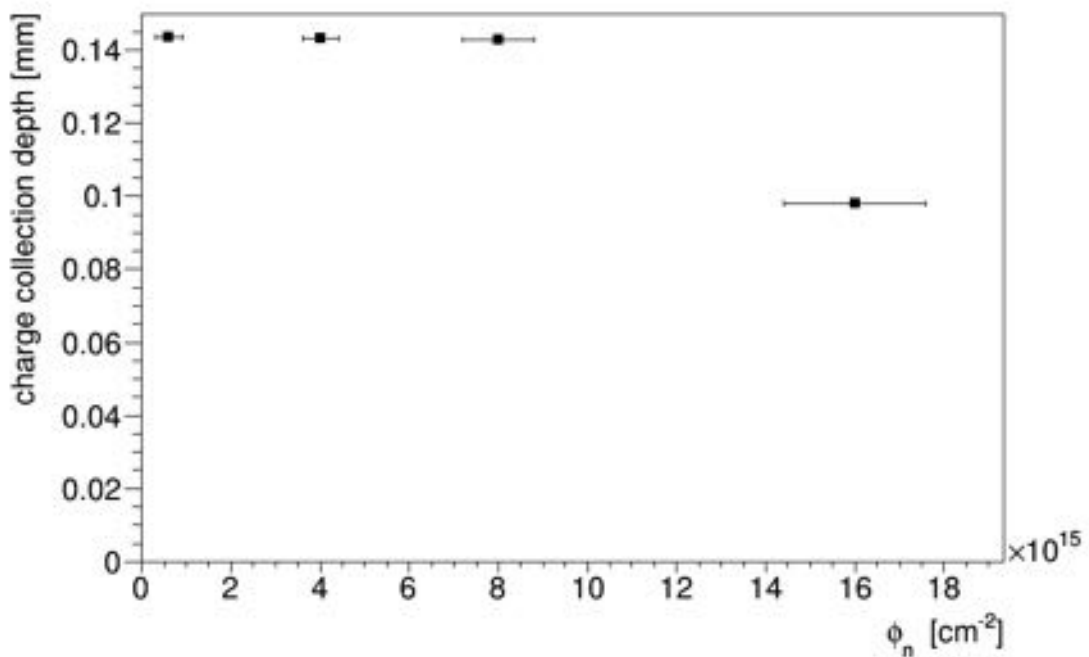
Figure 7.50 – The charge collection depth as a function of fluence for all neutron irradiated samples. The error on the fluences is conservatively assumed to be 10%, only for the lowest fluence, it is assumed to be 50%. On top: All samples were measured at a bias voltage of 800 V, except for the lowest fluence, which was measured only up to 600 V. Only for the highest fluence a significant decrease in charge collection depth is visible. At the bottom: All samples measured at 300 V bias voltage. The charge collection depth decreases with increasing fluence.

7.3.4. Comparison of Irradiation Particles

In literature it has been shown, that the radiation damage induced by neutrons and protons is different. Irradiation with neutrons leads predominantly to defect clusters and high-energetic charged particles like protons lead to a mix of point and cluster defects [83]. How these microscopic differences translate into differences in the detector's performance and charge collection however is still under investigation. A well studied difference between the particles is the generation of donors. For example the introduction rate of the E(30K) defect, an electron trap, is larger by a factor of 6 for proton irradiations than for neutron irradiations [84]. The introduction rates for different defects from Thermally Stimulated Current (TSC) measurements are shown in Table 8, they were kindly provided by E. Fretwurst. More information on the TSC setup and measurement can be found in [84].

Defects	**23 GeV Protons** g_{int} [cm^{-1}]	**Neutrons** g_{int} [cm^{-1}]
E(30K)	6.5×10^{-2}	1.1×10^{-2}
Sum(V_n)	1.4	1.1

Table 8 – Introductions rates from TSC spectra for 23 GeV protons and neutrons, from E. Fretwurst (UHH). The generation rate of the E(30K) defect is larger by a factor of 6 for protons than for neutrons.

To see how this microscopic defect influences the charge collection of the sensor, the impact of the shallow defect E(30K) on the electric field has been simulated using the Hamburg Penta Trap Model, which is explained in more detail in Chapter 8.1. The simulation of the electric field as a function of depth in the sensor for an equivalent fluence of $\Phi_{eq} = 4 \times 10^{15}$ cm^{-2} is shown in Figure 7.51.

On the left side is the electric field for proton irradiation, which shows the double junction. On the right side the electric field for neutrons is very high at the n^+ side and the sensor appears only partially depleted. With electric fields this high the generation of avalanches is possible. This shape of the electric field has also been extracted from Edge Transient Current Technique (Edge-TCT) measurements on neutron-irradiated strip sensors [85].

A comparison between the different irradiations at a bias voltage of 800 V, only $\Phi_n = 0.6 \times 10^{15}$ cm^{-2} at 600 V and the non-irradiated sensor at 120 V can be seen in Figure 7.52. The temperature for all measurements was the same at -30 C. While an absolute charge calibration is still outstanding, the shapes of the charge collection profiles however
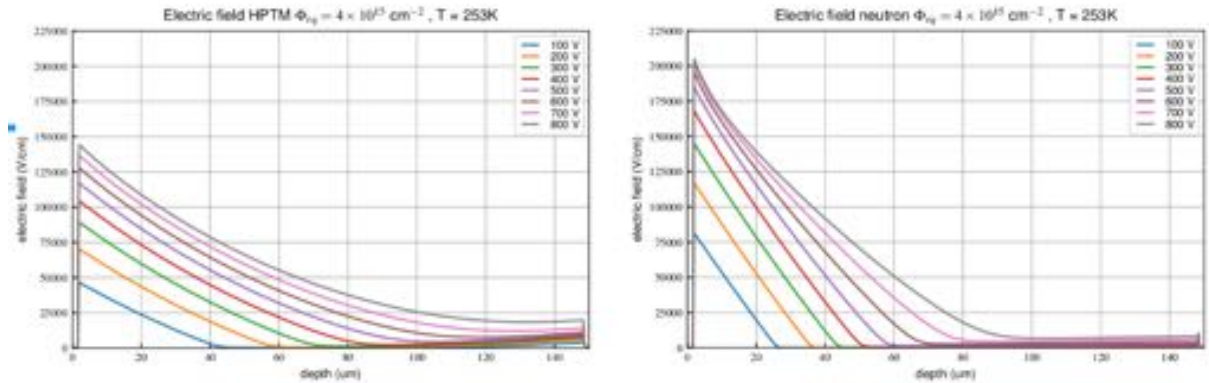
Figure 7.51 – The electric field as a function of depth in the sensor for protons (left) and neutron (right) with an equivalent fluence of $\Phi_{eq} = 4 \times 10^{15}\,\mathrm{cm}^{-2}$. For protons a double junction is visible, the neutron irradiated sensor is only partially depleted, with a high electric field at the n^+ side. Figure from J. Schwandt.

are independent of the different chip gains. The feature of the gain spread between different chips is explained in Chapter 6.3. For neutron irradiated sensors, the sensor half away from the implants shows a steep decline in charge collection compared to the proton samples, where charge is collected over the entire sensor depth.

This difference in charge collection profile shape between neutrons and protons corresponds to the simulation of the different electric fields in the sensor, where the neutrons also exhibit a steeper decline towards the backside.
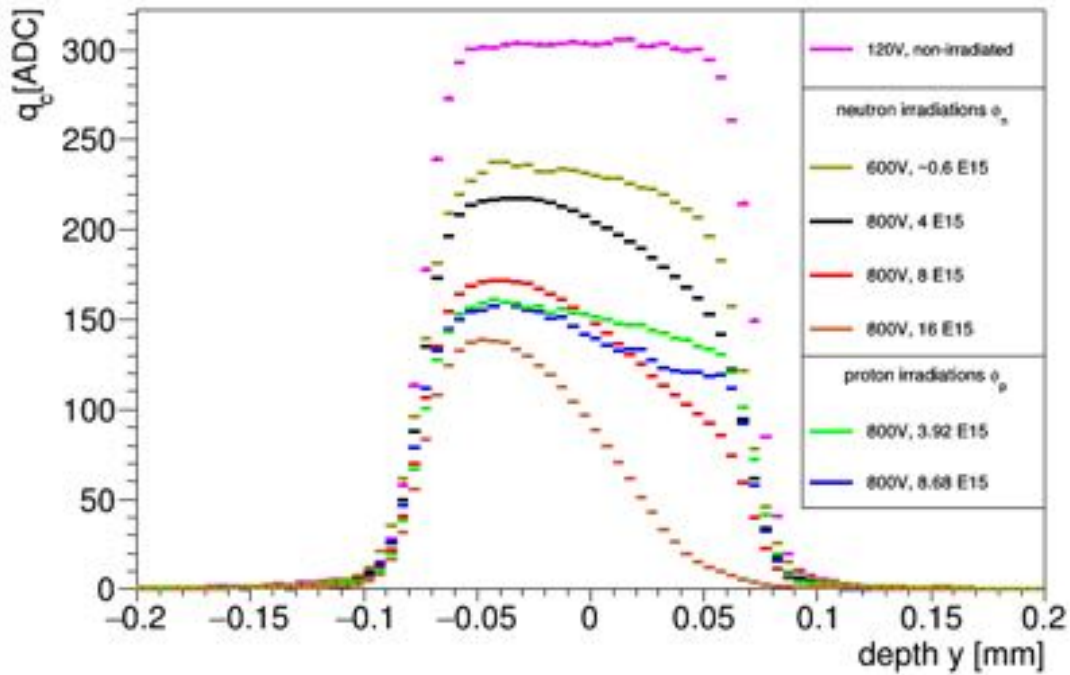
Figure 7.52 – Collected charge as a function of depth in the sensor for all fluences. The colors indicated the irradiation type and bias voltage. The neutron irradiated sensors show a steeper decline in charge towards the backside of the sensor compared to the proton irradiated sensors.

7.4. Radiation Damage of Silicon Sensors: Comparison to Literature

Silicon sensors have been studied intensively over the past decades. However the relation between microscopic defects and the macroscopic detector performance is not yet entirely understood nor theoretically predicted for the higher irradiated sensors with $\Phi_{eq} > 5 \times 10^{15}\,\mathrm{cm}^{-2}$. This chapter aims to give an overview of previous studies performed to understand the effects of radiation damage on the charge collection of silicon sensors. Most comparison are done under the NIEL Hypothesis, explained in Chapter 2.4.3. However, it was found that the generation of point defects does not scale with NIEL and is indeed dependent on particle type [86]. From the investigation of proton irradiation with different energies it was found that there is a correlation between the leakage current and the concentration of three deep defects (namely the V2, V3 and H(220K) defects). At least five defects are found to be responsible for the space charge, with positive contributions from the E(30K) and B_iO_i defects, or negative contributions from three deep acceptors H(116K), H(140K) and H(152K) [87].

7.4.1. ATLAS Phase II Pixel Sensors

The ATLAS Phase II pixel sensors have $50 \times 50\,\mu m^2$ pixel cells bonded to ATLAS FE-I4 readout chips with a standard pixel pitch of $250 \times 50\,\mu m^2$. With the Edge-TCT method, where infrared light from a sub-ns pulsed laser is focused to a μm-size spot and scanned across the cut edge of a sensor, the charge collection of the sensors is investigated. Electron-hole pairs are hereby generated along the light beam in the sensor, more detailed information on this technique can be found in [88]. The absolute value of the induced current is dependent on the exact laser focus and power, as well as the surface properties of the sensor edge, leading to a comparability of charges only within one measurement and not for different sensors [89]. The sensors investigated also have an active thickness of $150\,\mu m$. They were measured at $-20°C$ for irradiations with neutrons of $\Phi_{eq} = 5$ and $10 \times 10^{15}\,cm^{-2}$. An example of the charge collection profile obtained from Edge-TCT for the higher fluence is shown in Figure 7.53. It is observed that charge is collected over the entire sensor for all bias voltages. This is accredited to the electric field being present in the entire detector volume already at low bias voltages, which is explained by space charge polarization and low free carrier concentration in highly irradiated material [89].
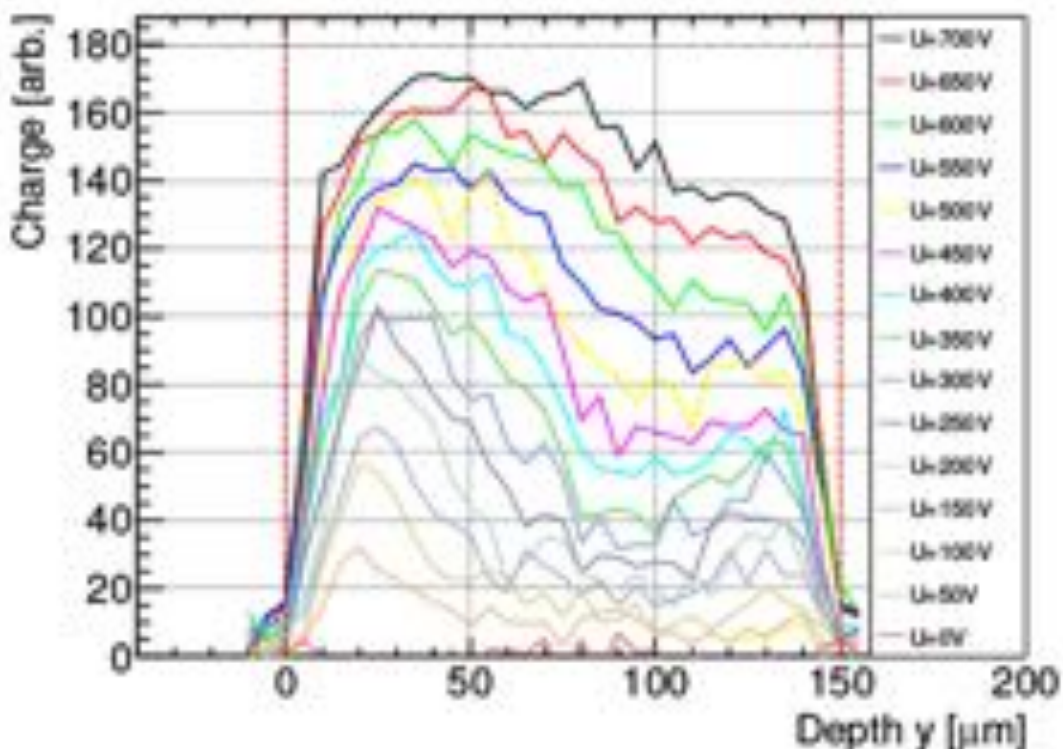
Figure 7.53 – The collected charge as a function of depth in the sensor for a sensor irradiated with $\Phi_{eq} = 1 \times 10^{16}\,cm^{-2}$ with different applied bias voltages, from [89].

The difference between the ATLAS sensors and the sensor investigated in this thesis are

summarized in Table 9. While sensor type and irradiation are basically the same, the measurement methods are conceptionally different. For Edge-TCT, the sensor edge has to be smooth and the method is highly dependent on the surface properties of the sensor. An infrared laser with a beam diameter of 8-12 µm is used and the laser beam is scanned along the sensor depth and the long pixel pitch. The collected charge depends strongly on the integration time. Contrary to edge-on analysis, where the beam enters at different positions in the pixel, the focus of the laser beam is focussed at a single position. In addition, the ATLAS sensors have a full depletion around 30 V which means they have considerably lower doping concentration of the bulk region than the sensors used in this analysis. Thus, it is expected that the charge collection saturates earlier for the ATLAS sensors also after irradiation. However, for the highest neutron fluence the charge is still increasing at bias voltages above 700 V for both measurement methods. In the Edge-TCT measurements the double junction effect is observed. This was not observed for the data analyzed from neutron irradiated sensors in this thesis, as shown in Figure 7.48. However, due to the different pixel sizes, the weighting fields of both sensors are different and thus their charge collection profile cannot directly be compared.

	ATLAS Phase II pixel sensors	CMS Phase II pixel sensors
sensor type	n^+p	n^+p
material	CiS4 [89], [90]	FDB
thickness	150 µm	150 µm
pixel size	$50 \times 50 \,\mu m^2$	$25 \times 100 \,\mu m^2$
irradiation particle	neutrons	neutrons
fluence	$\Phi_{eq} = 5, 10 \times 10^{15} \, cm^{-2}$	$\Phi_{eq} = 3.6, 7.2, 14.4 \times 10^{15} \, cm^{-2}$
measurement method	Edge-TCT	Edge-on in test beam
temperature	$-20°C$	$-30°C$
observations:		
double junction	yes	no
full depletion at	10 - 30 V [91]	70 V

Table 9 – Comparison of the sensor and measurement characteristics of the ATLAS Phase II pixel sensors and the CMS Phase II pixel sensors investigated in this analysis.

7.4.2. Strip Sensors

Further insight into the effects of radiation damage by reactor neutrons has been studied using n$^+$p-strip detectors. More information on the working principle of strip sensors can be found in [88]. Using Edge-TCT, velocity profiles of strip sensors with an active thickness of 285 µm have been obtained. From these a double peaked electric field for neutron irradiation of $\Phi_{eq} = 1 \times 10^{16}$ cm^{-2} has been derived [85]. The resulting electric field profiles for different bias voltages are shown in Figure 7.54. The resulting electric fields show a steep decline towards the backside and only a small double junction for this thickness. The steep decline on the front side is accordance with the decline in the charge collection profiles in this analysis. Due to the smaller thickness of the sensors used in this analysis and the track resolution it is possible that such a small double junction cannot be detected with the edge-on beam measurements. Furthermore the weighting potentials for strips and pixel sensors are different.
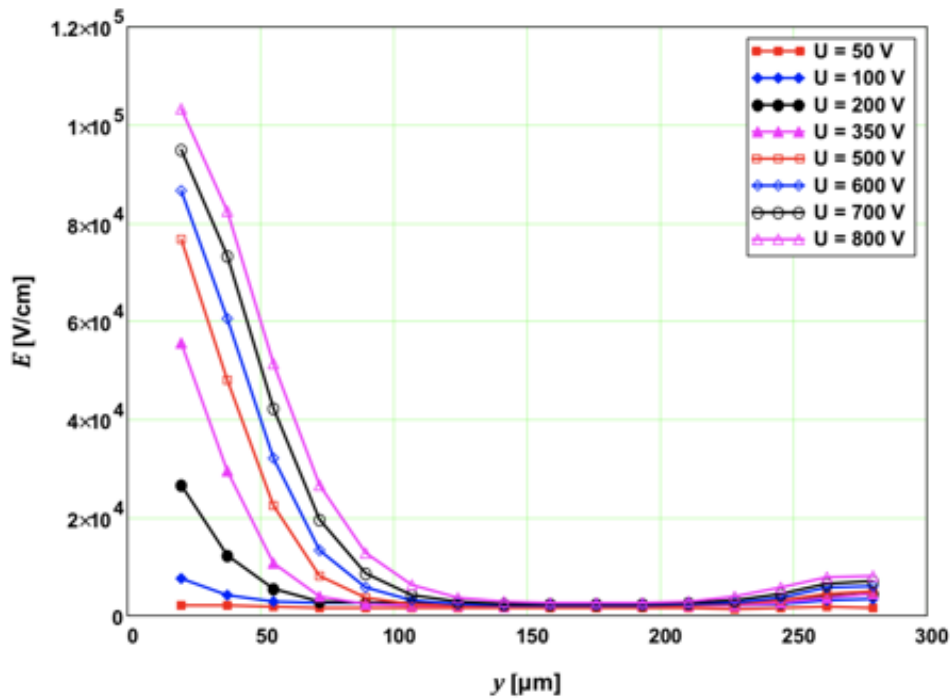
Figure 7.54 – The electric field as a function of applied reverse bias voltage for strip sensors irradiated to $\Phi_{eq} = 1 \times 10^{16}$ cm^{-2}, from [85].

From the electric field the total charge carrier density N_{tot} as a function of sensor depth [85] can be calculated as

$$N_{tot}(y) = \frac{\mathrm{d}E(y)}{\mathrm{d}y} \cdot \frac{\epsilon_{Si}}{q_0} \quad . \tag{45}$$

N_{tot} can be positive or negative, the resulting distributions are shown in Figure 7.55.

These distributions are expected since the electrons are collected at y=0 and move in this direction, resulting in an excess of electrons at low y and vice versa for the holes. The change in sign happens approximately in the middle of the sensor, with the maxima at the position of the electrodes.

The reason for the existence of two space charge regions is the diffusion of carriers from the highly doped regions into the poorly doped bulk, assisted by flushing out the free carriers by the electric field in the front, reverse biased n^+p junction [92]. At the backside pp^+ junction the SCR balances out field currents and diffusion.
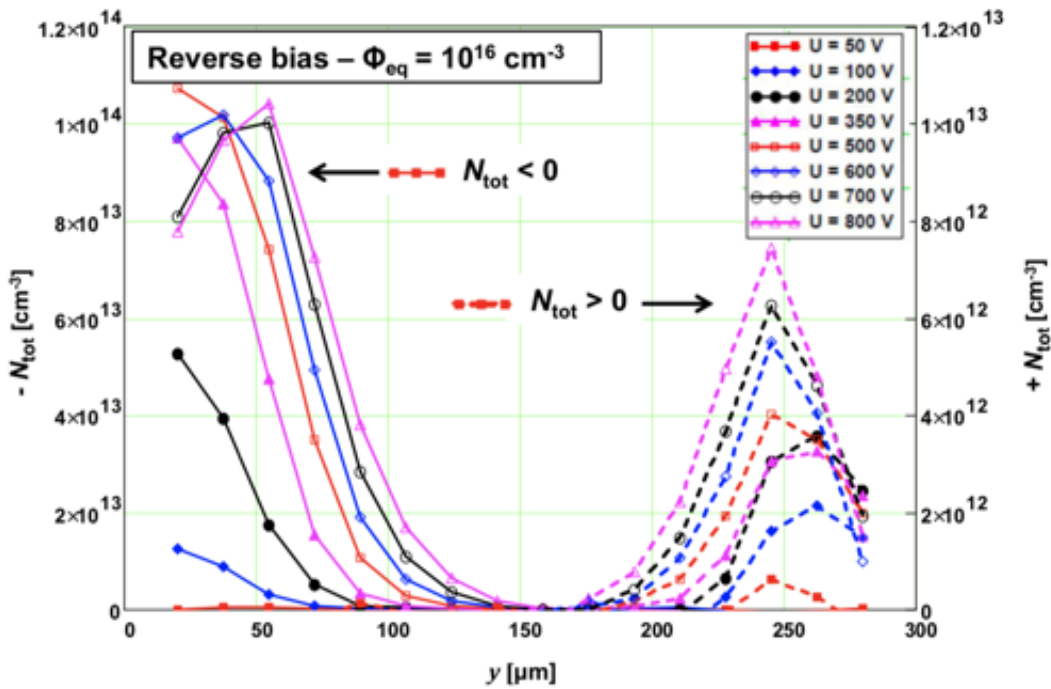
Figure 7.55 – The total charge carrier density distributions $N_{tot}(y)$, obtained from the derivative of the electric field for sensors irradiated with $\Phi_{eq} = 1 \times 10^{16}$ cm^{-2}. The dashed lines at higher y values correspond to a positive $N_{tot}(y)$ and the solid lines at lower y values correspond to a negative $N_{tot}(y)$, from [85].

In another study, for the same sensors the electric field obtained from the velocity profiles was parameterized by a simple model assuming constant total effective space charge at the junction and at the back electrode. It was shown that the assumption of a constant N_{tot} with increasing fluence describes the evolution of the SCR at the junction. The introduction rates of effective acceptors show saturation at the high fluence end [92]. For pion irradiated detectors a more uniform and symmetric velocity profile compared to neutron irradiation was found, due to the high oxygen concentration and related deep active donor generation. With additional neutron irradiation the electric field is increased at the main

junction. For the comparison of proton irradiated sensors and neutron irradiated ones, it was found that the proton irradiated sensors exhibit a more distinguishable double junction, albeit their smaller peak fields [93]. The same difference was found comparing the charge collection profiles of neutron and proton irradiated sensors from edge-on measurements, as discussed in Chapter 7.3.4.

Thus, the charge collection profiles obtained from the edge-on analysis are in accordance with previous studies on the effects of radiation damage from different particle types.

7.5. Edge-on Tomography

To investigate the charge sharing between neighboring pixels in the x-direction, the $25\,\mu m$ direction perpendicular to the beam, the so called edge-on tomography plots, 2d charge collection maps, are produced and analyzed. They show the charge injected as a function of pixel-track coordinate in x and track depth in y and thus enable to obtain position dependent charge collection, which provides information on the radiation damage in the sensor.

For the first time due to the non-zero suppressed chip, the negative charge induced in the neighboring pixels can be visualized. The charge induced in a pixel can be understood as the difference in weighting potential Φ_w between the collection point of the electron y_1 and its generation point y_0 multiplied with the elementary charge, as discussed in Chapter 2.2.1. The entire collected charge in one pixel consists of the signal induced by the movement of electrons as well as holes.

The weighting potential is a purely geometrical quantity and is defined as 1 at the readout electrode and 0 at all other electrodes. An example of the weighting potential calculated for the $25\,\mu m$ pixels is shown in Figure 7.56. The direct neighbor of the readout pixel does not collect much charge. As shown, there is no difference in the weighting potential between the generation point of the charge and its collection point for the neighbor pixel, thus no charge is collected. The edge-on tomography plots show the negative charge induced in the next-neighbor pixel of the readout electrode. For the next neighbor the weighting potential is not symmetric so that the collected charge can be negative. The negative charge induced in the neighbors decrease with increasing distance to the readout pixel, however it never reaches zero. The theory of the weighting field and the weighting potential for irradiated and non-irradiated pixel sensors is discussed in Chapter 2.2.1. The edge-on tomography plots for the sensors investigated in this thesis are shown in Figures 7.58 - 7.63 for different bias voltages. As an example, the plot for a sensor irradiated with $\Phi_n = 4 \times 10^{15}\,cm^{-2}$ at a bias voltage of $800\,V$ is shown in Figure 7.57. The middle of the readout pixel i is at $x = 0$ and the (next-) neighboring pixels start at $\pm 12.5\,\mu m$
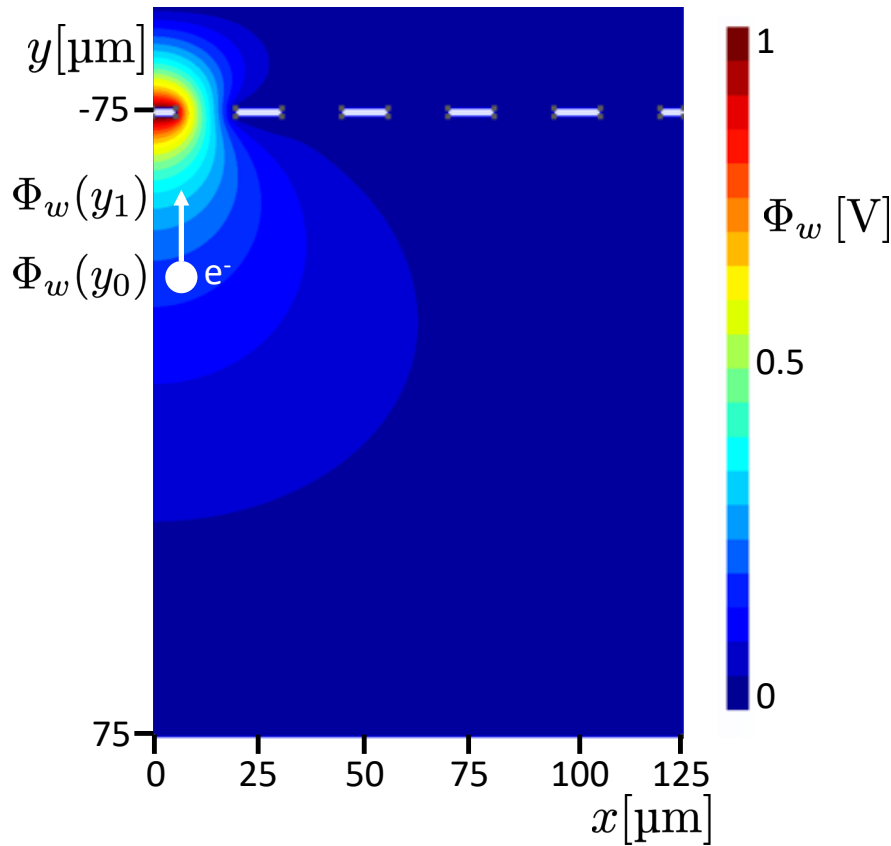
Figure 7.56 – Simulation of the weighting potential for the 25 μm direction of the pixels. The weighting potential is defined as 1 V at the readout electrode and 0 V at all other electrodes. The charge Q induced in a pixel by an electron can be understood as the elementary charge times the difference in weighting potential Φ_w between the collection point of the electron y_1 and its generation point y_0. Simulation provided by J. Schwandt.

(± 37.5 μm), indicated by the dark blue boxes in the figure. In this case, the pixel closest to the track is considered the readout pixel. The black dashed lines indicate the active thickness of the sensor and the position of the implants. The color white represents charges around 0 ADC, as the color legend implies. The negative charge induced in the next-neighbor pixels is visible in dark orange. The maximum charge is collected close to the pixel implant at ~ 75 μm and is decreasing towards the backside of the sensor, as was also shown in Figure 7.52. With the tomography plots also the position dependence of the charge collection in the sensor as a function of bias voltage can be visualized. After irradiation the charges are trapped before they drift through the entire weighting field. Negative charge appears more often at low bias voltages, at high bias voltages the drift is faster and less charge is trapped. For comparison, in Figure 7.58 also the tomography for the same neutron irradiated sensor at a lower bias voltage of 150 V is shown. For the readout electrode charge is no longer collected over the entire sensor depth. The negative
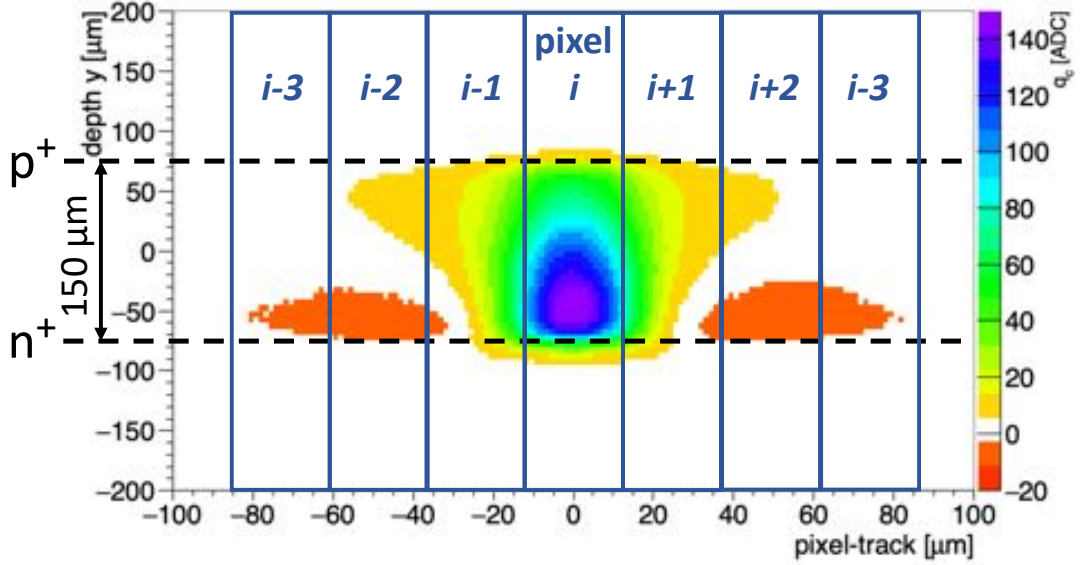
Figure 7.57 – Edge-on tomography plot for a sensor irradiated with $\Phi_n = 8 \times 10^{15} \, \mathrm{cm}^{-2}$ at 800 V bias voltage. The charge is shown as a function of the position of the particle track in x (25 μm direction) and y (150 μm depth) in the sensor. The black dashed lines indicate the active thickness of the sensor and the position of the implants. The middle of the readout pixel i is at $x = 0$ and the (next-) neighboring pixels start at $\pm 12.5 \, \mu\mathrm{m}$ ($\pm 37.5 \, \mu\mathrm{m}$), indicated by the dark blue boxes.

charge in the next-neighbor pixels has increased as expected.

The diffusion of charges at the backside of the sensor is visible at high bias voltages for all irradiated sensors, as charge is collected here even from the next-neighbors. For the non-irradiated sensor, this is visible at the end of the respective depleted region at voltages below full depletion, compare Figure 7.59. The depletion starts from the pixel implants. In general, the plots are expected to be symmetric to the readout pixel. However, slight differences might be visible due to the pulse pileup, explained in Section 4.4.3. Especially for the sensors with a non-uniform irradiation, the pileup which is position dependent, can lead to an asymmetric charge collection around the readout pixel as some pixels pulse heights are more influenced by their neighbors than others. This is the case for the sensor irradiated to $\Phi_p = 3.92 \times 10^{15} \, \mathrm{cm}^{-2}$ in Figure 7.60. For the sensor irradiated to $\Phi_p = 8.68 \times 10^{15} \, \mathrm{cm}^{-2}$ the drop in charge collection from the implants to the backside is clearly visible, as the color blue is only visible in a small part of the sensor.
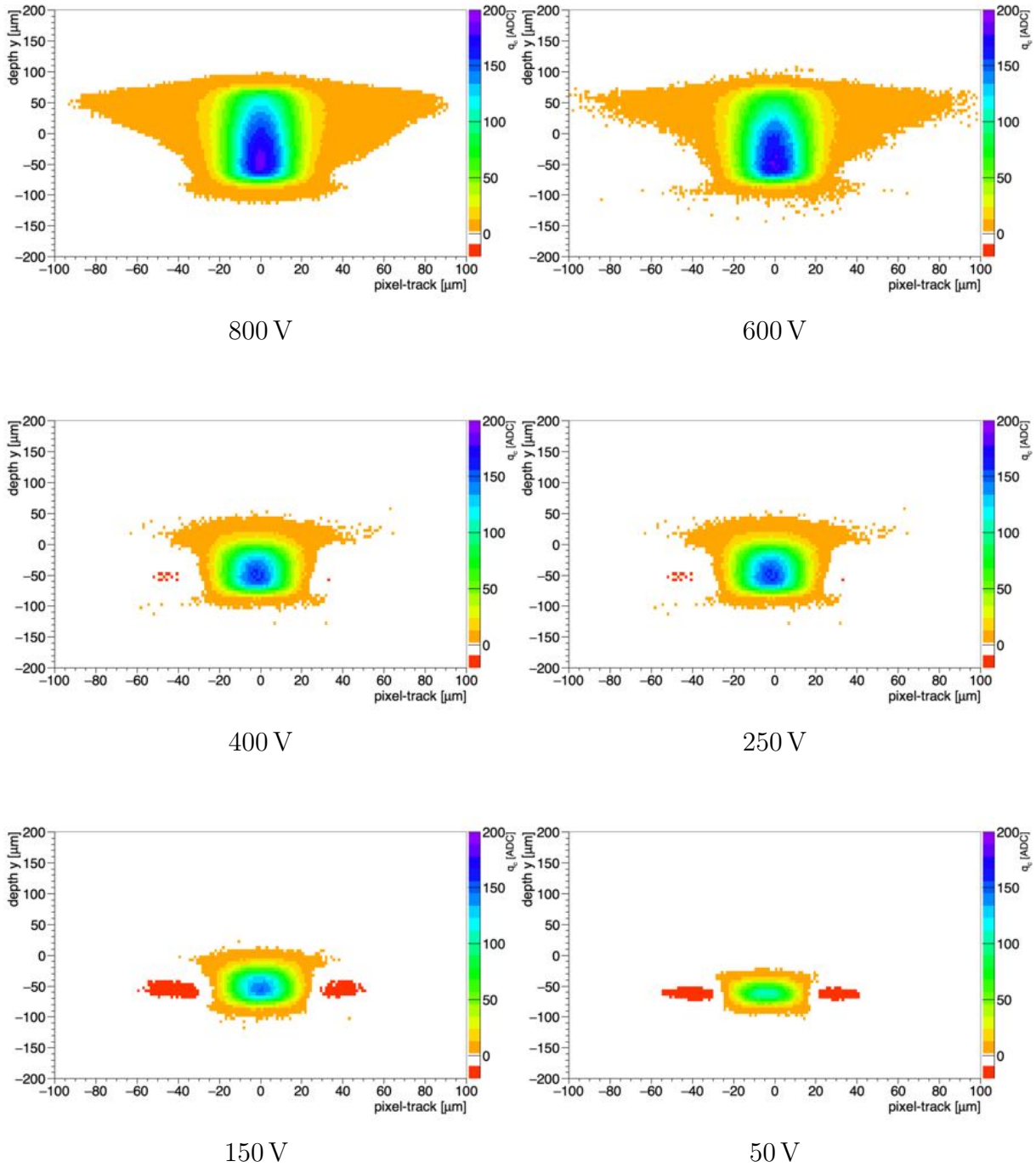
Figure 7.58 – Edge-on tomography plot for a neutron irradiated to $\Phi_n = 4 \times 10^{15}\,\mathrm{cm}^{-2}$ for different bias voltages. For further explanation see Figure 7.57.

120 V

40 V

30 V

20 V

9 V

5 V
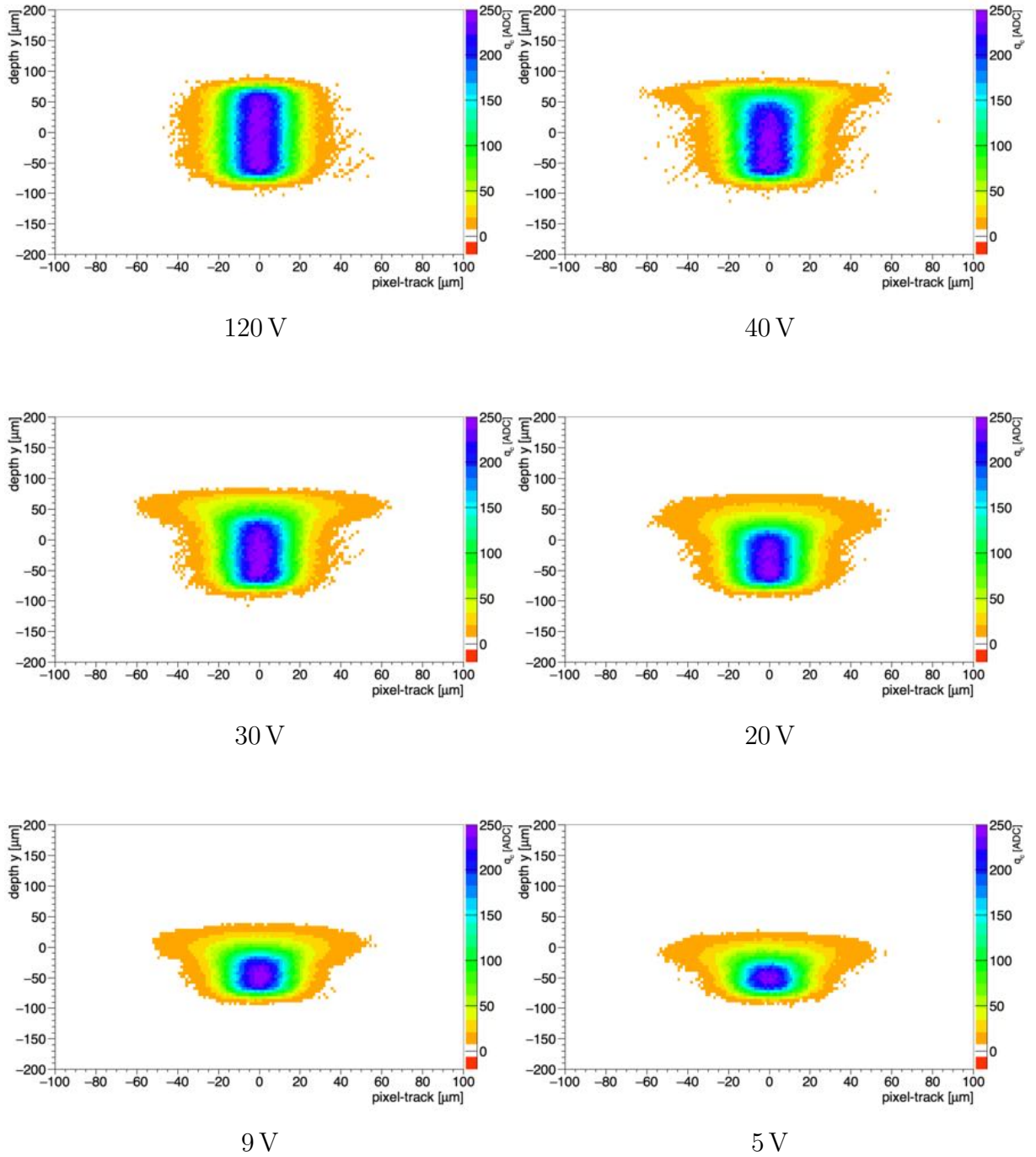
Figure 7.59 – Edge-on tomography plots for the non-irradiated sensor. For further explanation see Figure 7.57
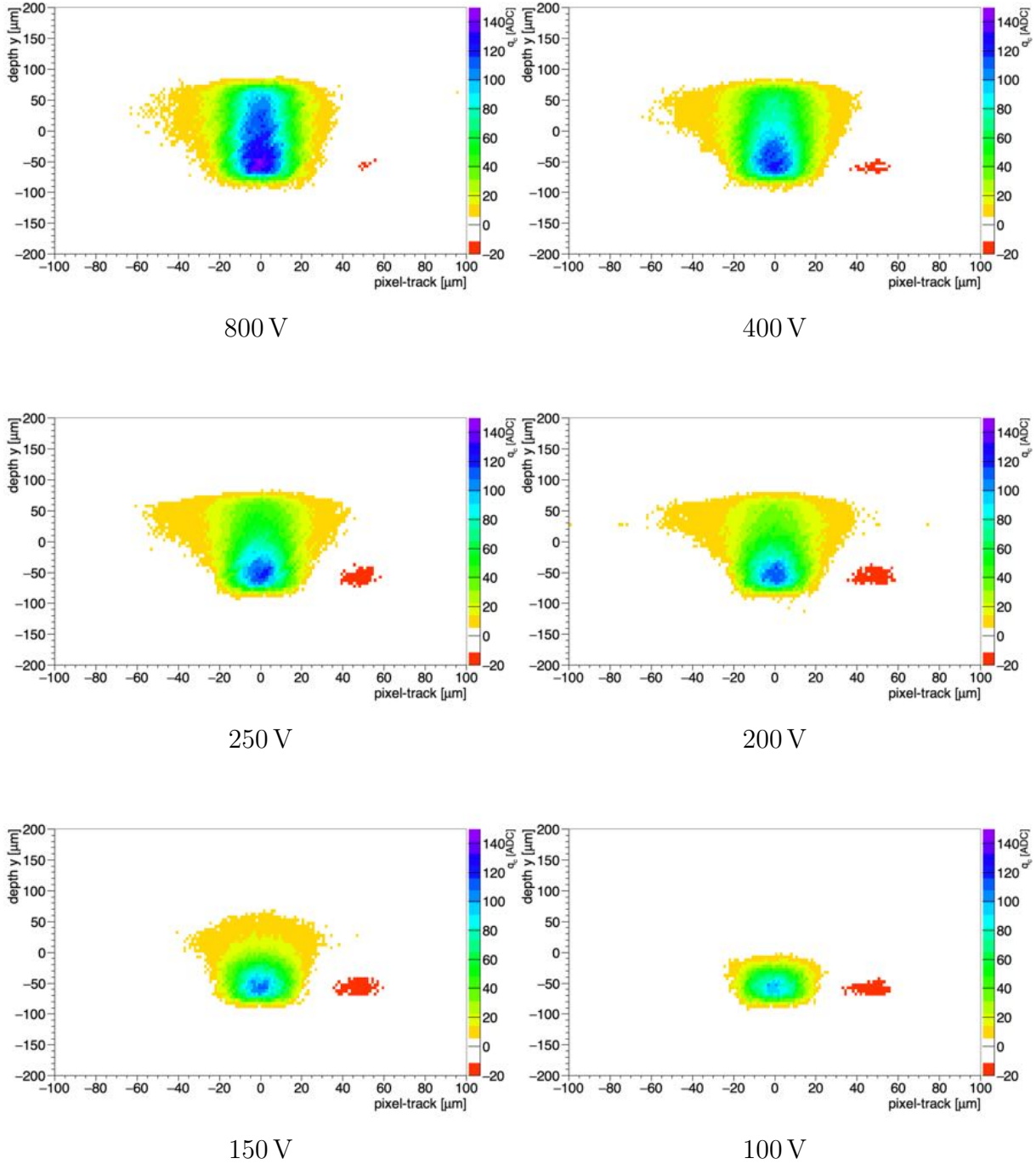
Figure 7.60 – Edge-on tomography plots for a sensor irradiated to $\Phi_p = 3.92 \times 10^{15} \, \mathrm{cm}^{-2}$ for different bias voltages. For further explanation see Figure 7.57. The plot is not symmetrical to the readout pixel, likely due to the pulse pileup.
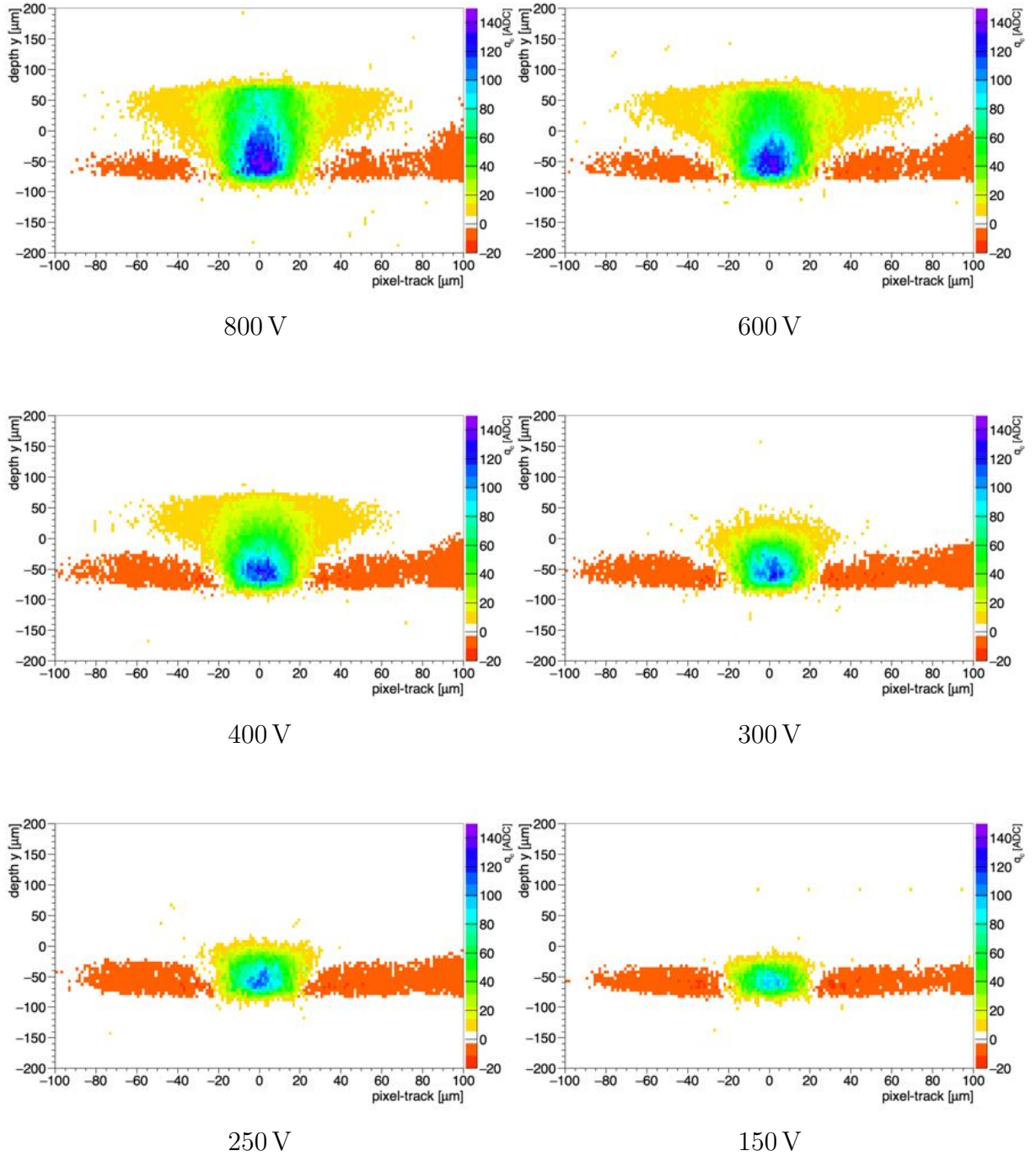
Figure 7.61 – Edge-on tomography plots for a sensor irradiated to $\Phi_p = 8.68 \times 10^{15}\,\mathrm{cm}^{-2}$. For further explanation see Figure 7.57.

800 V

600 V

400 V

300 V

250 V

150 V
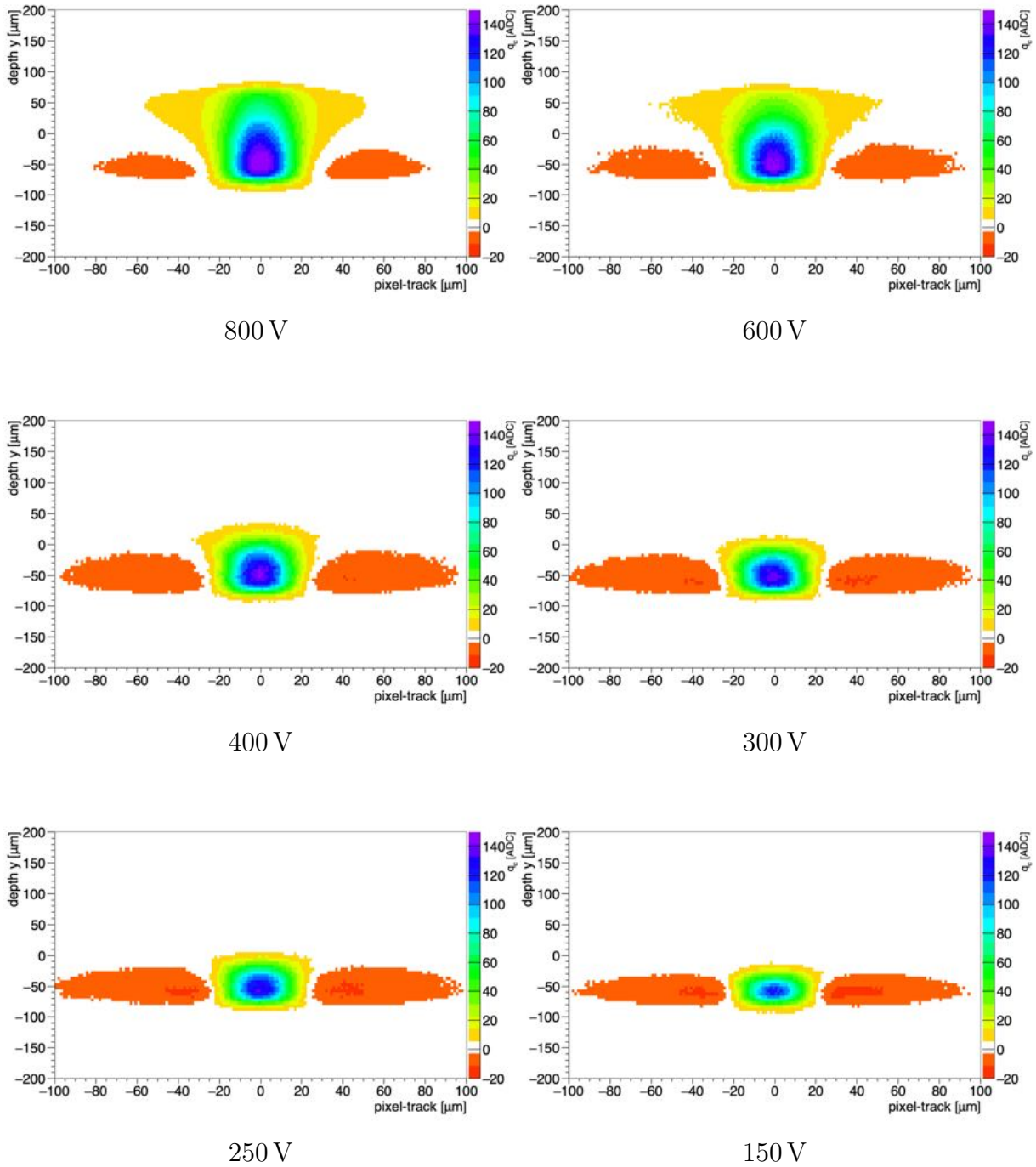
Figure 7.62 – Edge-on tomography plots for the sensor irradiated to $\Phi_n = 8 \times 10^{15}\,\mathrm{cm}^{-2}$. For further explanation see Figure 7.57.

800 V   600 V

350 V   250 V
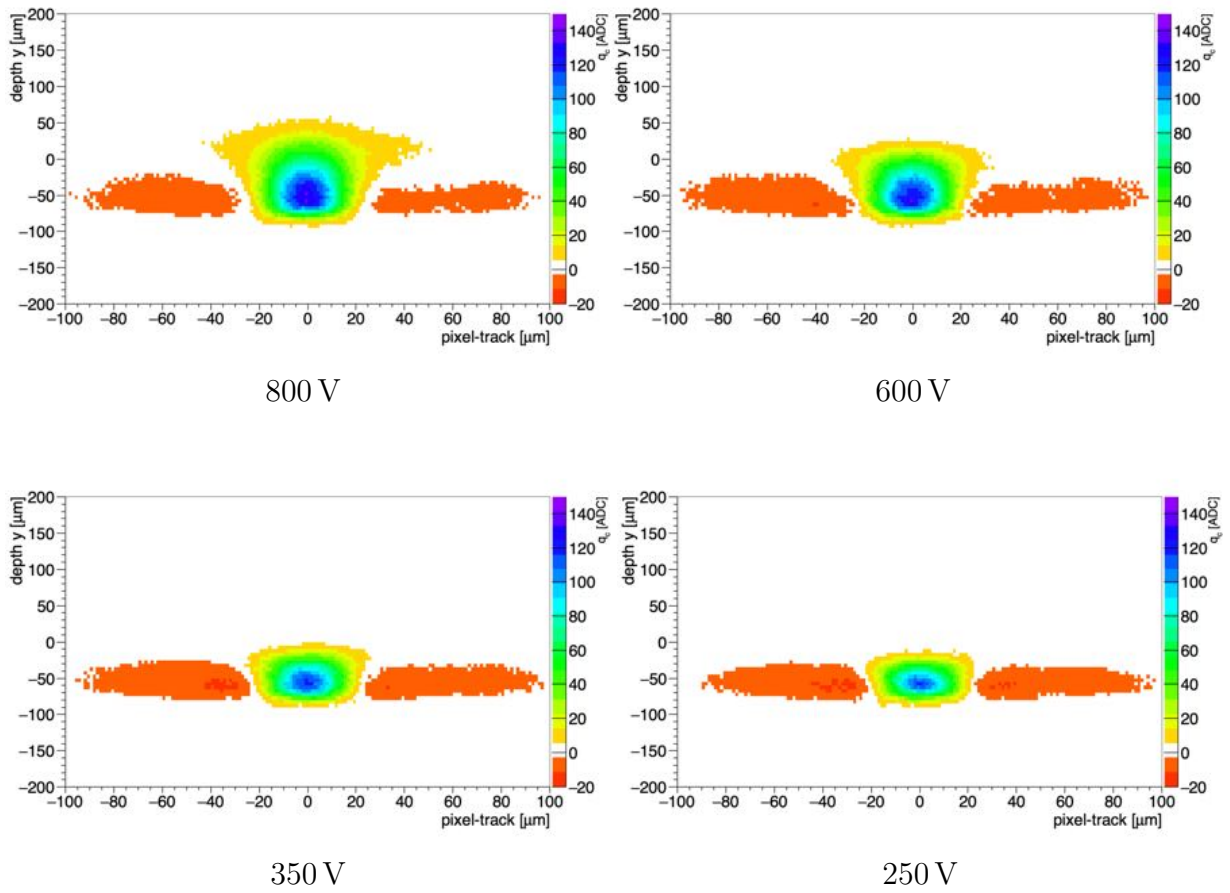
Figure 7.63 – Edge-on tomography plots for a sensor irradiated to $\Phi_n = 16 \times 10^{15}\,\text{cm}^{-2}$. For further explanation see Figure 7.57. Even at 800 V charge is not collected over the entire sensor depth.

8. Simulation of Edge-on Data

To describe the data taken with the edge-on measurements, a simulation of the data was performed. The chosen model and method are described in the following.

List of own contributions The author's contributions to the results presented in this chapter include:

- application of the test beam data analysis on the simulated data to achieve comparability.

The simulation was done with the help of Dr. J. Schwandt, who provided the TCAD simulations and Dr. D. Pitzl, who provided me with the PIXELAV code adaptation for the edge-on simulation. The original PIXELAV code is from Prof. M. Swartz.

8.1. The Hamburg Penta Trap Model

The Hamburg Penta Trap Model (HPTM) is a new model for the Technology Computer Aided Design (TCAD) simulation of the damage in silicon by high fluence proton irradiation developed by J. Schwandt. It was developed out of the necessity to describe the I-V, C-V and CCE measurements of pad diodes simultaneously for fluences greater than $\Phi_{eq} = 10^{15}\,\mathrm{cm}^{-2}$, as all previously available models did not match the data accurately. The parameters of the HPTM are summarized in Table 10. Five defects, 3 donors and 2 acceptors are necessary to describe the data. The trap concentrations of defects N can be calculated as

$$N = g_{int} \cdot \Phi_{eq} \; . \tag{46}$$

More information on the calculations and details of the HPTM can be found in [94] and [95].

8.2. Simulation with PIXELAV

PIXELAV is a detailed simulation of pixel sensors, intended as a partial replacement for test beam measurements [96]. The simulation contains a proper model of charge deposition by primary hadronic tracks to be able to model $\delta-$rays. In addition, a model of the charge drift including mobilities, 3d diffusion and the Hall Effect is included as well as a realistic electric field map. Contrary to many other simulation programs, also a simulation of radiation damage including charge trapping effects with charge induction

Defect	Type	Energy	g_{int} [cm^{-1}]	σ_e [cm^2]	σ_h [cm^2]
E30K	Donor	$E_C - 0.1\,\text{eV}$	0.0497	2.300E-14	2.920E-16
V_3	Acceptor	$E_C - 0.458\,\text{eV}$	0.6447	2.551E-14	1.511E-13
I_p	Acceptor	$E_C - 0.545\,\text{eV}$	0.4335	4.478E-15	6.709E-15
H220	Donor	$E_V + 0.48\,\text{eV}$	0.5978	4.166E-15	1.965E-16
C_iO_i	Donor	$E_V + 0.36\,\text{eV}$	0.3780	3.230E-17	2.036E-14

Table 10 – The defects of the HPTM, their energy levels, their introduction rates and crossections from J. Schwandt.

are implemented in PIXELAV. Furthermore, a simulation of electronic noise, response and threshold effects is included. More detailed information on PIXELAV can be found in [96].

For the description of the data taken in the edge-on beam, PIXELAV is used with an electric field calculated from Synopsys TCAD [97] as input. The TCAD calculation of the electric field is based on the HPTM, as introduced in the previous section and was performed by J. Schwandt. The entire simulation workflow is sketched in Figure 8.1.

The output from PIXELAV is then read out with ROOT and additional smearing to simulate the track resolution of the beam telescope is added. The selection of events in the analysis is the same as used for the test beam data.

The temperature for calculating the electric field for the non-irradiated sensor was set to 293 K, for $\Phi_{eq} = 2 \times 10^{15}\,\text{cm}^{-2}$ to 258 K and for $\Phi_{eq} = 4 \times 10^{15}\,\text{cm}^{-2}$ to 253 K. The electric field from TCAD has $51 \times 51 \times 151$ grid points. For the simulation of the edge-on beam with PIXELAV, a pixel array of 21×21 pixels is defined. The induced signal is then calculated for a 5×5 pixel array of $100 \times 25\,\mu\text{m}^2$, similiar to the ROI from the beam data. To save time only every tenth charger carrier is transported through the sensor. The beam enters along the 100 μm pixel direction and the active thickness is 150 μm. The Hall factors were set to 1.12 for electrons and 0.9 for holes. For each bias voltage 100k events are simulated, which are initialized by a random seed. A 45 GeV/c pion is then propagated through the silicon and electron-hole pairs are created. For the calculation of the number of electron-hole pairs, an average ionization energy of $I_0 = 3.645\,\text{eV}$ is used. The electron-hole pairs are propagated in the applied electric field until they reach the boundaries of the sensor. The maximum time for their propagation is set to 125 ns, corresponding to
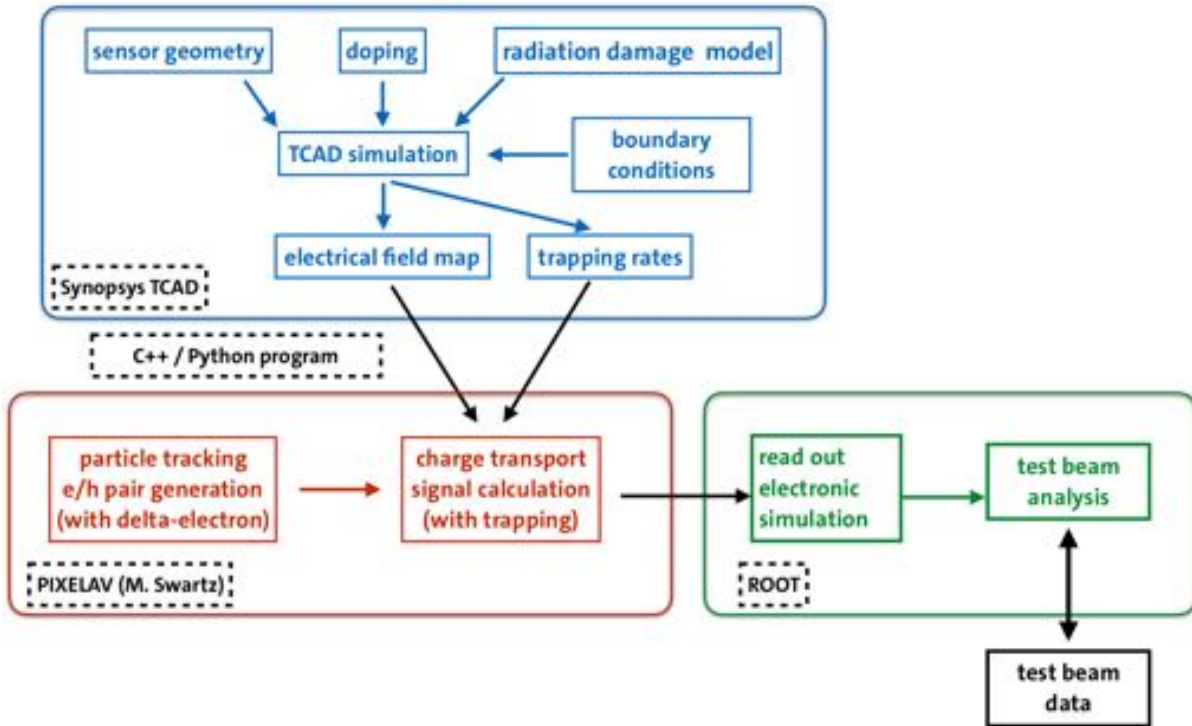
Figure 8.1 – An illustration of the different components of the simulation for the edge-on test beam data from J. Schwandt. The electric field is calculated with Synopsys TCAD and is used as an input for the simulation with PIXELAV. This output is then read out and analyzed in the same way as the test beam data.

the ROC4SENS readout time with telescope. The output of the PIXELAV simulation is the charge deposited per event in each pixel, which can then be used to select the events as it was done in the data analysis. In the selection with ROOT a smearing of 11 μm is applied to the track to simulate the telescope track resolution. For the charge all pixels are added within one column, however in the simulation charge is only induced into one pixel.

In Figure 8.2 the comparison of data and simulation for a non-irradiated sensor is shown. The simulation is scaled to match the integral of the data at 120 V. The simulation assumes room temperature, while the data was taken at $-30°$C. Nevertheless, for a non-irradiated sensor, where the leakage current is minimal, the difference in temperature is negligible. A good agreement with the shape of the data is visible for bias voltages above 30 V. However, for lower voltages the simulation exhibits an enhanced charge collection at the back side of the sensor, which was not confirmed in the beam test data. The simulation assumes a high p$^+$ concentration on the backside in the order of $\sim 10^{19}$cm^{-3}, which is the reason for the increased charge collection on the backside [98].

For irradiated sensors, the trapping times for electrons and holes determine the shape of
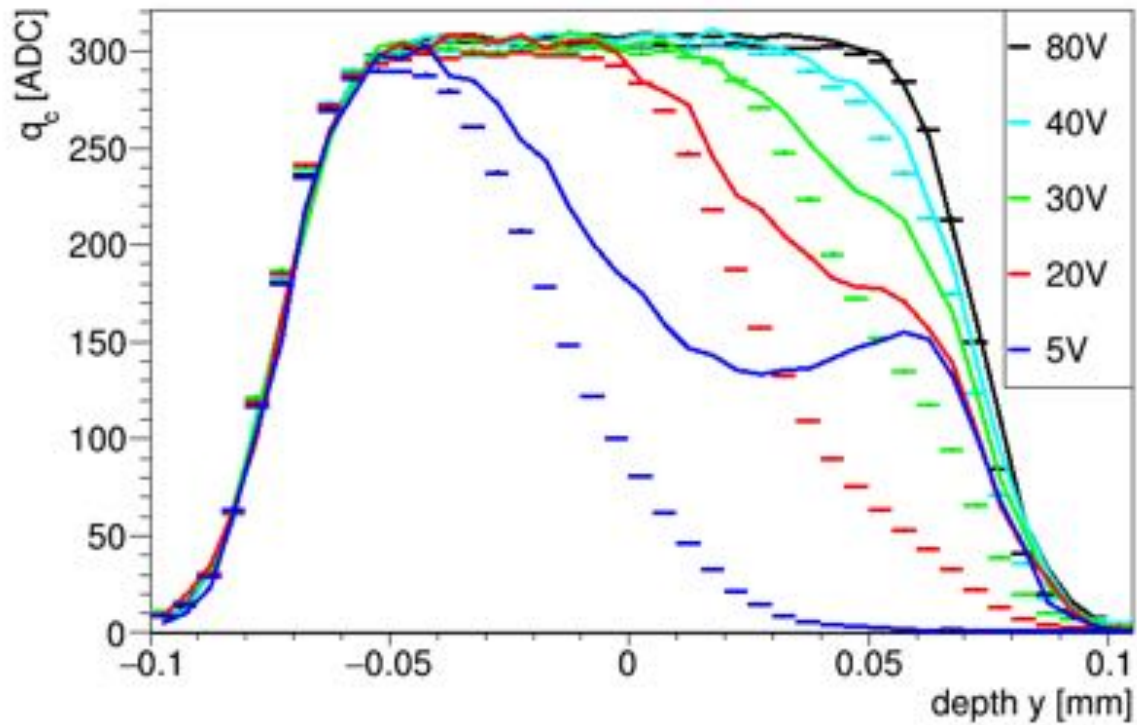
Figure 8.2 – Comparison of data (points) and simulation (solid lines). The data is from a non-irradiated sensor at $-30°$C, the simulation is scaled to match the integral of the data at 120 V. The simulation was performed at $+20°$C. For bias voltages greater than 30 V the shape of the simulation is in good agreement with the data, for lower voltages the simulation expects an enhanced charge collection at the back side of the sensor.

the charge collection profiles, explained in Chapter 7.3. The trapping times for electrons and holes are variable in the simulation and were chosen to fit the test beam data. Different trapping times at multiple bias voltages are shown in Figures 8.3-8.4. Only sensor irradiated with protons are compared to the simulation. The edge-on data for a sensor irradiated to $\Phi_{eq} = 2.3 \times 10^{15}$ cm^{-2} at $-18°$C is shown as points, the simulation is done for sensors irradiated to $\Phi_{eq} = 2.0 \times 10^{15}$ cm^{-2} at $-20°$C. The integral over the simulated data at 600 V was scaled to match the integral over the data at 600 V for each set of trapping times individually. The resulting scale factor for each set of trapping times was used for all other bias voltages as well so the simulated ratio between the bias voltages remains unchanged. It is visible that the different trapping times change the charge collection at the front and backside. From the comparison of the different bias voltages it was found that $\tau_e = 4.8$ ns and $\tau_h = 4.8$ ns, depicted as the blue line in the figure fits the data shapes at different bias voltages qualitatively best. Therefore all further comparisons of data and simulation are done with these trapping times.
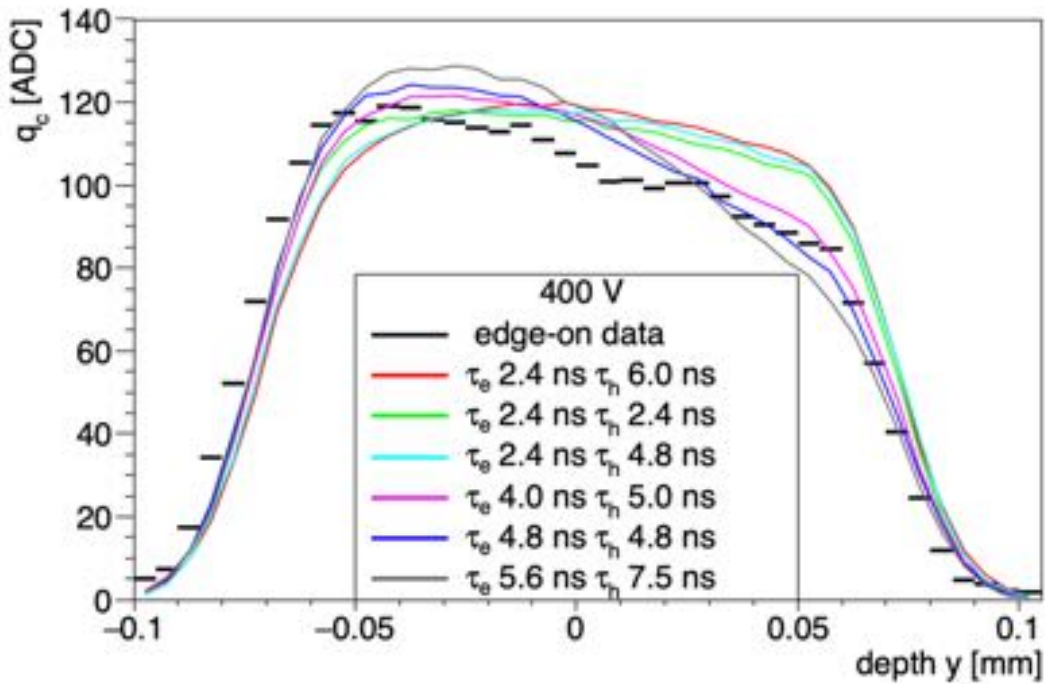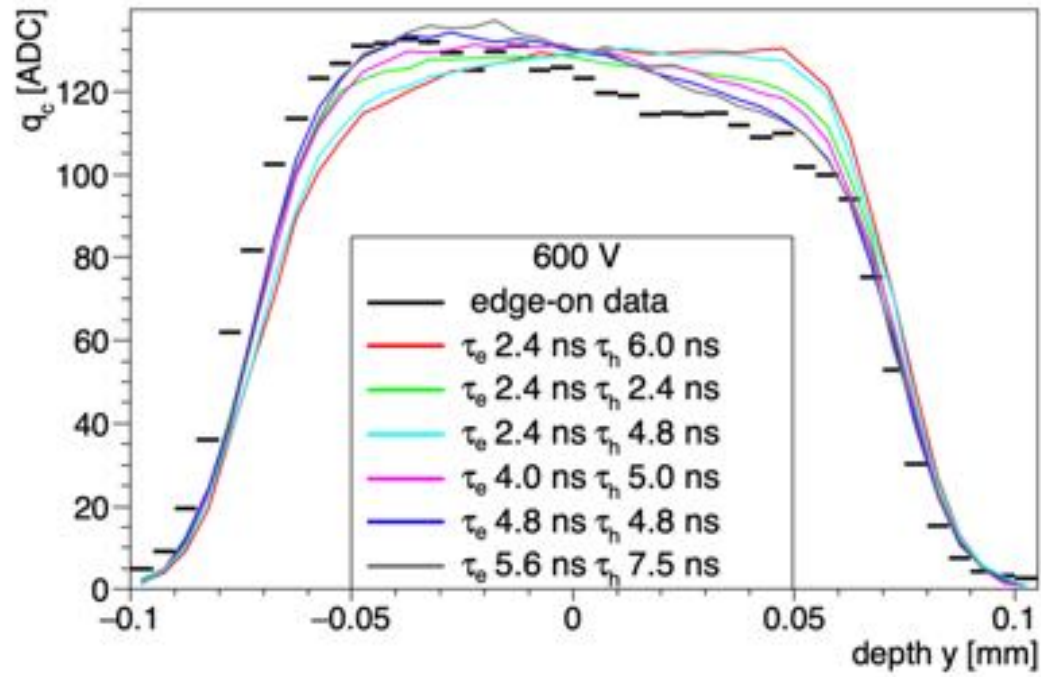
Figure 8.3 – Comparison of data (points) and simulation (solid lines) for different simulated trapping times at 600 V and 400 V bias voltage. The simulation was performed for sensors irradiated to $\Phi_{eq} = 2.0 \times 10^{15}\,\mathrm{cm}^{-2}$ at $-20°$C.

In Figure 8.5 the agreement between data and simulation is shown for a sensor irradiated to $\Phi_{eq} = 2.3 \times 10^{15}\,\mathrm{cm}^{-2}$ at $-18°$C. The simulation was performed for sensors irradiated
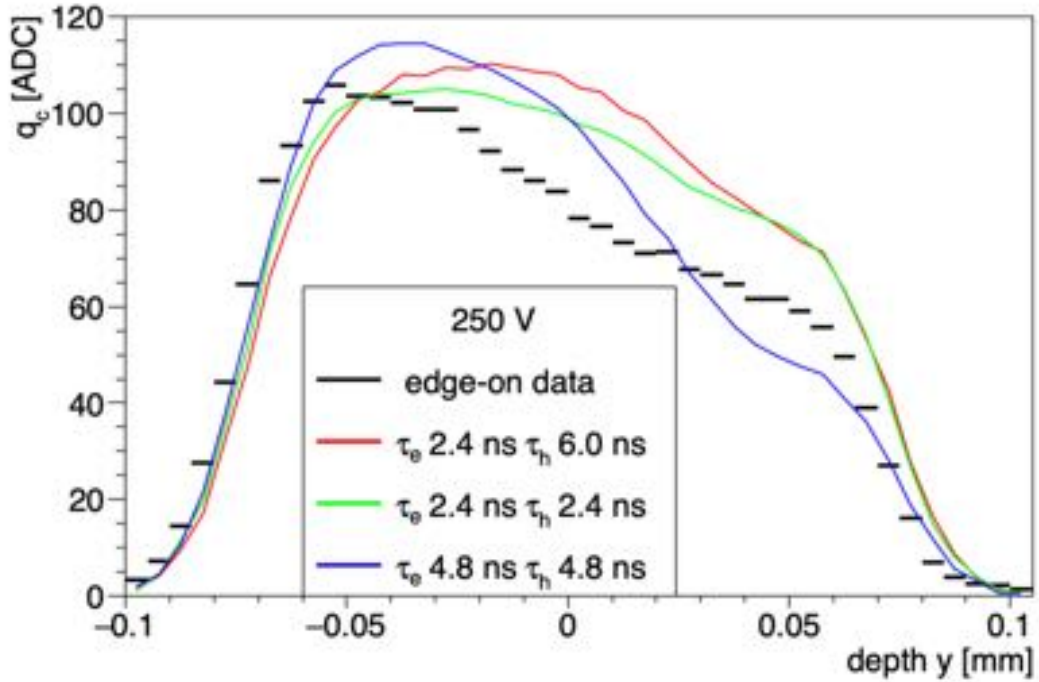
Figure 8.4 – Comparison of data (points) and simulation (solid lines) for different simulated trapping times at 250 V bias voltage. The sensor irradiation is the same as in Figure 8.3.

to $\Phi_{eq} = 2.0 \times 10^{15}\,\mathrm{cm}^{-2}$ at $-20°\mathrm{C}$. The simulation produces the dependence of the charge collection on the depth rather well for bias voltages greater than 300 V, for lower voltages the agreement is worse. Especially for 150 V and 100 V the simulation overestimates the charge collection depth starting from the implants by $\sim 0.015\,\mathrm{mm}$. The shape itself however looks similiar with a local maximum of the charge towards the backside of the sensor.

To be able to compare the shape of the charge collection profile in data and simulation in more detail, Figure 8.6 shows the data and simulation for intermediate bias voltages. For this comparison each simulated profile is scaled to match the integral of their respective bias voltages. At 400 V bias voltage the shape of data and simulation agree, at 200 V and 250 V the shape starts to differ in the charge collection at the back side. At 150 V the simulation shows a small peak at the sensor backside, which is not seen in data. However, on the front side, the simulation exhibits less charge collection.

Further comparison between data and simulation is done at a higher proton fluence. A sensor irradiated to $\Phi_{eq} = 5.2 \times 10^{15}\,\mathrm{cm}^{-2}$ and measured edge-on at $-30°\mathrm{C}$ was compared to a simulation performed with a sensor irradiated to $\Phi_{eq} = 4.0 \times 10^{15}\,\mathrm{cm}^{-2}$ at $-20°\mathrm{C}$. Figure 8.7 shows the comparison. The simulation is scaled to the integral of the data
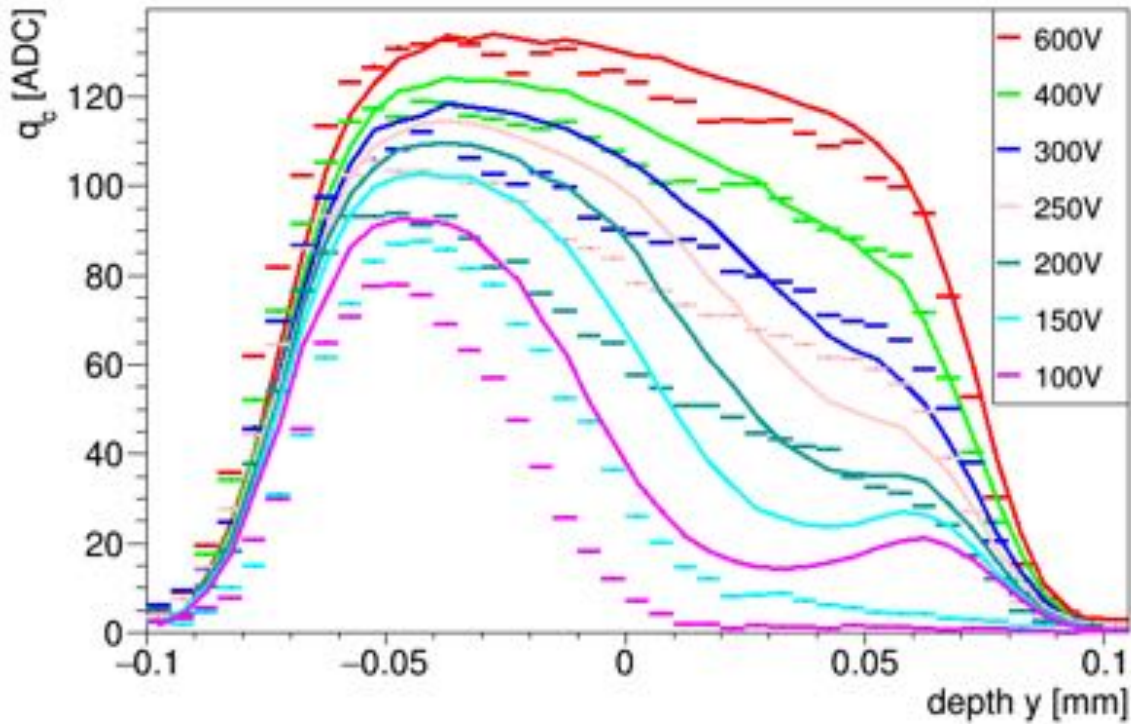
Figure 8.5 – Comparison of data (points) and simulation (solid lines). The sensor is irradiated to $\Phi_{eq} = 2.3 \times 10^{15}\,\mathrm{cm}^{-2}$ at $-18°$C, the simulation is scaled to match the integral of the data at 600 V. The simulation was performed for sensors irradiated to $\Phi_{eq} = 2.0 \times 10^{15}\,\mathrm{cm}^{-2}$ at $-20°$C. For bias voltages greater than 300 V the shape of the simulation is in good agreement with the data, for lower voltages the agreement is worse.

at 700 V. The voltage dependence in simulation is clearly different from the dependence in data, as the charge collected at the sensor front side decreases faster with decreasing bias voltage in data than in simulation. For bias voltages below 400 V the simulation overestimates the charge collection depth by $\sim 0.015\,\mathrm{mm}$. The entire shape of the charge collection profiles from data and simulation however look similiar.

As previously done for the lower proton fluence, for a better comparison of the individual shapes, in Figure 8.8 the simulated profiles are scaled to match the integral of their respective bias voltages. It is visible that the shapes of the charge collection profiles are in good agreement for the chosen bias voltages. Additionally, for a direct comparison of the voltage dependence, the total collected charge as a function of bias voltage is shown in Figure 8.9. For the lower irradiation, the aforementioned higher charge collection in simulation at lower bias voltages is visible. However, the charge collection in data and simulation saturates around the same bias voltage of 700-800 V. For $\Phi_{eq} = 5.2 \times 10^{15}\,\mathrm{cm}^{-2}$ in data there is no saturation of charge collection visible. The simulation at $\Phi_{eq} =$
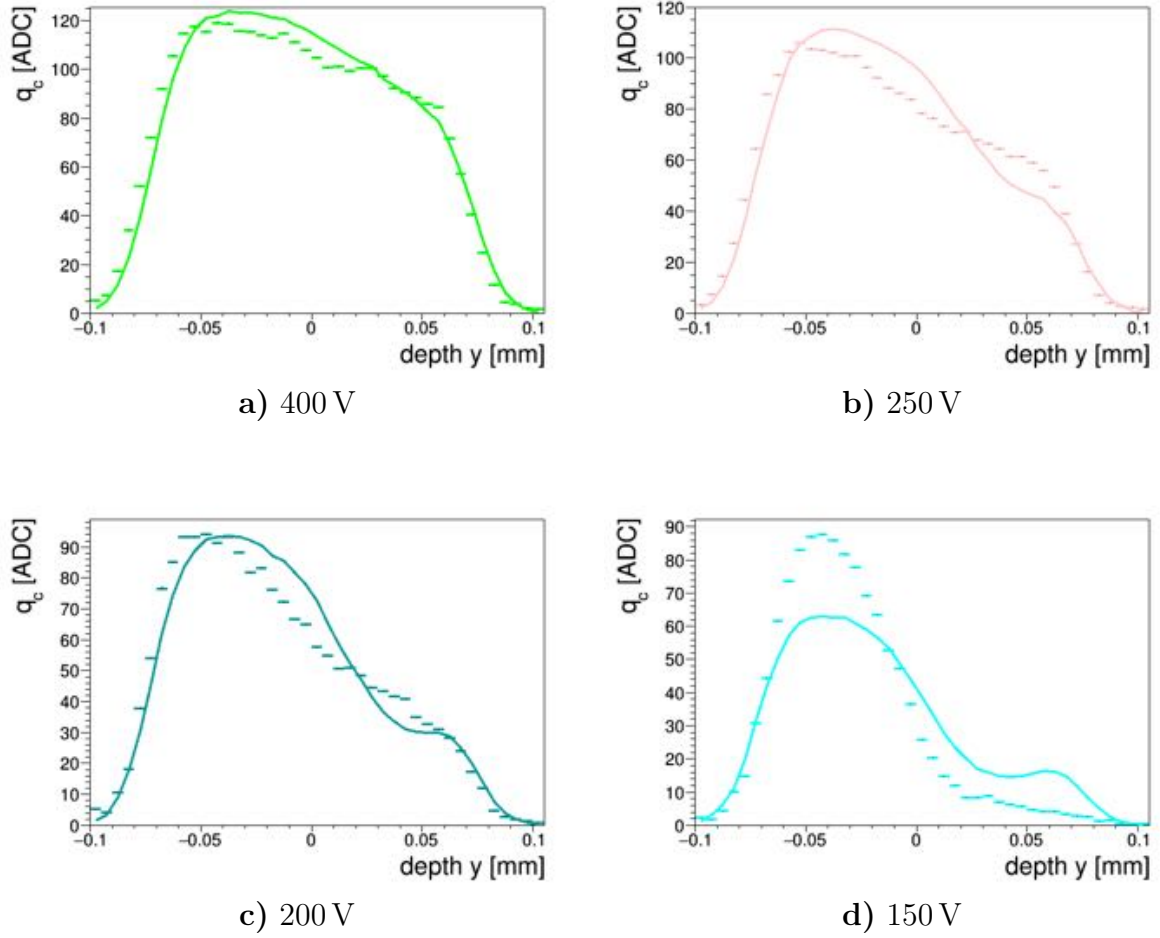
Figure 8.6 – Comparison of data and simulation for different bias voltages and $\Phi_{eq} = 2.3 \times 10^{15}\,\mathrm{cm}^{-2}$. Here, the simulation is scaled to the integral of each bias voltage individually to allow a more detailed shape comparison.

$4.0 \times 10^{15}\,\mathrm{cm}^{-2}$ however saturates around $700\,\mathrm{V}$. This shows that the simulation is able to reproduce the shape but still needs an improved voltage dependence.

Overall the simulation describes the data qualitatively for the higher bias voltages. For lower bias voltages the charge collection is slightly overestimated by the simulation. The shape of the charge collection however is well reproduced for all irradiations, even though fluence and temperature of simulation and data are only similar and not exactly the same. The charge collection profiles taken with the edge-on test beam will be used for further improvement of the simulation. As of now, the HPTM is the only model that describes the charge collection per depth of highly irradiated pixel sensors qualitatively at all. For fluences below $\Phi_{eq} = 1 \times 10^{15}\,\mathrm{cm}^{-2}$ a two-trap model by M. Swartz [99] can also be used to describe the charge collection per depth. The Perugia model [100], which only assumes
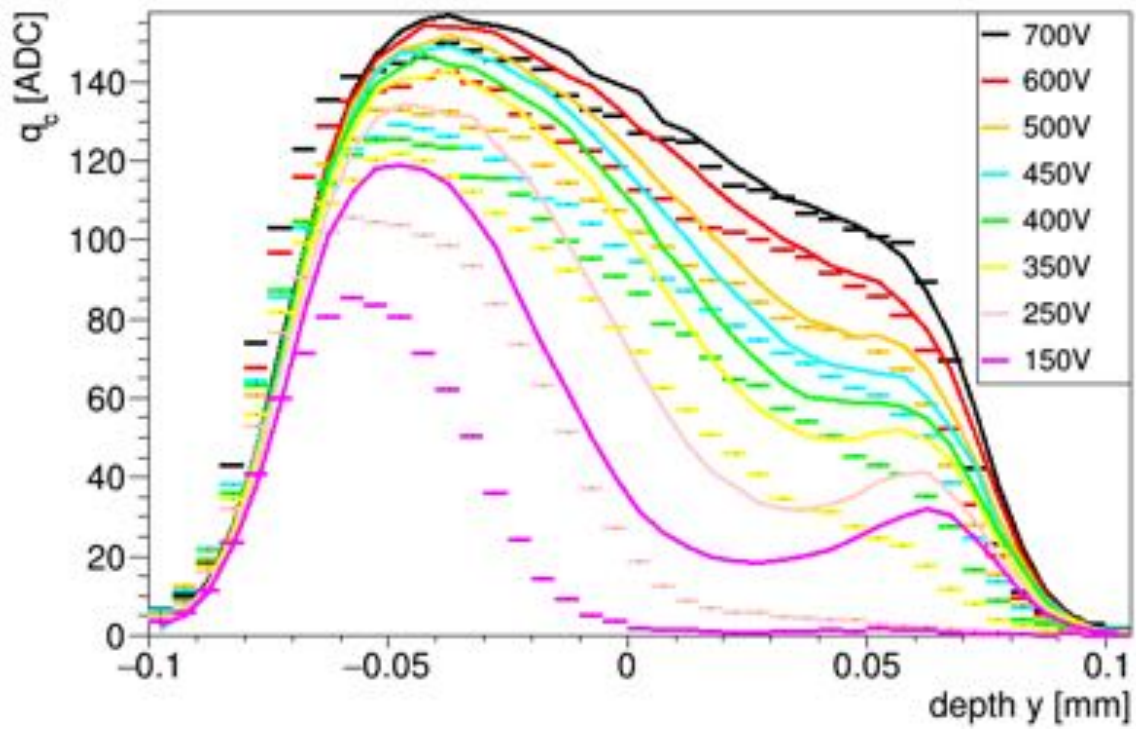
Figure 8.7 – Comparison of data (points) and simulation (solid lines). The sensor is irradiated to $\Phi_{eq} = 5.2 \times 10^{15}\,\mathrm{cm}^{-2}$ at $-30°\mathrm{C}$, the simulation is scaled to match the integral of the data at 700 V. The simulation was performed for sensors irradiated to $\Phi_{eq} = 4.0 \times 10^{15}\,\mathrm{cm}^{-2}$ at $-20°\mathrm{C}$.

three traps, does not describe the diode data, which the HPTM was tuned on, as shown in [95].
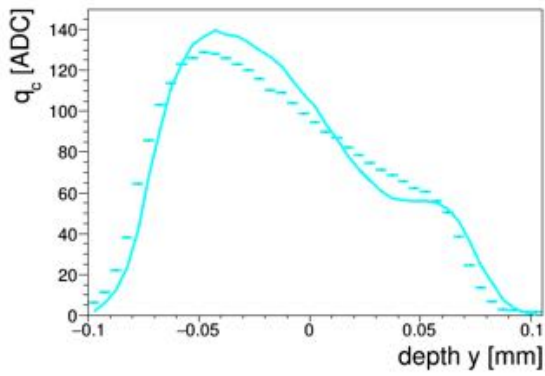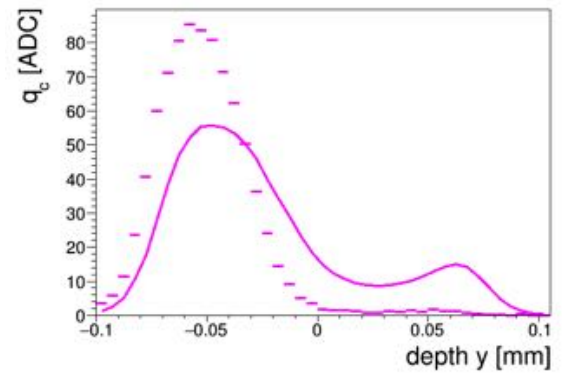
a) 450 V   **b)** 150 V

Figure 8.8 – Comparison of data and simulation for different bias voltages at $\Phi_{eq} = 5.2 \times 10^{15} \, \mathrm{cm}^{-2}$. Here, the simulation is scaled to the integral of each bias voltage individually to allow a more detailed shape comparison.
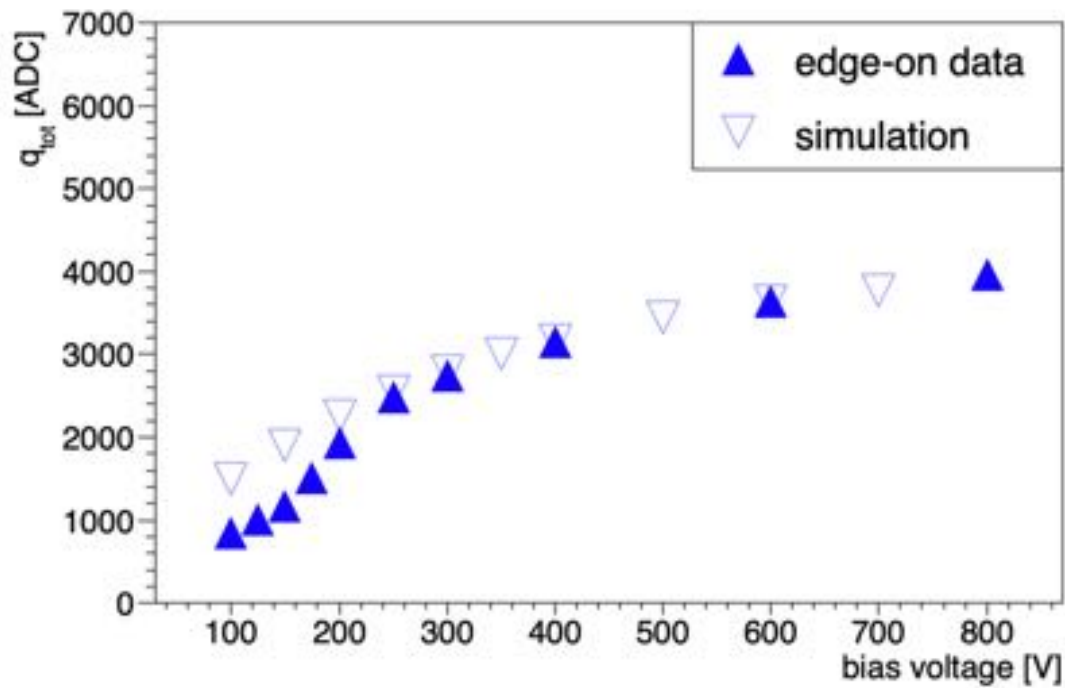
$$\Phi_{eq} = 2.3 \times 10^{15} \, \text{cm}^{-2}$$
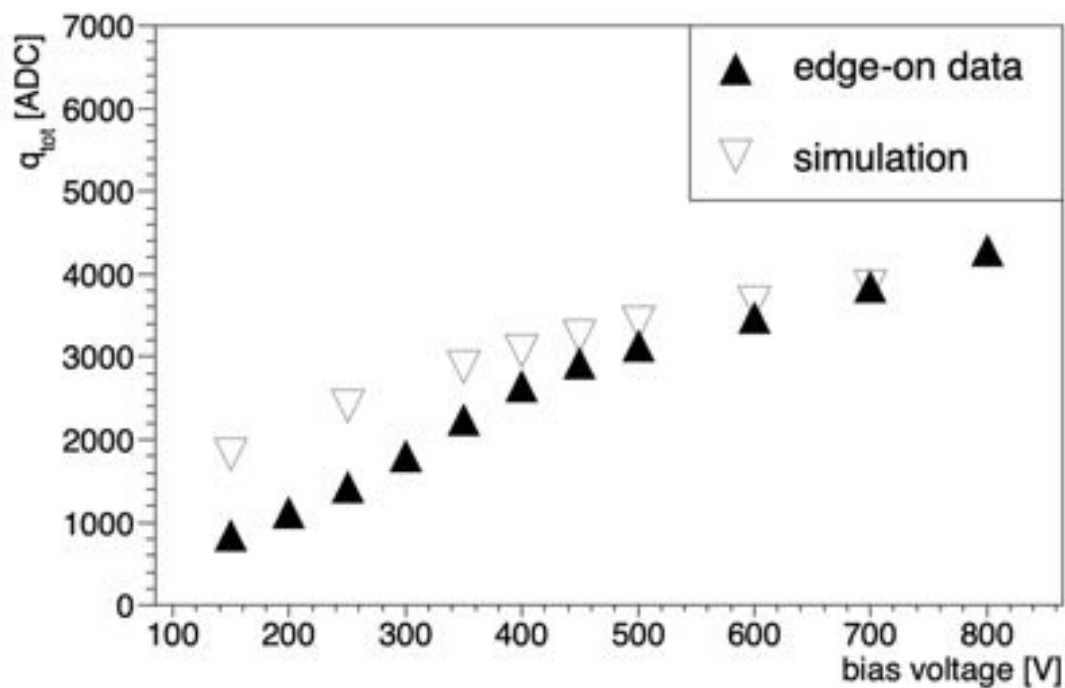
$$\Phi_{eq} = 5.2 \times 10^{15} \, \text{cm}^{-2}$$

Figure 8.9 – The total collected charge as a function of bias voltage in data and simulation. Scaling as in Figures 8.5 and 8.7. For $\Phi_{eq} = 5.2 \times 10^{15}$ cm^{-2} the charge collection in simulation saturates at a lower bias voltage than in data.

9. Pixel Resolution

The resolution of the pixelated sensor can be measured without the help of an external beam telescope as a reference plane. The pixels before and after the hit pixel itself can be used as reference and thus allow for in-silicon tracking as the beam hits the sensor edge-on. A rotation by an angle ϕ around the sensor's y-axis enables charge sharing to investigate the position resolution of the individual pixel. The beam momentum of all measurements for the intrinsic detector resolution is set to $5.6\,\text{GeV}$. The measurement setup is shown in Figure 9.1. The rotation angles and the alignment of the sensor are set via the laser alignment system at the DESY testbeam facility. The beam is positioned straight onto the sensor, which is defined as $\phi_{\text{set}} = 0°$. The systematic uncertainty on the absolute value of the angles from the alignment with the laser is conservatively estimated to be one degree. The uncertainties on the step sizes of one or two degrees between the measurement points can be corrected for in data. All distributions shown are for a non-irradiated sensor with a p-stop default design at $120\,\text{V}$ bias voltage unless it is stated otherwise. For each rotation step $40\,000$ events were collected, except for the optimal angle where $160\,000$ events were collected.
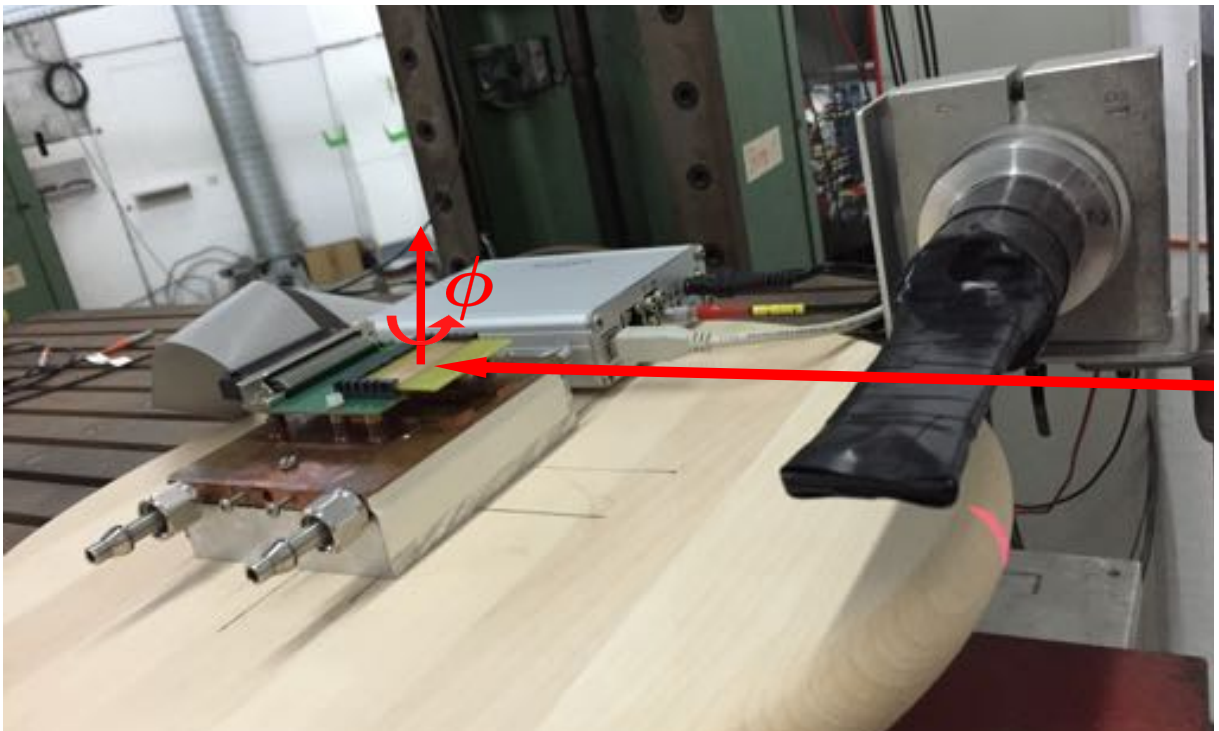
Figure 9.1 – Picture of the measurement setup for the intrinsic position resolution of the silicon sensor. The beam, indicated by the red arrow, hits the sensor edge-on. The sensors position resolution is investigated for different rotations ϕ around the sensor's y-axis.

List of own contributions The author's contributions to the results presented in this chapter include:

- conducting the resolution measurements,

- implementation of the presented analysis.

The pixel resolution measurement is based on software provided by Dr. D. Pitzl. Prof. Dr. Klanner assisted in the discussion of the employed methods and their validity.

9.1. Event Selection

The data acquisition for the edge-on analysis is explained in detail in Chapter 6. For the measurements of the pixel resolution the principles remain, mainly the setup is changed, as no telescope or cooling is used. As visible in Figure 9.1, a PMT mounted edge-on is used as a trigger, no external timing reference is used.

The same ROI data taking principle is used as explained in Chapter 6.1. Only the size of the ROI is smaller, as only an area of 5×7 (columns$\times$rows) is stored around a hit pixel. The data is pedestal corrected from the first 100 events, similiar to Equation 29. The common-mode correction remains unchanged.

A threshold on the pixel charge is applied, as only pixels i with a charge $q_i > 10\,\mathrm{ADC}$ were considered. As only a non-irradiated sensor is measured, the gain equalization and calibration to electrons, explained in Chapter 6.2 is used.

The collected charge q_c consists of the sum of all pixels with charge above threshold per column j

$$q_c(j) = \sum_{rows_j=i} q_i \quad \text{with } q_i > 10\,\mathrm{ADC}\,. \tag{47}$$

The corresponding y-coordinate of the charge is calculated from

$$y_j(q_c) = \frac{\sum_{rows_j} y_i \cdot q_i}{q_c}\,, \tag{48}$$

where y_i is the y-coordinate of the pixel row. For the further analysis the column dependence is dropped, as there is no column systematic, compare Chapter 7.1.3. From Figure 9.2 it is visible that the mean of all collected charges is constant over the entire sensor, as are the number of entries depicted in the inset.
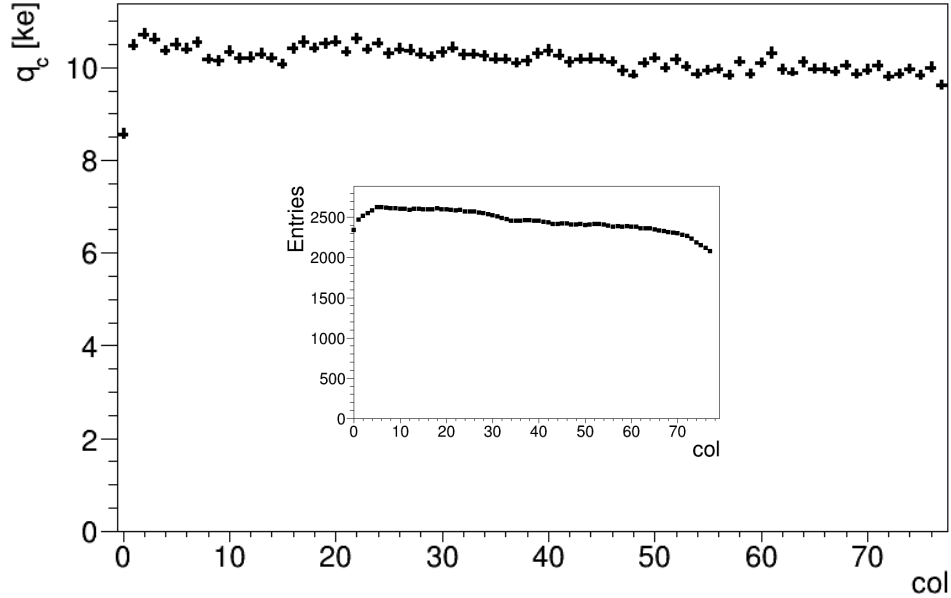
Figure 9.2 – An example of the mean collected charge as a function of pixel column at $\phi_{\mathrm{measured}} = 13°$. The inset shows the number of entries per column.

9.2. Resolution Measurement

The position resolution is investigated using 3 consecutive pixels to form a triplet. The triplet method was already introduced in Chapter 5.5 for the telescope track finding. Figure 9.3 shows a sketch of the beam traversing the sensor. With a rotation around the angle ϕ the number of pixel rows that are hit per column can be changed. The pixel column under investigation is the middle one, depicted as column 1. Columns 0 and 2 are used to calculate reference points.

The triplet residual dy is defined as

$$dy = y_1 - \frac{y_0 + y_2}{2}, \tag{49}$$

where $y_0 - y_2$ are the weighted average y-coordinates of the charge cluster for the respective pixel column.

The resolution is defined as the width of the triplet residual, defined in Equation 49. This residual distribution is greatly influenced by δ-rays, as they shift the cluster's y-positions, see Chapter 2.1.2. The best intrinsic resolution is expected when the charge is always shared over two pixels. The optimal angle for charge sharing over two pixels rows

157
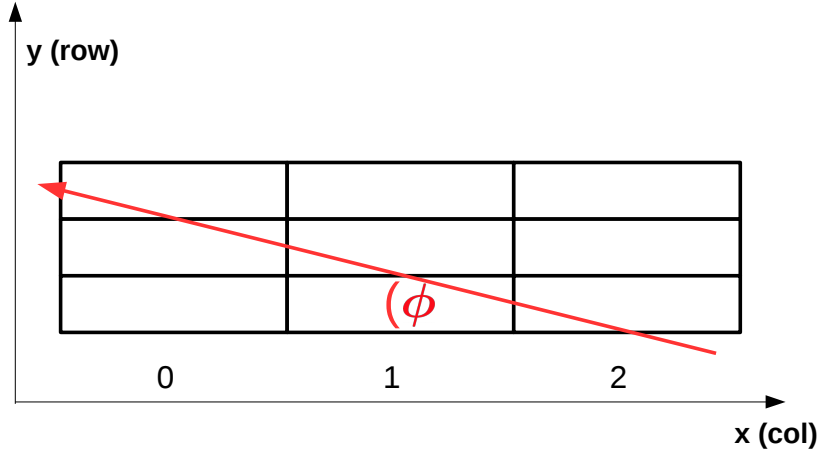
Figure 9.3 – Sketch of the geometry of the setup. The beam, depicted as the red arrow, traverses the sensor under the rotation angle ϕ. Depending on the angle, the charge is shared over a number of rows per pixel column. Column 1 is under investigation, while columns 0 and 2 are used to calculate reference points.

per column is calculated from the geometry for a $25 \times 100\,\mu m^2$ sensor as

$$\arctan\left(\frac{25}{100}\right) = 14.0°. \tag{50}$$

In Figure 9.4 the beam traversing the sensor along all 78 columns is shown and it is visible that on average two pixel rows per pixel column show a signal.

To cross-check the set angle ϕ_set, the track slope m is determined from the measurement itself and the measured angle $\phi_{measured}$ is calculated. The track slope is defined as

$$m = \frac{\Delta y}{\Delta x}\ ,\text{with}\quad \Delta x = x_{enter} - x_{exit}, \tag{51}$$

where Δx (Δy) is the number of columns (rows) the track passes from entering at (x_{enter}, y_{enter}) before exiting the sensor at (x_{exit}, y_{exit}), compare Figure 9.4. The slope is thus defined in number of pixels and for calculation of the angle, the different pixel pitches in x and y have to be considered. With Equation 50, one can also calculate $\phi_{measured}$ of a given track slope as

$$\arctan\left(\frac{25}{100} \cdot m\right) = \phi_{measured}. \tag{52}$$

The mean value of the slope is used for this equation. An example of the track slope for data taken at $\phi_\text{set} = 10°$ is shown in Figure 9.5. With Equation 52 this results in an angle of $\phi_{measured} = 10.26° \pm 0.05°$, where the error on the measured angle is calculated
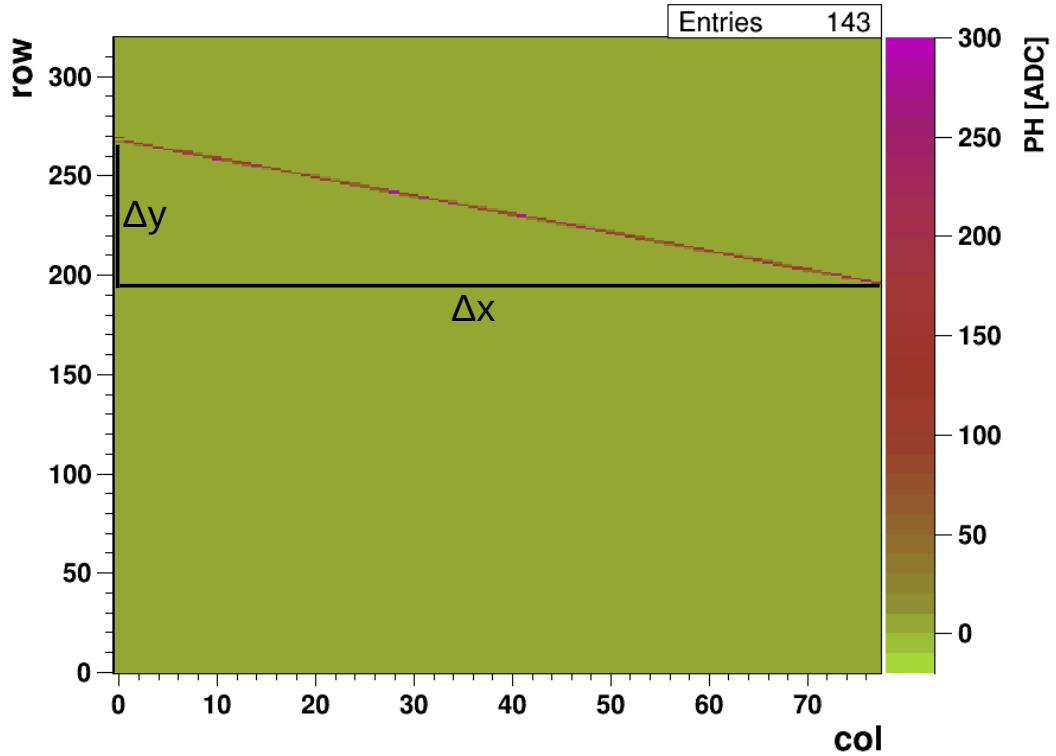
Figure 9.4 – Event display of the beam traversing the sensor $25 \times 100\,\mu m^2$ along all 78 columns at an angle of $\phi_{\text{measured}} = 13°$. At this angle, two pixel rows per column show a signal. The length of the track in pixel columns Δx and rows Δy is used to calculate the track slope.

via error propagation as

$$\Delta\phi_{\text{measured}} = 0.25 \cdot \frac{1}{1 + m^2} \cdot \Delta m \ , \tag{53}$$

where Δm is the error on the mean value of the slope.

All initially set angle values are checked with the measured ones, the ratio can be seen in Figure 9.6. For $\phi_{\text{set}} > 8°$, the angles are nearly identical as their ratio is within 5 percent to 1.

The mean number of hit pixels per column as a function of the rotation angle is shown in Figure 9.7. The average of two pixel rows per column is achieved around 14° as theoretically predicted.

Additional pixel hits due to δ-rays lead to a higher charge, so the residual distributions can be corrected by introducing a cut charge such that the influence of δ-rays is limited. As this analysis is done for a non-irradiated sensor, the gain equalization and gain calibration to ke explained in Chapter 6.2 is used. The Landau distribution of the charge peaks around
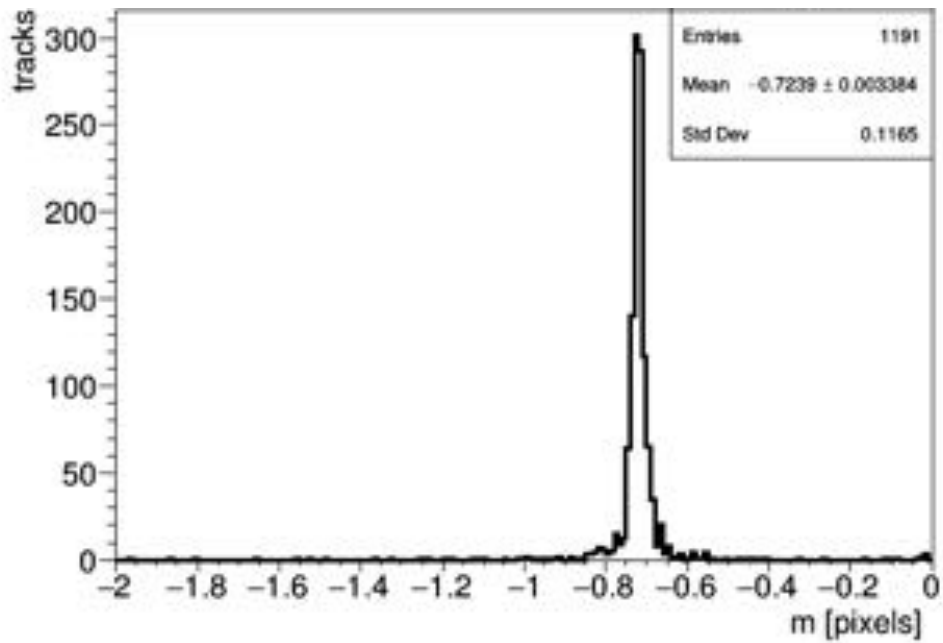
Figure 9.5 – The track slope for data taken at $\phi_{\text{set}} = 10°$. The mean value is used for the calculation of the angle.
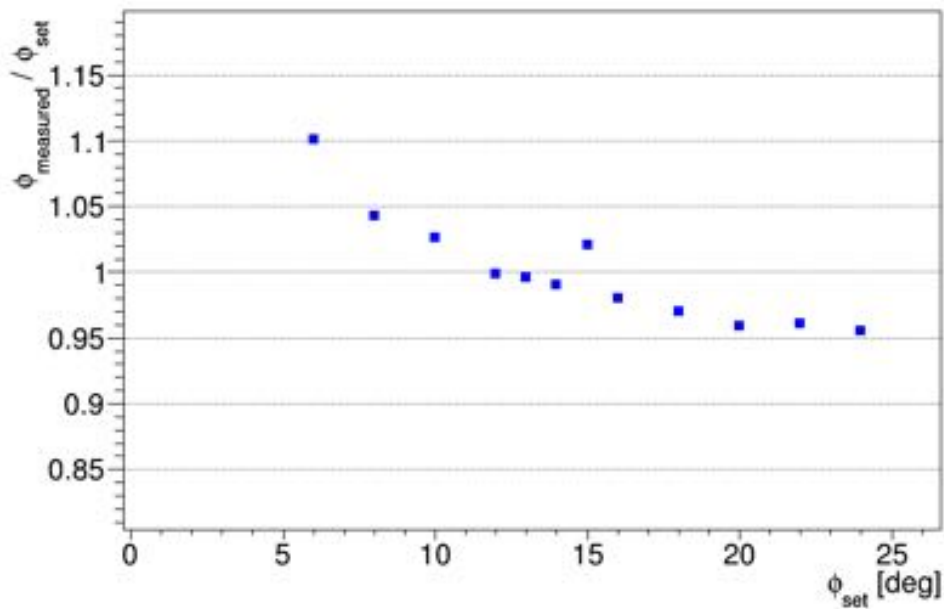
Figure 9.6 – The ratio between the set angle and the measured one. For $\phi_{\text{set}} > 8°$, the angles are within 5 percent of each other.

7 ke, cuts are therefore considered around this MPV, compare Figure 9.8. The track
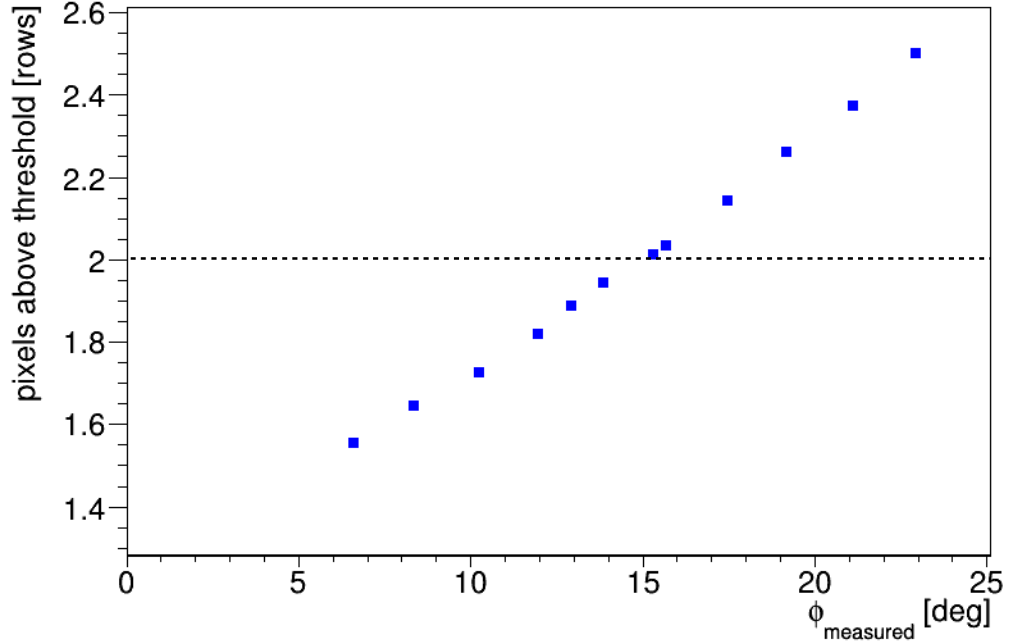
Figure 9.7 – The mean number of pixel rows per column above threshold as a function of the measured rotation angle. An average of two pixel rows per column, indicated by the dashed line, is achieved between 14-15°.

length t_{length} through the silicon at a measured angle is calculated from trigonometry as

$$t_{\text{length}}(\phi_{\text{measured}}) = \frac{100\,\mu\text{m}}{\cos(\phi_{\text{measured}})} \; . \tag{54}$$

The expected MPV is calculated according to H. Bichsel [101] as

$$\text{MPV}_{\text{expected}} = t_{\text{length}} \cdot (100.6 + 35.5 \cdot \ln(t_{\text{length}}) \cdot \frac{1}{I_0} \; , \tag{55}$$

where I_0 is the average energy needed for ionization in silicon. The Landau MPV as a function of angle is shown in Figure 9.9. The measured charge increases with angle by ~1 ke over 16°, which is more than the calculated expected MPV. Differences are likely due to the uncertainty in the charge calibration of the sensor and the non-uniformity of the chip itself in terms of charge. Equation 55 shows that the MPV unlike the mean does not scale linearly with the track length in silicon, compare also [11] p. 451. As the mean of the Landau distribution is strongly influenced by a cut on the charge, it was not considered.

To select a cut on the collected charge, the residual distribution is displayed for different charge intervals at $\phi_{\text{measured}} = 11.2°$ in Figure 9.10. Shown are no restriction on the
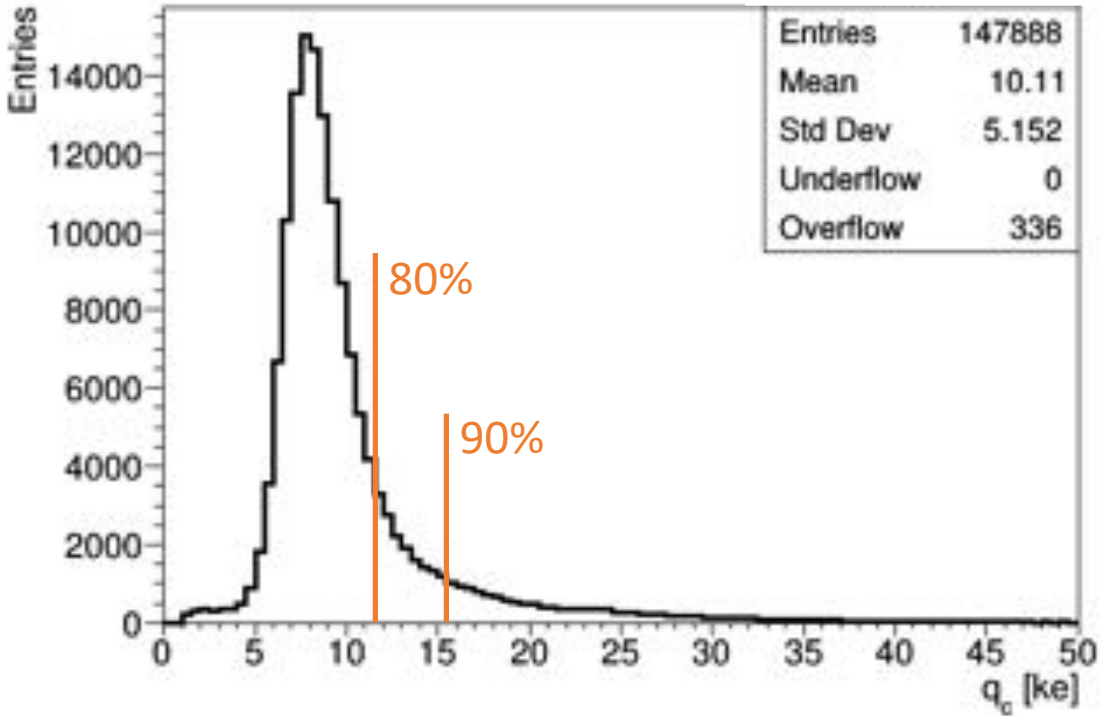
Figure 9.8 – The Landau distribution for data taken with a non-irradiated sensor at an angle of $\phi_{\text{measured}} = 14°$. The MPV is around 7.5 ke, which is expected, as the charge was calibrated to 11 ke for a thickness of 150 μm. The orange lines indicate a cut at 80 % and 90 % of the Landau distribution.

collected charge, $q_c < 11$ ke and $q_c > 11$ke. The charge is restricted accordingly on all three pixel columns. The residual distribution peaks around zero, for $q_c > 11$ke the distribution broadens visibly which is attributed to the influence of delta rays. For $q_c < 11$ ke the residual distribution is narrower and the influence of δ-rays is reduced. As the Landau distribution changes for the different angles, as previously shown in Figure 9.9, a cut of $q_c < 11$ ke might cut deeper into the Landau peak for higher angles. To ensure comparability between measurements, a cut on 80 % of the Landau distribution is chosen, which roughly corresponds to about 11 ke, as shown in Figure 9.8. Therefore for the further analysis of the intrinsic sensor resolution only events with a collected charge within the first 80% of their Landau distribution are analyzed.

The Mean Absolute Deviation (MAD) is defined as

$$\text{MAD } y = |dy| \times \text{pitch}. \tag{56}$$

In Figure 9.11 the MAD is shown as a function of collected charge with the Landau distribution on top. The minimum MAD coincides with the peak of the Landau distribution,
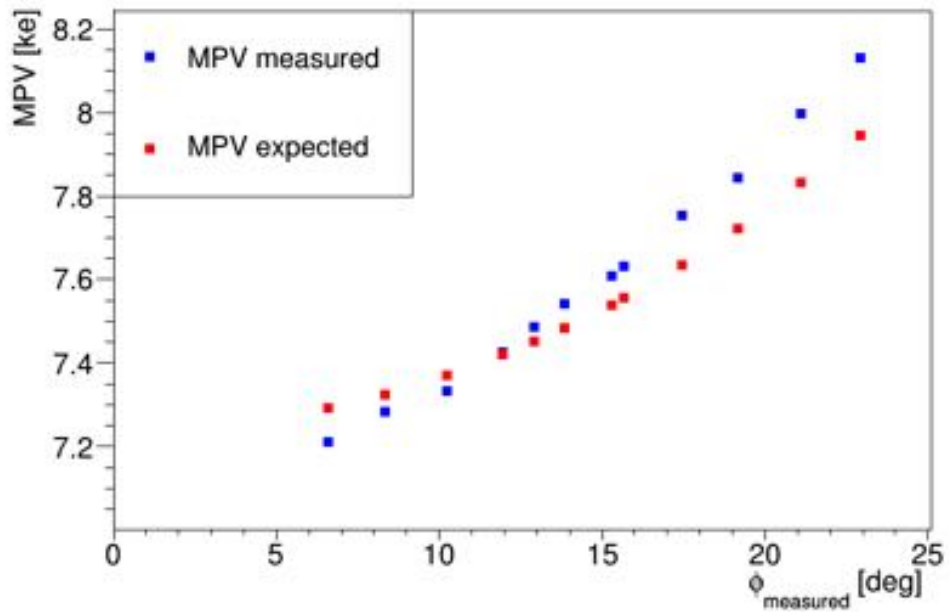
Figure 9.9 – The Landau MPV as a function of incidence angle. The measured charge increases with angle by $\sim$1 ke over 16°.
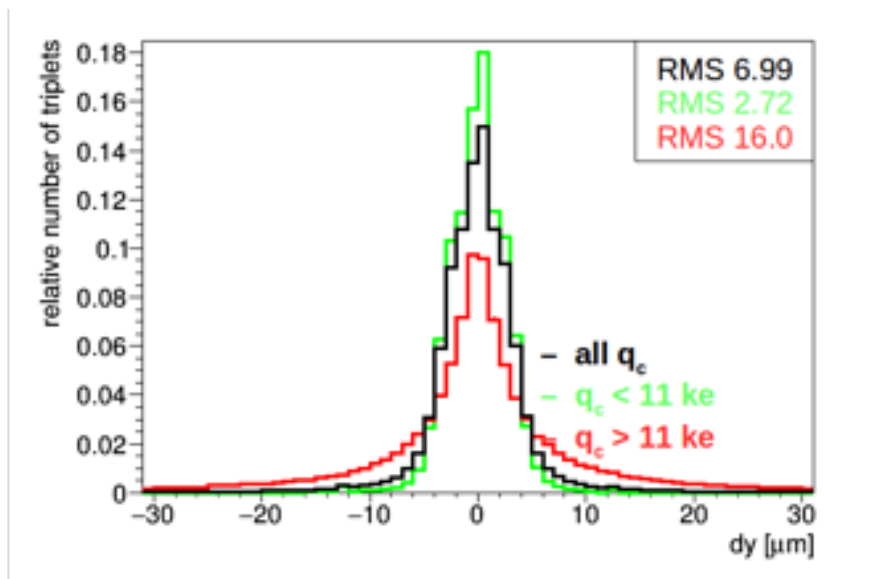
Figure 9.10 – The triplet residual distribution for data taken at an angle of $\phi_{\mathrm{measured}} = 11.2°$. The colors indicate the different restrictions of the charge. Each histogram is normalized to the total number of entries, therefore the relative number of triplets is shown.

from then on the MAD increases with increasing charge. Additional information on the MAD as a function of position in the pixel can be found in Appendix D.

To obtain the intrinsic resolution, the column size of all three pixel columns is limited to
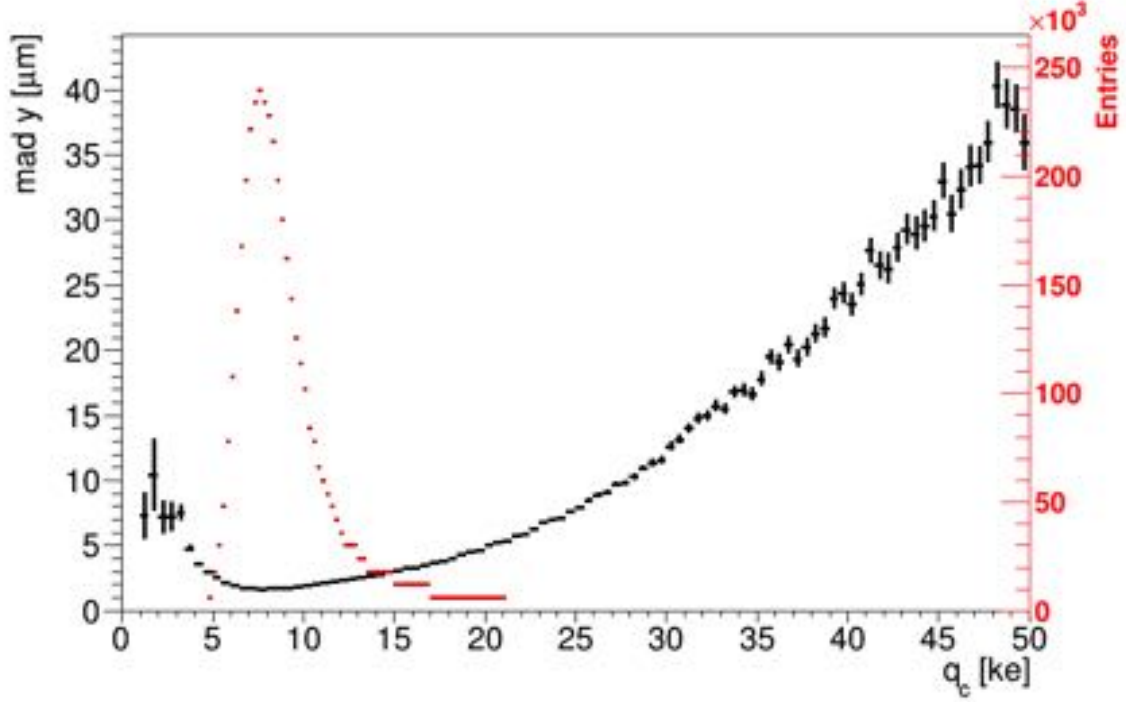
Figure 9.11 – The Mean Absolute Deviation (MAD) as a function of the charge in black overlayed with the Landau distribution in red at $\phi_{\text{measured}} = 11.2°$. The minimum MAD is reached at the peak of the Landau distribution, from there on the MAD increases with increasing charge.

two rows or less. The RMS of the residual distribution of the selected events is calculated. The influence of outliers on the RMS, e.g. δ-rays, is limited due to the cut on the charge and column size. The resolution σ_{DUT} of only one pixel column is calculated from the RMS σ_{dy} of the residual distribution of the three pixel columns as

$$\sigma_{dy} \cdot \frac{\sqrt{3}}{2} = \sigma_{DUT}. \tag{57}$$

The obtained values for the resolution depend on the applied rotation angles, compare Figure 9.12. The resolution has a minimum, when the charge is always shared between two adjacent pixels. The minimum of the resolution is visible for a rotation angle of 14° and the position resolution for a $25 \times 100 \, \mu\text{m}^2$ pixel is determined as $\sigma_{DUT} = 2.0 \, \mu\text{m}$ at $5.6 \, \text{GeV}$ beam momentum with an error on the nanometer scale. In this measurement the resolution was measured in the $25 \, \mu\text{m}$ segmentation of the pixel sensor and the corresponding thickness in this setup is then $100 \, \mu\text{m}$. The error on the resolution $\Delta_{\sigma_{DUT}}$ is

calculated via error propagation from the RMS error as

$$\Delta_{\sigma_{DUT}} = \frac{\sqrt{3}}{2}\Delta_{\sigma_{dy}} \ .$$

(58)
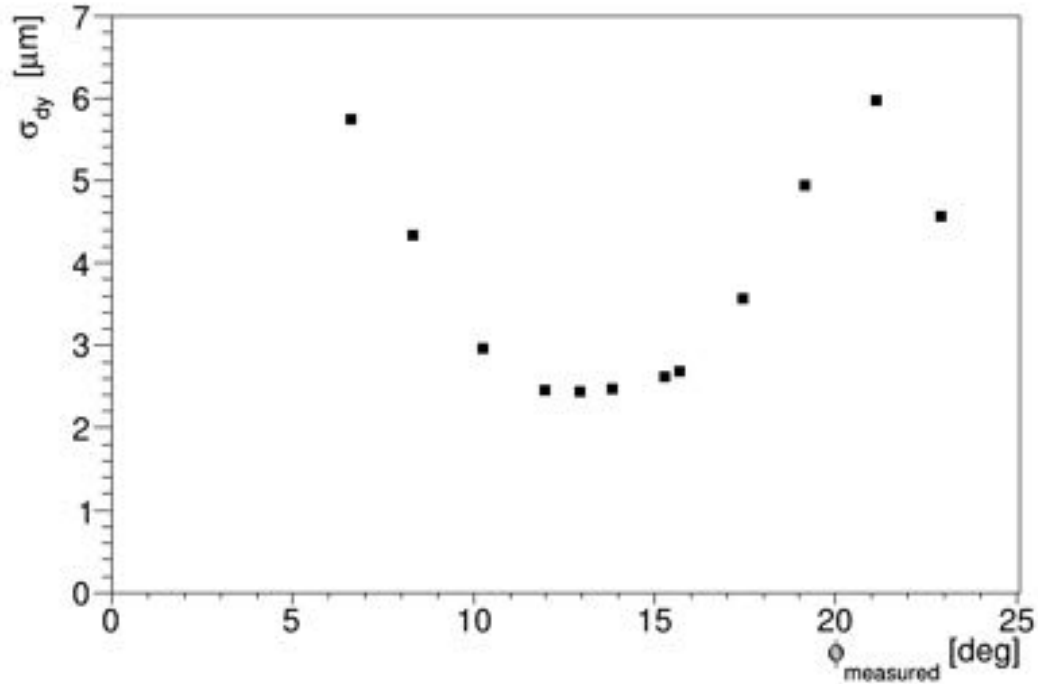
Figure 9.12 – The pixel resolution as a function of the rotation angle. A minimum of the resolution is visible around 14°.

To get an idea on how the resolution of the pixel depends on the active thickness of the sensor, one can also combine two or more columns to define a plane and thus create a larger active thickness. The cut on the charge is adjusted accordingly. The resulting resolutions for the different thicknesses are plotted in Figure 9.13. However, this is only an indicator on how the resolution evolves with thickness, as the beam did not traverse more than 100 μm at a time. In addition, also the resolution obtained by the dreimaster (three consecutive pixel planes) and the spatial resolution from telescope measurements with a $50 \times 50 \,\mu\text{m}^2$ sensor are displayed. For the dreimaster measurements the intrinsic resolution is displayed, as it was extrapolated to infinite beam momentum. The resolution for the dreimaster setup was kindly provided by I. Zoi, UHH. The resolution from telescope measurements with a maximum implant pixel design was provided by F. Feindt, UHH. The resolution from the dreimaster, where the resolution is also measured in the 25 μm segmentation of the pixel sensor but the active thickness is 150 μm, is very similar to the

pixel resolution of the sensor measured in this setup. One difference being, that in the dreimaster analysis the first 90% of the Landau distribution were used, which might lead to a slightly worse resolution, as adding more high charges decreases the resolution, see Figures 9.10 and 9.11. For a direct comparison with the dreimaster setup, the resolution was recalculated using 90 % of the charge distribution, which is a cut at $\sim 15.5\,\mathrm{keV}$. As a result, $\sigma_{DUT} = 2.4\,\mathrm{\mu m}$ with errors on the nanometer level was determined, which is in good agreement with the result from the dreimaster of $\sigma_{DUT} = 2.4 \pm 0.1\,\mathrm{\mu m}$. The resolution for a 3d sensor was taken from [102], it is quoted as 3-4 $\mathrm{\mu m}$ at optimal angle. The 3d sensor was also measured at DESY testbeam with the ROC4SENS. The analysis is very similiar, except for the charge being cut on both sides of the Landau peak. All resolutions are calculated for the optimal angle of each geometry.
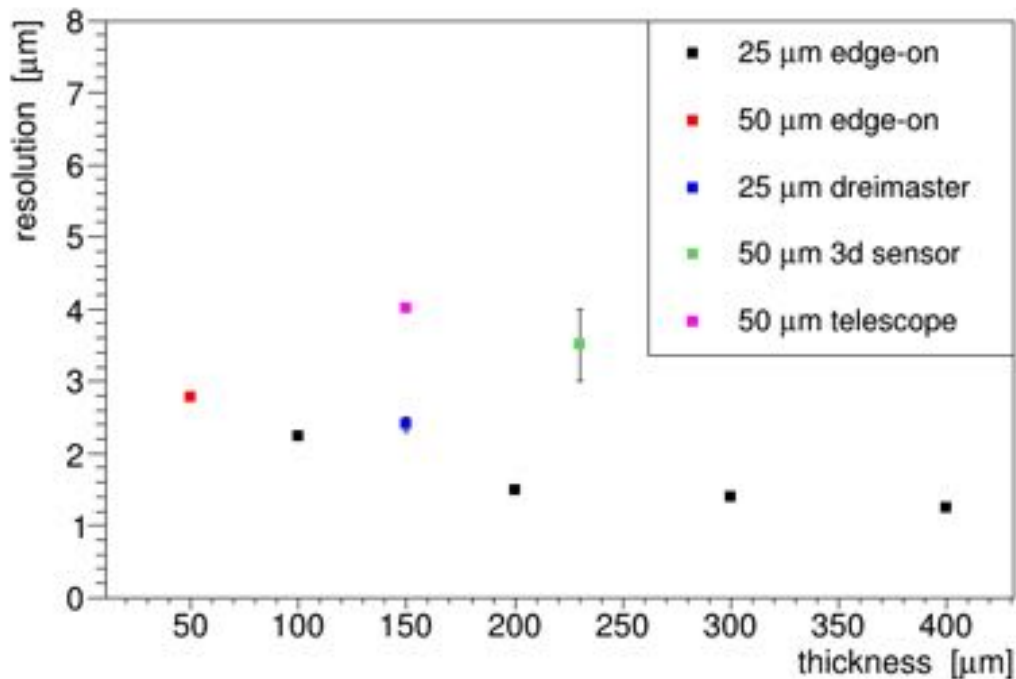
Figure 9.13 – The position resolution as a function of sensor thickness for different measurement setups and sensor geometries. The obtained values are derived from the optimal angle for each geometry.

10. Summary and Conclusion

For the Phase 2 upgrade of the Inner Tracker of the CMS detector, many different designs of n$^+$p, planar pixel sensors with pixel sizes of $50 \times 50\,\mu m^2$ and $25 \times 100\,\mu m^2$ and an active thickness of $150\,\mu m$ have been designed and bump bonded to ROC4SENS read-out chips. The sensors were irradiated to fluences of up to $\Phi_p = 8.68 \times 10^{15}\,cm^{-2}$ at the CERN IRRAD in Geneva and to fluences of up to $\Phi_n = 16 \times 10^{15}\,cm^{-2}$ at the TRIGA MARK II reactor in Ljubljana. The sensors were investigated with the DATURA telescope at the Beamline 21 of the DESY Test Beam facility.

Previous studies into the dependence of charge collection on the depth in the silicon sensor have applied the grazing angle technique. However, with thinner sensors this method suffers a lot from resolution effects. Therefore the grazing angle technique was refined to the edge-on method, where the beam hits the sensor parallel to the sensor surface and travels at one depth through the entire length of the sensor. For the edge-on setup with the cooling box, the telescope track resolution at the position of the sensor was determined as $\sigma_{track} = 11.00 \pm 0.27\,\mu m$.

In this thesis, the edge-on method is used to measure the charge collection of $25 \times 100\,\mu m^2$ pixel sensors as a function of depth for different operating conditions. Reference measurements with a non-irradiated sensor and chip were performed. With test pulse measurements, the difference in gain between all $24\,000$ pixels of the ROC4SENS was measured as 3% without irradiation. After irradiation, the test pulses indicate a spread between the pixel responses of up to 8%. For the non-irradiated sensor, these differences can be compensated by a gain equalization and calibration of the charge to the expected charge deposition of a MIP transversing $150\,\mu m$ of silicon, as the relation between charge and voltage of the test pulse of the ROC4SENS is not well known. Furthermore, delay scans indicate that the pulse shape of the test pulse and the test beam data are different for irradiated sensors. The difference in gain between different non-irradiated chips with the settings used at test beam was determined as 7%.

The influence of radiation damage from neutrons and $23\,GeV$ protons on the charge collection profile is compared. As the total signal consists of electrons and holes, it is possible to gain information on their respective signal contribution after irradiation. The signal of charges generated close to the implant is dominated by hole drift and therefore allows to investigate the effect of hole trapping and the signal of charges generated close to the backside provides information on the electron trapping. For neutron irradiated sensors,

the charge collection profile exhibits for all fluences a steep decline towards the backside, which is attributed to the steep decline in the electric field. No double-junction was visible for neutron irradiated sensors. In comparison, for proton irradiated sensors at low bias voltages an indication of an increased charge collection at the backside was found. As an absolute charge calibration of the ROC4SENS is not possible, measurements on different sensors irradiated to different fluences cannot be directly compared. Therefore, only the non-homogeneous proton irradiation allowed for a comparison of different fluences on the same sensor. The total collected charge decreases with fluence. The biggest difference in charge collection for the different fluences of one sensors is found at small bias voltages, where the differences are already visible in the charge collection profiles. In addition, the temperature dependence of the charge collection was measured. The measurement temperature was determined from the leakage current of the sensor. A rise in temperature of $12°C$ leads to 15% less total collected charge, whereas about 7% difference was found in previous measurements. However, the measurements in this thesis and the previous ones both suggest no saturation of the charge collection for sensors irradiated to $\Phi_{eq} > 5 \times 10^{15}\,\mathrm{cm}^{-2}$ for bias voltages below $800\,\mathrm{V}$.

From fits to the edges of charge collection profile the active thickness of the different sensors materials has been determined. For a non-irradiated FDB sensor an active thickness of $146 \pm 1\,\mathrm{µm}$ was determined and for a proton-irradiated FTH sensor an active thickness of $148 \pm 1\,\mathrm{µm}$. The sensors were ordered with an active thickness of $150 \pm 10\,\mathrm{µm}$, so the differences are within the specifications. With the same method the charge collection depth as a function of fluence has been investigated. It was shown, that the charge collection depth decreases with increasing fluence. This change in active sensor depth needs to be taken into account for resolution studies, as it changes the optimal angle for charge sharing. The optimal angle increases with increasing fluence.

Due to the non-zero suppressed chip, the negative charge induced in the neighboring pixels was visualized for the first time. With these so called edge-on tomography plots, it is possible to investigate the charge sharing between the neighboring pixels in the $25\,\mathrm{µm}$ direction perpendicular to the beam. Also the diffusion of charge across multiple pixels at the sensor backside is reflected for different bias voltages. For irradiated sensors, a particle track going through the readout pixel induces negative charge close to the pixel implant in the next-neighbor pixels. The negative charges are attributed to the non-symmetrical weighting field for the next-neighbor pixel implants. It was shown that the negative charges appear for irradiations below $\Phi_{eq} = 5 \times 10^{15}\,\mathrm{cm}^{-2}$ only at bias voltages

under 400 V. For higher irradiations the negative charges appear already at 800 V.

Furthermore, the position resolution of the pixel cell itself was measured for different angles of beam incidence without an external beam telescope as a reference plane. Instead the pixels before and after the hit pixel itself are used as reference and thus allow for in-silicon tracking as the beam hits the sensor edge-on. The resolution for a $25 \times 100 \, \mu m^2$ pixel sensor was determined to be 2.2 µm with errors on the nanometer level. The result is in good agreement with the intrinsic sensor resolution from the dreimaster setup, where the active thickness of the sensor is 150 µm instead of 100 µm as for the edge-on measurement.

As an outlook, the charge collection profiles obtained in this analysis can be used to further improve the Hamburg Penta Trap model. As of now, the HPTM does not use any position-dependent information as input but still at least qualitatively reproduces the charge collection as a function of depth at different bias voltage in a highly irradiated sensor ($\Phi_{eq} > 5 \times 10^{15} \, cm^2$). It was shown that the voltage dependence of the charge collection profiles needs to be improved. For a better understanding of the charge trapping, the trapping times can be varied depending on their position in the sensor. Furthermore, the fluence dependence of the trapping times can be investigated further, as not much data exist for these high irradiation fluences. Additionally, the HPTM can be expanded to also include damage from neutrons for a better comparison between different irradiation particles. With these measurements further insight into the macroscopic effects of radiation damage of different particles on the sensor performance is provided which can be used in the refinement of models describing the position dependent radiation damage in silicon pixel sensors.

Appendices

A. Additional Sensor Designs

This section provides the geometries of additional pixel designs from the CMS Phase II pixel campaign and an overview of all sensors analyzed in this thesis. In Figure A.1 the geometry of a maximum implant design is shown. The sensors analyzed in this thesis, with irradiations of $\Phi_p = 8.68 \times 10^{15}\,\mathrm{cm^{-2}}$ and $\Phi_n = 16 \times 10^{15}\,\mathrm{cm^{-2}}$ are maximum implant designs. The default design is shown in Figure 4.2. An overview of all sensors and their properties is given in Table 11.
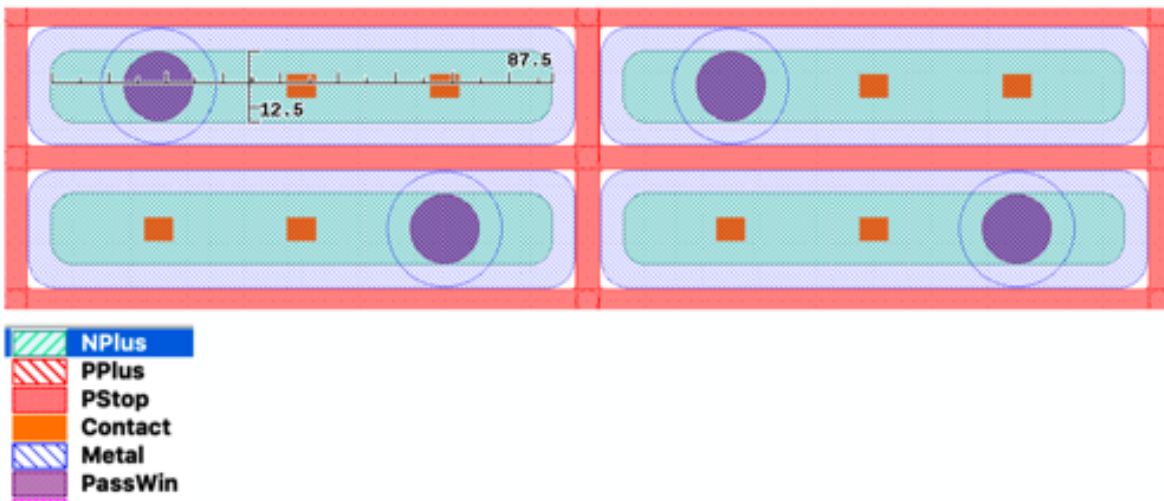
Figure A.1 – Geometry of a maximum implant design. The sensors analyzed in this thesis, with irradiations of $\Phi_p = 8.68 \times 10^{15}\,\mathrm{cm^{-2}}$ and $\Phi_n = 16 \times 10^{15}\,\mathrm{cm^{-2}}$ are maximum implant designs.
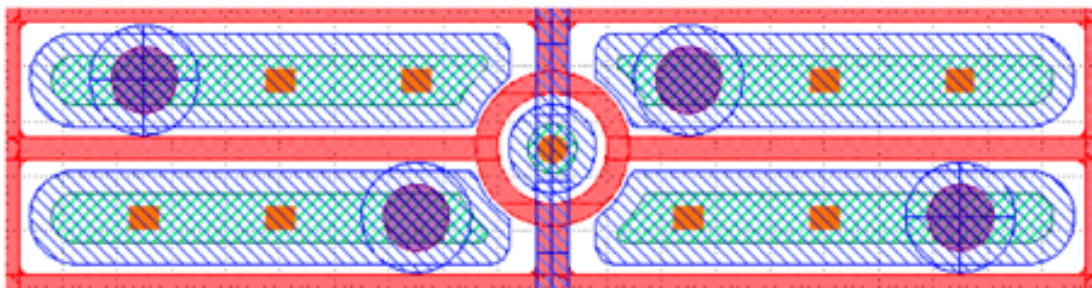
Figure A.2 – Design of a pixel sensor with a bias dot. Color legend as in Figure A.1.

Module No.	Wafer Material	Sensor Design	Fluence $[10^{15}\,\mathrm{cm}^{-2}]$
120	FTH	default	$\Phi_p = 3.3$
193	FTH	max. implant	$\Phi_p = 6.6$
194	FDB	default	$\Phi_n = 0.6$
195	FDB	default	$\Phi_n = 4$
196	FDB	default	$\Phi_n = 8$
197	FDB	max. implant	$\Phi_n = 16$
223	FDB	default	$\Phi = 0$

Table 11 – Overview of the sensors and their properties analyzed in this thesis.

B. Additional Distributions

This section provides additional monitoring plots used during data taking and the later event selection. Figure B.1 shows the number of reconstructed triplets from the telescope hits for a non-irradiated sensor at 120 V bias voltage. Per event there is still an average of two tracks. The triplet method is explained in Chapter 5.5. After using the reference module as a timing reference, the number reduces to an average of one, see Figure B.2.

Entries	240400
Mean	2.108
Std Dev	1.352
Underflow	0
Overflow	0
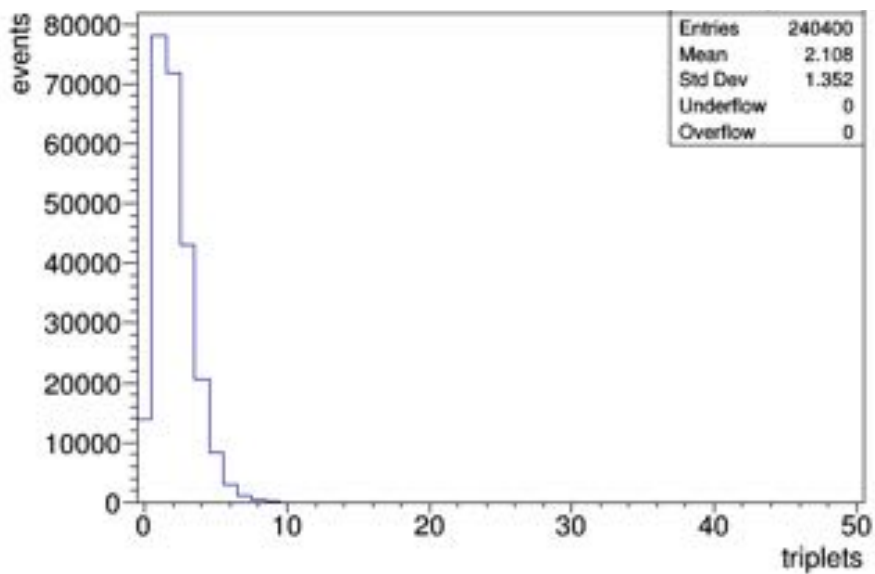
Figure B.1 – Number of triplets per event for the non-irradiated sensor at 120 V bias voltage.

During data taking, the RMS of the pixel hits is monitored and shown for an irradiated sensor at 800 V bias voltage in Figure B.3. With the hit definition of four times the noise, explained in Chapter 6.1, this leads to a hit needing at least $\sim$24 ADC.
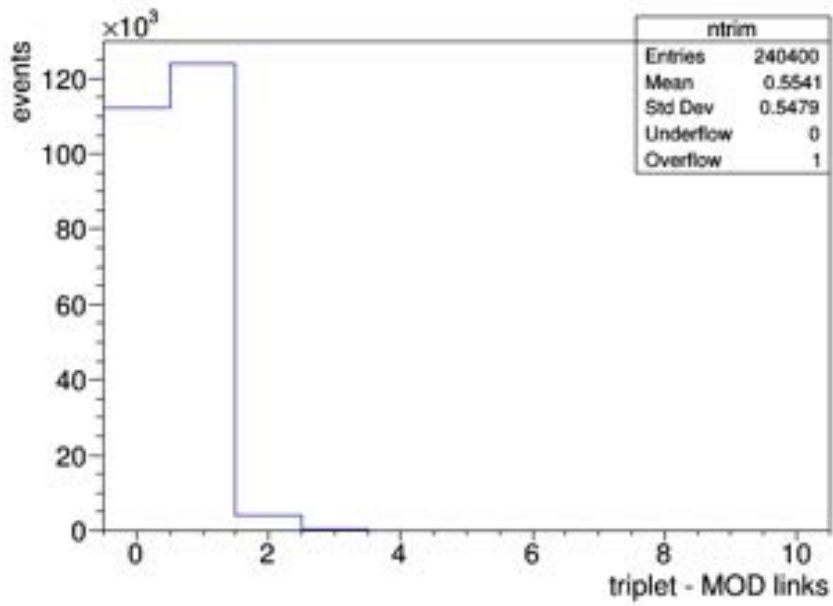
Figure B.2 – Number of triplets per event with link in the module for the non-irradiated sensor at 120 V bias voltage.
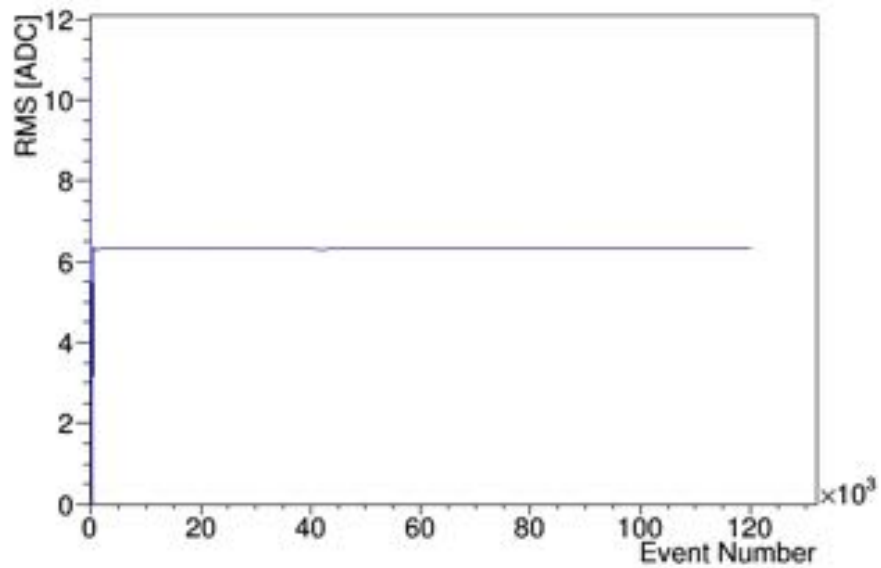
Figure B.3 – The RMS of ΔPH for a sensor irradiated to $\Phi_p = 3.3 \times 10^{15}\,\mathrm{cm}^{-2}$ at 800 V bias voltage.

C. Signal Definition: Total Collected Charge

This section provides the differences in the collected charge at different bias voltages for a sensor irradiated to $\Phi_p = 8.68 \times 10^{15}\,\mathrm{cm}^{-2}$ for the different signal definitions in Chapter 7.1.2.

<div align="center">

800 V   400 V

250 V   150 V

</div>
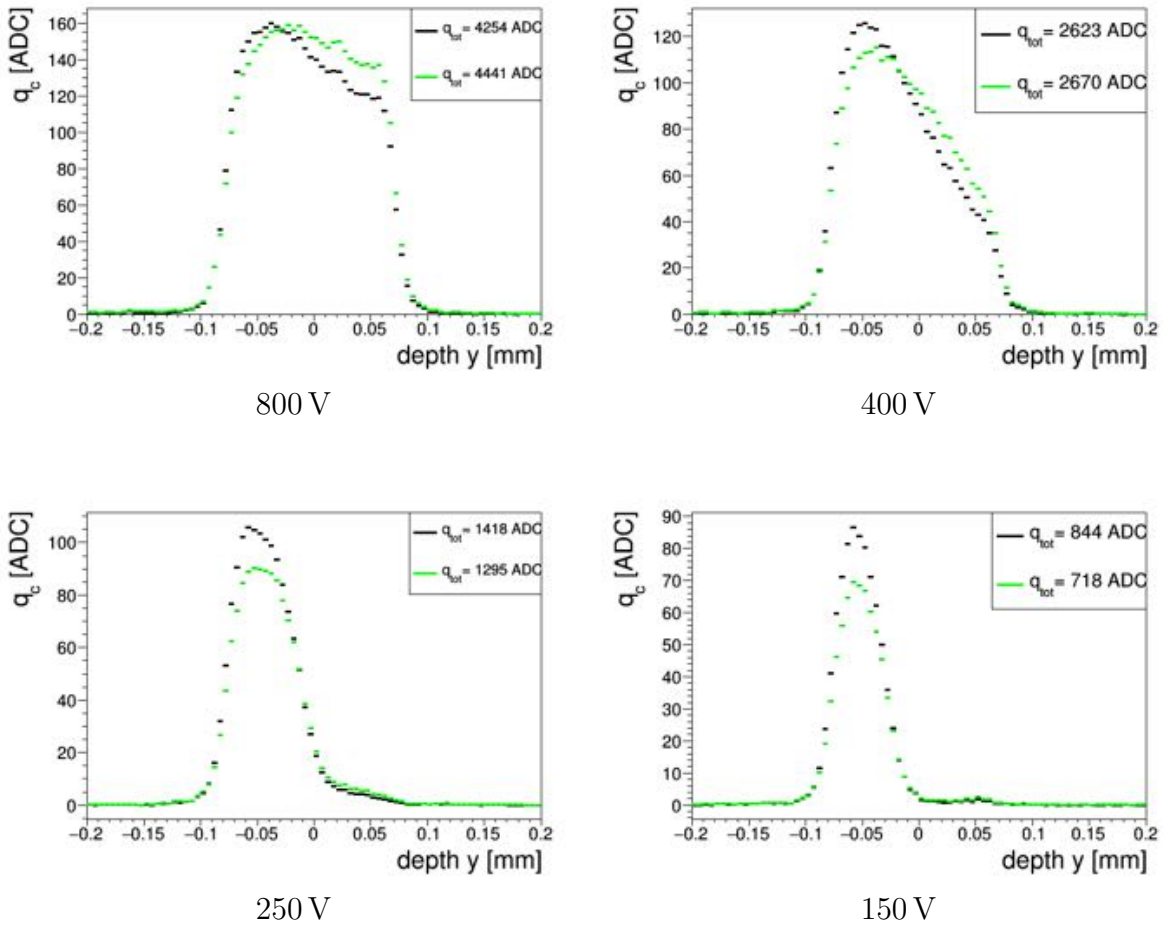
Figure C.1 – Comparison of the different signal definitions for a sensor irradiated to $\Phi_p = 8.68 \times 10^{15}\,\mathrm{cm}^{-2}$. In black the sum of 3 pixels and in green the sum of 5 pixels. Only at 800 V and 400 V the sum of 5 pixels results in a higher charge.

D. Pixel Resolution: Position-Dependent Distributions

This chapter provides additional information and in-pixel distributions of the analysis into the intrinsic resolution of the pixel sensors. All distributions are at an angle of $\phi_{\mathrm{measured}} = 11.2°$ for a $25 \times 100\,\mathrm{\mu m}^2$ pixel sensor. The MAD as a function of pixel columns is shown in Figure D.1. It is stable over the entire sensor, so no column dependence is visible.
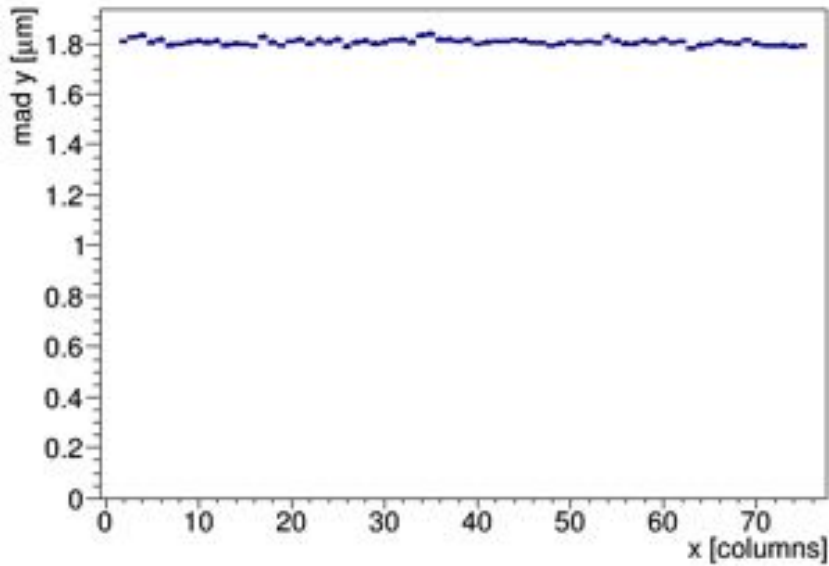
Figure D.1 – The MAD as a function of pixel columns, no column dependence is visible.

The residual dy as a function of position in the pixel is shown in Figure D.2. The pixel pitch in the y-direction is $25\,\mathrm{\mu m}$, so around the middle of the pixel the absolute residual increases, while at the pixel edges, where the charge is shared over more pixels the residuals is close to 0. Here the position is calculated from the information of two pixels and thus more precise. Figure D.3 shows the corresponding distribution of the number of pixels that are above threshold as a function of the position in pixel. If the beam hits the pixel in its middle, the charge is only deposited under this pixel, so the number of pixels is 1. If the beam hits close to the middle, only a fraction of charge is collected in an adjacent pixel, which might still be below threshold and thus the position used for the residual calculation is slightly off, leading to the maxima of the residual in Figure D.2. Towards the pixel edges the charge is always shared over two pixels.

The charge correlation between the charge registered in plane 0 q_0 and in plane 1 q_1 is shown in Figure D.4. As expected for the edge-on incidence, if a hit around the Landau peak of $7\,\mathrm{ke}$ is registered in plane 0 it is also registered in plane 1. Sometimes a delta ray
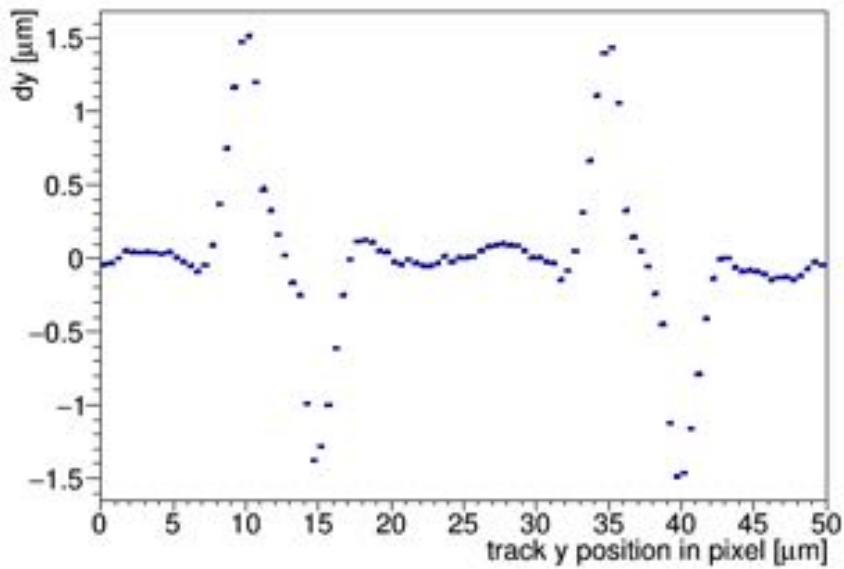
Figure D.2 – The residual as a function of position in the pixel. Around the middle of the pixel at $12.5\,\mu\text{m}$, the residual increases. Towards the pixel edges, where the charge is shared over two pixel the residual is at its minimum.
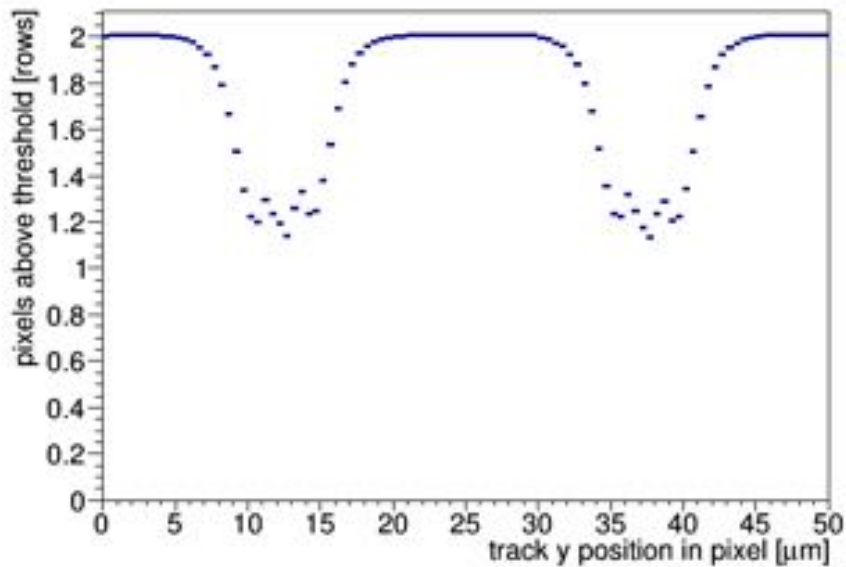
Figure D.3 – The number of pixels above threshold as a function of position in the pixel. Towards the pixel edges, charge is always shared over 2 pixels. Only if the beam hits the middle of the pixel, it is registered only in this pixel. The more the beam deviates from the middle the more pixels share the charge.

splitting off nearly perpendicular to the beam can lead to more charge in one plane, while the other only registers the beam particle.
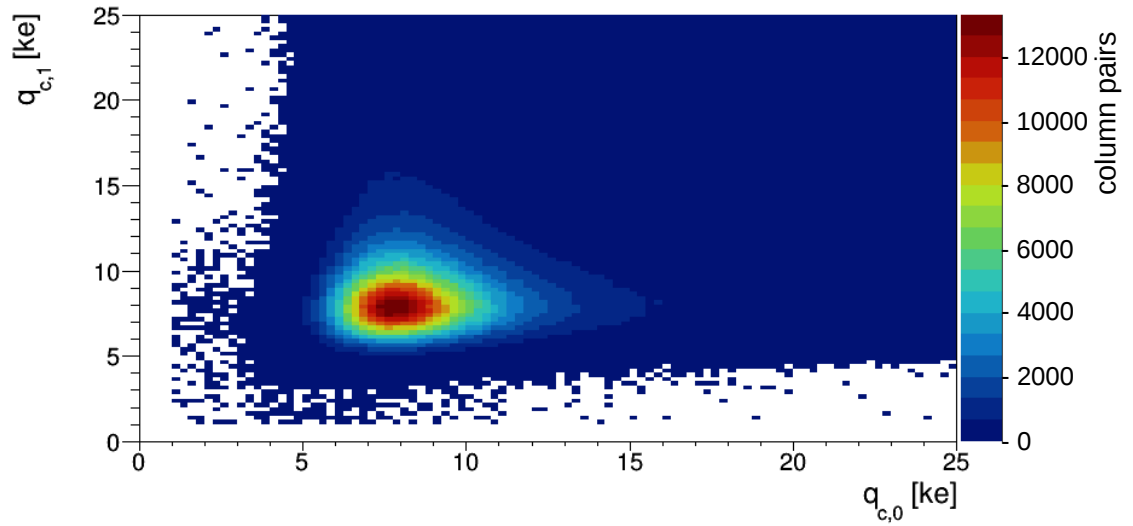
Figure D.4 – The charge correlation between the charge registered in column 0 and column 1. The majority of hits is centered around the Landau peak value of $7\,\text{ke}$ (red area).

List of Figures

List of Tables

List of Acronyms

ADC	Analog-to-Digital Converter
APD	Avalanche Photodiode
BPIX	Barrel Pixel Detector
CCE	Charge Collection Efficiency
CMOS	Complementary Metal-Oxide Semiconductor
CMS	Compact Muon Solenoid
CSC	Cathode Strip Chamber
DATURA	DESY Advanced Telescope Using Readout Acceleration
DT	Drift Tube
DTB	Digital Test Board
DUT	Device Under Test
EB/EE	Electromagnetic Barrel/Endcap Calorimeter
ECAL	Electromagnetic Calorimeter
FDB	Float Zone Direct Bonded
FPGA	Field-Programmable Gate Array
FPIX	Forward Pixel Detector
FTH	Float Zone Thinned
FWHM	Full Width Half Maximum
GEM	Gas Electron Multiplier
HB/HE/HF/HO	Hadronic Barrel/Endcap/Forward/Outer Calorimeter
HCAL	Hadronic Calorimeter
HDI	High Density Interconnect
HLT	High Level Trigger
HPD	Hybrid Phoodiode
HPTM	Hamburg Penta Trap Model
IP	Interaction Point
IT	Inner Tracker
LHC	Large Hadron Collider
MAD	Mean Absolute Deviation
MIP	Minimum Ionizing Particle
MOD	Reference Module
MPV	Most Probable Value
NIEL	Non-Ionizing Energy Loss
OT	Outer Tracker
PCB	Printed Circuit Board

PFET	P-channel Field-Effect Transistor
PMT	Photo Multiplier Tube
PU	Pileup
PS	Proton Synchrotron
RBI	Read Bit In
RBO	Read Bit Out
RMS	Root Mean Square
RPC	Resistive Plate Chamber
ROC	Read Out Chip
ROI	Region Of Interest
SCR	Space Charge Region
SiPM	Silicon Photomultiplier
TBM	Token Bit Manager
TCAD	Technology Computer Aided Design
TLU	Trigger Logic Unit
TSC	Thermally Stimulated Current
WLS	Wavelength Shifting

References

[1] A. Stevenson and C. A. Lindberg. *New Oxford American Dictionary*. Oxford University Press, 2011. ISBN: 9780195392883. URL: `https://www.oxfordreference.com/view/10.1093/acref/9780195392883.001.0001/acref-9780195392883`.

[2] S. L. Glashow. "Partial-symmetries of weak interactions". In: *Nuclear Physics* 22.4 (1961), pp. 579–588. ISSN: 0029-5582. DOI: `https://doi.org/10.1016/0029-5582(61)90469-2`.

[3] A. Einstein. "Ist die Trägheit eines Körpers von seinem Energieinhalt abhängig?" In: *Annalen der Physik 18* (1905), pp. 639–641.

[4] S. Middelhoek et al. "Silicon sensors". In: *Measurement Science and Technology* 6.12 (1995), pp. 1641–1658. DOI: `10.1088/0957-0233/6/12/001`.

[5] D. Bortoletto. "How and why silicon sensors are becoming more and more intelligent?" In: *Journal of Instrumentation* 10.08 (2015), p. C08016. DOI: `10.1088/1748-0221/10/08/c08016`.

[6] F. Hartmann. *Evolution of Silicon Sensor Technology in Particle Physics*. Springer International Publ., 2017. ISBN: 978-3-319-64434-9. DOI: `10.1007/978-3-319-64436-3`.

[7] S. Tkaczyk et al. "The CDF silicon vertex detector". In: *Nuclear Instruments and Methods in Physics Research Section A: Accelerators, Spectrometers, Detectors and Associated Equipment* 342.1 (1994), pp. 240–250. ISSN: 0168-9002. DOI: `10.1016/0168-9002(94)91434-6`.

[8] N. Wermes et al. *Pixel Detectors, From Fundamentals to Applications*. Springer-Verlag, 2006. ISBN: 3-540-28332-3. DOI: `10.1007/3-540-28333-1`.

[9] P. Schütze. "Silicon Pixel Detectors - Performance after Irradiation and Application in Three-dimensional imaging". Ph.D. thesis. Universität Hamburg, 2019. URL: `https://bib-pubdb1.desy.de/record/429067`.

[10] J. R. Fiebiger and R. S. Muller. "Pair-Production Energies in Silicon and Germanium Bombarded with Low-Energy Electrons". In: *Journal of Applied Physics* 43.7 (1972), pp. 3202–3207. DOI: `10.1063/1.1661685`.

[11] M. Tanabashi et al. "Review of Particle Physics". In: *Phys. Rev. D* 98 (3 2018), p. 030001. DOI: `10.1103/PhysRevD.98.030001`.

[12] L. D. Landau. "On the energy loss of fast particles by ionization". In: *Journal of Physics* 8.4 (1944), pp. 201–205. URL: `https://cds.cern.ch/record/216256`.

[13] J. Schwandt and R. Klanner. "On the weighting field of irradiated silicon detectors". In: *Nuclear Instruments and Methods in Physics Research Section A: Accelerators, Spectrometers, Detectors and Associated Equipment* 942 (2019), p. 162418. ISSN: 0168-9002. DOI: `10.1016/j.nima.2019.162418`.

[14] H. Spieler. "Semiconductor Detector Systems". In: (2007). DOI: `10.1093/acprof:oso/9780198527848.001.0001`.

[15] C. Jacoboni et al. "A review of some charge transport properties of silicon". In: *Solid-State Electronics* 20.2 (1977), pp. 77–89. ISSN: 0038-1101. DOI: `https://doi.org/10.1016/0038-1101(77)90054-5`.

[16] E. J. Schioppa et al. "Study of Charge Diffusion in a Silicon Detector Using an Energy Sensitive Pixel Readout Chip". In: *IEEE Transactions on Nuclear Science* 62.5 (2015), pp. 2349–2359. ISSN: 0018-9499. DOI: `10.1109/TNS.2015.2475124`.

[17] V. L. Vinetskii and G. A. Kholodar. "CHAPTER 5 - Quasichemical Reactions Involving Point Defects in Irradiated Semiconductors". In: *Physics of Radiation Effects in Crystals*. Ed. by R.A. JOHNSON and A.N. ORLOV. Vol. 13. Modern Problems in Condensed Matter Sciences. Elsevier, 1986, pp. 283–344. DOI: `10.1016/B978-0-444-86946-3.50011-5`.

[18] V. Chiochia and M. Swartz and Y. Allkofer and D. Bortoletto and L. Cremaldi and S. Cucciarelli and A. Dorokhov and C. Hörmann and D. Kim and M. Konecki and D. Kotlinski and K. Prokofiev and C. Regenfus and T. Rohe and D.A. Sanders and S. Son and T. Speer. "A double junction model of irradiated silicon pixel sensors for LHC". In: *Nuclear Instruments and Methods in Physics Research Section A: Accelerators, Spectrometers, Detectors and Associated Equipment* (2006). New Developments in Radiation Detectors. ISSN: 0168-9002. DOI: `https://doi.org/10.1016/j.nima.2006.05.199`. URL: `https://www.sciencedirect.com/science/article/pii/S0168900206010850`.

[19] A. Vasilescu. *The NIEL scaling hypothesis applied to neutron spectra of irradiation facilities and in the ATLAS and CMS SCT*. Tech. rep. ROSE/TN/97-2. 1997.

[20] Michael Moll. "Radiation damage in silicon particle detectors: Microscopic defects and macroscopic properties". Ph.D. Thesis, Universität Hamburg, 1999. PhD thesis, p. 251. URL: `http://bib-pubdb1.desy.de/record/300958`.

[21] A. Vasilescu and G. Lindströem. *Notes on the fluence normalisation based on the NIEL scaling hypothesis*. Tech. rep. ROSE/TN/2000-02. 1997.

[22] Ioana Pintilie et al. "Radiation-induced point- and cluster-related defects with strong impact on damage properties of silicon detectors". In: *Nuclear Instruments and Methods in Physics Research Section A: Accelerators, Spectrometers, Detectors and Associated Equipment* 611.1 (2009), pp. 52–68. ISSN: 0168-9002. DOI: `10.1016/j.nima.2009.09.065`.

[23] M. Huhtinen. "Simulation of non-ionising energy loss and defect formation in silicon". In: *Nuclear Instruments and Methods in Physics Research Section A: Accelerators, Spectrometers, Detectors and Associated Equipment* 491.1 (2002), pp. 194–215. ISSN: 0168-9002. DOI: `10.1016/S0168-9002(02)01227-5`.

[24] E. Mobs. *The CERN accelerator complex - August 2018. Complexe des accélérateurs du CERN - Août 2018*. General Photo. 2018. URL: `https://cds.cern.ch/record/2636343`.

[25] O. S. Brüning et al. *LHC Design Report*. CERN Yellow Reports: Monographs. CERN, 2004. URL: `https://cds.cern.ch/record/782076`.

[26] B. Schmidt. "The High-Luminosity upgrade of the LHC: Physics and Technology Challenges for the Accelerator and the Experiments". In: *Journal of Physics: Conference Series* 706 (2016), p. 022002. DOI: `10.1088/1742-6596/706/2/022002`.

[27] *CMS detector website*. URL: `https://cms.cern/detector`.

[28] E. Focardi. "Status of the CMS Detector". In: *Physics Procedia* 37 (2012), pp. 119–127. DOI: `10.1016/j.phpro.2012.02.363`.

[29] A. Dominguez and et al. *CMS Technical Design Report for the Pixel Detector Upgrade*. 2012. DOI: `10.2172/1151650`.

[30] D. Pitzl et al. "Type inversion in silicon detectors". In: *Nuclear Instruments and Methods in Physics Research Section A: Accelerators, Spectrometers, Detectors and Associated Equipment* 311.1 (1992), pp. 98–104. ISSN: 0168-9002. DOI: `10.1016/0168-9002(92)90854-W`.

[31] M. Meinhard et al. "Performance of the modules for layer 1 of the CMS phase 1 pixel detector upgrade". In: *Journal of Instrumentation* 12.12 (2017), p. C12002. DOI: `10.1088/1748-0221/12/12/c12002`.

[32] H. C. Kästli. "Frontend electronics development for the CMS pixel detector upgrade". In: *Nuclear Instruments and Methods in Physics Research Section A: Accelerators, Spectrometers, Detectors and Associated Equipment* 731 (2013), pp. 88–91. ISSN: 0168-9002. DOI: `10.1016/j.nima.2013.05.056`.

[33] J. Antonelli. *FPix Module Testing Reference Guide*. 2015.

[34] CMS Collaboration. "Test beam performance measurements for the Phase I upgrade of the CMS pixel detector". In: *Journal of Instrumentation* 12.05 (2017), P05022. DOI: `10.1088/1748-0221/12/05/p05022`.

[35] CMS Collaboration. *The Phase-2 Upgrade of the CMS Tracker*. Tech. rep. CERN-LHCC-2017-009. CMS-TDR-014. Geneva: CERN, 2017. URL: `https://cds.cern.ch/record/2272264`.

[36] R. Arcidiacono. "The CMS ECAL Phase-2 Upgrade for High Precision Timing and Energy Measurements". In: *2018 IEEE Nuclear Science Symposium and Medical Imaging Conference Proceedings (NSS/MIC)*. 2018, pp. 1–2. DOI: `10.1109/NSSMIC.2018.8824584`.

[37] The CMS Collaboration. *CMS Physics: Technical Design Report Volume 1: Detector Performance and Software*. Technical Design Report CMS. Geneva: CERN, 2006. URL: `http://cds.cern.ch/record/922757`.

[38] D. Contardo et al. *Technical Proposal for the Phase-II Upgrade of the CMS Detector*. Tech. rep. CERN-LHCC-2015-010. LHCC-P-008. CMS-TDR-15-02. Geneva, 2015. URL: `https://cds.cern.ch/record/2020886`.

[39] The CMS Collaboration. "The CMS experiment at the CERN LHC". In: *Journal of Instrumentation* 3.8 (2008), S08004. DOI: `10.1088/1748-0221/3/08/s08004`.

[40] M. Titov. *Perspectives of Micro-Pattern Gaseous Detector Technologies for Future Physics Projects*. 2013. arXiv: `1308.3047 [physics.ins-det]`.

[41] *The CMS muon project: Technical Design Report*. Technical Design Report CMS. Geneva: CERN, 1997. URL: `http://cds.cern.ch/record/343814`.

[42] The CMS collaboration. "Performance of CMS muon reconstruction in pp collision events at $\sqrt{s} = 7\,\text{TeV}$". In: *Journal of Instrumentation* 7.10 (2012), P10002. DOI: `10.1088/1748-0221/7/10/p10002`.

[43] The CMS Collaboration. "The CMS trigger system". In: *Journal of Instrumentation* 12.1 (2017), P01020. DOI: `10.1088/1748-0221/12/01/p01020`.

[44] The CMS Collaboration. "The CMS high level trigger". In: *The European Physical Journal C - Particles and Fields* 46.3 (2006), pp. 605–667. ISSN: 1434-6052. DOI: `10.1140/epjc/s2006-02495-8`.

[45] CMS Collaboration. *The Phase-2 Upgrade of the CMS Tracker*. Tech. rep. CERN-LHCC-2017-009. CMS-TDR-014. Geneva: CERN, 2017. URL: `https://cds.cern.ch/record/2272264`.

[46]   FLUKA. URL: https://fluka.cern.

[47]   W Adam et al. "P-Type Silicon Strip Sensors for the new CMS Tracker at HL-LHC". In: *Journal of Instrumentation* 12 (2017), P06018–P06018. DOI: 10.1088/1748-0221/12/06/P06018.

[48]   M.E. Dinardo. "The pixel detector for the CMS phase-II upgrade". In: *Journal of Instrumentation* 10.4 (2015), p. C04019. DOI: 10.1088/1748-0221/10/04/c04019.

[49]   G. Steinbrueck. *Development of planar pixel sensors for the CMS Inner Tracker at the High-Luminosity LHC*. Tech. rep. CMS-CR-2020-073. 2020. DOI: 10.1016/j.nima.2020.164438.

[50]   Newsletter of the EP Department CERN. *Designing pixel readout chips at CERN: From dream to reality.* accessed on 25/06/2019. URL: https://ep-news.web.cern.ch/content/designing-pixel-readout-chips-cern-dream-reality.

[51]   Hamamatsu Photonics K.K. URL: http://hamamatsu.com.

[52]   *"Sylgard"*. "accessed: 12/05/2020". URL: https://www.dow.com/content/dam/dcc/documents/en-us/productdatasheet/11/11-31/11-3184-sylgard-184-elastomer.pdf?iframe=true.

[53]   Joern Schwandt. *CMS Pixel detector development for the HL-LHC*. Tech. rep. Geneva: CERN, Jan. 2018. DOI: 10.1016/j.nima.2018.08.121. URL: https://cds.cern.ch/record/2304744.

[54]   H Moriceau et al. "Overview of recent direct wafer bonding advances and applications". In: *Advances in Natural Sciences: Nanoscience and Nanotechnology* 1.4 (Feb. 2011), p. 043004. DOI: 10.1088/2043-6262/1/4/043004.

[55]   A. S. Grove. *Physics and Technology of Semiconductor devices*. John Wiley & Sons, 1967.

[56]   M. Glaser, F. Ravotti, and M. Moll. "Dosimetry Assessments in the Irradiation Facilities at the CERN-PS Accelerator". In: *IEEE Transactions on Nuclear Science* 53 (2005), PI5-1–PI5-7. DOI: 10.1109/RADECS.2005.4365632.

[57]   E. León-Florián, C. Leroy, and C. Furetta. *Particle fluence measurements by activation technique for radiation damage studies*. Tech. rep. CERN-ECP-95-15. CERN-ECP-95-015. Geneva: CERN, 1995. URL: http://cds.cern.ch/record/288409.

[58]   P. Allport et al. "Experimental determination of proton hardness factors at several irradiation facilities". In: *Journal of Instrumentation* 14.12 (2019), P12004. ISSN: 1748-0221. DOI: 10.1088/1748-0221/14/12/p12004.

[59] K. Ambrožič et al. "Characterization of gamma field in the JSI TRIGA reactor". In: *EPJ Web Conf.* 170 (2018), p. 04001. DOI: 10.1051/epjconf/201817004001.

[60] V. Cindro. *Transnational access to TRIGA Mark II reactor.* AIDA meeting, 2018.

[61] S. Wiederkehr. "The effective lifetime of $B_s^0 \to \mu^+\mu^-$ and designing a readout chip for pixel sensor development". Diss. ETH NO. 25640. PhD thesis. ETH Zurich, 2018. DOI: 10.3929/ethz-b-000314130.

[62] R. Horisberger et al. *ROC4SENS - a short description.* 31. RD50 workshop, CERN, Nov. 20-22, 2017.

[63] S. Spannagel, Beat Meier, and Hanno Christopher Perrey. *The pxarCore Library - Technical Documentation, Reference Manual, and Sample Applications.* Tech. rep. CMS-NOTE-2016-001. Geneva: CERN, 2015. URL: http://cds.cern.ch/record/2137512.

[64] D. Pitzl. Private Conversation, 2019.

[65] Simon Spannagel. "Test Beam Measurements for the Upgrade of the CMS Pixel Detector and Measurement of the Top Quark Mass from Differential Cross Sections". University of Hamburg, 2016. PhD thesis. DOI: 10.3204/DESY-THESIS-2016-010.

[66] Intel FPGA. URL: https://www.intel.com/content/www/us/en/products/programmable.html.

[67] R. Diener et al. "The DESY II test beam facility". In: *Nuclear Instruments and Methods in Physics Research Section A: Accelerators, Spectrometers, Detectors and Associated Equipment* 922 (2019), pp. 265–286. ISSN: 0168-9002. DOI: https://doi.org/10.1016/j.nima.2018.11.133.

[68] DESY Test Beam Coordinators. *DESY II test beams webpage.* accessed: 25.08.2020. URL: https://particle-physics.desy.de/test_beams_at_desy/index_ger.html.

[69] EUDET project. accessed: 22/06/2020. URL: https://www.eudet.org/index_eng.html.

[70] AIDA 2020 project. accessed: 22/06/2020. URL: http://aida2020.web.cern.ch/.

[71] A. F. Zarnecki and P. Niezurawski. *EUDET Telescope Geometry and Resolution Studies.* 2007. arXiv: physics/0703058v1 [physics.ins-det].

[72] Physik Instrumente. URL: https://www.physikinstrumente.com.

[73] DESY. accessed: 26/05/2020. URL: https://telescopes.desy.de/Hardware#PI-stages_for_moving_DUTs.

[74] H. Jansen et al. "Performance of the EUDET-type beam telescopes". In: *EPJ Techniques and Instrumentation* 3.1 (2016), p. 7. ISSN: 2195-7045. DOI: 10.1140/epjti/s40485-016-0033-2.

[75] D. Cussans. "Status of the TLU v0.2". In: *EUDET-Memo-2009-29* (2009).

[76] P. Ahlburg et al. "EUDAQ–a data acquisition software framework for common beam telescopes". In: *Journal of Instrumentation* 15.1 (2020), P01038. ISSN: 1748-0221. DOI: 10.1088/1748-0221/15/01/p01038.

[77] R. Brun and F. Rademakers. *ROOT - An Object Oriented Data Analysis Framework*. Lausanne, 1996. URL: http://root.cern.ch.

[78] D. Pitzl. URL: https://github.com/pitzl/tele-scope.

[79] S. Spannagel and H. Jansen. *GBL Track Resolution Calculator v2.0*. 2016. DOI: 10.5281/zenodo.48795.

[80] V. Chiochia et al. "Simulation of the CMS prototype silicon pixel sensors and comparison with test beam measurements". In: *IEEE Symposium Conference Record Nuclear Science 2004*. 2 (2004), 1245–1250 Vol. 2. DOI: 10.1109/NSSMIC.2004.1462427.

[81] I. Kopsalis. *Edge effects in Si pad diodes fabricated on high-ohmic wafers*. internal group meeting talk. 2017.

[82] Thomas Pöhlsen. "Charge Losses in Silicon Sensors and Electric-Field Studies at the Si-SiO$_2$ Interface". PhD thesis. Universität Hamburg, 2013. URL: http://www-library.desy.de/cgi-bin/showprep.pl?thesis13-025.

[83] M. Moll. "Displacement Damage in Silicon Detectors for High Energy Physics". In: *IEEE Transactions on Nuclear Science* 65.8 (2018), pp. 1561–1582. DOI: 10.1109/TNS.2018.2819506.

[84] I. Pintilie et al. "Radiation induced point- and cluster - related defects with strong impact to damage properties of silicon detectors". In: *2008 IEEE Nuclear Science Symposium Conference Record*. 2008, pp. 1587–1596. DOI: 10.1109/NSSMIC.2008.4774712.

[85] R. Klanner et al. "Determination of the electric field in highly-irradiated silicon sensors using edge-TCT measurements". In: *Nuclear Instruments and Methods in Physics Research Section A: Accelerators, Spectrometers, Detectors and Associated Equipment* 951 (2020), p. 162987. ISSN: 0168-9002. DOI: `10.1016/j.nima.2019.1 62987`.

[86] M. Moll et al. "Relation between microscopic defects and macroscopic changes in silicon detector properties after hadron irradiation". In: *Nuclear Instruments and Methods in Physics Research Section B: Beam Interactions with Materials and Atoms* 186.1 (2002), pp. 100–110. ISSN: 0168-583X. DOI: `10.1016/S0168-583X(0 1)00866-7`.

[87] E. Donegani. "Energy dependent proton damage in silicon". PhD thesis. University of Hamburg, 2017. DOI: `10.3204/PUBDB-2017-08798`.

[88] F. Feindt. *Edge-TCT for the Investigation of Radiation Damaged Silicon Strip Sensors*. Universität Hamburg, Masterarbeit, 2016. Hamburg. DOI: `10.3204/PUBD B-2017-00850`.

[89] N. Savić et al. "Performance of irradiated thin n-in-p planar pixel sensors for the ATLAS Inner Tracker upgrade". In: *Journal of Instrumentation* 12.12 (2017), pp. C12007–C12007. DOI: `10.1088/1748-0221/12/12/c12007`. URL: `https://do i.org/10.1088%2F1748-0221%2F12%2F12%2Fc12007`.

[90] N. Savić. "Development of pixel detectors for the Inner Tracker Upgrade of the ATLAS experiment". PhD thesis. Ludwig-Maximilians-Universität München, 2017. URL: `https://edoc.ub.uni-muenchen.de/22272/7/Savic_Natascha.pdf`.

[91] N. Savić et al. "Thin n-in-p planar pixel modules for the ATLAS upgrade at HL-LHC". In: *Nucl. Instrum. Meth. A* 845 (2017), pp. 154–158. DOI: `10.1016/j.nim a.2016.05.113`.

[92] G. Kramberger. "Modeling of electric field in silicon micro-strip detectors irradiated with neutrons and pions". In: *Journal of Instrumentation* 9.10 (2014), P10016. DOI: `10.1088/1748-0221/9/10/p10016`.

[93] M. Mikuž. "Drift Mobility and Electric Field in Silicon Detectors Irradiated with Neutrons and Protons up to 10^{17} neq/cm^2". In: *2015 IEEE Nuclear Science Symposium San Diego, CA* (2015).

[94] J. Schwandt et al. *A new model for the TCAD simulation of the silicon damage by high fluence proton irradiation*. 2019. arXiv: `1904.10234 [physics.ins-det]`.

[95] J. Schwandt. "A new model for the TCAD simulation of the silicon damage by high fluence proton irradiation". In: 32nd RD50 Workshop. Talk. 2018. URL: https://indico.cern.ch/event/719814/contributions/3022491/.

[96] M. Swartz. *A Detailed Simulation of the CMS Pixel Sensor*. Tech. rep. CMS-NOTE-2002-027. Geneva: CERN, July 2002. URL: https://cds.cern.ch/record/687440.

[97] Synopsys TCAD. URL: https://www.synopsys.com/silicon/tcad.html.

[98] J. Schwandt. Private Conversation, 2020.

[99] M. Swartz et al. "Observation, modeling, and temperature dependence of doubly peaked electric fields in irradiated silicon pixel sensors". In: *Nuclear Instruments and Methods in Physics Research Section A: Accelerators, Spectrometers, Detectors and Associated Equipment* (2006). DOI: 10.1016/j.nima.2006.05.002. URL: http://dx.doi.org/10.1016/j.nima.2006.05.002.

[100] Francesco Moscatelli et al. ""Combined Bulk and Surface Radiation Damage Effects at Very High Fluences in Silicon Detectors: Measurements and TCAD Simulations"". In: *IEEE Transactions on Nuclear Science* (). DOI: 10.1109/TNS.2016.2599560.

[101] Hans Bichsel. "Straggling in thin silicon detectors". In: *Rev. Mod. Phys.* 60 (3 1988), pp. 663–699. DOI: 10.1103/RevModPhys.60.663. URL: https://link.aps.org/doi/10.1103/RevModPhys.60.663.

[102] E. Currás et al. "First study of small-cell 3D Silicon Pixel Detectors for the High Luminosity LHC". In: *NIM A* arXiv:1806.01435 (June 2018). 20 pages, 19 figures, 8 p. DOI: 10.1016/j.nima.2019.04.037.

Acknowledgements

Many people have helped me during the past years and contributed to the work of this thesis. I would like to thank all my colleagues at the UHH detector lab for their help, especially my supervisor Prof. Dr. Erika Garutti. I thank Prof. Dr. Peter Schleper for giving me the opportunity to work on this thesis and for being the second examiner of this thesis.

The test beam measurements and their analyses would have been impossible without the help of Dr. Daniel Pitzl. Thank you for the support. I would like to thank Dr. Jörn Schwandt for his help with the simulation.

I had the pleasure of sharing an office with many people over the years, my special thanks goes to Finn Feindt and Mohammadtaghi Hajheidari for their valuable input and proof-reading of this thesis.

I would also like to thank my family for their support and patience.